Correlating X-ray microanalysis and cathodoluminescence data from III-nitride semiconductors

PhD Thesis

Lucia Spasevski

The Semiconductor Spectroscopy and Devices research group

Department of Physics

University of Strathclyde, Glasgow

July 2021

Declaration of author's right

This thesis is the result of the author's original research. It has been composed by the author and has not been previously submitted for examination which has led to the award of a degree.

The copyright of this thesis belongs to the author under the terms of the United Kingdom Copyright Acts as qualified by University of Strathclyde Regulation 3.50. Due acknowledgement must always be made of the use of any material contained in, or derived from, this thesis.

Signed:

Date:

Abstract

Research in group III- nitride semiconductors has seen major developments during the last couple of decades. One of the materials that satisfy requirements for optoelectronic devices in the ultra-violet (UV) spectral range and high power, high frequency electronic devices is the AlGaN. Performance and reliability of these devices will strongly depend on the electronic properties of epitaxial layers which are critically affected by structural defects and unintentional and intentional doped impurities. This thesis presents research on III- nitride semiconductors, in particular AlGaN and GaN materials. It is focused on characterization of AlGaN materials and the effects of n- and p-type doping, AlN content, occurrence of defects and crystal orientation on its quality. Different electron microscopy techniques are used to investigate luminescence, composition and doping properties of semiconductor structures and their correlation with surface features. The main techniques used for the characterization consisted of cathodoluminescence spectroscopy (CL) for the probing of luminescence properties, secondary electron (SE) and backscattered electron (BSE) imaging for investigation of the sample morphology and wavelength dispersive X-ray (WDX) spectroscopy for compositional analysis. The type of growth method and choice of substrate have a great influence on the surface morphology and luminescence homogeneity of the AlGaN layer, with compositional inhomogeneity of the MBE samples confirmed only on sub μm level but having lower emission intensity compared to MOCVD samples. The thesis presents detailed steps of a procedure to quantify trace elements and investigates the associated challenges. The whole process of measurement optimization for Mg and Si dopants is described and final recipe on how to measure the concentration of major (alloy) and minor Si/Mg (dopant) elements is presented. A systematic study of polar and semipolar n-type doped AlGaN/AlN layers grown on sapphire by (MOCVD) with varied Si/group-III ratios in the gas phase was accomplished. The AlN incorporation was higher in the polar samples and the highest values of Si incorporations were observed for the polar samples with the highest Si/III ratios, while saturation of Si incorporation was seen for the semipolar samples at higher Si/III ratios. CL point spectra showed how changes in the relative intensity of the NBE peaks and impurity transitions depend strongly on the growth conditions and surface orientations. The semipolar samples showed better compositional homogeneity. A study was also performed on AlGaN:Mg samples to study the impurity transitions and luminescence properties of non LED epilayer

samples grown on MOCVD AlN/sapphire templates and more complicated LED structures with different numbers of MBE-grown layers. MBE samples showed superior quality to other combinations of MBE and MOCVD structures, mainly due to problems associated with the transfer of sample between different reactors and the introduction of impurities that will form different defects within the material. Finally, some proposals for future work are presented.

Acknowledgements

I would like to extend my gratitude and thanks to all the people who helped and supported me during the course of my PhD.

First and foremost, I would like to thank my supervisor Prof. Rob Martin, who provided me with excellent support, advise, encouragement and patience throughout my PhD journey. This work would not have been possible without it and I feel privileged to had his guidance.

I would like to thank Dr. Paul Edwards, who taught how to use the cathodoluminescence system, and for his unlimited patience whenever I needed some assistance with microscopes or an advice. I will always remember enjoying solving cryptic puzzles during lunch breaks.

Thank you to Dr. Carol Trager-Cowan for always being there for her students and her support and guidance and sharing her knowledge and advice in fruitful discussions.

I am very grateful to Dr. Jochen Bruckabauer for his kind and caring manner and also experimental help accompanied by useful discussions.

Another big thank you goes to all the people in the SSD group,

Specially to my dear colleague Catherine Brasser, I have enjoyed sharing office with her and all the problems and happy moments together. Dr. Gergely Ferenczy, for making coffee breaks more interesting. PhD would not be the same without having you all there: Douglas Cameron, James Denholm, Dale Waters, Daniel A. Hunter, Aeshah M. A. Alasmari, Pavlos Bozinakis, Matat Jablon, Fabien Massabuau, Naresh Kumar, Gunnar Kusch, Elena Pascal… I have always enjoyed spending time with you all on Level 2 around the coffee table.

I would also like to extend a big thank you to all the collaborators who have provided me with samples:

From the Tyndall National Institute, Prof. Peter Parbrook, Dr. Pietro Pampili, Dr. Vitaly Z Zubialevich, Dr. Duc V Dinh. Dr. Johannes Enslin, Dr. Tim Wernicke, Dr. Frank Mehnke and Dr. Michael Kneissl from Technische Universität Berlin. My collaborators in the University of Bristol, Dr. Ben Buse. I would like to thank for teaching me how to use electron microbe and later on for all the help with the paper.

For the financial support I would like to acknowledge the University of Strathclyde.

My friends in Croatia, who I missed deeply but luckily we stayed connected, Korana, Dario, Marija, Ana, Djuro, Sonja, Tomislav, Hrvoje, Iva, Petra and of course my dear colleagues from University, our group Kemicarke (Chemists).

I would also like to thank my family, my parents, Marin and Diana, grandma Katica for their continued support throughout my studies. Specially to my dear sister Sofia, who spent so many hours talking with me and encouraging me, I cannot imagine having better sister.

My biggest gratitude goes to my husband Tomi, to whom I dedicate this work, who always supported me, believed in me and help me to achieve my dreams, without his love and help I wouldn't be able to come to the end of this long road.

List of Publications

First authored

1. Spasevski, L., et al., A systematic comparison of polar and semipolar Si-doped AlGaN alloys with high AlN content. Journal of Physics D: Applied Physics, 2020. 54(3): p. 035302.
2. Spasevski, L., et al., Quantification of Trace-Level Silicon Doping in $Al_xGa_{1-x}N$ Films Using Wavelength-Dispersive X-Ray Microanalysis. Microscopy and Microanalysis, 2021: p. 1-9.

Co-authored

1. Edwards, P.R., et al., *You Do What in Your Microprobe?! The EPMA as a Multimode Platform for Nitride Semiconductor Characterization.* Microscopy and Microanalysis, 2018. **24**(S1): p. 2026-2027.
2. Ajia, I.A., et al., *GaN/AlGaN multiple quantum wells grown on transparent and conductive (-201)-oriented β-Ga2O3 substrate for UV vertical light emitting devices.* Applied Physics Letters, 2018. **113**(8): p. 082102.
3. Trager-Cowan, C., et al., *Scanning electron microscopy as a flexible technique for investigating the properties of UV-emitting nitride semiconductor thin films.* Photonics Research, 2019. **7**(11): p. B73-B82.
4. Kusch, G., et al., *Influence of InN and AlN concentration on the compositional inhomogeneity and formation of InN-rich regions in In x Al y Ga1−x−y N.* Japanese Journal of Applied Physics, 2019. **58**(SC): p. SCCB18.
5. Enslin, J., et al., *Indium incorporation in quaternary In x Al y Ga1−x−y N for UVB-LEDs.* Japanese Journal of Applied Physics, 2019. **58**(SC): p. SC1004.
6. Skidchenko, E., et al., *Excitons in PL Spectra of Cu(In,Ga)Se2 Single Crystals.* Physics of the Solid State, 2019. **61**(5): p. 918-924.

List of figures

List of tables

List of Abbreviations

AFM Atomic force microscope

AlGaN Aluminium Gallium nitride

AlN Aluminium nitride

BN Boron nitride

BSE Backscattered electrons

BSF Basal plane stacking fault

C-coating Carbon coating

CBM Coneduction-band maximum

CCD Charge-coupled device

CL Cathodoluminescence

CH crystal field hole

COMPO Composition image

DAP Donor-acceptor pair transition

DL detection limit

DNA Deoxyribonucleic acid

D-SIMS Dynamic secondary ion mass spectrometry

DT Dead time

DUV deep ultra-violet

DX centre distorted donor

EBL Electron-blocking layer

EBIC Electron beam-induced current

ECCI Electron channelling contrast imaging

EDX energy-dispersive spectrometer

EL Electroluminescence

ELOG Epitaxial lateral overgrowth technique

EPMA Electron microprobe

ESEM Environmental scanning electron microscope

EQE External quantum efficiency

E–T Everhart Thornley detector

FE Field-emission

FEG field emission gun

FET Field effect transistor

FWHM Full width at half maximum

GaAs Gallium arsenide

GaN Gallium nitride

GSL Graded superlattice

HH heavy hole

HEMT High-electron-mobility transistor

HPC hexagonally close packed structure

HSI Hyperspectral imaging

IC Intermittent contact mode

InGaN Indium gallium nitride

InN Indium nitride

InP Indium phosphide

InSb Indium antimonide

IQE Internal quantum efficiency

JM Johnson's figure of merit

LA-ICP-MS Laser ablation inductively coupled plasma mass spectrometry

LEE light-extraction efficiency

LH light hole

LD Laser diode

LDE Synthetic multi-layered diffracting crystal

LDE1L Large synthetic multi-layered diffracting crystal

LED Light-emitting diode

LiF Lithium fluoride crystal

MBE Molecular beam epitaxy

MC Monte Carlo simulation

MCA Multichannel analyser

MISFET Metal-insulator-semiconductor field effect transistor

MOCVD Metal-organic chemical vapour deposition

MOVPE Metal-organic vapour phase epitaxy

MQW Multiple quantum well

NADH nicotinamide adenine dinucleotide

NBE Near band edge

NPSS Nanopatterned sapphire substrates

NR nonradiative recombination rate

PAMBE Plasma assisted molecular beam epitaxy

PCA Principal component analysis

PET penta erythro crystal

PHA Pulse-height analysis

PL Photoluminescence

PSPD Position sensitive photodetector

PPB One part per billion

PPM One part per million

PSF Prismatic stacking fault

RHEED Reflection high-energy electron diffraction

RNA Ribonucleic acid

RSF Relative sensitivity factors

RTA Rapid thermal annealing

SCA Single channel analyser

SE Secondary electron

SE Schottky-emission

SEM Scanning electron microscope

SiC Silicon carbide

SIMS Secondary ion mass spectrometry

SO spin-orbit coupling band

SDD Silicon-drift detector

SQW Single quantum well

SF Stacking fault

2DEG Two-dimensional electron gas

TAP Thallium acid phthalate crystal

TAPL Large thallium acid phthalate crystal

TD Threading dislocation

TDD Threading dislocation density

TE Thermionic emission

TEM Transmission electron microscope

TMAl Trimethylaluminium

TMGa Trimethylgallium

TOF Time-of-flight analysers

TOPO Topography image

QW Quantum well

UHV Ultra high vacuum

μ-PIXE Micro particle-induced X-ray emission

UV Ultra-violet

VBM Valence-band maximum

WDX Wavelength dispersive X-ray spectroscopy

Z Atomic number

ZAF matrix effects (atomic number, absorption and fluorescence)

Contents

Chapter 1

1. Introduction

The 20th century was marked by important technological inventions, such as discovery of the p-n junction and later emergence of red and yellow/green light emitting diodes (LEDs) in the 1960s and yellow in the 1970s. An LED emitting efficiently in the blue part of spectrum was still missing and theoretical predictions were that it won't be possible to grow p-type wide bandgap semiconductor [1]. However, not everyone abandoned that possibility and Professor Isamu Akasaki and Hiroshi Amano of Nagoya University and Shuji Nakamura employed by Nichia Chemicals, worked on the synthesis of GaN crystals with p-type doping. Professor Akasaki made a breakthrough in 1989 with the world's first GaN p-n junction light emitting diode. It was a major technological discovery and big push for the nitride semiconductors field [2]. Another important discovery was use of an aluminium nitride (AlN) buffer layer that improved the crystal quality [3]. The invention of the blue LED and laser in the 1990s helped to establish many new industries, such as solid state traffic lights, UV nitride lasers in high density DVD recorders, solid state white light illumination, high temperature devices, nano-structures and biotechnology [4].

Significant progress in the field of GaN optoelectronic devices has been made in the last two decades, especially for LEDs and lasers operating in the blue and near-UV spectral range. LEDs based on III-nitrides have revolutionized the lighting industry. In addition, III-nitride solar cells and thermoelectric development will be essential for the sustainable and renewable energy economy [5]. GaN is also a favourable material for high-temperature and high-power electronic devices because of its large bandgap. GaN based heterojunction bipolar transistors and field-effect transistors are developing significantly [6]. By 2023, the market for GaN-based semiconductor devices is predicted to reach 22.5 billion dollars [7].

The group III-nitrides (GaN, AlN, InN) and their alloys have many outstanding physical properties, such as high thermal conductivity, large critical electric field, high saturation electron drift velocity, small dielectric coefficient [8].

The bandgaps of the III-nitride semiconductors cover a large spectral range from deep ultraviolet (~200 nm) to near infrared (~1900 nm). AlN-rich AlGaN is of particular interest due to its low lattice mismatch and dislocation density when grown on AlN single crystal substrates versus heterogenous growth on non-native substrates. AlGaN alloys with a continuous wide direct band gap have been shown to be the most suited compound semiconductor for device in the UV range (~363-200 nm) and to have the potential to replace traditional UV emitters such as Hg lamps. AlGaN material is particularly employed for deep UV radiation purposes (<285 nm) like water- and air purification [9]. The AlGaN and AlInN are the only III-nitrides alloy systems with direct and tunable band gap in the UV region. However, the growth of AlInN is more challenging compared to AlGaN due to the bigger difference in growth temperature of InN (~600°C) and AlN (~1200-1600°C), compared to GaN (~1100°C) [10].

However, research still continues in order to produce higher efficiency LEDs and lasers based on III-nitrides covering the deep UV, visible and near -IR spectral range. A lot of effort is being invested on the synthesis and characterisation of nitride materials and processes necessary to develop devices based on them [11]. The limited use of III-nitrides for those spectral ranges can be ascribed to presence of large densities of defects and dislocations caused by a lack of suitable lattice-matched substrates, large polarization fields resulting in quantum-confined Stark effect and challenges associated with doping.

In this work, the luminescence characteristics and compositional properties of III-nitride GaN and AlGaN epitaxial layers are investigated. Cathodoluminescence (CL) spectroscopy of $Al_xGa_{1-x}N$ structures allowed analysis of near band edge emission in the UV spectral range above 4.0 eV as well as various deep impurity transition peaks in the blue-UV range 2.7–4.8 eV. Wavelength dispersive X-ray (WDX) spectroscopy was used to determine the AlN mole fraction ($x \approx 0.57$–0.85), Si dopant concentration (3×10^{18} –1×10^{19} cm^{-3}) and Mg dopant concentration (2×10^{19} –8×10^{19} cm^{-3}) in various series of $Al_xGa_{1-x}N$ samples. After a short introduction to the III-nitride materials and devices in Chapter 2, the experimental methods used in this thesis are described in Chapter 3. In Chapter 4 cathodoluminescence and wavelength dispersive spectroscopy are employed to investigate AlGaN layers grown using MOCVD

and MBE techniques. The quantification of Si (n-type dopant) content at low concentration is studied in Chapter 5. This optimal procedure was then employed to investigate the composition of polar and semipolar AlGaN layers together with their luminescence properties in Chapter 6. AlGaN layers doped with Mg (quantum wells and different types of LED samples) are examined using the same techniques described in Chapter 7. Finally, Chapter 8 gives a summary of the main results of this thesis along with suggestions for future work.

1.1 Techniques and samples

This thesis presented work on the analysis of AlGaN and GaN, Si or Mg doped semiconductor materials by the SEM based techniques of CL hyperspectral imaging, SE, BSE imaging and WDX spectroscopy. Other measurement techniques, such as AFM and SIMS were provided by collaborators, these include: the group of Prof. Siddharth Rajan at Ohio State University[1], the group of Prof. M. Kneissl at TUBerlin[2] and the group of Prof. P. J. Parbrook at Tyndall National Institute[3]. Different types of samples were analysed and the results are presented in four chapters depending on type of samples or measurements performed. Chapters include "Analysis of AlGaN layers" for samples where the main research interest was focussed on the properties of AlGaN layers grown using MOCVD and MBE techniques on different substrates and with inclusion of different layers, "Measurement of Si at low concentration" is oriented towards Si dopants measurement optimization using WDX technique, "Polar and semipolar Si-doped AlGaN alloys" reports on a systematic study of luminescence properties and composition of polar and semipolar n-type doped AlGaN layers, and final experimental chapter "Measurement of Mg at low concentration at low concentration" revolves around Mg dopants measurements using WDX and luminescence characteristics of AlGaN: Mg samples (LED and non-LED samples).

[1]providing AFM mages

[2]providing SIMS measurements

[3]providing AFM and PL measurements

Chapter 2

2. Background

2.1 The III-nitrides

Group III-nitrides are compounds composed of elements from group III of the periodic table along with nitrogen from group V. They are comprised of BN, InN, GaN, and AlN, along with their ternary and quaternary alloys. These crystals exhibit wurtzite, zincblende, and rock salt structures. The crystal structure depends on the degree of ionicity, with crystals of high ionicity tending to show wurtzite structures [12].

III-nitrides family members: AlN, GaN, InN and their alloys offer many advantageous properties. They have a large potential to be used in optoelectronic devices (emitters and detectors) and high power/temperature electronic devices. However, these semiconductors are a lot harder to grow than the regular Si and GaAs semiconductors. They have direct bandgaps ranging from 0.7 eV for InN to 3.4 eV for GaN to 6.0 eV for AlN [13]. After fundamental breakthroughs made by Akasaki, Amano and Nakamura, this alloy system is now known as the base for the highly successful technology of blue lasers and blue and white LEDs [3,14-16]. The aforementioned Japanese researchers were awarded the Nobel Prize for Physics in 2014 for their work on III-nitride light emitters.

SiC and silicon have indirect band gaps and are unsuitable for opto-electronic materials. Contrarily, the tunable range of direct bandgaps (0.7−6.0 eV) make the III-nitrides suitable candidates for optoelectronic devices that emit and absorb in the different regions of electromagnetic spectrum such as infrared, visible, and deep ultraviolet. This enables devices such as light emitting diodes (LED's) and laser diodes (LD's) emitting anywhere from the far infrared to deep ultraviolet spectral region. For example, introduction of some InN into the GaN lattice causes the alloy bandgap to reduce and the emission is shifted towards the blue and the green. Adding increasing amounts of AlN has the opposite effect of shortening the emission wavelength [17].

The III-nitride semiconductors are characterised by large electronic polarization fields (spontaneous and piezoelectric) which affects the electronic properties (band diagrams, charge distributions) of layered structures. Wurtzite crystals exhibit polarization fields along the c (0001) axis. Polarization fields, when suitably controlled, can be exploited for engineering device structures. For example, polarization can be used to induce free carriers (doping), and facilitate activation of deep carriers, to create tunable heterojunction band offsets or to achieve below-gap optical transitions [18]. Another advantage is their relatively high thermal conductivities, thermal stabilities, electric breakdown fields, and electron mobility which makes them a perfect candidate for high power electronic devices [19]. Contrary to most III-nitrides semiconductors, such as GaAs and InP, the III-nitride crystals prefer to have the hexagonal wurtzite structure rather than a zincblende crystal structure. The material properties of AlN, InN and GaN including the energy band-gaps, dielectric constants, lattice constants, stiffness constants, piezoelectric constants and effective electron masses are tabulated in Table 2.1 [7,12,20-23]

Table 2.1: Material properties of wurtzite AlN, GaN and InN crystals.

Material Properties	AlN	GaN	InN
Band gap, E_g (300 K)(eV)	6.2	3.39	0.63
Dielectric constant ε_r	8.5	8.9	15.3
electron mobility (bulk)(300 K) [cm^2/ Vs]	300	440	70−250
Lattice constant, a_0 (nm)	0.3112	0.3188	0.354
Lattice constant, c_0 (nm)	0.4982	0.5185	0.5705
c_0/a_0 ratio	1.6190	1.6336	1.6270
Piezoelectric constant e_{33} (C/m^2)	-0.58	-0.33	-0.22
Piezoelectric constant e_{31} (C/m^2)	1.55	0.65	0.43
Spontaneous polarization (C/m^2)	-0.081	-0.029	-0.032

2.2 Crystal structure

Group III-nitrides can have the following crystalline structures: the wurtzite and zincblende. Under ambient conditions, the thermodynamically stable structure is wurtzite for bulk AlN, GaN, and InN. AlGaN can crystalize in stable hexagonal wurtizte and a metastable zincblende structure. Semiconductor layers analysed in this thesis possess the wurtzite structure. Both structures have a tetrahedral atomic coordination where each cation (Al or Ga) is surrounded by four anion (N) atoms [24].

The wurtzite structure consists of two interpenetrating hexagonally close packed (HCP) sublattices. One sublattice contains group III atoms (e.g. gallium, indium, or aluminium atoms) and the other group V nitrogen atoms. One sublattice is offset by $3/8 \times c_0$, where c_0 is the height of the hexagonal lattice cell. Due to the differences in electronegativity of the N and group III atoms, the crystal structure is non-centrosymmetric [25]. A schematic diagram of wurtzite structure is shown in Figure 2.1.
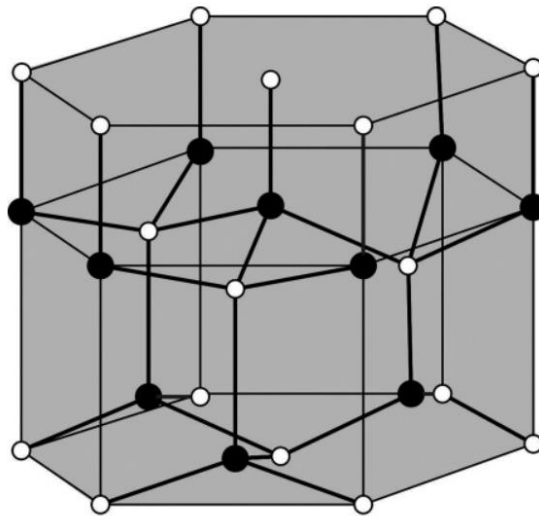
Figure 2.1: Ball-and-stick model of wurtzite crystal structure. The large spheres are the group III elements, and the smaller spheres are atoms of the group V element, nitrogen. From Ref [26].

The bonds between Ga and N atoms are predominantly covalent, but due to the difference in the electronegativity of Ga and N atom, (N is the most the most electronegative group V element, strong electron affinity generated from its

$1s^22s^22p^3$ electronic configuration), the covalent sp^3 Ga-N hybrid bonds also has a significant ionic contribution [20].On the contrary, in GaAs, InP and InSb the covalent contribution is dominant. Like in the case of GaN, AlGaN also has higher degree of ionicity compared to other III-nitrides semiconductors (such as AlGaAs) which will result in strong chemical bonds and affect many of the AlGaN properties [27]. The difference in ionic radii between the constituent atoms of III-nitrides is significant: 76 pm for Ga, 30 pm for N and 60 pm for As. As a result, the lattice constants will be smaller for the III-nitride semiconductors, as shown in Figure 2.2.
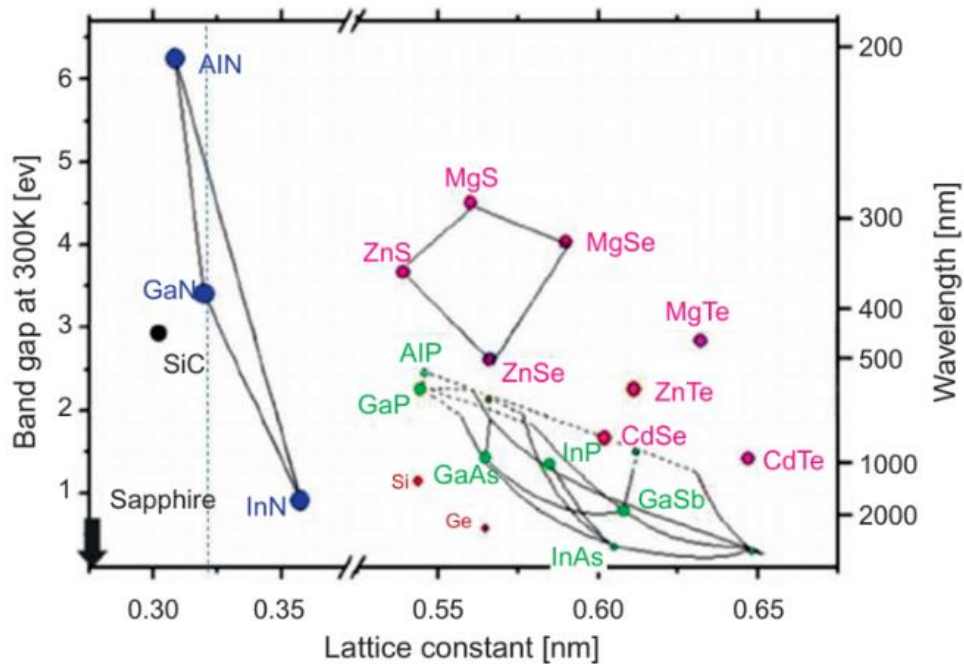
Figure 2.2: Bandgaps of different semiconductor materials vs lattice constant. From Ref. [28]

The wurtzite crystal structure is not symmetric in the [0001] and [000$\bar{1}$] directions, which are described as having Ga- or N- termination (N-face is a 180° rotation from Ga-face) (Figure 2.3). The crystal structure grown along the c-axis ([0001] direction) are called crystals with Ga-face polarity and those crystals grown in the [000$\bar{1}$] direction possess N-face polarity. GaN grown for the device fabrication purposes are mostly Ga-face due to their ease of growth with high quality compared to N-face structures.
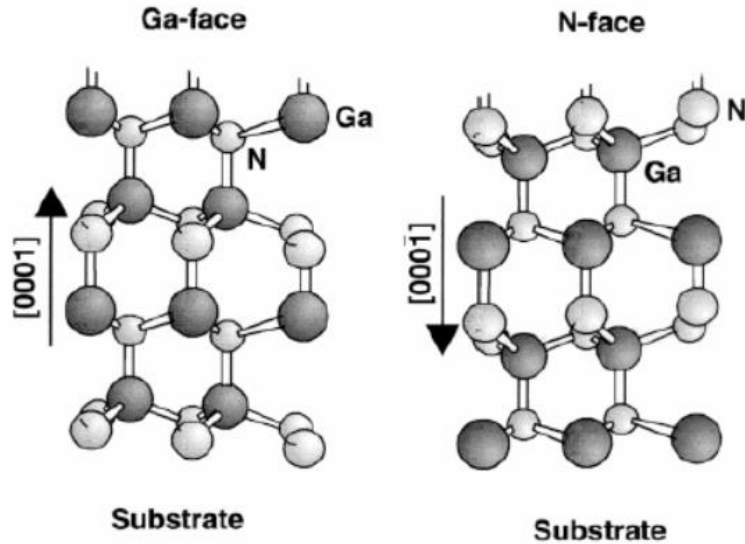
Figure 2.3: Wurtzite crystal structure for the Ga-face and N-face polarities of GaN. From Ref [29].

The wurtzite crystal of GaN is grown in the form of a structure that consists of alternating bi-atomic closely-packed planes of Ga and N pairs stacked in an ABABAB sequence along the wurtzite direction [0001] and in the zincblende structure stacking order is ABCABC along the [111] direction. The differences between the wurtzite and zincblende structures are shown in Figure 2.4. The fundamental difference between these structures is the interaction with the second nearest neighbour. Considering the cation B and the vertical bond to the nearest neighbour anion atom, b. In the zincblende case, shown in (a), the next-nearest neighbour is in a "new" site C, whilst in the wurtzite case the relevant bond is rotated so the next-nearest neighbour is in site A as for the cation layer just below B. This gives an ABCABC stacking sequence for anions (or cations) in zincblende, compared to ABABAB in wurtzite.

Interactions between the ions cause a decrease in the ratio of the lattice parameters of the hexagonal phase, c/a, and an increase in u value, dimensionless internal parameter (non-ideality factor). In ideal wurtzite structure, the lattice parameters are $c/a = \sqrt{8/3} = 1.663$ and $u = 3/8 = 0.375$. The internal parameter u is defined as the anion-cation bond length along the c-axis (also the nearest neighbour distance or the interatomic distance)[30].
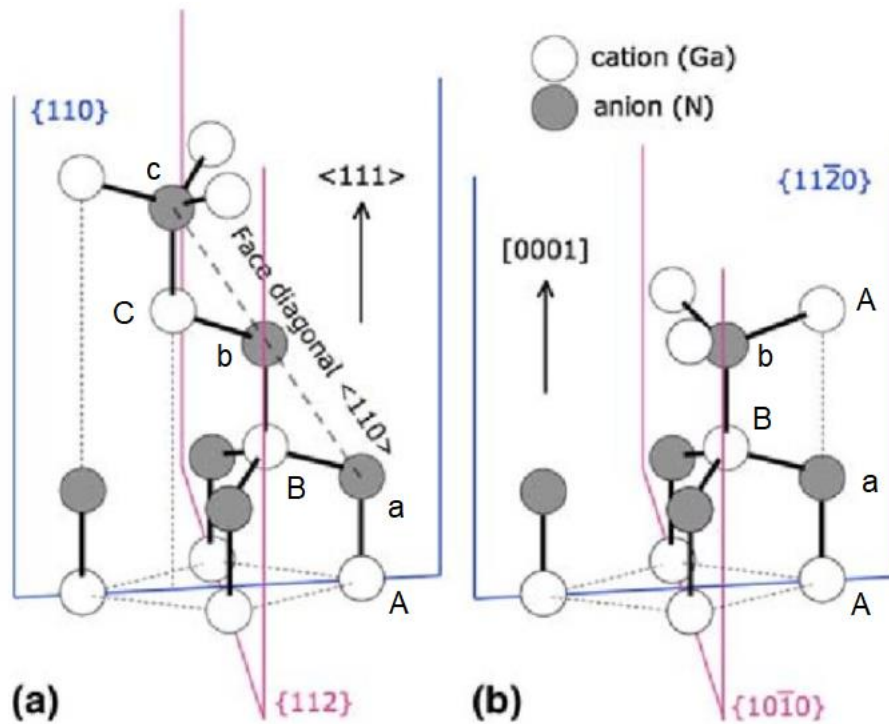
Figure 2.4. Perspective view of (a) zincblende and (b) wurtzite structures drawn with the polar axis parallel to each other. The white and black spheres indicate the cation and anion atoms, A, B, C (a, b, c) denote the cation (anion) position. From Ref. [31].

Because of the different metal cations, the c/a ratios of AlN, GaN and InN are different. Different crystal planes (a-, c-, m-, and r-planes) are shown in Figure 2.5. Different planes will exhibit quite different behaviour in terms of polarization, mixed versus unmixed surface terminations, and atomic arrangements in the respective planes [32].
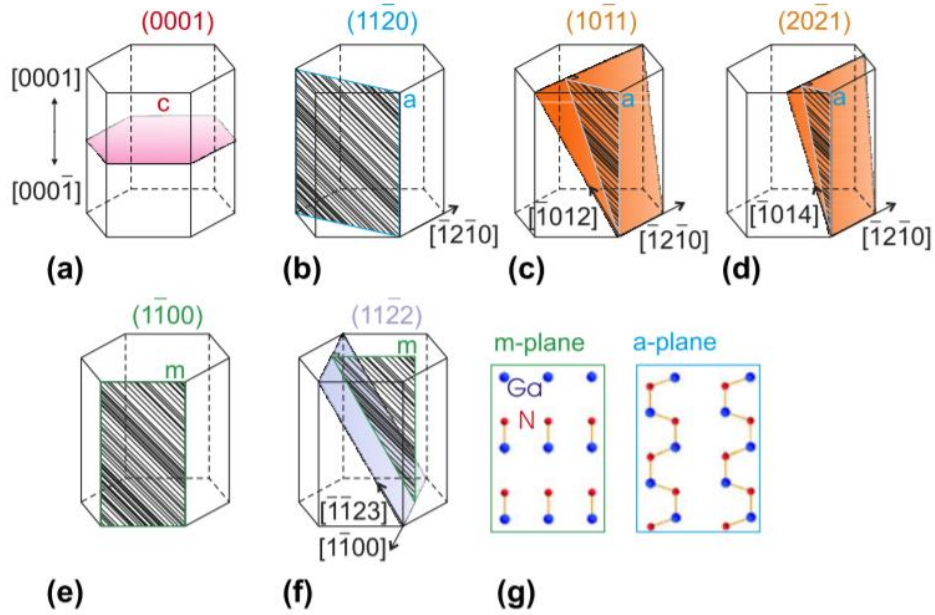
Figure 2.5: Important crystallographic planes of the wurtzite structure: (a) polar c-plane [33], nonpolar (b) a-plane ($11\bar{2}0$) and (e) m-plane ($1\bar{1}00$), semipolar planes of m-group (c) ($10\bar{1}1$) and (d) ($20\bar{2}1$) and a-group (f) ($11\bar{2}2$) are shown. The a-plane and m-plane are perpendicular to the m-group and a-group semipolar surfaces, respectively. From Ref. [34].

In this thesis, the samples studied were oriented in c-plane and a-semipolar plane. The number of bonds/area is small for the c planes, they have lowest free energy, and arise most often during growth, cleaving and etching [35]. The asymmetry of the wurtzite structure will impact the polarization fields and the chemical reactivity of different planes. For example, the Ga-face surface is nonreactive in acids and bases while the N-face surface etches in bases.

The crystal structure of the wurtzite system together with partially ionic (partially covalent) bond of Al, Ga and In to N atom will lead to the relatively strong piezoelectric and spontaneous polarization effects, that are a crucial characteristic of the nitride devices [36]. In III-nitrides, although the covalent bond parallel to the c-axis is strongly ionic and is primarily responsible for the spontaneous polarization, the other three covalent bonds in the tetrahedral structure are also equally ionic. This ionic character combined with the crystals non ideality factor gives rise to large polarization effects. Because this polarization occurs in III-nitride materials under zero strain it is known as spontaneous polarization. Wurtzite structures have spontaneous polarization

along the c-axis [24]. Apart from spontaneous polarization, additional polarization effects can also be introduced in the lattice structure through strain. If external stress is applied, the lattice parameters c and a of the crystal structure will try to modify themselves to accommodate the stress thus changing the polarization strength. This additional polarization in strained III-nitrides crystals is called piezoelectric polarization. For optoelectronic devices, spontaneous and piezoelectric polarization can be problematic due to the quantum confined Stark effect. For example, when III nitride quantum wells are grown along the polar axis, both the piezoelectric and spontaneous electric fields cause the bands to bend, as shown in Figure 2.6. Due to this band bending the overlap of the electron and hole wavefunctions is poor, which causes a reduction of the internal quantum efficiency and a shift of the emission wavelength.
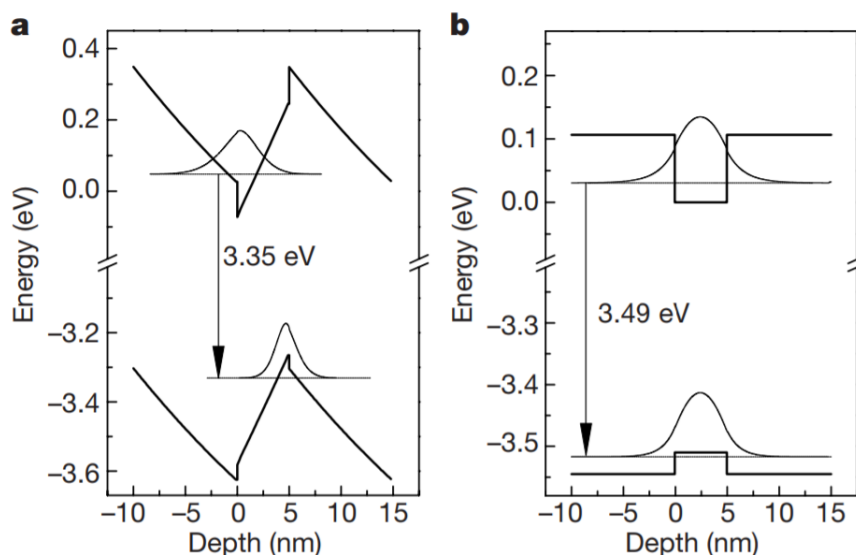
Figure 2.6: Schematic representation of band profiles and electron and hole wave functions from Ref. [37] for (5 nm GaN)/(10 nm $Al_{0.1}Ga_{0.9}N$) quantum wells grown along the a) polar and b) non-polar orientations.

This problem can be minimised by using a non-polar orientation [38]. Growth along c-direction has been extensively studied while growth along other directions needs to be further developed. On the other hand, the polarization may be used in a positive way to use the electric fields to create polarization induced electron or hole gases and to avoid difficulties related to obtaining highly conductive AlGaN [39].

2.3 Band structure

The wurtzite crystals of AlN, GaN and InN all have direct-transitions bandgap structures in contrast to AlN and BN cubic structures with indirect bandgaps. The bandgap values are shown in Table 2.1. The difference in bandgap structures of wurtzite and zincblende system is shown in Figure 2.7. For the wurtzite system, the energy at the Γ-point is split into three levels due to the crystal field and spin–orbit coupling and the three resulting valence bands are called heavy hole (HH or A band), light hole (LH or B band), and crystal field hole (CH or C band), respectively. While, for the zincblende system the valence bands are HH, LH and spin-orbit coupling band (SO). The crystal-field interaction is not present in the zincblende due to its crystallographic symmetry, and therefore there are no polarization field effects along the <001> directions [40].
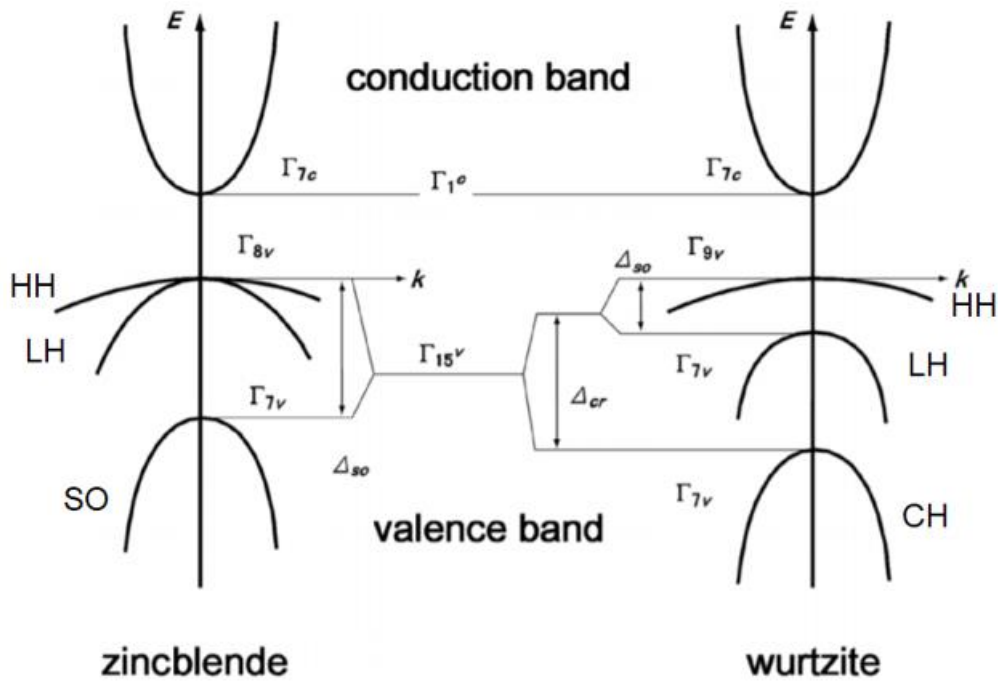
Figure 2.7: Band structures of zincblende and wurtzite structures near the Γ-point. From Ref [12].

The temperature dependence of the bandgap energy is often given by the semi-empirical Varshni formula resulting in the following relationship:

$$E_g(T) = E_0 - \alpha T^2/(T + \beta) \tag{2.1}$$

where α and β are fitting parameters characteristic of a given material. In certain cases β can even be negative, so the better solution would be to replace it with the three parameter thermodynamic function to fit the temperature dependences, as presented in Ref. [41]:

$$E_g(T) = E_g(0) - S < \hbar\omega > [\coth(< \hbar\omega >/2kT) - 1] \qquad (2.2)$$

Where $Eg(0)$ is the band gap at zero temperature, S is a dimensionless coupling constant, and ($\hbar\omega$) is an average phonon energy.

The lattice constants of the alloys generally follow Vegard's law and are proportional to the mole fractions of binary crystals, with AlInP and AlInN as exceptions[42] [43]. The energy bandgap, $E_g(x)$, of a semiconductor composed of two semiconductor compounds, each with bandgaps E_gA and E_gB, can be approximated as:

$$E_g(x) = E_{gA}x + E_{gB}(1 - x) - bx(1 - x) \qquad (2.3)$$

where x is the molar fraction and b is termed the bowing constant, there are still likely to be fluctuations in the reported values for the bowing constant. The bandgap energy of AlGaN depends on the Al content, and at room temperature, ranges from 3.5 to 6.2 eV. The bandgap is direct for all compositions [36].

2.4 Doping of III-nitrides

Doping control is mandatory for the fabrication of most optical and electrical devices. N-and P-type layers are required in devices, such as LEDs, laser diodes, photodiodes and bipolar transistors. If a lattice atom is substituted by a dopant with extra electrons in the outer shell it is called a donor and the process is called n-doping. If an atom with fewer electrons in the outer shell than the substituted atom is incorporated into the crystal lattice, it acts as an acceptor and the process is called p-doping.

The activation energy of donors is given by the following equation:

$$E_D = 13.56 \left(\frac{1}{\varepsilon_r}\right)^2 \frac{m_e}{m_o} \ [eV] \qquad (2.4)$$

Where ε_r is the relative dielectric constant of material, and m_e is the effective mass of conduction band electrons. For example, the activation energy of Si in GaN was determined to be 30 meV (from Hall effect and PL measurements). This value is in good agreement with a hydrogen-like model (Eq.2.3) [12]. At increased donor concentrations, the impurity potentials from different donors start to overlap and the donor activation energy E_D decreases. When a critical doping concentration is achieved the material will undergo a Mott transition, which is the transition from an insulator to a metal [44]. For n-type AlGaN with 70% AlN the reported critical concentration is $\sim 1.5 \times 10^{19}/cm^3$ [45].

2.4.1 Doping of GaN

Possible donors used in GaN are Si, O (substituting N with O), Se and Ge. N-type doping of GaN using Si is a well understood process, Si-doped GaN is routinely grown with bulk electron mobility above 300 cm^2/Vs. Si will act as a single shallow donor incorporating on a Ga-site, with near complete donor ionization at room temperature. Different Si concentrations can be incorporated from 10^{17} to 10^{19} cm^{-3}. Some structural problems, like cracking, can occur in heavily doped and thick films. The tensile strain from doping arises due to substitution of Si in place of Ga in the GaN lattice which will result in a net contraction of the lattice as the Si atoms (100 pm) are smaller than the Ga atoms (130 pm)[46,47]. Furthermore, Si dopant is able to "pin" the dislocations, preventing them from absorbing the tensile stress that develops during growth. Consequently, Si-doped films are usually under higher levels of tensile stress compared to undoped GaN films, which will result in film cracking due to the absence of other stress relief mechanisms [48].

In 1989, highly resistive Mg-doped GaN crystals were transformed into conducting p-type films by irradiation with a low-energy electron beam. Hydrogen desorption was found to be the important effect producing acceptor activation and p-type GaN films [2]. Mg will form an "quasi –shallow "acceptor state in GaN which is located more than 170 meV above the valence band edge. Due to the nature of this acceptor level only several percent ionization is possible at room temperature, which explains the need for excessively high Mg

concentrations in order to achieve 10^{17} cm^{-3} concentration of Mg in GaN. Due to high Mg concentration the hole mobility will be degraded (bellow 10 cm^2/Vs) resulting in resistive (>2Ω/cm) films [27].

2.4.2 Doping of AlGaN alloys

N-and P-type AlGaN layers are necessary in LEDs and LD devices. For AlGaN alloys p-type doping is a major challenge which is even more challenging with increase in AlN content. Low p-type conductivity will reduce the optical efficiency of the devices. P-type GaN can be used instead of p-type AlGaN but it is absorbing for λ<363 nm [49].

2.4.2.1 P-type AlGaN

One of the biggest challenges in DUV AlGaN optoelectronics is ineffective p-type doping. Mg is the most widely used dopant for p-type doping and so far the only one to produce controlled p-type conductive AlGaN[50]. Several effects are responsible for this, including large acceptor ionization energy, limitations to dopant solubility and low formation energies of compensating defects [49]. The activation energy of Mg increases with AlN content and is even higher than the activation energy of Si. It increases from ~160 meV in GaN to 510-630 meV in AlN [51,52]. Besides for AlGaN, Mg is also most commonly employed in InGaN based visible LEDs and LDs. Mg readily incorporates on a cation site as an acceptor. For Mg concentrations >4× 10^{19}cm^{-3} it has been reported to cause defects such as inversion domains which decrease free carrier concentration and mobilities [53]. As-grown Mg doped MOCVD AlGaN is highly resistive due to the formation of neutral complexes between H and Mg and needs annealing with N$_2$ or O$_2$ to activate the Mg acceptors [54]. At 45% AlN content a low resistivity of 8 Ω cm was recorded at room temperature [55], whereas at higher AlN content of 70% the resistivity increased to 100000 Ω cm [56]. A more recent study reported low resistivity of 47 Ω cm for 70% AlN content AlGaN [57]. Therefore, it is crucial to find the optimal growth regime where high Mg concentration is achievable without a high concentration of compensating defects, such as V$_N$ [58,59].

2.4.2.2 N-type AlGaN

To achieve the n-type conductivity in AlGaN, Si is commonly employed due to relative ease of incorporation as a substitutional impurity on the cation site, acting as a donor. Si is used as an n-type dopant for the entire alloy range from GaN to AlN. It is also an effective donor in the n-type InGaN. It becomes more difficult to dope AlGaN for higher AlN content, due to the nonlinear increase in the activation energy with AlN content [60,61]. Consensus on Si activation energy is still missing, but experimentally reported values cover the range from ~63 meV to 577 meV for AlN [62-68]. Due to the high activation energy, high doping levels are necessary in order to obtain optimal conductivity.

Also, the resistivity of Si-doped AlGaN (primarily determined by the change in free carrier concentration) increases with an increase in the AlN content and the free carrier concentration and mobility decrease with an increase in the AlN content [62,69]. The resistivity in high AlN content AlGaN was found to increase from 0.026 Ω cm to 2.62 Ω cm as the AlN content increased from x~0.82 to x~0.95 [70]. This decrease in conductivity can be from either an increase in the activation energy of the Si donor, an increase in compensation effects, or both. According to first principle calculations the dominant mechanisms of dopant compensation are V_{Al}^{3+} [71], DX centre (distorted donor) formation for Si and O impurities at high AlN content [72,73] and cation vacancies complexes with low formation energies [74]. The DX-centre is formed by breaking one of the tetrahedral bonds and trapping of one additional electron whereby it undergoes a large lattice relaxation. The name "DX" comes from donor D together with another unknown constituent X [75]. In order to achieve highly conductive n- or p-type Al-rich AlGaN alloys identification and elimination of compensating defects is necessary [70,76]. Despite many theoretical and experimental studies universal agreement about donor activation energies and the main mechanism responsible for strong increase in n-type resistivity for high AlN content alloys is still missing [49]. However, for the limitations in n-type doping of high AlN content AlGaN, both increasing donor activation energy and increasing compensating defect formation are identified as contributing factors [49].

2.5 Defects in III-nitrides

Control and reduction of lattice defects is an essential aspect of the development of III-nitrides semiconductors. Point defects consist of missing atoms, i.e. vacancies or vacancy complexes, or atoms sitting on non-intrinsic lattice sites within the crystal. Point defects will impact the electrical conductivity of the semiconductors. Without the point defects the AlN-rich AlGaN or AlN would be insulating at room temperature due to their large bandgaps [27]. It is possible to qualitatively study point defects by measuring their luminescence with cathodoluminescence (CL) due to the creation of defect bands within the bandgap [27]. In this thesis, in addition to the AlGaN NBE luminescence measured by CL, luminescence from different peaks associated with radiative recombinations involving defect centres in the bandgap are recorded, some of them including single charged group-III vacancy complex (V_{III} complex)$^{1-}$, doubly charged cation vacancy complex and (V_{III} complex)$^{2-}$ and triply charged cation vacancy (V_{III})$^{3-}$ for n-type material (Chapter 6). For the p-type material the observed defect peaks include (V_{III} complex)$^{1-}$, V_N, $Mg_{III}^{+}H_i$ complex and Mg^{III} defects (Chapter 7). Since the samples under study consist of Si doped and Mg doped AlGaN, separate sections will be dedicated to defects occurring in n- and p-type AlGaN. In this section the formation energies of different defects are shown in order to help explain the occurrence and change in intensity of the defect peaks recorded in the CL spectra. Overall, association of the different peaks with different acceptor states in the semiconductor offers valuable information for optimisation of the semiconductor growth.

2.5.1 Point defects

Point defects are zero dimensional defects; they can be formed by atoms sitting on non-intrinsic lattice sites within the crystal. Point defects affect the electrical conductivity of semiconductors. It is important to study point defects, both intentionally and unintentionally incorporated. In this thesis impurities are quantified by WDX spectroscopy and secondary ion mass spectroscopy (SIMS) and vacancies and vacancy complexes were determined by CL spectroscopy.

Point defects will cause additional states within the bandgap and consequently material will have characteristic optical properties. Therefore, it is possible to qualitatively study point defects by studying the optical properties. It is difficult to determine the concentration of vacancies and vacancy complexes, although positron annihilation spectroscopy has been used for qualitative determination [27].

2.5.2 Extended defects

This type of defect extends in one or more dimensions. Two types of extended defects are dislocations and stacking faults. The presence of extended defects will also affect the material properties. Defects will distort crystal structure and induce strain fields which can attract point defects due to a local change in the chemical potential. Some extended defects will act as scattering centres and reduce conductivity of the material by affecting the mobility or act as nonradiative recombination centres which reduce quantum efficiencies in optoelectronic devices. They can also be conductive and act as electrical leakage paths in vertical devices. Dislocations can be categorised as edge, screw and mixed type. Figure 2.8 shows the structure of edge and screw dislocations. The dislocation lines and Burgers vector are perpendicular in the case of edge dislocations and parallel for screw dislocations. When an excess $(11\bar{2}0)$ plane is introduced an edge dislocation is formed with a Burgers vector of $b = 1/3 < 11\bar{2}0 >$. While, screw dislocations are formed due to the localized atomic steps and have a Burgers vector of $b = < 0001 >$. Mixed dislocations have a Burgers vector of $b = 1/3 < 11\bar{2}3 >$. Dislocations are known as threading dislocations if the dislocation line is parallel to the growth direction [27].
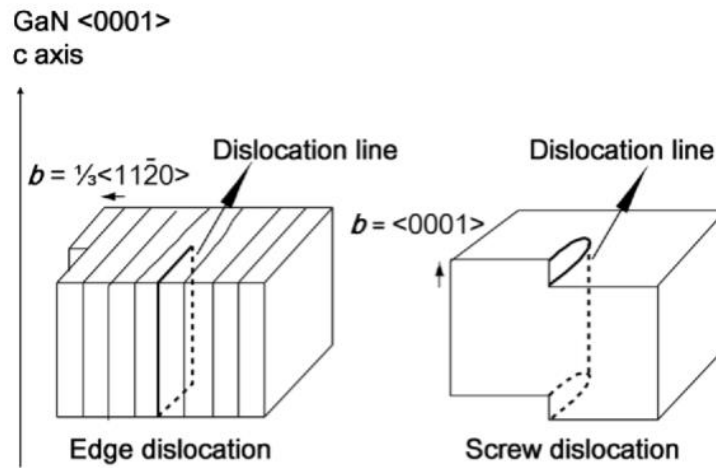
Figure 2.8: Structures of edge and screw dislocations. From Ref. [12].

Many dislocations in heterostructures are caused by the stress or strain introduced due to the differences in lattice and thermal expansion constants between epitaxial layers or substrates. Stacking faults (SFs) are associated with partial dislocations, which have Burgers vectors that are not equivalent to a lattice vector. They are most commonly observed and studied in non-polar films and represent a major obstacle in achieving high-quality non-polar film. SFs are classified as prismatic stacking faults (PSFs) and basal plane stacking faults (BSFs) [77,78].

Both type of defects (extended and point defects) contribute to the electrical properties of the AlGaN layers. Overall, all types of dislocations affect the device performance in a negative way and the best way to get significant improvement in device performance would be to minimize the number of dislocations [79].

2.5.3 Compensating defects in III-nitrides

Different types of point defects can introduce electron states within the bandgap. More details about compensating defects can be found in [80]. Trap states introduced by defects in the bandgap often reduce the electrical conductivity. They can be associated with specific luminescence peaks from nitrides, making it possible to use cathodoluminescence spectroscopy in this thesis and to confirm the existence of different defects.

The equilibrium concentration of impurities or native defects can be expressed as:

$$c = N_{sites} exp^{-E_F/k_B T}$$

(2.5)

where E_F is the formation energy, N_{sites} is the number of sites where the defect or impurity can be incorporated, k_B is the Boltzmann constant, and T the temperature. Eq. (2.5) shows that defects with a high formation energy will occur in low concentrations. The formation energy depends on the chemical potentials which in turn depends on the growth conditions. The distribution of point defects can be engineered during growth via chemical potential control or Fermi level control [80]. Most as-grown III-nitrides exhibit n-type conductivity due to the presence of shallow donors, which is often attributed to native defects such as vacancies or interstitials. For the wide bandgap semiconductors self-compensation by incorporation of donors occurs due to formation of vacancies during growth. This mechanism explains the reduced doping efficiencies for both n-type and p-type nitrides [81].

Density-functional theory with hybrid functionals calculations are systematically employed to investigate the neutral and charged native point defects (vacancy, interstitial, and antisite defect) in III-nitrides in terms of local geometry relaxation, formation energies, and electronic and diffusion properties. The identification and control of point defects in III-nitrides is extremely important due to their profound impact on device performance and reliability [82].

For example, dislocations can introduce mid-bandgap sates for electrons, acceptor like, in n-type doped material or donor like, in p-doped material. The traps present in nitrides have a large energy depth relative to the band edges [59]. It is helpful to plot formation energies as a function of E_F in order to examine the behaviour of defects and impurities with the change of doping level. Figure 2.9, shows a schematic illustration of point defects in wurtzite III-nitrides. The vacancy defect is N or X atom (X represents Ga, Al, and In) missing from a lattice site (V_N and V_X), and the antisite defect occurs when N

and X atoms exchange their positions (N_X and X_N). There are two tetrahedral interstitials (te), two octahedral interstitials (oc), and four dumbbell interstitials.
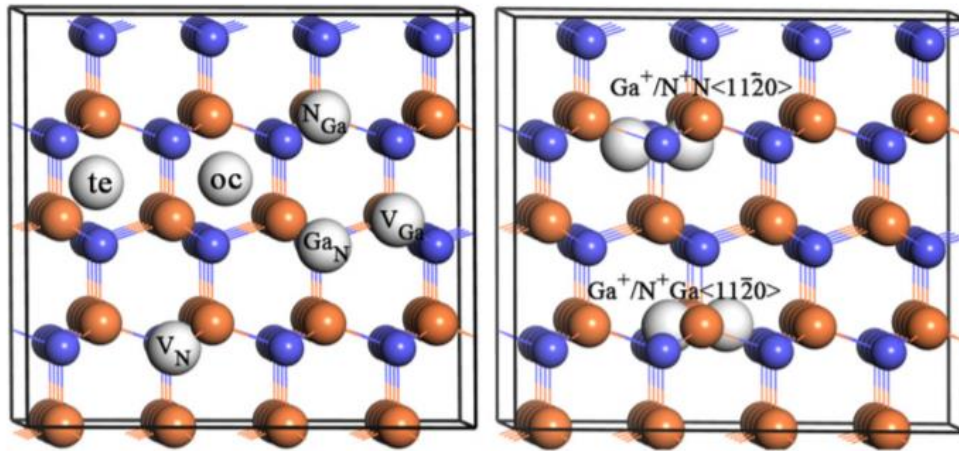
Figure 2.9: Schematic illustration of vacancies, antisite defects, tetrahedral, and octahedral interstitial (left) and the dumbbell interstitials (right) in GaN. Blue balls represent N atoms, orange balls Ga atoms, and white balls defects and interstitials. In AlN (InN) crystal, Al (In) atoms replace Ga atoms. From Ref [82].

Boguslawski et al. studied native defects with a charge state q in GaN and showed that the doping efficiencies were strongly decreased by the formation of Ga vacancy and interstitial Ga [86]. Fig. 2.10 shows the formation energies of various point defects in GaN as a function of the Fermi energy. Only segments corresponding to the lowest energy charge state are shown. $E_F = 0$ corresponds to the valence band maximum (VBM). The slope of the line represents the charge state and thermodynamic transitions are indicated by circles. From the plot it is evident that V_N, Ga_{oc}, and Ga_{te} are donor-type defects, while V_{Ga} is acceptor-type. V_N is the lowest energy donor-type defect. N_i, N_{Ga}, and Ga_N may act as either donor or acceptor, depending on the location of the Fermi level [81]. Three stable charged states are predicted within the bandgap for the N vacancy. V_N in the charge state of $q = +3$ state is more stable when the Fermi level is close to the valence-band maximum (VBM), and V_N also occurs in the neutral and $q = +1$ states; but the 2+ charged state has higher formation energy. The Ga vacancies can occur in the 1+, 0, 1−, 2−, and 3− charge states, but the 3− charged V_{Ga} has the lowest formation energy when the Fermi level is close to the conduction band, under n-type conditions. Therefore, Ga vacancies

would become the acceptor like defect and will act as a compensating centre for shallow donors. Compared to vacancies, the antisite defects are much less stable due to larger lattice distortion.

Figure 2.10(b) shows the formation energies of point defects in AlN for different charge states as a function of E_F position. From the plot it is evident that N vacancy has high formation energy and therefore this transition level should not be responsible for the unintentional n-type conductivity in AlN. V_N defects act as shallow donor in GaN but in AlN, they are deep donors, due to the increases of the donor level depth as the bandgap of nitride decreases. On the other hand, the Al vacancy has a lower formation energy compared to the N vacancy especially for the region close to the conduction band maximum (CBM). V_{Al} is acting as both a shallow acceptor and a compensating centre for donors. Deeper donor and higher compensation levels in AlN strongly reduce the efficiency of both n-type and p-type doping.
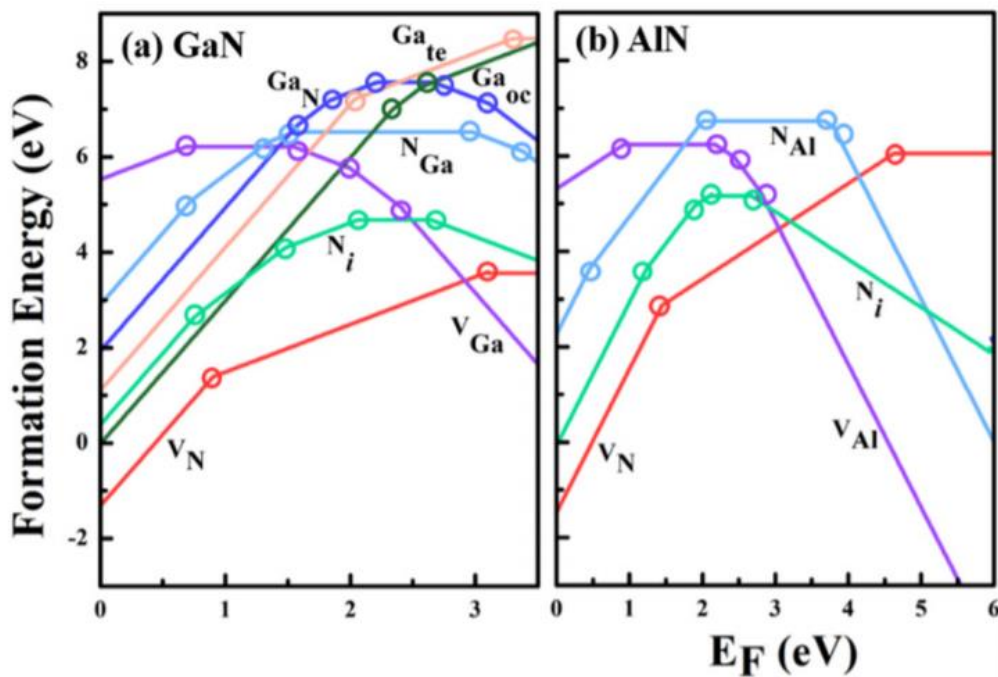
Figure 2.10: Formation energies under N-rich conditions as a function of the Fermi level for native point defects in (a) GaN, (b) AlN respectively. From Ref [82].
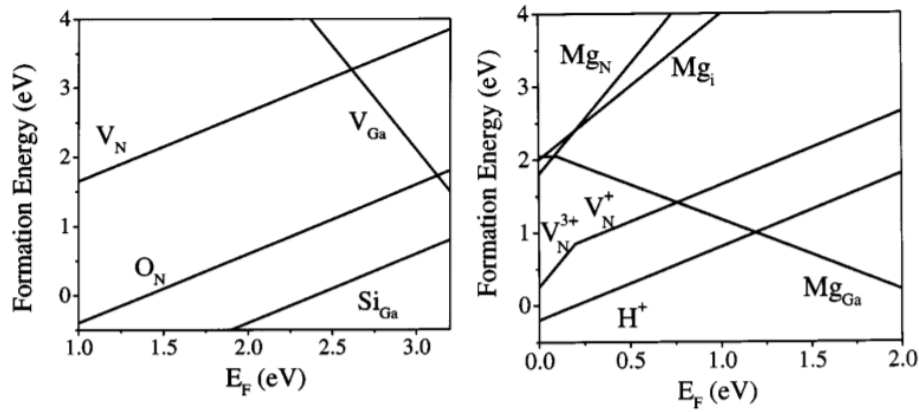
Figure 2.11: Left: Formation energy versus Fermi energy for native defects (nitrogen and gallium vacancies) and donors (oxygen and silicon) in GaN. Right: Formation energy as a function of Fermi level for Mg in different configurations. Also included are the native defects and interstitial H. From Ref [80].

Figure 2.11. also shows formation energy for impurities in GaN. For n-type doped GaN, in Fig. 2.11(left) it is evident that O and Si have much lower formation energies than V_N and these impurities can be readily incorporated in n-type GaN. Both O and Si form shallow donors in GaN. Si_{Ga} and O_N are singly charged donors. For the case of p-type GaN, Fig. 2.11 (right), Mg prefers the substitutional Ga site, and incorporation of Mg on substitutional N sites (Mg_N) or on interstitial sites (Mg_i) is unfavourable. Hydrogen incorporates much more readily in p-type than in n-type GaN. In p-type GaN, H behaves as a donor (H^+), compensating acceptors. The nitrogen vacancy has a significantly lower formation energy in p-type material and can act as a compensating centre, from the plot it is visible that increase in Mg concentration (decrease in Fermi energy) will result in the decrease of nitrogen vacancy formation energy. Yet when hydrogen is present, it has a formation energy much lower than that of the nitrogen vacancy [80].

Overall, for interstitials and antisite defect it has been shown that they do not have a major role in self-compensation due to their high energy of formation caused by large difference in atomic radii and partial covalent bonding [22]. In all nitrides, N vacancy can be a donor and cation vacancy act as an acceptor [85]. The most stable defects are identified as V_N (was found to be stable in 3+, 1+ and neutral state) and cation vacancies V_{Ga}, V_{Al} [45]. Different theoretical

calculations are necessary for the identification and control of point defects in group III nitrides, which will help in finding a way to reduce the impact of defects on device performance and reliability. More work still has to be done in the field of group III nitrides defects because a comprehensive study of the various defects and a direct comparison of the likely point defects for each nitride is still missing. A problem is also that the experimental and theoretical data about the band structures of point defects and irradiation defect states of nitrides are limited and even conflicting to each other [81].

2.5.3.1 Compensating defects in n-type AlGaN

Modelling of defects in alloys is even more challenging, usually conclusions about AlGaN are drawn by interpolating between results for GaN and AlN. For practical purposes, we can consider defect complexes in AlGaN (combinations of a small number of neighbouring point defects) to be point defects as well. Oxygen is a common unintentional impurity and silicon a common intentional and unintentional dopant in Al-rich AlGaN. O substitutes directly on the N site and acts as a donor at all Fermi levels below the conduction band minimum (CBM). However, at high Fermi levels in AlN and Al-rich AlGaN, O forms compensating DX centres. In a DX centre (substitutional defect) impurity is displaced away from the regular on-site geometry, defect is negatively charged, and will therefore trap free carriers. In this configuration O_N behaves as a compensating acceptor rather than a donor [83]. Silicon is commonly used as an intentional n-type dopant in AlGaN alloys. It substitutes on the cation site and acts as a donor in GaN and Ga-rich AlGaN. Also like O, Si transitions to a DX configuration at high Fermi levels in AlN, but not in GaN, indicating there is a threshold AlN content for the DX behaviour in AlGaN [84]. Theoretical predictions of this AlN content threshold vary widely, including x = 0.24 [85], x = 0.6 [86], and x = 0.94 [84]. However, Collazo et al. experimentally observed a sharp increase in donor activation energy for Si-doped AlGaN at x = 0.8, which could be related to DX transition [87].

Different defects are present in AlGaN, beside already mentioned cation vacancy $(V_{III})^{3-}$, defects complexes comprising of cation vacancy complex with oxygen having two-negative charges $(V_{III} \text{ complex})^{2-}$ and one negative charge

(V_{III} complex)$^{1-}$ have been identified. The energy levels of these deep level centres are pinned to a common energy level in vacuum. The cation vacancy and its complex in undoped and Si-doped AlGaN alloys, particularly in Al-rich alloys have small formation energies and are easily formed during the crystal growth [88]. In AlGaN C_N impurity can also form complexes with the O_N and Si_{III} [89]. By suppressing the concentrations of these defects the conductivity and material quality could be improved [90].

2.5.3.2 Compensating defects in p-type AlGaN

More details about defects in AlGaN: Mg can be found in [91]. The impurity transitions in Mg doped AlGaN will be different from the impurity transitions in n-type AlGaN alloys [88]. Point defects that are expected in high AlN content AlGaN doped with Mg are defects related to the V_N. That emission can be attributed to the transition of electrons bound to triply charged nitrogen vacancies to neutral magnesium impurities [92]. V_N^{3+} deep donors can compensate free holes in acceptor doped materials, thus monitoring the CL intensity of the peak can help with the p-type conductivity optimisation. The nitrogen vacancy with triple positive charges has smaller formation energy than those with a single positive charge and the one with 2+ charge is unstable. Other observable defect peak in AlGaN:Mg are related to the $Mg_{III}^+H_i$ complex and Mg_{III} defects according to [93] and [92]. Another expected defect is the one related to the transition of electrons in the conduction band or bound to shallow donors to neutral Mg acceptors but it hasn't been observed in our studied samples (Chapter 7) [91].

2.6 Devices based on III-nitrides

The following sections contain brief introduction about the devices relevant for this thesis. More details about the devices and their application can be found in Refs.[25,35,94,95].

2.6.1 UV-LEDs

Development of III-nitride UV LEDs started with research on blue LEDs that began with the original work from Maruska et al. at Stanford University in 1972. They were examining electroluminescence from Mg-doped GaN devices. Later on, the first functioning GaN:Mg LED was demonstrated in 1972 [96]. In 1983, Khan et al. worked on MOCVD deposition of GaN and applied prior work to grow AlGaN alloys [97]. In 1986, Amano et al. used a buffer layer that helped with the structural quality of GaN and AlGaN films [3]. The first UV/visible p-n junction diode was demonstrated in 1993 [98].

There are many different applications that require UV emission where UV LEDs can be employed as light sources. More details about UV-LEDs can be found in review by Kneissl and Rass [99]. The ultraviolet light can be divided into three regions, namely: UVA (400–320 nm), UVB (320–280 nm), and UVC (280–200 nm) by changing the composition of the AlGaN active region.

For the UVA region, the LEDs can be used for curing of resins, polymers, inks, paints, coatings, and adhesives. In the UVB region, LEDs can be utilised for the treatment of skin conditions, such as psoriasis and vitiligo or for the plant growth lighting. The UVC region can be important for the area of sensing, many biomolecules are absorbing within this region, such as NADH, tryptophan, tyrosine, collagens, elastin, and lipo-pigments. The UVC light can be used for germicidal and water purification applications, due to ability of high-energy photons to disrupt DNA or RNA of microorganisms. In order to shift the emission towards shorter wavelength more aluminium is introduced into the crystal, which will cause some negative effects that will limit device characteristics. Some of them are: degradation of the material quality, difficulty in achieving ohmic contacts and larger amounts of UV light trapped inside the semiconductor.

Nonetheless, UV LEDs are an emerging technology whose market share is steadily growing. While traditional UV sources, such as mercury, metal-halide, xenon and deuterium lamps are still present they have been slowly replaced by UV LEDs. UV LEDs are competitive in many high-end applications compared to UV lamps, they are environmentally friendly option and it is possible to adjust

its emission wavelengths by changing the material bandgap of their active regions.

In the last 15 years UV LEDs have significantly progressed and they performance is now comparable to some visible LEDs. Fig. 2.12 shows improvement of UV-C LED over the years in terms of external quantum efficiency (EQE). With the improvement of structural quality of AlGaN alloys and evolution of the devices design the efficiency has been also improving, but it does not exceed 15% [99-103]. From the plot it is visible how the maximum reported EQE of UV-C LEDs is close to devices operating in the "green gap" [104]. AlGaN material is appropriate for DUV light source due to many advantages, such as: high efficiency optical emission from quantum wells, it can be p- or n-type doped, offers longer lifetime (over 10000 h) compared to ultrahigh-pressure mercury lamps (100−2000 h) and contain non-toxic materials contrary to mercury lamps [105].
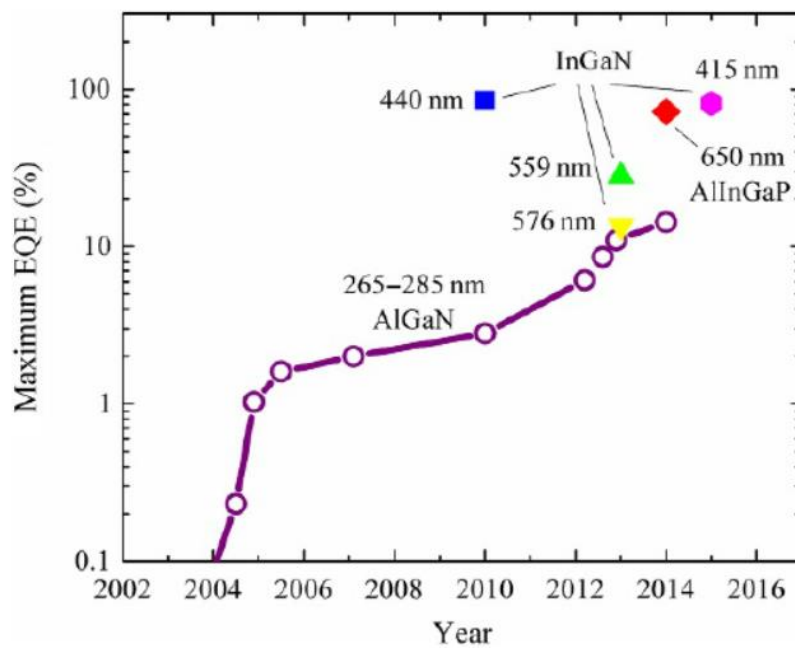
Figure 2.12: Historic improvement of UV-C LED efficiency and current state-of -the-art visible LED efficiency. Figure from [49].

Still, a drawback in their performance is related to difficulties in achieving high crystalline quality of AlGaN layers on sapphire substrates due to high density of threading dislocations (TDs), resulting in high nonradiative (NR) recombination rate in the device active region [49]. A TDD of the order of

$10^8-10^9 cm^{-2}$ is required for the appropriate device function [106]. Recently reported threading dislocation densities of AlGaN and AlN templates are of about $5 \times 10^8 /cm^2$ [105].

The challenges relating efficiency of UV LEDs are illustrated in Figure 2.13. Overall device performance can be improved by resolving four major obstacles; improvement in light extraction, internal quantum efficiency (IQE) (through advances in epitaxial growth and bandgap engineering), reduction of electrical losses and heat dissipation.
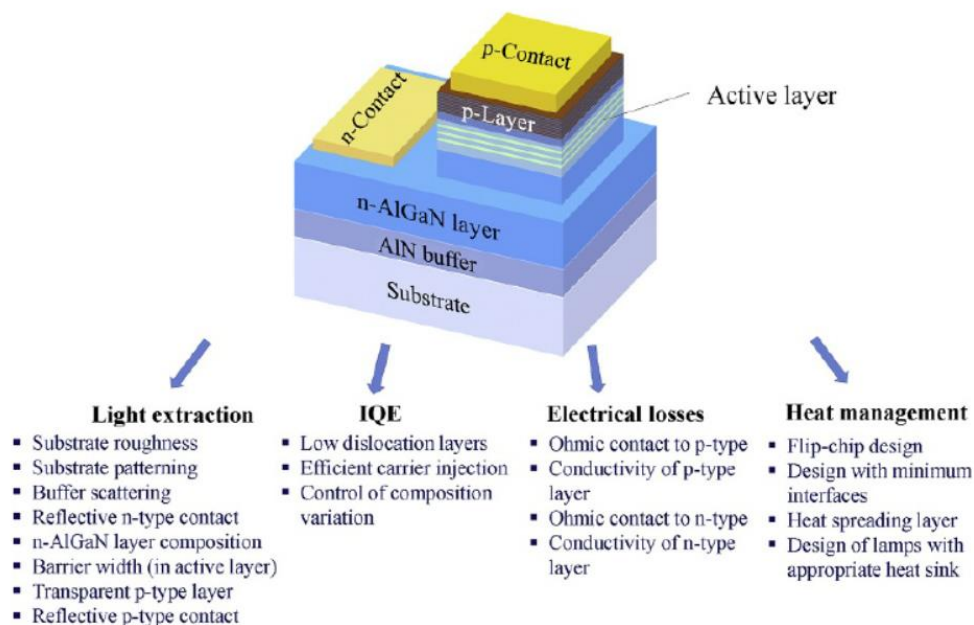
Figure 2.13 Semiconductor layers of a typical UV LED epitaxially grown on a substrate and factors affecting LED efficiency. From [49].

The potential of UV LEDs is not fully exploited and work is still needed in order to reduce their price, optical power and efficiency, to extend their working lifetime and most of all, reduce cost. For the AlGaN LEDs further work will have to involve reduction of alloy fluctuations in the AlGaN MQW region (discussed in further chapters of the thesis). That is the reason why in-depth understanding of AlGaN fundamental properties is necessary to improve epitaxial technology.

2.6.2 Transistors based on III-nitrides

III-nitrides have great impact on the semiconductor electronics. GaN based field-effect transistors (FETs) are useful for amplification and switching in high temperature and high-power environment. The AlGaN/GaN heterojunction has a large band discontinuity that enables GaN devices with improved output power density and improved thermal conductivity, which means they can operate effectively at higher temperature [11]. Some of the advantageous properties for III-nitride FETs include: high breakdown electric field (for GaN $(3 \times 10^6 \text{ V cm}^{-1}$, value ten times larger than Si or GaAs), high electron mobility and saturation velocity, polarization doping, large conduction band offset energies between channel and barrier, substrates with good thermal conductivity, high resistance to oxidation effects, low intrinsic carrier concentration and reduction of leakage currents. These properties offer major advantages in the trade-off between operating voltage and cut-off frequency that limits the operation of FETs.

Table 2.2 contains the major parameters of different semiconductor materials and the Johnson's figure of merit (JM) calculated to compare their power-frequency limits. The JM is based solely on material properties and can be used to compare different materials for high frequency and high power applications, which require large breakdown voltage and high electron velocity [107].

Table 2.2: Material properties related to the power performance at high frequencies [107].

	Si	GaAs	4H-SiC	GaN	Diamond
Eg (eV)	1.1	1.42	3.26	3.39	5.45
n_i (cm^{-3})	1.5×10^{10}	1.5×10^6	8.2×10^{-9}	1.9×10^{-10}	1.6×10^{-27}
ε_r	11.8	13.1	10	9.0	5.5
μ_n (cm^2/Vs)	1350	8500	700	1200(bulk) 2000(2DEG)	1900
v_{sat} (10^7cm/s)	1.0	1.0	2.0	2.5	2.7

E_{br} (MV/cm)	0.3	0.4	3.0	3.3	5.6
Θ (W/cmK)	1.5	0.43	3.3−4.5	1.3	20
JM $= \dfrac{E_{br}v_{sat}}{2\pi}$	1	2.7	20	27.5	50

where Eg is the band gap energy, n_i intrinsic carrier concentration, ε_r relative dielectric constant, μ_n mobility of electron, v_{sat} electron saturation velocity, E_{br} electron breakdown field, Θ thermal conductivity and JM Johnson's figure of merit.

The polarization effect at the AlGaN/GaN heterojunction interface results in formation of an electron carrier density ($\sim 10^{13}$ cm^{-2}) that is five times larger compared to AlGaAs/GaAs heterostructure. Also, an electron drift velocity of 2×10^7 cm s^{-1} at high electric fields of GaN is achieved [108]. From the table 2.2 it is evident how GaN has much higher JM value (27.5) compared to GaAs JM (2.7), but also the ability of GaN to form heterojunctions makes it superior compared to SiC, in spite of having similar breakdown fields and saturation electron velocities [107].

The nitride FETs are mostly employed for microwave and mm-wave power amplifiers and switches and power electronics as converters. One of the important applications is for high frequency devices for microwave power transmission amplifiers for third generation mobile telephone base stations and wireless technology used in broadband internet communication.

The first report on the fabrication of AlGaN/GaN heterojunction FETs was by Khan et al. in 1994 [109]. The basic elements of the FET structure are shown in the Figure 2.14 using a cross-section of a GaN-based heterojunction FET. The AlGaN/GaN heterostructure is created when the AlGaN barrier (doped or undoped) is grown on a relatively thick GaN layer. They include channel, gate metal and barrier between them, source and drain contact regions and structures to provide isolation between devices (mesa etches or implants to render epilayers non-conducting).
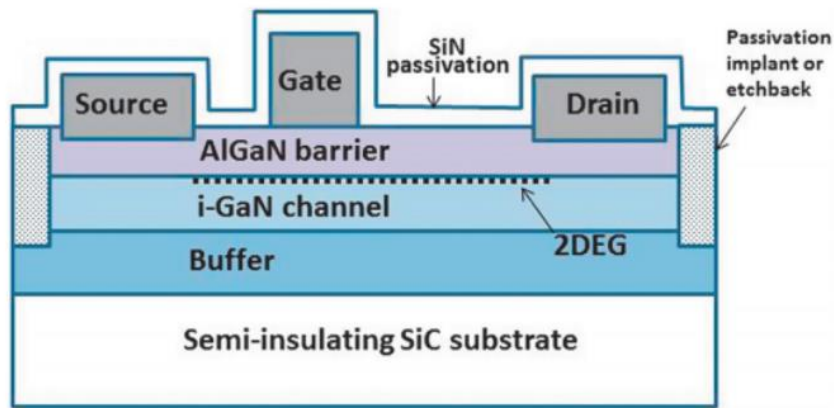
Figure 2.14. Cross-section of a representative AlGaN/GaN heterojunction FET. From Ref [35]

Different types of AlGaN materials (MOCVD and MBE) are used as an n-type channel and discussed in Chapter 4. The quality of the channel depends on the type of substrate, growth method, and level of doping in carrier supply layer. Channel conductivity is function of the carrier concentration and the carrier mobility in the electric field [110]. Crystalline defects in the AlGaN layer have been reported to be a source of leakage currents in AlGaN/GaN devices [111]. Another problem is the current collapse which is the large decrease in current at high voltage operation that may be related to deep levels in the AlGaN and GaN layers and at the AlGaN surface. Under high voltage operating conditions, electrons are injected from the gate electrode into the AlGaN surface or GaN buffer layer and trapped in the deep levels, resulting in the creation of a depletion layer and subsequent current collapse, but it may be suppressed by use of field plates [112]. That is the reason for a big demand in the improvement of AlGaN layer and consequently device properties.

As in Fig. 2.14, wide band gap barriers (which can be partially etched underneath the gate to produce enhancement mode device) are used with narrower bandgap channels and the gates are formed by Schottky barrier between gate metal and underlying semiconductor. Contacts to source and drain are often produced by ohmic alloying. An additional layer under the channel can be employed to improve confinement of carriers to the barrier-channel heterointerface. A high carrier density, two-dimensional electron gas (2DEG) is generated at the AlGaN/GaN heterointerface due to spontaneous and piezoelectric polarization effects. The existence and the quality of this 2DEG

has a significant consequence on the electronic transport along the interface and to the properties of the final device [35]. The polarization effects in the III-nitrides are large enough to produce 2DEG even without intentional doping of AlGaN layer. In undoped and doped structures the maximum sheet charge caused by piezoelectric polarization depends on the AlN content and on the thickness of the AlGaN layer in the AlGaN/GaN heterostructure. Higher AlN content of gating layer provides a high sheet carrier density with associated high carrier mobility. This will result in higher band discontinuity and therefore improved carrier confinement, and stronger spontaneous polarization and piezoelectric effects that will contribute to a higher sheet charge density in the channel. Also, the higher band gap of the AlGaN layer provides a higher composite breakdown field [110]. The combination of the large carrier density and high breakdown voltage enables high power output operation.

Figure 2.15. shows a schematic band diagram for the gate/barrier channel region of an AlGaN/GaN FET together with associated charge densities. A heterostructure or heterojunction is formed between two semiconductors with different energy band-gaps E_g, permittivities ε, work functions $q\varphi$, and electron affinities χ. When the wide band gap semiconductor is in contact with the narrow band gap semiconductor, a discontinuity in conduction band E_c and valence band E_v is present. It will produce a triangular quantum well, and the 2DEG will be created. In a typical FET shown in Fig. 2.15 there is a positive polarisation charge ΔP_{int} at the barrier/channel interface. This polarization charge will affect the threshold voltage (V_{th}) and the conduction band offset ΔE_c (at barrier/channel interface) and the Schottky barrier height Φ_b. An electric field E_b can appear at the backside of the channel. A charge density N_b within the barrier is produced by doping with Si or unintentionally by trapped charges.
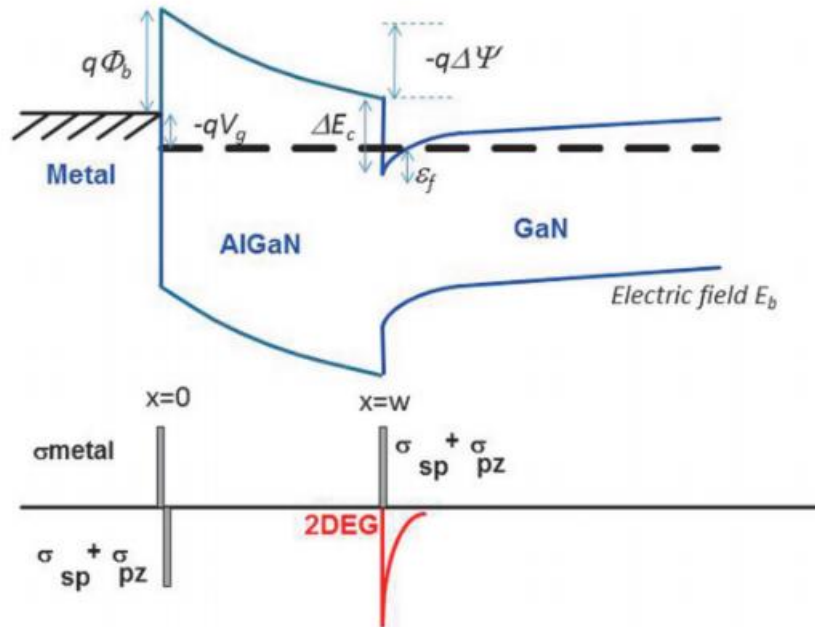
Figure 2.15: Band diagram for AlGaN/GaN FET. From Ref [35].

A general I-V (current-voltage) characteristic curve (I_d -V_{gs} -V_{ds}) as a result of channel charge density modulation can be used for all two-dimensional FETs, as illustrated in Fig.2.16. Where I_d represents drain current, V_{gs} gate source voltage and V_{ds} drain-source voltage.
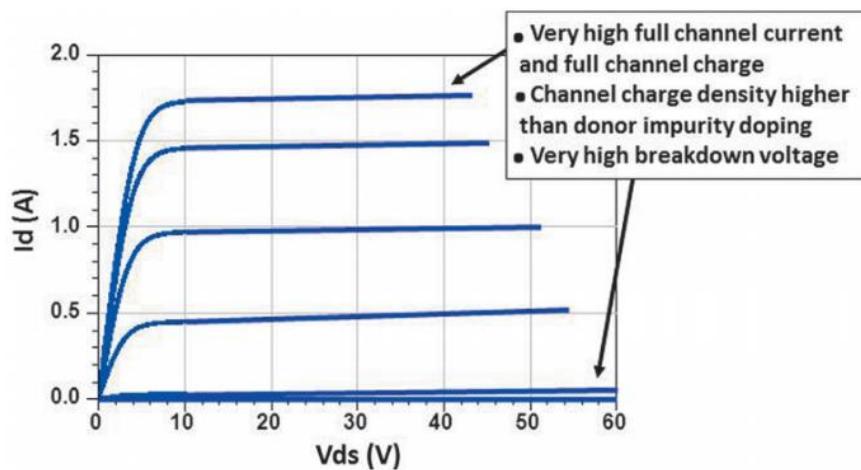
Figure 2.16: I_d -V_{ds} characteristics of a representative AlGaN/GaN FET. From Ref [35].

AlGaN/GaN devices are being continuously developed for use in HEMT devices for high power and RF applications, such as emerging 5G technology [113]. Future work on nitride transistors is oriented to reduce the cost of devices

by combining high resistance AlN buffer layers with low cost n-SiC substrates and high resistance Si substrates [108].

2.7 Conclusion

This chapter presented a general overview of the III-nitrides semiconductors, including their properties and applications. The types of crystal and band structures are discussed. The importance of doping control is explained along with different challenges associated with doping of GaN and AlGaN material. Further discussion evolves around n- an p-type doping of AlGaN material, since both types are analysed within the scope of the thesis. Since the control and reduction of lattice defects is an essential aspect of the development of III-nitrides semiconductors, different types of defects are also explored. These include point defects, extended and compensating defects, with an emphasis on compensating defects in n- and p-type AlGaN material. Lastly, the chapter also includes a brief introduction to the UV-LEDs and transistor devices relevant for this thesis.

Bibliography

[1]   M. R. Krames, H. Amano, J. J. Brown, and P. L. Heremans, *Introduction to the issue on high-efficiency light-emitting diodes*, IEEE Journal of Selected Topics in Quantum Electronics **8**, 185 (2002).

[2]   H. Amano, M. Kito, K. Hiramatsu, and I. Akasaki, *P-Type Conduction in Mg-Doped GaN Treated with Low-Energy Electron Beam Irradiation (LEEBI)*, Japanese Journal of Applied Physics **28**, L2112 (1989).

[3]   H. Amano, N. Sawaki, I. Akasaki, and Y. Toyoda, *Metalorganic vapor phase epitaxial growth of a high quality GaN film using an AlN buffer layer*, Applied Physics Letters **48**, 353 (1986).

[4]   N. Zheludev, *The life and times of the LED - A 100-year history*, Nature Photonics **1**, 189 (2007).

[5]   C. Zhou *et al.*, *Review—The Current and Emerging Applications of the III-Nitrides*, ECS Journal of Solid State Science and Technology **6**, Q149 (2017).

[6]   M. O. Manasreh, in *III-Nitride Semiconductors: Electrical, Structural and Defects Properties*, edited by O. Manasreh (Elsevier, Amsterdam, 2000), pp. 1.

[7]   https://www.dal.ca/sites/electron-microprobe-lab/analysis.html.

[8]   U. Schwarz, *Ultraviolet laser diodes: Indium-free success*, Nature Photonics **2**, 521 (2008).

[9]   A. Khan, K. Balakrishnan, and T. Katona, *Ultraviolet light-emitting diodes based on group three nitrides*, Nature Photonics **2**, 77 (2008).

[10]   R. Butté *et al.*, *Current status of AlInN layers lattice-matched to GaN for photonics and electronics*, Journal of Physics D: Applied Physics **40**, 6328 (2007).

[11]   H. Morkoç, *Potential applications of III–V nitride semiconductors*, Materials Science and Engineering: B **43**, 137 (1997).

[12]   S. Yoshida *et al.*, in *Wide Bandgap Semiconductors: Fundamental Properties and Modern Photonic and Electronic Devices*, edited by K. Takahashi, A. Yoshikawa, and A. Sandhu (Springer Berlin Heidelberg, Berlin, Heidelberg, 2007), pp. 25.

[13]   J. Lutz, H. Schlangenotto, U. Scheuermann, and R. De Doncker, in *Semiconductor Power Devices: Physics, Characteristics, Reliability*, edited by J. Lutz *et al.* (Springer Berlin Heidelberg, Berlin, Heidelberg, 2011), pp. 17.

[14]   S. N. Shuji Nakamura, *Gan growth using gan buffer layer*, Japanese Journal of Applied Physics **30**, L1705 (1991).

[15]   H. Amano, M. Kito, K. Hiramatsu, and I. Akasaki, *P-type conduction in Mg-doped GaN treated with low-energy electron beam irradiation (LEEBI)*, Japanese Journal of Applied Physics **28**, L2112 (1989).

[16]   S. Nakamura, N. Iwasa, M. S. Masayuki Senoh, and T. M. Takashi Mukai, *Hole compensation mechanism of p-type gan films*, Japanese Journal of Applied Physics **31**, 1258 (1992).

[17]   E. T. Yu and M. O. Manasreh, 2003).

[18]   P. Kivisaari, J. Oksanen, and J. Tulkki, *Polarization doping and the efficiency of III-nitride optoelectronic devices*, Applied Physics Letters **103**, 211118 (2013).

[19]   B. Monemar, *III-V nitrides - Important future electronic materials*, Journal of Materials Science: Materials in Electronics **10**, 227 (1999).

[20]   F. Bernardini, V. Fiorentini, and D. Vanderbilt, *Spontaneous polarization and piezoelectric constants of III-V nitrides*, Physical Review B **56**, R10024 (1997).

[21]   O. Ambacher *et al.*, *Two-dimensional electron gases induced by spontaneous and piezoelectric polarization charges in N- and Ga-face AlGaN/GaN heterostructures*, Journal of Applied Physics **85**, 3222 (1999).

[22]   O. Ambacher *et al.*, *Two dimensional electron gases induced by spontaneous and piezoelectric polarization in undoped and doped AlGaN/GaN heterostructures*, Journal of Applied Physics **87**, 334 (2000).

[23]   J. L. Weyher *et al.*, *Morphological and structural characteristics of homoepitaxial GaN grown by metalorganic chemical vapour deposition (MOCVD)*, Journal of Crystal Growth **204**, 419 (1999).

[24]   O. Ambacher, *Growth and applications of Group III-nitrides*, Journal of Physics D: Applied Physics **31**, 2653 (1998).

[25]   K. Takahashi, A. Yoshikawa, and A. Sandhu, *Wide bandgap semiconductors : fundamental properties and modern photonic and electronic devices / [internet resource]* (Berlin : Springer, Berlin, 2007), 1st ed. 2007.. edn.

[26]   J. S. Galsin, in *Solid State Physics*, edited by J. S. Galsin (Academic Press, 2019), pp. 1.

[27]   O. O. Manasreh and M. O. Manasreh, *III-Nitride Semiconductors: Electrical, Structural and Defects Properties* (Elsevier Science & Technology, Oxford, NETHERLANDS, THE, 2000).

[28]   A. E. Willner, R. L. Byer, C. J. Chang-Hasnain, S. R. Forrest, H. Kressel, H. Kogelnik, G. J. Tearney, C. H. Townes, and M. N. Zervas, *Optics and Photonics: Key Enabling Technologies*, Proceedings of the IEEE **100**, 1604 (2012).

[29]   M. J. Murphy, *Molecular beam epitaxial growth of normal and inverted two-dimensional electron gases in AlGaN/GaN based heterostructures*, Journal of Vacuum Science and Technology B: Microelectronics and Nanometer Structures **17**, 1252 (1999).

[30]   K. Hirata, H. Yamada, M. Uehara, S. A. Anggraini, and M. Akiyama, *First-Principles Study of Piezoelectric Properties and Bonding Analysis in (Mg, X, Al)N Solid Solutions (X = Nb, Ti, Zr, Hf)*, ACS Omega **4**, 15081 (2019).

[31]   H. Masui, S. C. Cruz, S. Nakamura, and S. P. Denbaars, *Geometrical Characteristics and Surface Polarity of Inclined Crystallographic Planes of the Wurtzite and Zincblende Structures*, Journal of Electronic Materials **38**, 756 (2009).

[32]   C. X. Ren, *Polarisation fields in III-nitrides: effects and control*, Materials Science and Technology **32**, 418 (2016).

[33]   H. Zhou, S. J. Chua, and C. Peng, *Al incorporation in AlGaN on (112¯2) and (0001) surface orientation*, Journal of Crystal Growth **292**, 5 (2006).

[34]   O. Romanyuk, P. Jiříček, T. Paskova, and I. Bartoš, *Polarity of GaN with polar {0001} and semipolar {10-11}, {20-21}, {11-22} orientations by x-ray photoelectron diffraction*, Journal of materials research **30**, 2881 (2015).

[35]   R. Chu and K. Shinohara, *III-Nitride Electronic Devices* (Elsevier Science & Technology, 2019).

[36]   R. A. Ferreyra, C. Zhu, A. Teke, and H. Morkoç, in *Springer Handbook of Electronic and Photonic Materials*, edited by S. Kasap, and P. Capper (Springer International Publishing, Cham, 2017), pp. 1.

[37]   P. Waltereit, O. Brandt, A. Trampert, H. T. Grahn, and et al., *Nitride semiconductors free of electrostatic fields for efficient white light-emitting diodes*, Nature **406**, 865 (2000).

[38]   P. Waltereit, O. Brandt, A. Trampert, H. T. Grahn, J. Menniger, M. Ramsteiner, M. Reiche, and K. H. Ploog, *Nitride semiconductors free of electrostatic fields for efficient white light-emitting diodes*, Nature **406**, 865 (2000).

[39]   J. Simon, V. Protasenko, C. Lian, H. Xing, and D. Jena, *Polarization-Induced Hole Doping in Wide–Band-Gap Uniaxial Semiconductor Heterostructures*, Science **327**, 60 (2010).

[40]   A. Ashrafi and C. Jagadish, *Review of zincblende ZnO: Stability of metastable ZnO phases*, Journal of Applied Physics **102**, 071101 (2007).

[41]   K. P. O'Donnell and X. Chen, *Temperature dependence of semiconductor band gaps*, Applied Physics Letters **58**, 2924 (1991).

[42]   K. Lorenz, N. Franco, E. Alves, I. M. Watson, R. W. Martin, and K. P. O'Donnell, *Anomalous ion channeling in AlInN/GaN bilayers: determination of the strain state*, Physical review letters **97**, 085501 (2006).

[43]   K. Wang *et al.*, *Optical energies of AlInN epilayers*, Journal of Applied Physics **103**, 073510 (2008).

[44]   N. F. Mott, *Metal-Insulator Transition*, Reviews of Modern Physics **40**, 677 (1968).

[45]   S. Bharadwaj, S. M. Islam, K. Nomoto, V. Protasenko, A. Chaney, H. Xing, and D. Jena, *Bandgap narrowing and Mott transition in Si-doped Al0.7Ga0.3N*, Applied Physics Letters **114**, 113501 (2019).

[46]   A. Dadgar, F. Schulze, T. Zettler, K. Haberland, R. Clos, G. Straßburger, J. Bläsing, A. Diez, and A. Krost, *In situ measurements of strains and stresses in GaN heteroepitaxy and its impact on growth temperature*, Journal of Crystal Growth **272**, 72 (2004).

[47]   I.-H. Lee, I.-H. Choi, C.-R. Lee, E.-j. Shin, D. Kim, S. K. Noh, S.-J. Son, K. Y. Lim, and H. J. Lee, *Stress relaxation in Si-doped GaN studied by Raman spectroscopy*, Journal of Applied Physics **83**, 5787 (1998).

[48]   M. A. Moram, M. J. Kappers, F. Massabuau, R. A. Oliver, and C. J. Humphreys, *The effects of Si doping on dislocation movement and tensile stress in GaN films*, J. Appl. Phys. **109** (2011).

[49]   Z. Mi and C. Jagadish, *III-nitride semiconductor optoelectronics [internet resource]* (Cambridge, MA : Academic Press is an imprint of Elsevier, 2017).

[50]   D. Nilsson and k. o. b. Linköpings universitet. Institutionen för fysik, *Doping of High-Al-content AlGaN Grown by MOCVD* (Department of Physics, Chemistry and Biology (IFM), Linköping University, 2014).

[51]   K. B. Nam, M. L. Nakarmi, J. Li, J. Y. Lin, and H. X. Jiang, *Mg acceptor level in AlN probed by deep ultraviolet photoluminescence*, Applied Physics Letters **83**, 878 (2003).

[52]   Y. Taniyasu, M. Kasu, and T. Makimoto, *An aluminium nitride light-emitting diode with a wavelength of 210 nanometres*, Nature **441**, 325 (2006).

[53]   A. Chakraborty, C. G. Moe, Y. Wu, T. Mates, S. Keller, J. S. Speck, S. P. DenBaars, and U. K. Mishra, *Electrical and structural characterization of Mg-doped p-type Al0.69Ga0.31N films on SiC substrate*, Journal of Applied Physics **101**, 053717 (2007).

[54]   Neugebauer and C. G. Van de Walle, *Hydrogen in GaN: Novel aspects of a common impurity*, Physical review letters **75**, 4452 (1995).

[55]   S. R. Jeon, Z. Ren, G. Cui, J. Su, M. Gherasimova, J. Han, H. K. Cho, and L. Zhou, *Investigation of Mg doping in high-Al content p -type Al x Ga 1 − x N (0.3 < x < 0.5)*, Appl. Phys. Lett. **86** (2005).

[56]   M. L. Nakarmi, K. H. Kim, M. Khizar, Z. Y. Fan, J. Y. Lin, and H. X. Jiang, *Electrical and optical properties of Mg-doped Al 0.7 Ga 0.3 N alloys*, Appl. Phys. Lett. **86** (2005).

[57]   T. Kinoshita, T. Obata, H. Yanagi, and S.-I. Inoue, *High p-type conduction in high-Al content Mg-doped AlGaN*, Appl. Phys. Lett. **102** (2013).

[58]   J. Neugebauer and C. G. Van de Walle, *Theory of Point Defects and Complexes in GaN*, MRS Proceedings **395**, 645, 645 (1995).

[59]   C. G. Van de Walle and J. Neugebauer, *First-principles calculations for defects and impurities: Applications to III-nitrides*, Journal of Applied Physics **95**, 3851 (2004).

[60]   P. Pampili and P. J. Parbrook, *Doping of III-nitride materials*, Materials Science in Semiconductor Processing **62**, 180 (2017).

[61]   F. Mehnke, X. T. Trinh, H. Pingel, T. Wernicke, E. Janzén, N. T. Son, and M. Kneissl, *Electronic properties of Si-doped Alx Ga1−xN with aluminum mole fractions above 80%*, Journal of Applied Physics **120**, 145702 (2016).

[62]   B. Borisov, V. Kuryatkov, Y. Kudryavtsev, R. Asomoza, S. Nikishin, D. Y. Song, M. Holtz, and H. Temkin, *Si-doped AlxGa1−xN(0.56⩽×⩽1) layers grown by molecular beam epitaxy with ammonia*, Applied Physics Letters **87**, 132106 (2005).

[63]   R. Collazo, S. Mita, J. Xie, A. Rice, J. Tweedie, R. Dalmau, and Z. Sitar, *Progress on n-type doping of algan alloys on aln single crystal substrates for uv optoelectronic applications*, Physica Status Solidi (C) Current Topics in Solid State Physics **8**, 2031 (2011).

[64]   M. Hermann, F. Furtmayr, A. Bergmaier, G. Dollinger, M. Stutzmann, and M. Eickhoff, *Highly Si-doped AlN grown by plasma-assisted molecular-beam epitaxy*, Applied Physics Letters **86**, 192108 (2005).

[65]   M. L. Nakarmi, K. H. Kim, K. Zhu, J. Y. Lin, and H. X. Jiang, *Transport properties of highly conductive n-type Al-rich AlxGa1−xN(x⩾0.7)*, Applied Physics Letters **85**, 3769 (2004).

[66]   B. Neuschl *et al.*, *Direct determination of the silicon donor ionization energy in homoepitaxial AlN from photoluminescence two-electron transitions*, Applied Physics Letters **103**, 122105 (2013).

[67]   N. T. Son, M. Bickermann, and E. Janzén, *Shallow donor and DX states of Si in AlN*, Applied Physics Letters **98**, 092104 (2011).

[68]   Y. Taniyasu, M. Kasu, and N. Kobayashi, *Intentional Control of n-type Conduction for Si-doped AlN and AlxGa1—xN with High Al Content*, physica status solidi (b) **234**, 845 (2002).

[69]   F. Mehnke *et al.*, *Highly conductive n-AlxGa1−xN layers with aluminum mole fractions above 80%*, Applied Physics Letters **103**, 212109 (2013).

[70]   T. W. Frank Mehnke, Harald Pingel, Christian Kuhn, Christoph Reich, Viola Kueller, Arne Knauer, and M. W. Mickael Lapeyrade, and Michael Kneissl, *Highly conductive n-AlxGa1−xN layers with aluminum mole fractions above 80%*, Applied Physics Letters **103**, 212109 (2013).

[71]   C. Stampfl and C. G. Van de Walle, *Theoretical investigation of native defects, impurities, and complexes in aluminum nitride*, Physical Review B **65**, 155212 (2002).

[72]   L. Gordon, J. L. Lyons, A. Janotti, and C. G. Van de Walle, *Hybrid functional calculations of DX centers in AlN and GaN*, Physical Review B **89**, 085204 (2014).

[73]   L. Silvestri, K. Dunn, S. Prawer, and F. Ladouceur, *Hybrid functional study of Si and O donors in wurtzite AlN*, Applied Physics Letters **99**, 122109 (2011).

[74]   D. F. Hevia, C. Stampfl, F. Viñes, and F. Illas, *Microscopic origin of n-type behavior in Si-doped AlN*, Physical Review B **88**, 085202 (2013).

[75]   D. V. Lang, R. A. Logan, and M. Jaros, *Trapping characteristics and a donor-complex (DX) model for the persistent-photoconductivity trapping center in Te-doped AlxGa1-xAs*, Physical Review B **19**, 1015 (1979).

[76]   S. F. Chichibu, H. Miyake, Y. Ishikawa, M. Tashiro, T. Ohtomo, K. Furusawa, K. Hazu, K. Hiramatsu, and A. Uedono, *Impacts of Si-doping and resultant cation vacancy formation on the luminescence dynamics for the near-band-edge emission of Al0.6Ga0.4N films grown on AlN templates by metalorganic vapor phase epitaxy*, Journal of Applied Physics **113**, 213506 (2013).

[77]   *Extended Defects in Semiconductors*, Materials Today **10**, 61 (2007).

[78]   D. B. Holt and B. G. Yacobi, *Extended Defects in Semiconductors : Electronic Properties, Device Effects and Structures* (Cambridge University Press, Cambridge, UNITED KINGDOM, 2007).

[79]   W. Knap, C. Skierbiszewski, K. Dybko, J. Łusakowski, M. Siekacz, I. Grzegory, and S. Porowski, *Influence of dislocation and ionized impurity scattering on the electron mobility in GaN/AlGaN heterostructures*, Journal of Crystal Growth **281**, 194 (2005).

[80]   C. G. Van De Walle and J. Neugebauer, *Defects and doping in III-V nitrides*, Materials Science Forum **258-263**, 19 (1997).

[81]   C. Freysoldt, B. Grabowski, T. Hickel, J. Neugebauer, G. Kresse, A. Janotti, and C. G. Van De Walle, *First-principles calculations for point defects in solids*, Reviews of Modern Physics **86**, 253 (2014).

[82]   Y. Gao, D. Sun, X. Jiang, and J. Zhao, *Point defects in group III nitrides: A comparative first-principles study*, J. Appl. Phys. **125** (2019).

[83]   J. S. Harris, B. E. Gaddy, R. Collazo, Z. Sitar, and D. L. Irving, *Oxygen and silicon point defects in ${\mathrm{Al}}_{0.65}{\mathrm{Ga}}_{0.35}\mathrm{N}$*, Physical Review Materials **3**, 054604 (2019).

[84]   L. Gordon, J. Lyons, and A. Janotti, *Hybrid functional calculations of DX centers in AlN and GaN*, Physical Review B (Condensed Matter and Materials Physics) **89** (2014).

[85]   C. Park and D. Chadi, *Stability of deep donor and acceptor centers in GaN, AlN, and BN*, Physical Review B - Condensed Matter and Materials Physics **55**, 12995 (1997).

[86]   P. Bogusławski and J. Bernholc, *Doping properties of C, Si, and Ge impurities in GaN and AlN*, Physical Review B - Condensed Matter and Materials Physics **56**, 9496 (1997).

[87]   R. Collazo, S. Mita, J. Xie, A. Rice, J. Tweedie, R. Dalmau, and Z. Sitar, *Progress on n-type doping of AlGaN alloys on AlN single crystal substrates for UV optoelectronic applications*, physica status solidi c **8**, 2031 (2011).

[88]   N. Nepal, M. L. Nakarmi, J. Y. Lin, and H. X. Jiang, *Photoluminescence studies of impurity transitions in AlGaN alloys*, Applied Physics Letters **89**, 092107 (2006).

[89]   P. Reddy *et al.*, *Pinning of energy transitions of defects, complexes, and surface states in AlGaN alloys*, Appl. Phys. Lett. **116** (2020).

[90]   R. Dahal, J. Li, A. Sedhain, B. Pantha, J. Y. Lin, and H. X. Jiang, in *CLEO: 2011 - Laser Science to Photonic Applications*2011), pp. 1.

[91]   M. L. Nakarmi, N. Nepal, J. Y. Lin, and H. X. Jiang, *Photoluminescence studies of impurity transitions in Mg-doped AlGaN alloys*, Applied Physics Letters **94**, 091903 (2009).

[92]   M. L. Nakarmi, N. Nepal, C. Ugolini, T. M. Altahtamouni, J. Y. Lin, and H. X. Jiang, *Correlation between optical and electrical properties of Mg-doped AlN epilayers*, Applied Physics Letters **89**, 152120 (2006).

[93]   J. L. Lyons, A. Janotti, and C. G. Van de Walle, *Shallow versus Deep Nature of Mg Acceptors in Nitride Semiconductors*, Physical Review Letters **108**, 156403 (2012).

[94]   B. Gil and Oup, *III-nitride semiconductors and their modern devices [internet resource]* (Oxford : Oxford University Press, Oxford, 2013).

[95]   K. M. Gupta and N. Gupta, in *Advanced Semiconducting Materials and Devices*, edited by K. M. Gupta, and N. Gupta (Springer International Publishing, Cham, 2016), pp. 385.

[96]   H. P. Maruska, D. A. Stevenson, and J. I. Pankove, *Violet luminescence of Mg-doped GaN*, Applied Physics Letters **22**, 303 (1973).

[97]   M. A. Khan, R. A. Skogman, R. G. Schulze, and M. Gershenzon, *Electrical properties and ion implantation of epitaxial GaN, grown by low pressure metalorganic chemical vapor deposition*, Applied Physics Letters **42**, 430 (1983).

[98]   I. Akasaki, H. Amano, H. Murakami, M. Sassa, H. Kato, and K. Manabe, *Growth of GaN and AlGaN for UV/blue p-n junction diodes*, Journal of Crystal Growth **128**, 379 (1993).

[99]   M. Kneissl, in *III-Nitride Ultraviolet Emitters: Technology and Applications*, edited by M. Kneissl, and J. Rass (Springer International Publishing, Cham, 2016), pp. 1.

[100]   H. Hirayama, N. Maeda, S. Fujikawa, S. Toyoda, and N. Kamata, *Recent progress and future prospects of algan-based high-efficiency deep-ultraviolet light-emitting diodes*, Japanese Journal of Applied Physics **53**, 100209 (2014).

[101]   C. Pernot *et al.*, *Development of high efficiency 255-355 nm AlGaN-based light-emitting diodes*, Physica Status Solidi (A) Applications and Materials Science **208**, 1594 (2011).

[102]   M. Shatalov *et al.*, *Algan deep-ultraviolet light-emitting diodes with external quantum efficiency above 10%*, Applied Physics Express **5**, 082101 (2012).

[103]   M. Shatalov *et al.*, *High power algan ultraviolet light emitters*, High power AlGaN ultraviolet light emitters **29**, 084007 (2014).

[104]   H. Hirayama, Y. Enomoto, A. Kinoshita, A. Hirata, and Y. Aoyagi, *Efficient 230–280 nm emission from high-Al-content AlGaN-based multiquantum wells*, Applied Physics Letters **80**, 37 (2002).

[105]   Y. Nagasawa and A. Hirano, *A Review of AlGaN-Based Deep-Ultraviolet Light-Emitting Diodes on Sapphire*, Applied Sciences **8** (2018).

[106]   H. Hirayama, T. Yatabe, T. Ohashi, and N. Kamata, *Remarkable enhancement of 254-280 nm deep ultraviolet emission from AlGaN quantum wells by using high-quality AlN buffer on sapphire*, physica status solidi c **5**, 2283 (2008).

[107]   U. K. Mishra, L. Shen, T. E. Kazior, and Y. Wu, *GaN-Based RF Power Devices and Amplifiers*, Proceedings of the IEEE **96**, 287 (2008).

[108]   H. Miyamoto *et al.*, in *Wide Bandgap Semiconductors: Fundamental Properties and Modern Photonic and Electronic Devices*, edited by K. Takahashi, A. Yoshikawa, and A. Sandhu (Springer Berlin Heidelberg, Berlin, Heidelberg, 2007), pp. 231.

[109]   M. Asif Khan, J. N. Kuznia, D. T. Olson, W. J. Schaff, J. W. Burm, and M. S. Shur, *Microwave performance of a 0.25 µm gate AlGaN/GaN heterostructure field effect transistor*, Applied Physics Letters **65**, 1121 (1994).

[110]   P. Javorka, *Fabrication and Characterization of AlGaN/GaN High Electron Mobility Transistors*, (2004).

[111]   T. Hashizume, J. Kotani, and H. Hasegawa, *Leakage mechanism in GaN and AlGaN Schottky interfaces*, Applied Physics Letters **84**, 4884 (2004).

[112]   S. C. Binari, P. B. Klein, and T. E. Kazior, *Trapping effects in GaN and SiC microwave FETs*, Proceedings of the IEEE **90**, 1048 (2002).

[113]   A. S. A. Fletcher, D. Nirmal, L. Arivazhagan, and J. Ajayan, 2019), pp. 239.

Chapter 3

3. Experimental Methods

This chapter introduces the experimental techniques used in the study of III-nitride semiconductor samples. The main techniques used in this work are scanning electron microscopy, cathodoluminescence and wavelength dispersive X-ray spectroscopy. Techniques that will be discussed relating to results provided by collaborators include secondary ion mass spectrometry and atomic force microscopy. The principles of scanning electron microscopy and the specific microscopy techniques used to acquire data presented in this thesis will be described in more detail. Cathodoluminescence (CL) imaging/spectroscopy and wavelength dispersive X-ray spectroscopy (WDX) are presented in terms of instrument setup, general principles of operation and type of information that can be obtained by each technique. More information about the subject can be found in the book "Electron Microscopy and Analysis" by Goodhew et al. [1], in the book chapter "Cathodoluminescence hyperspectral imaging in geoscience" by Edwards and Lee [2] and in the paper from Edwards et al. [3].

3.1 Scanning electron microscopy

A scanning electron microscope (SEM) is primarily used for observation of specimen surfaces. When the specimen is irradiated with an electron beam (electron probe), secondary electrons are emitted from the specimen surface. Using the two dimensional scanning of the probe over the specimen surface and by acquiring the image from the detected secondary electrons, topography of the sample is examined.

The SEM consists of electron optical system, specimen chamber, various detectors, display unit and operation system. The main components of electron optical systems are an electron gun, a condenser and an objective lens, required to produce an electron probe, and a scanning coil used to scan the probe. The whole system is under high vacuum (except in the case of the environmental scanning electron microscope (ESEM)) in order to minimize electron-gas

interactions. The electron gun function is to produce an electron beam and accelerate the electrons produced in a voltage range of typically $1-30$ kV.

Two different SEMs have been used in this thesis: an FEI Quanta FEG 250 (CL imaging) and a JEOL JXA-8530F electron probe microanalyser (EPMA). The working principle of both is similar and a schematic diagram of the EPMA is presented in Fig. 3.1.
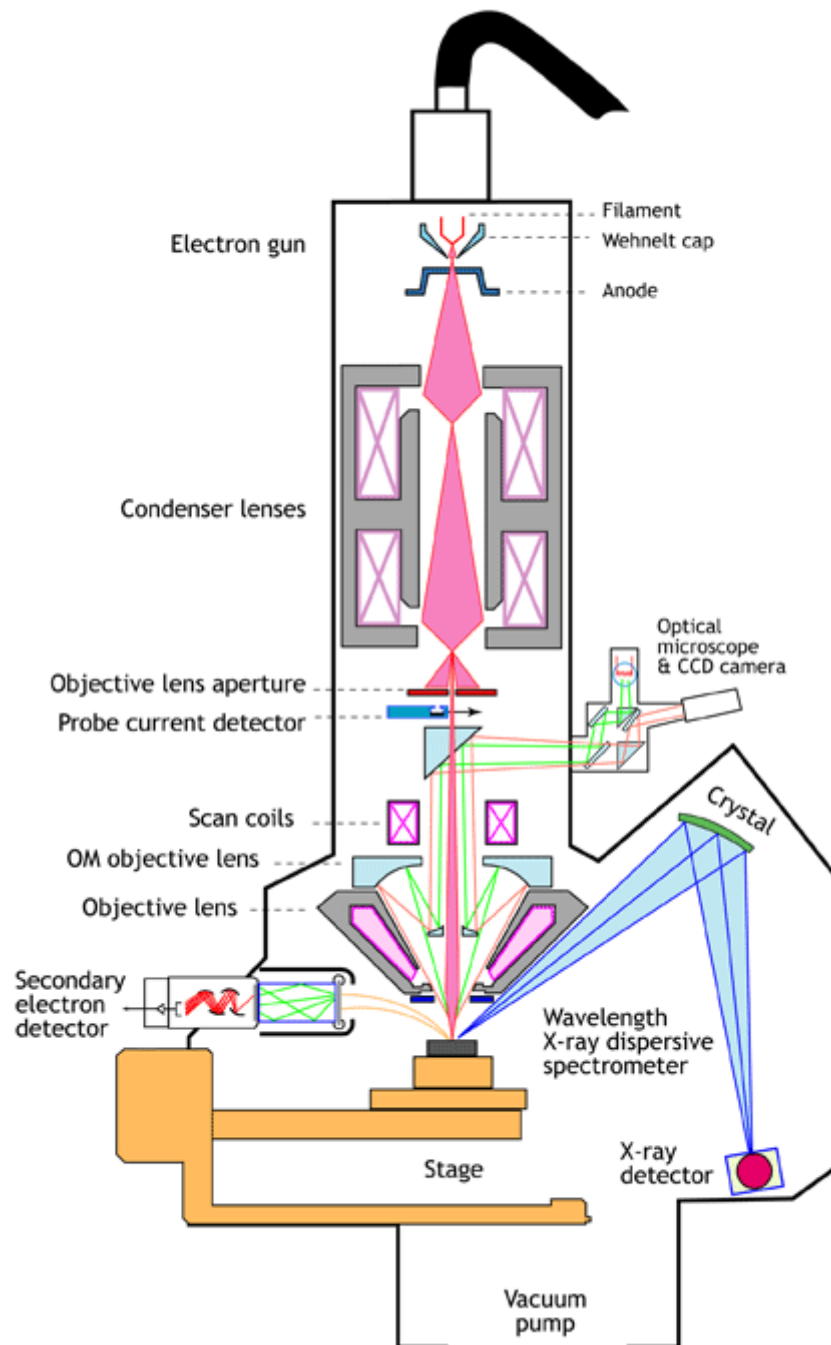
Fig. 3.1: Schematic diagram of the main features of an EPMA [4].

3.1.1 Electron sources

The electron gun produces an electron beam. There are three types of electron guns: TE (thermionic emission) gun, FE (field-emission) gun and SE (Schottky-emission) gun. The schematic diagram of an electron gun is shown in Figure 3.2. This figure depicts the simplest gun with a heated tungsten wire, a filament (cathode) used to produce electrons. Other more expensive types employ lanthanum hexaboride crystals: LaB_6. By heating a filament at high temperature (around 2800 K) thermoelectric emission is achieved. Produced thermoelectrons flow towards the metal plate (anode) by applying a positive voltage (1 to 30 kV) to the anode. A Wehnelt electrode is placed between cathode and anode with applied negative voltage to it, for the adjustment of current of the electron beam and its focusing. The crossover point, finest point of the beam, is referred to as the actual electron source with a diameter of $15-20$ µm.
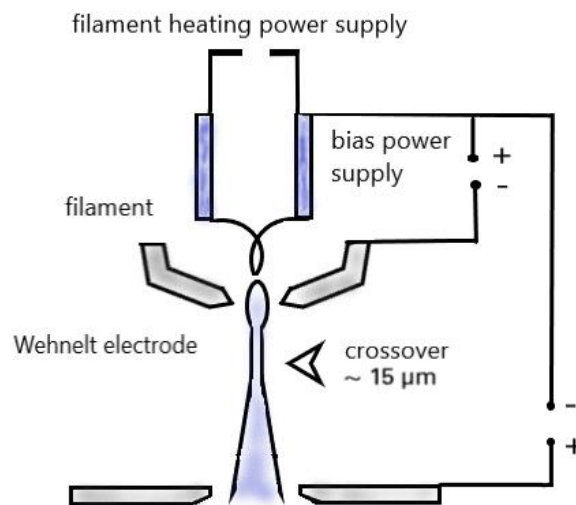
Figure 3.2: Construction of a TE electron gun, drawn after original from [5].

The electron gun used for high-resolution SEM is the FE gun. The FE gun requires an ultra-high vacuum of about 10^{-8} Pa. It works on the principle of the field-emission effect that occurs when a high electric field is applied to a metal surface. The construction of the gun is shown in Fig. 3.3.

A tungsten wire is used as a cathode, but a single crystal tungsten is welded to it, with the tip of the crystal (emitter) having a radius of about 100 nm. A few

kV of (positive voltage) is applied to a metal plate (extracting electrode) and the produced electric field is proportional to 1/radius, so the small tip radius leads to the high electric field, which in turn leads to the tunnelling effect and emission of electrons from the cold emitter. The emitted electrons will pass through the hole in the middle of the extracting electrode which is placed below it; when a voltage is applied to this electrode, an electron beam of certain energy is formed. This same arrangement is found in all types of emitters. An FE gun produces a much smaller electron source compared to a TE gun. Another advantage of the FE gun is the small energy spread of the beam, due to lack of emitter heating. Energy spread is mostly important for low voltage observation. In a cold FE gun, the cathode can be cleaned occasionally by turning on the flashing power supply in order to remove adsorbed gas from the cathode surface.
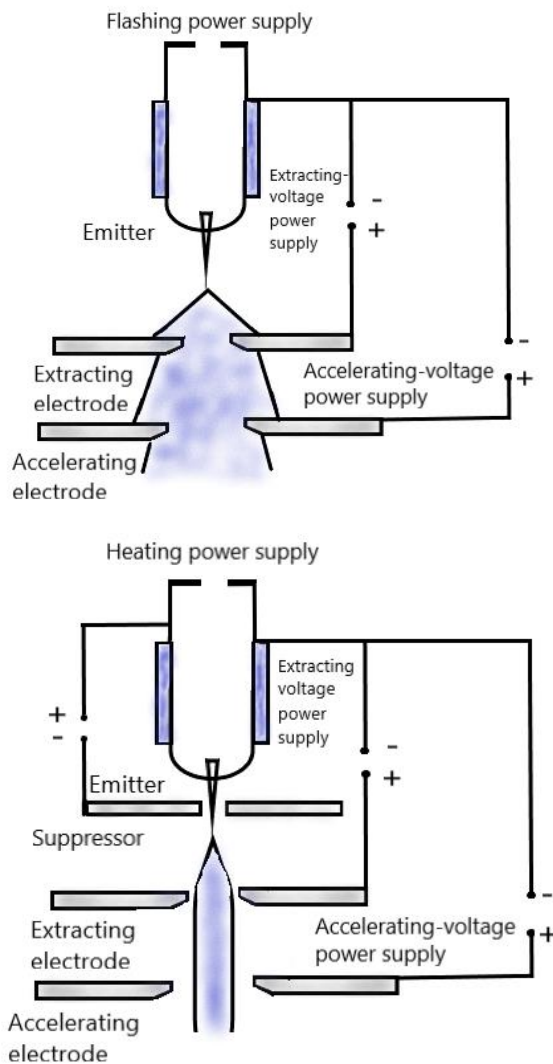
Figure 3.3: Construction of a cold electron gun (up) and Schottky gun (down) drawn after original from [5].

The Schottky emission gun works on the principle of thermally assisted tunnelling that occurs when a high electric field is applied to a heated metal surface. The construction of the gun is shown in Fig. 3.3. The difference compared with an FE gun is that a tungsten single crystal is coated with ZrO, and the tip is heated. The purpose of the ZrO is to reduce the work function, in order to achieve high emission current at a relatively low cathode temperature (around 1800 K). The design of the gun also differs by the addition of a suppressor, used to apply a negative voltage to the electrode for shielding of thermoelectrons from the emitter. The advantage of the SE gun compared to FE is the generation of a larger probe current and removal of the need to flash the cathode. The FEI Quanta 250 FEG-SEM and JEOL JXA-8530F EPMA used in this work are both equipped with a Schottky field emission gun.

The four major parameters that describe the beam properties in a SEM are; the voltage at which the electrons are being accelerated as they travel through the electron column, the convergence angle of the electron-beam cone, the beam current that hits the sample and the electron beam diameter. The beam current will have greatest influence on the electron beam diameter. Consequently, the spot size can be limited by the beam current due to Coulombic repulsion of the electrons in the beam. Spot size, referred also as probe size, shape, and current are important parameters for the performance of all types of electron microscopes. In this thesis spot size is noted together with other instrumental parameters used to acquire CL spectrum. For the Quanta 250, FEI instruments use a number which they refer to as "spot size" which is a measure of the beam current. The spot number change influences both the focused electron beam area and the beam current. The lower is the spot number, the lower is the beam current. For example, for high resolution work, a smaller spot size is desirable, while larger spot sizes are more suitable for low magnification and X-ray analysis. Both the irradiated area and the beam current increase with the spot number which has a range from 1 to 7 (factory pre-set list). There is always a compromise between the spot size and the number of electrons in the probe (current) that has to be sufficient for the signal collection. The EPMA

instrument allows direct control over the beam current using a Faraday cup, allowing a current to be quantitatively specified in nanoamps.
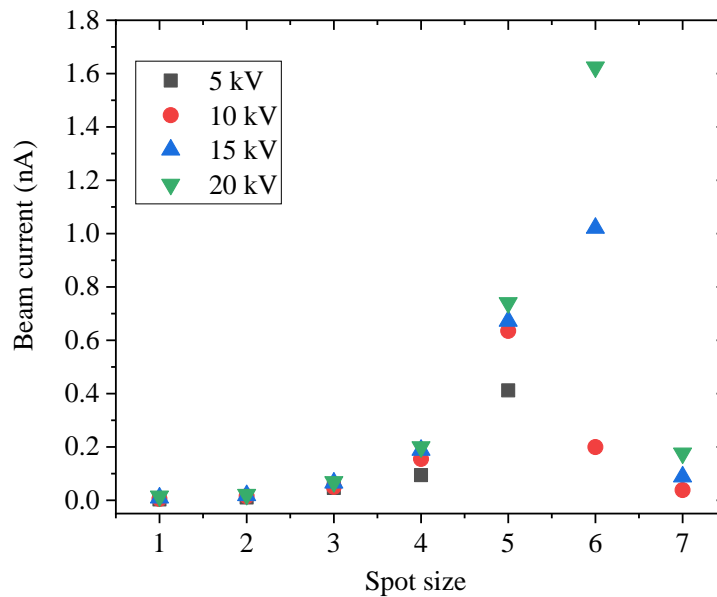
Figure 3.4: Relation between spot size and probe current, measured with 30 μm aperture at 10.2 mm working distance.

3.1.2 Electron-sample interaction

When the electron beam hits a surface it interacts with the atoms in that sample. Image formation in the SEM depends on the acquisition of signal acquired from the electron beam and specimen interaction. Detail description can be found in [6]. These interactions can be divided into two major categories: elastic and inelastic interactions. Elastic interaction occurs with a negligible energy loss during the collision and by a wide-angle directional change of the scattered electrons. It is caused by a deflection of the incident electrons by the specimen atomic nucleus or by outer shell electrons of similar energy. Incident electrons that are elastically scattered through an angle of more than 90° and re-emerge from the sample are called backscattered electrons (BSE) and are used as an imaging signal. Backscattered electrons have energies ranging up to E_0 (the incident electron energy) and elements of high atomic number (Z) have a large probability of high angle deflection compared to low-Z elements.

During inelastic scattering, primary beam electrons transfer energy to that atom. It occurs via different interactions between the incident electrons and atoms of the sample. The rate of energy loss will depend on the target material. It will result in ionization of specimen atoms and generation of secondary electrons (SE) (defined as possessing energies of less than 50 eV) that are also used for imaging. Because of their low energy, only those electrons that originate within a few nanometres of the surface are able to escape from sample. A number of other signals are produced during the electron beam-sample interaction, including the emission of characteristic X-rays, Auger electrons and cathodoluminescence that can be used for the material characterization. Many of the results in this thesis are based on detection of the CL signal and/or characteristic X-rays, and these will be discussed in more detail in the following sections.
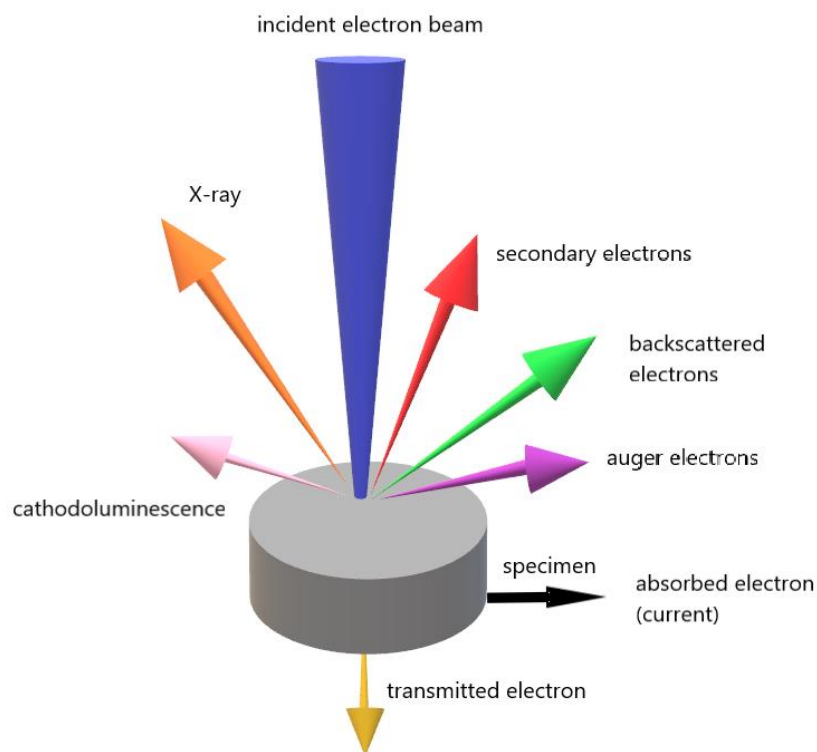
Figure 3.5: Signals generated by electron-sample interactions.

3.1.3 Secondary electron and backscattered imaging

In SEM, two types of electrons are primarily detected: backscattered electrons (BSE) and secondary electrons (SE). As introduced in the previous section, BSE come from deeper regions of the sample, while SE originate from surface regions. Therefore, they carry different types of information. BSE images show high sensitivity to differences in atomic number while SE imaging can provide more detailed surface information.

The backscattered electron image contains two types of information: one on specimen composition and other on specimen topography. Usually BSE detectors are solid state detectors with p-n junctions. They work on the principle of generation of electron-hole pairs in the detector through impact ionisation. The number of the generated electron-hole pairs depends on the energy of the backscattered electrons and determines the electrical current generated within the p-n junction. The BSE detectors are typically placed above the sample, concentrically to the electron beam, consisting of symmetrically divided parts. It is possible to use specific quadrants of the detector in different combinations, in order to extract specific information, such as surface topography or atomic number contrast. To separate these two types of information, two or more semiconductor detectors are positioned symmetrically with respect to the optical axis. The signals acquired from each segment are amplified with the preamplifier, and then processed with the main amplifier in such a way that a composition image (COMPO) is obtained by addition of the signals and a topography image (TOPO) is obtained by subtraction of them.
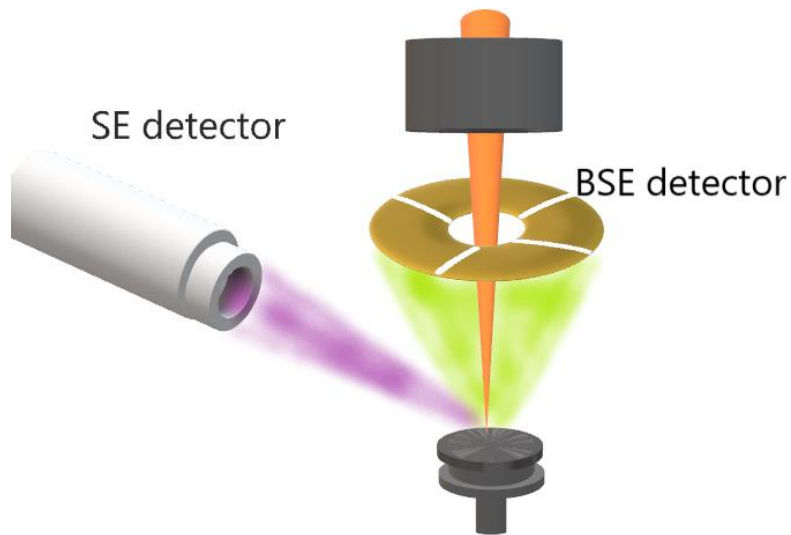
Figure 3.6: Typical position of the backscattered and secondary electron detectors. Redrawn after original from [7].

The shallow depth of production of detected secondary electrons makes them ideal for examining topography. The most frequently used type of SE detector is the Everhart-Thornley detector. A low positive voltage (few hundred volts) is applied to the Faraday cage to attract the relatively low energy secondary electrons. A scintillator placed inside the Faraday cage has a high positive voltage (10 kV) to accelerate the incoming electrons where they can be further converted to visible photons which are detected using a photomultiplier. The SE detector is placed at the side of the electron chamber, at an angle, because there is no room directly above the sample, which is not crucial because it attracts SEs emerging from the sample at all angles.
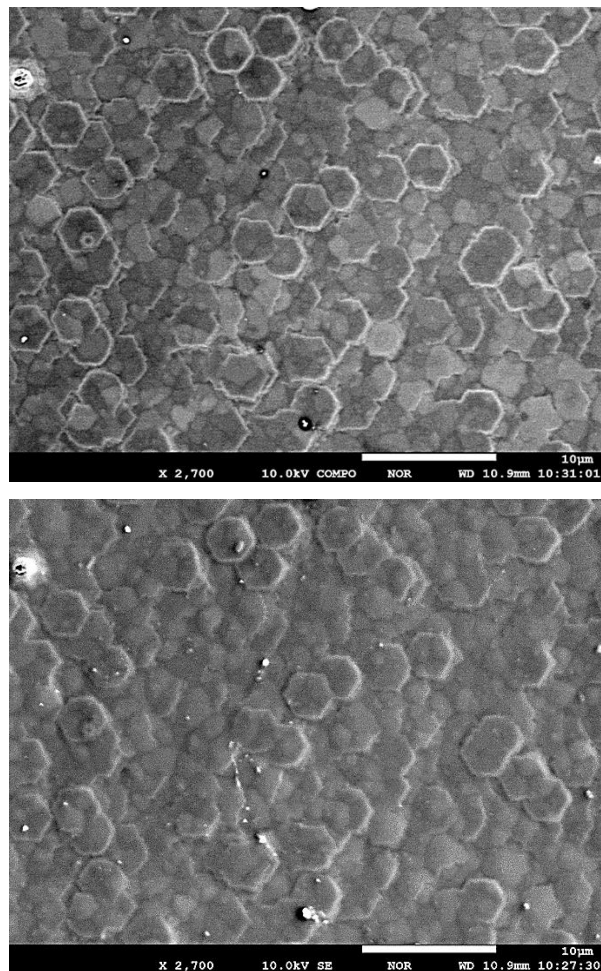
Figure 3.7 AlGaN alloy: Up image taken with the BSE detector and down image taken simultaneously with the SE detector.

Fig.3.7 depicts the difference in the signals captured with SE and BSE detectors from a sample of AlGaN. In the BSE image the difference in atomic number is more enhanced with bright edges around hexagon features indicating a region of higher atomic mass, in this case a GaN rich region. The SE image better depicts surface topography and more surface details are observable. Difference in brightness is caused by the difference in the incidence angle of the electron beam, (secondary electron yield increases with the tilt angle of specimen surface) and shadowing effect. In this thesis BSE image and X-ray maps of the same area were often compared because they confirm each other, in the way that if the contrast in one is caused by topographic effects, this would have shown up as inverted contrast in the other. Seeing bright edges in both therefore unambiguously points to higher mass regions in a way that one or other by itself would not (more details in Chapter 6). If a specimen with a uniform composition

is observed, backscattered electron intensity will depend on crystal orientation; this type of image contrast is called electron channeling contrast (ECCI) [8].

3.1.4 The environmental SEM

As mentioned before, the electrons that enter the specimen lose their energy and they are absorbed in the specimen. When a specimen is conductive, these absorbed electrons flow through the specimen stage. If the specimen is non-conductive, electrons are stopped in the sample, that is, charging occurs. In the case of charging, the number of electrons flowing to the specimen is different from the number that exit from the specimen. Usually, the specimen becomes negatively charged at the irradiation point; if the irradiation continues, discharge will take place and the potential will return to the original value. During the charging process, the electron beam is deflected from a charged potential causing a shift of the probe and image distortion. Negative charging will also affect secondary electrons trajectories and their detection efficiency, resulting in parts of the image appearing to "glow" (being brighter) or cause geometry distortion in the image as electron production is artificially enhanced or the beam is unintentionally defected. Positive potential can build up when more electrons are emitted from the sample than supplied from electron beam. The positively charged regions rather than glowing brighter, get darker, because the secondary electron (SE) emission is reduced. Positive charging is far less detrimental than negative charging, the main result being a loss of some valuable signal electrons as they are re-absorbed by the positively charging surface [9].

The most common method to prevent charging is conductive coating. The nonconductive sample is coated with a high-conductive thin metal film (e.g. Au, Pt, Au-Pd, Pt-Pd) or carbon.

Non-conductive samples can be observed in the low vacuum SEM (environmental SEM). For insulators (dry ceramics, polymers and semiconductors) the obvious key advantage of the ESEM is the removal of the need to apply a conductive coating. More details about ESEM can be found in [10]. In a high vacuum SEM the pressure inside the specimen chamber is kept at 10^{-3} to 10^{-4} Pa, but in a low vacuum mode the pressure can be increased to a

several hundreds of Pa. The gun chamber still requires a high vacuum so a pressure-limiting aperture is usually placed between the electron-beam path and specimen chamber. When the vacuum in specimen chamber is decreased, the number of residual gas molecules is increased. Many of these gas molecules are ionized by the secondary electrons emerging from sample and any areas of charge will result in ions of the required charge sign being attracted in order to neutralise the charge. The resulting conduction path between the sample and detector is used as a method of measuring the SE emission. As explained, due to the charging, anomalous contrast arises in high vacuum mode which is not present in the low vacuum mode. The electron-gas interactions can also lead to a broadening of the spot size of the electron beam and result in the decrease of the spatial resolution. In order to reduce worsening of the resolution in the low vacuum, the total distance through which electrons travel is kept as short as possible, so that most of the incident electrons do not undergo any large-angle collisions. The signal electron detection system in ESEM is also different from a conventional SEM. The Everhart Thornley (E–T) detector in conventional SEM does not work in a gaseous environment due to its high bias, while the BSE detector is still operational in this environment as are other specialised low-vacuum SE of detectors. Charging of the sample affects the SE image far more compared to the higher-energy BSE. The bias of the SE detector can be grounded or negatively (reverse) biased, in order to reject the SE and only allowing those high-energy BSEs that are in the proper geometrical relationship to the detector to be collected. Also, sample tilting can be helpful to improve signal collection and strength [9].

3.2 Cathodoluminescence spectroscopy

One of the signals produced after interaction of electron beam with sample is cathodoluminescence (CL), or simply put the light emission. CL is dependent on a large number of variables as temperature, chemical composition, crystal structure, presence of defects, and strain. In semiconductors the luminescence occurs as a result of radiative recombination of an electron and a hole. These charge carriers can be excited in different ways, with optical excitation (PL), electron-beam excitation (CL), excitation by carrier injection (EL) and

excitation by high energy nuclear radiation. In this work CL was used for characterization of the semiconductor material. In the semiconductors different forms of excitation energy will lead to emission of light, so it is possible to compare photoluminescence (PL), electroluminescence (EL) and CL. Even though they produce similar result they will differ in excitation process of electron-hole pairs, generation rate and volume. In CL each electron in electron beam can generate multiple electron-hole pairs compared to PL where each photon, from the light source, can only generate one electron-hole pair. The main advantages of the CL are the high spatial resolution, the possibility to obtain more depth-resolved information by varying the electron beam energy, and the ability to to obtain complementary information from other SEM modes, such as WDX for example. In CL the spatial resolution is determined by the distribution of excess carriers in the material, and is therefore not limited by diffraction in the collection and excitation optics which has allowed the technique to be pushed beyond the micron scale.

In semiconductors the CL emission can occur through various recombination processes. The luminescence transitions can be divided into (i) intrinsic, fundamental or near bandgap, and (ii) extrinsic, or characteristic transitions. The intrinsic transitions are result of recombination of electrons and holes across the fundamental energy gap. The emission spectra which depends on the presence of impurities, are of extrinsic nature. A simplified set of radiative transitions that lead to luminescence emission is given in Fig. 3.8.
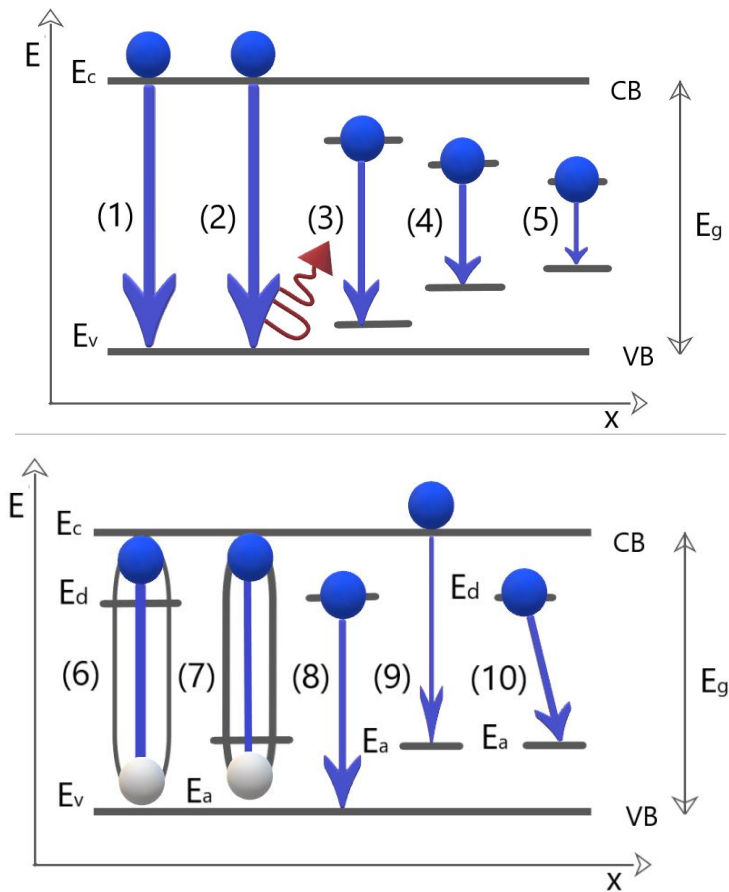
Figure 3.8: Drawn after original from [11]. With E_C the conduction band energy level; E_V the valence band energy level and E_g the band gap ($E_C - E_V$); E_d and E_a the donor and acceptor energy level respectively.

Processes $1-5$ are intrinsic recombination transitions in order of decreasing transition energy, and processes $6-10$ are extrinsic recombinations in the presence of impurity levels. Process 1 represents direct band-to band transition (spontaneous emission), recombination of an electron from the conduction band and a hole with the same momentum vector from the valence band. In nitrides, the NBE peak is dominated by free exciton (electron-hole pair), not bound electron-hole pair. Process 2 is an indirect band-to-band transition with emission of a wavevector-conserving phonon. Process 3 represents exciton decay which is noticeable at low temperatures; in nitrides the free exciton binding energy is high enough that they exist at RT. At low temperatures multiple excitons can bind together and form excitonic molecules, so process 4 represents transition due to excitonic molecules and the resulting transition energy of this transition is lower than that of the free exciton. Process 5 is the luminescence due to electron-hole drop, which is observable in high density excitonic gas below a

well-defined temperature and is accompanied by a broadening of excitonic resonances and a band-gap reduction. At low temperatures the free exciton can be easily trapped by various impurities and centres, such as neutral donors (D^0) and neutral acceptors (A^0) forming complexes called bound excitons. Processes 6 and 7 represent decay of donor bound and acceptor bound excitons, respectively. Processes 8 and 9 show transitions which start or finish on donor or acceptor states localised in the gap. Similar transition can occur from deep donors and deep acceptors and lead to recombination emission with energies well below the band gap. That type of transition is shown in process 10 and is called donor-acceptor pair (DAP) transition. The energy of this emission depends on the separation of the donor and acceptor ions, leading to the broad emission. CL spectra are dominated with emission lines associated with free excitonic states, donor-acceptor pair bands and defect-related features with variations due to changes in alloying, strain, doping and carrier concentration. CL images show the spatial distribution of these phenomena, and the distribution of defects can be visualized due to their higher rates of non-radiative recombination (and therefore lower CL intensity). That is the reason why cathodoluminescence spectroscopy has proved to be a powerful technique for the examination and is one of the main experimental tool of this thesis. CL is especially beneficial for study of the wide bandgap materials, as the expense of deep UV lasers is one reason why PL is difficult for these materials.

An example of the CL spectrum of a Si doped AlGaN layer, in which three different peaks can be distinguished, is shown in Fig. 3.9. The near band edge (NBE) peaks arises due to recombination from the conduction band to the valence band of the AlGaN layer. The other two peaks arise due to the recombination from an electron in the conduction band with a hole in two different acceptor states in the sample.
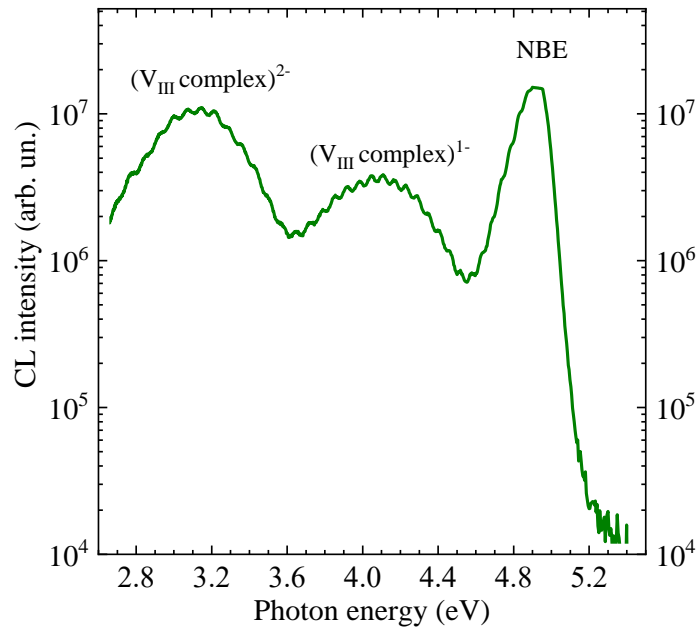
Figure 3.9: The CL spectrum for a polar n-AlGaN sample (A5P), showing emission peaks due to near band-edge (NBE) emission and group III vacancy complexes.

3.2.1 CL Experimental setup

All cathodoluminescence spectra in this thesis were acquired in a CL setup that was designed and assembled in our laboratory. The CL system used for hyperspectral imaging is designed by Dr. Paul R. Edwards, and is installed in a commercial FEG SEM (FEI Quanta 250). All CL measurements are performed at room temperature. In this setup, the electron beam is perpendicular to the axis of the detection optics. In order to achieve better light collection, the sample is mounted on a stub which is pretilted by 45° (shown in Figure 3.10).
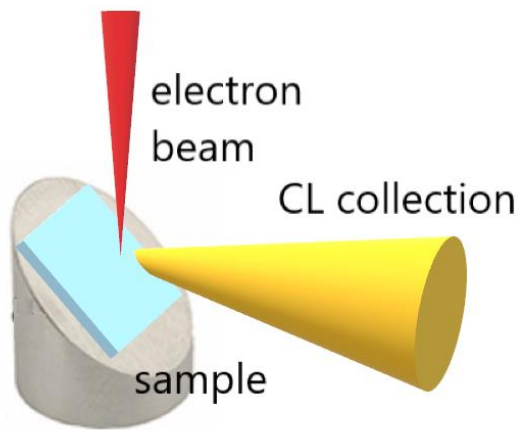
Figure 3.10: Schematic diagram of the light collection geometry.

The emitted light is collected and collimated by a Schwarz schild-type reflecting objective (numerical aperture of 0.28) and focused using an off-axis paraboloidal mirror onto the entrance slit (25, 50 or 100 µm) of a 1/8 m spectrograph (Oriel MS125) with exchangeable diffraction gratings. The light is detected by an electron-multiplying CCD (Andor Technology, Newton DU970-UVB). The reflecting objective design does not suffer from either chromatic aberration or absorption at short wavelength. Another advantage is the use of off-axis light collection which means there is no object between the pole piece of the microscope and the sample, making it possible to use short working distances or to tilt the sample.

3.2.2 Hyperspectral CL imaging

Hyperspectral CL imaging is the acquisition of the full CL spectrum at each point in a scan. Such a measurement results in the accumulation of a multidimensional data set ("data cube"), or hyperspectral image, containing the full set of spectrally and spatially resolved luminescence information. Fig. 3.11 is a representation of the image acquisition principle.
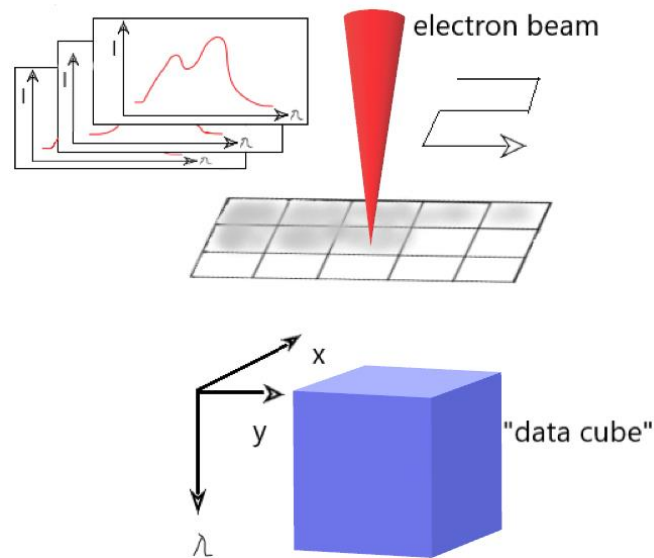
Figure 3.11: CL hyperspectral image acquisition, drawn after original from [12].

For the data collection in this thesis the analysis software: Cathodoluminescence Hyperspectral Imaging and Manipulation Program (CHIMP) developed by Dr. Paul R. Edwards is used.

The most obvious advantage of the hyperspectral mode of measuring CL is that more data is acquired in a single measurement. Another one is the ability to deconvolve spectral features through either peak fitting or the use of multivariate statistical analysis methods. The dataset can then be manipulated to yield different information as a function of position, e.g.: integrated intensity (panchromatic image), wavelength slice (monochromatic image), peak wavelength, peak width, deconvolved peak parameters of multiple peak profiles, or chromaticity (i.e. calculated "real" colour).

The number of spectral channels in an HSI dataset is often very large (CCD arrays typically having over 1000 channels). The analysis of hyperspectral data requires some method of reducing the raw data into a more useable form in order to extract the required information. The simplest way of extracting 2-D images from the multi-dimensional dataset is achieved by integrating the spectrum between two wavelength limits, and repeating for each spatial pixel. In that manner monochromatic images are generated from the hyperspectral image, but the exact centre wavelength and bandpass can be finely tuned after data acquisition, and the multiple images can be extracted from the same dataset. Different parameters extracted from the spectra can be mapped: for example,

peak or centroid wavelengths, peak widths, maximum intensity, etc. Peak fitting method can be employed for mapping of the isolated peak and non-linear least-squares minimisation algorithms are used to simultaneously fit multiple peaks to each spectrum in turn, in the hyperspectral image (e.g. Gaussian or Lorentzian). Another analysis tool is principal component analysis (PCA). PCA finds the main contributing factors of a data set (the principal components) and allows to re-plot the data set as a function of these components.

3.3 Electron probe microanalysis (EPMA)

The origins of EPMA go back to the discovery of X-rays in 1895, with the first electron microprobe developed by Raimond Castaing in 1950 by fitting a crystal spectrometer to a modified electron microscope [13]. Using the developed instrument, Castaing established the basic principles of quantitative EPMA. Since the release of the first commercial electron microprobe in 1958 by the CAMECA company, many improvements were made in the electron probe system, as well as in the x-ray spectrometers that have been improved in terms of stability, reproducibility and detection limits. EPMA is a non-destructive analytical technique and is based on the measurement of characteristic x-ray intensities emitted by the elements present in the sample when the latter is bombarded with a focused electron beam. The emitted X-rays can be analysed with two different types of spectrometer, a wavelength-dispersive spectrometer (WDX) and an energy-dispersive spectrometer (EDX), both techniques being used for qualitative and quantitative analysis. EPMA offers quantitative analytical capabilities with the imaging capabilities of a scanning electron microscope (SEM), allowing detailed x-ray mapping of composition contrast. Modern EPMA instruments typically possess up to five WDXs, each of which is fitted with different diffracting crystals that reflect specific wavelengths. The EPMA used for measurements in this thesis is equipped with four WDX spectrometers, which will be explained in more detail.

3.3.1 Generation of X-rays

When a high energy electron scatters from an atom, it can eject electrons from the atom's inner low-energy shells (known as K, L and M shells), creating vacancies that are filled by electrons moving from the atom's outer high-energy shells. With the movement of electrons from outer to inner shells the energy is released, and the energy of the emitted X-rays corresponds to the energy difference between the shells involved in the transition. Since every element has its own unique energy level spacing between shells, this process produces characteristic X-ray emissions that can be used to identify the element. Inner-shell ionization is responsible for the emission of characteristic X-rays. Emission of bremsstrahlung takes place when the electron is decelerated in the electrostatic field of the target atom. Bremsstrahlung emission is the source of the continuous background in an X-ray spectrum. Before emerging from the surface, generated X-rays may interact with the sample atoms through different mechanisms, mainly photoelectric absorption, and as a result, fluorescent X-rays may be emitted.
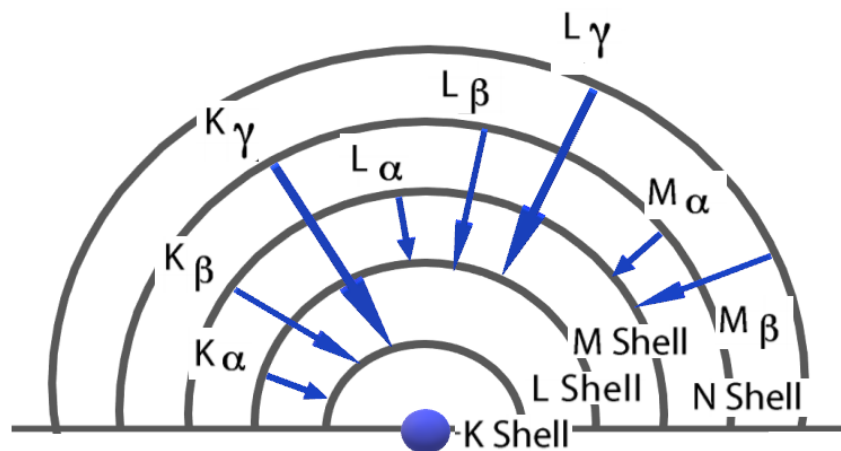
Figure 3.12: Schematic diagram of the different atomic inner atomic shells and main possible transitions to these shells that release characteristic x rays. Redrawn after original from [14].

3.3.2 X-ray detectors

An electron microprobe is usually equipped with several wavelength dispersive spectrometers (WDX) and an energy dispersive spectrometer (EDX) for the X-ray spectroscopy.

3.3.2.1 Energy Dispersive Spectrometer (EDX)

EDX analysis systems, also referred as EDS, consist of three basic parts: a detector, a pulse processor and a multi-channel analyser. The detector is based on a semiconductor device, with the lithium-drifted silicon or Si(Li) detector previously widely used but nowadays largely replaced with the silicon-drift detector (SDD). In order to minimize electronic noise, the detector must be cooled. Si(Li) detectors are cooled with liquid nitrogen, while SDD employ thermoelectric (Peltier) cooling.

Firstly, the X-ray is converted into a charge by the impact ionization of atoms in the semiconductor crystal. The electrons are raised into the conduction band of the semiconductor and are free to move within the crystal lattice. When an electron is raised into the conduction band it leaves behind a hole, which behaves like a free positive charge within the crystal. The incoming X-ray will produce a series of electron-hole pairs in the semiconductor crystal. The number of such electron-hole pairs generated is proportional to the energy of the incoming X-ray. Due to a high voltage bias applied across the crystal electrons and holes will move to electrodes on opposite sides of the device, producing a charge signal that is converted into the voltage signal by the field effect transistor (FET) preamplifier which is passed to the pulse processor. The output from the preamplifier is a voltage "ramp" where each X-ray appears as a voltage step on the ramp.

The pulse processor removes noise from the signal, discriminates the energies of the incoming X-rays and discriminates between X-rays that arrive in the detector closely spaced in time. The time spent removing the noise can be varied

by adjusting the time constant or process time of the detector system. A longer process time means the signal is processed more slowly and the resolution of the spectral peaks is improved, with the increase in dead time. During the dead time system is not processing incoming X-rays but the previously collected signal. The system dead time also depends on the X-ray count rate. At high count rates, the pulse processor may not be able to differentiate between two incoming X-rays.

The size of the produced signal in the pulse processor will be proportional to the energy of the incoming X-ray. The output from the pulse processor is passed to a multi-channel analyser or computer display. A multichannel analyser (MCA) is used to analyse electrical pulses and construct an X-ray spectrum for the entire energy range (0 keV to E_0) in the form of energy histogram. The energy range of the spectrum is divided into a number of channels, e.g., 1024, 2048 or 4096 channels, with energy widths of typically 5, 10 or 20 eV per channel. The number of X-rays with the relevant energy is assigned to each channel, and the result displayed as a histogram of intensity (number of X-ray counts) versus energy.

When performing EDX analysis user has to select the optimal process time and beam current in order to achieve acceptable X-ray count rate and detector dead time, as well as the desired spectral resolution. There is always a "trade-off" between count rate and resolution, in which the choice depends on the application [15, 16].
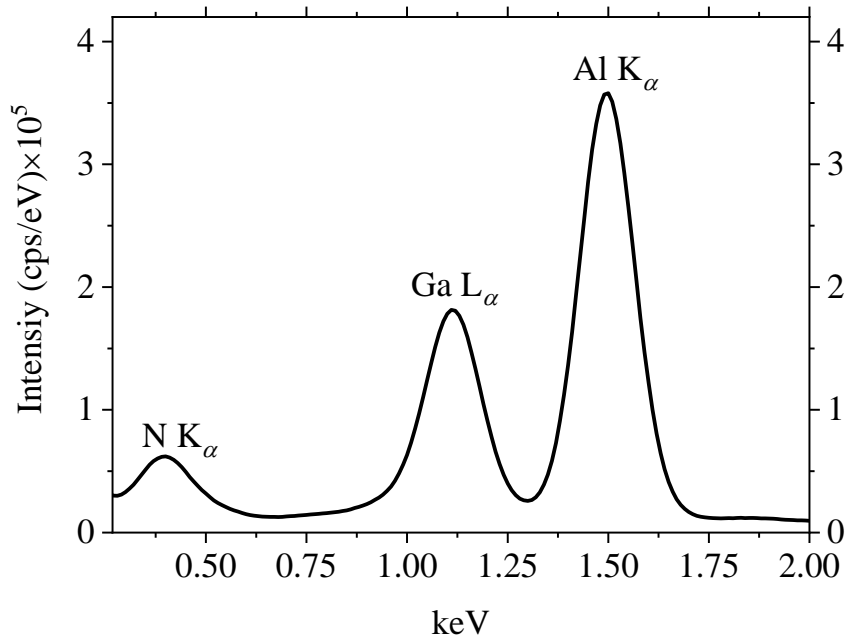
Figure 3.13: Typical EDX spectrum of AlGaN (sample CP2).

3.3.2.2 Wavelength Dispersive Spectrometer (WDX)

While the EDX detector converts the energy of each individual X-ray into a voltage signal of proportional size, WDX analysis (also referred as WDS) classifies and counts the incoming X-rays in terms of their characteristic wavelengths. The most significant difference between WDX and EDX systems is their energy resolution. A Mn K_α X-ray line on an EDX system is typically $130-150$ eV wide. On a WDX system, the same X-ray line will only be about 10 eV wide. Due to this improved spectral resolution the amount of overlap between peaks of similar energies is much smaller on the WDX system. The second disadvantage with EDX systems is the low count rates and poor reproducibility. Typically, a WDX system will have a count rate about $10\times$ that of an EDX system. The disadvantages of WDX system are higher time consumption, greater sample damage and chamber contamination due to the high beam currents required, and high cost.

WDX systems works on the principle of X-ray diffraction by which X-rays of different wavelengths are separated. The spectrometer consists of an analysing crystal and a detector known as proportional counter. Whether an X-ray photon

will diffract depends on its wavelength, the orientation of the crystal, and the crystal lattice spacing.

Reflection (signal) only occurs when conditions for constructive interference between the beams are met. These conditions are met when the difference in path length equals an integral number of wavelengths. This condition is described by Bragg's law:

$$n\lambda = 2d \sin\theta \qquad\qquad (3.1)$$

where λ is the wavelength of the X-ray, d is the lattice spacing of the crystal, θ is the angle of incidence and diffraction and n is the order of reflection. In WDX different types of crystals are available, having different $2d$ values.

Only X-rays of a given wavelength will enter the detector. In WDX, the X-ray source (the sample from which the X-rays are emitted), the analysing crystal and the detector are positioned on the circumference of a focusing circle known as the Rowland circle and the sample height needs to be fixed with respect to the spectrometer. To ensure this, electron microprobes are equipped with reflected-light microscope, allowing the height sample to be determined by means of optical focus. Crystals must be curved to maintain the same incidence angle as X-rays emitted from a point source. The take-off angle remains the same when crystal and the sample are moved.

From the geometrical configuration of the instrument, λ is related to L, the distance between the sample and the analysing crystal by the following relation:

$$L = n\lambda R/d \qquad\qquad (3.2)$$

where, R is the radius of the focusing circle (140 mm or 100 mm on JEOL).
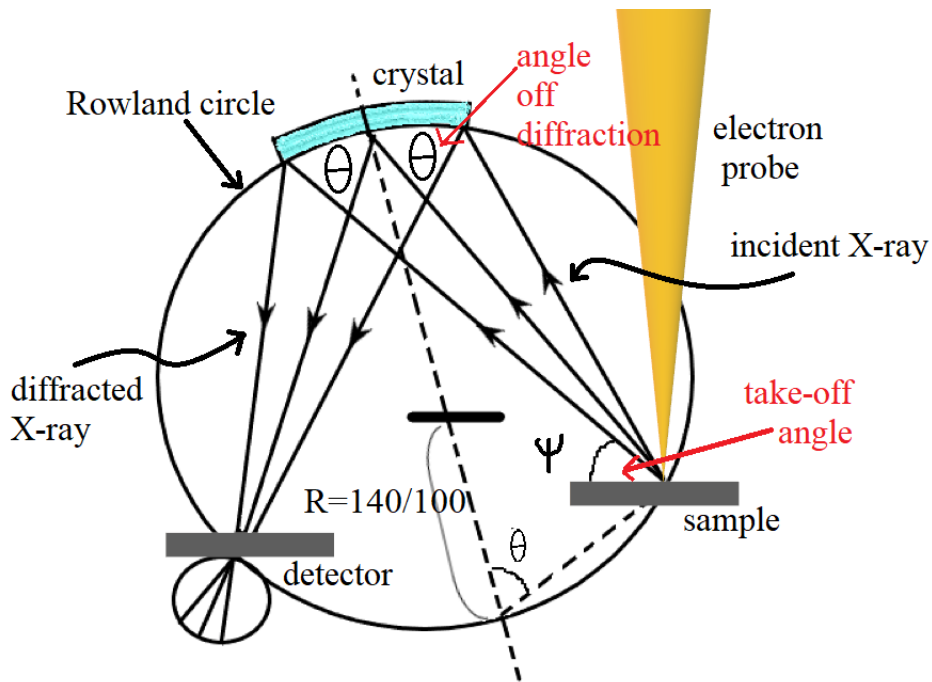
Figure 3.14: Rowland circle. Drawn after original from [17].

To measure X-rays of another wavelength, the crystal and detector are moved to a new position. A specific spectrometer can measure only one X-ray wavelength at a time, therefore EPMA is equipped with multiple WDX spectrometers, in order to measure multiple elements simultaneously.

The detector used in WDX is known is a gas proportional counter and consists of a gas filled tube with a thin tungsten wire maintained at a potential of $1-3$ kV. There are different types of counters used: flow counters and sealed counters. X-rays enter the tube through a thin window and ionize the gas atoms. The electron ejected from the gas atom may ionize other gas atoms. The tungsten wire collects the charge and creates a voltage pulse that is amplified and counted by the electronics. The type of gas used in the counter depends on the wavelength of the X-ray being detected. The quantum efficiency of Xe is greater for short wavelength X-rays so LiF and PET crystals are combined with sealed Xe counters in WD spectrometers. Ar, diluted with 10 % methane (P-10 gas), has a better quantum efficiency for long wavelength X-rays and is combined with TAP or LDE spectrometers for light element detection. The signal generated in the proportional counter passes through a preamplifier to produce a small negative voltage pulse. In turn, this pulse passes through the main amplifier that inverts, amplifies and shapes the pulse such that its voltage has Gaussian distribution. The voltage of the amplifier output pulse is directly

proportional to the energy of the X-ray that entered the proportional counter. Output pulses from the amplifier are fed into the single channel analyser (SCA). An SCA selects pulses within a preset voltage range and produces fixed rectangular pulses of a fixed voltage and duration compatible with scalar and rate-meter input requirements or the digital counting system. Selection of pulses within a predetermined voltage range is known as pulse-height analysis (PHA)[18-20].

3.3.3 WDX mapping

The capability of WDX mapping was employed in this thesis, correlating WDX X-ray intensities with position on the sample surface to yield a 2D map of elemental distributions. WDX mapping has traditionally been employed to image small scale compositional heterogeneities in geological materials, especially in mineral phases [21]. WDX maps have an advantage over EDX X-ray maps due to the superior spectral resolution of WDX and consequently being relatively free from X-ray interferences which results in accurate representation of sample compositions. Also the higher resolution reduces the relative contribution of bremsstrahlung, improving contrast. The main disadvantage of WDX is usually the limited number of spectrometers available to measure the constituents of a complex specimen and longer analysis time. In EDX mapping, all elemental maps are recorded simultaneously but maximum time available per pixel is only a few seconds, resulting in relatively poor counting statistics. Mapping to levels of 100 ppm can be achieved in the most favourable cases, while mapping of concentrations at 1000 ppm is achievable in most cases [22].

In compositional mapping, the spatial resolution is determined by the spacing of spot measurements and the X-ray excitation volume of the electron beam. It is recommended to use a beam size smaller than the pixel size to reduce overlapping. X-ray maps showing elemental distribution are semi-quantitative in principle, because they are constructed by collecting characteristic X-rays, and represent raw data that has not been corrected either for background or for matrix effects such as the mean atomic number, absorption and fluorescence (ZAF) effects. Similar to single spot analyses, a quantitative procedure is thus

also required to convert intensity X-ray maps to quantitative maps. In this thesis intensity maps have been converted to quantitative by using data from quantitative spot analysis.

X-ray maps are usually compared with an electron (secondary or backscattered) image. In this way, the distribution of elements can be correlated with specific phases or morphological features of the sample such as grain boundaries, inclusions, and defects (as shown in Fig. 3.15)

a)

b)
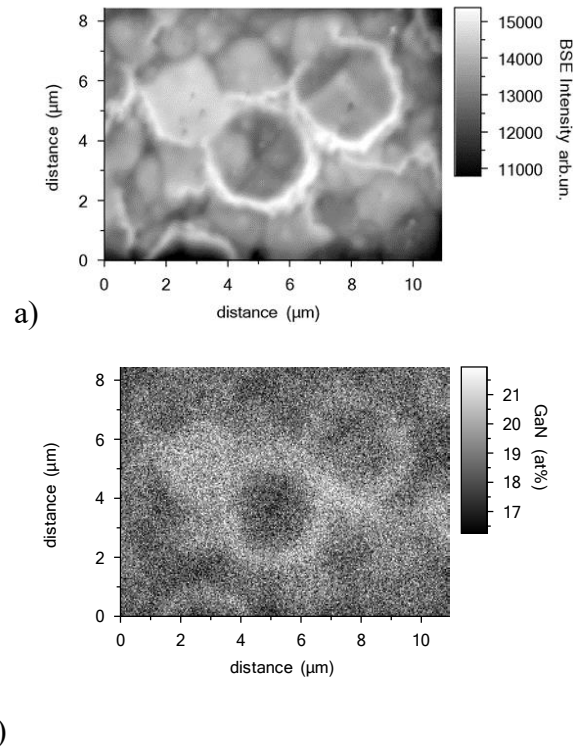
Figure 3.15: Composition mapping of the c-plane sample C1P (81% AlN mole fraction), a) BSE image of the measured area, b) GaN content map (at%) obtained from a WDX map of the Ga L_α X-ray intensity.

Fig. 3.15 shows a higher (lower) intensity of Ga L_α (Al K_α) X-rays around the hexagon edges; the same behavior is observed in the compositional BSE image (Ga-rich areas at grain perimeters seen also in the CL maps). Despite the challenging signal-to-noise ratio, inherent to X-ray counting statistics, we can see clear variations in the Ga distribution on a sub-µm length scale. The GaN alloy fraction was quantified (Fig.3.15b) using the measured GaN at% from WDX quantitative point data.

3.3.4 CASINO Modeling Tool

When analysing semiconductor samples analyst can have a control over the sampling depth and hence the X-ray spatial resolution and X-ray depth sensitivity with the adjustment of the accelerating voltage on the microscope. In order to check appropriate accelerating voltage for specific sampling depth Casino software may be applied. Throughout the thesis sampling depth was checked using this software package. Monte Carlo simulation software provides simulation of electron beam–sample interactions in a scanning electron microscope (SEM)[23]. The main part of a Monte Carlo program is the simulation of a complete electron trajectory. Software assumes a Gaussian-shaped electron beam, where it is possible to specify the electron-beam diameter representing 99.9% of the total distribution of electrons. As the electron travels within the sample, the program will correct the trajectories while crossing the interface between two regions. From simulated electron trajectories a lot of data can be extracted. Some of the typical data includes information about the absorbed energy in the sample also data can be represented in different ways depending on requirements.

Figure 3.16 shows an example of the overview distribution panel display for a 60 AlN content AlGaN, 240nm thick simulated using 200,000 electrons of 3 keV, beam radius 10 nm. Figure a) the maximum penetration depth in the sample of the electrons, b) beam energy deposition plot c) $\rho(\rho Z)$ curve of Al in AlGaN sample

a)
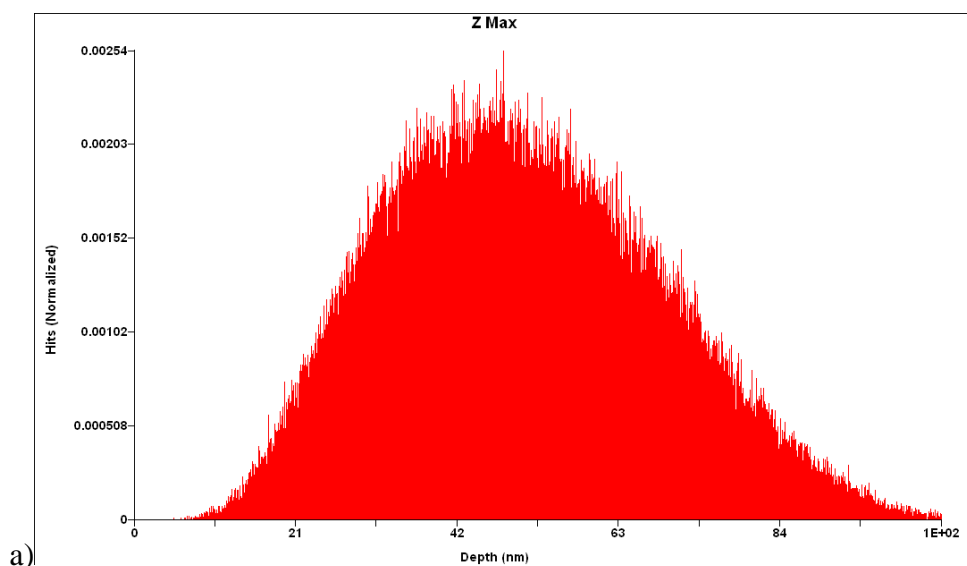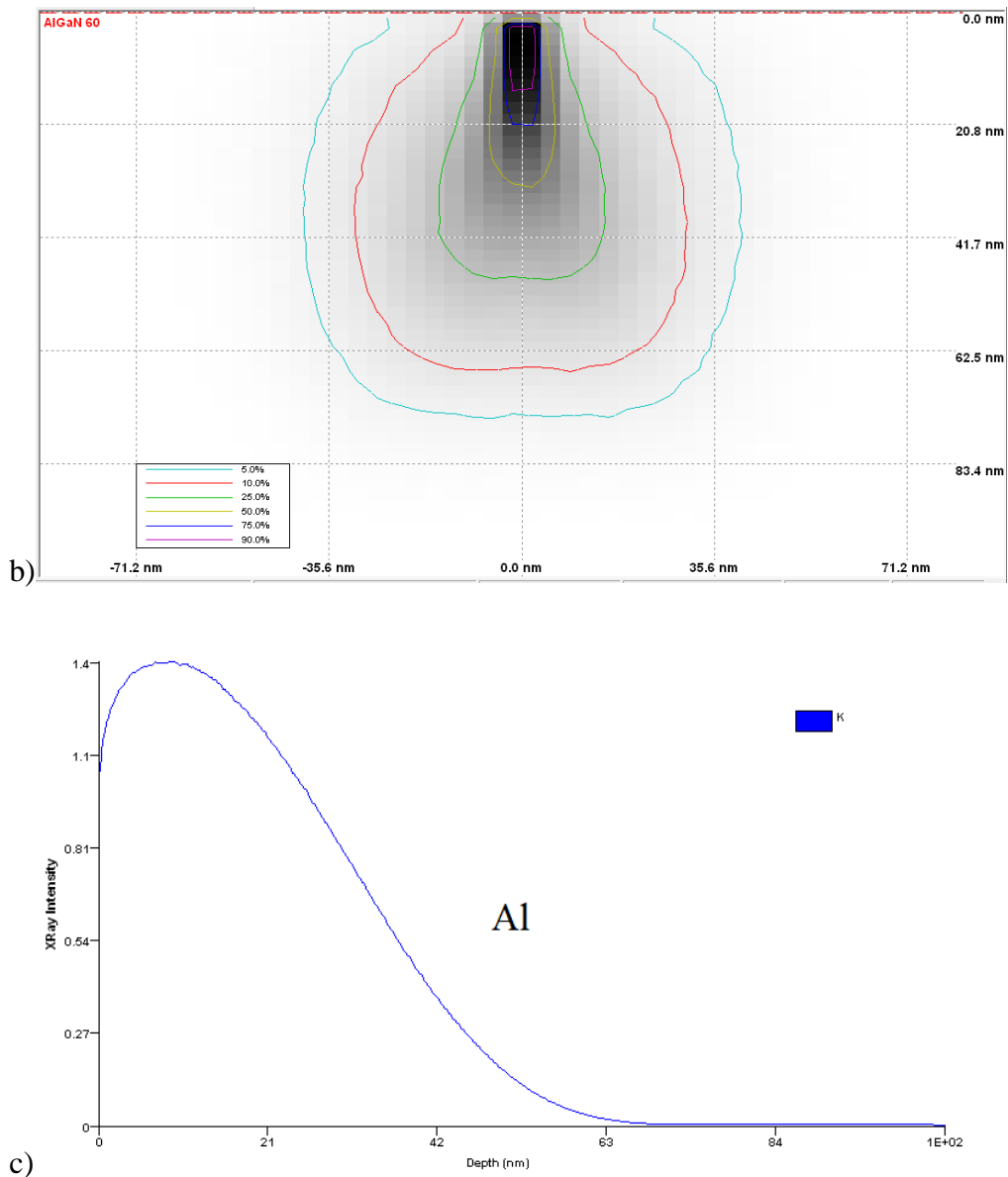
Figure 3.16: Monte Carlo simulation results on AlGaN 60%, simulated with beam energy of 3 kV: a) maximum penetration depth in the sample of the electron trajectories, b) cross-section view of absorbed energy c) $\rho(\rho Z)$ curve of Al.

The Energy by Position distribution (Fig. 3.16 b) is useful tool to investigate absorbed energy in the sample. It records, in a three-dimensional matrix of cubic elements, the amount of energy lost by all the simulated electron trajectories. It helps to study interactions in all the different layers of the matrix in the XY or XZ planes, for example we can conclude that when probing 60% AlN content AlGaN sample at 3 kV 90% of the beam energy is deposited within first 65 nm. Figure allows the display of energy contour lines calculated from the center of the landing point and shows the percentage of energy not contained within the line. For example, a 10% line is the frontier between an area containing 90% of

the absorbed energy and the rest of the sample. Image also displays a gray shading overlay of the density of absorbed energy. The gray shade ranges from light to dark as the density increases.

Another software feature is the generation of characteristic X-rays. Results are displayed in either classical $\rho(\rho z))$ curves (figure c) or as radial distributions (not shown here). $\rho(\rho z))$ curves give information about the X-ray generation depth of each chemical element in the sample (shown for Al). This information may then be useful in choosing appropriate SEM conditions for the quantitative analysis. Also the resulting calculations performed using Casino software for different electron beam conditions can then be correlated with the changes in the CL spectra and the SIMS data can be averaged to correspond to sample sampling depth probed on electron microscope.

3.4 Secondary Ion Mass Spectrometry (SIMS)

More details about the technique described in this sections can be found in Ref. [24] and [25]. SIMS data has been used in this thesis to calibrate WDX data for Si doping concentrations using a calibration relation (details in Chapter 5).

SIMS has become an irreplaceable tool for the characterization and analysis of semiconductor components and materials. It can be used to detect all elements in the periodic table (detection limit down to ppb level for many elements) and due to excellent elemental sensitivity and inherent depth profiling capabilities the technique is often the appropriate choice for semiconductor analysis. SIMS is mostly used for dopant profiling, mobile ion monitoring, process contamination diagnosis, thin film characterization, interface analysis and surface analysis. SIMS technique is destructive by its nature, as opposed to the non-destructive nature of WDX. Because both atomic and molecular species are produced during sputtering of the samples, not all elements in all matrices can be analysed quantitatively. The advantages of using SIMS over WDX for semiconductor analysis are the higher detection limit and ability to probe the atomic concentration as a function of depth. For example, in GaN the Si detection limit is 1×10^{16} atoms cm^{-3} compared to 3×10^{17} atoms cm^{-3} in AlN.

When a solid sample is sputtered by primary ions of a few keV energy, a fraction of the particles emitted from the target are ionized. The ejected species may include atoms, clusters of atoms and molecular fragments. Secondary ion mass spectrometry (SIMS) is based on the ionization and ejection of charged atomic and molecular species from the surface of a solid sample. The resulting secondary ions are then accelerated, focused, and analysed by a mass spectrometer. Results can be in the form of mass spectra, depth profiles or chemical maps of the sample area. SIMS can be utilised in various modes depending on the type of primary ion source (positive (e.g., Cs) or negative (e.g., O) ions), the type of mass spectrometer used for analysis of the secondary ions and the rate of erosion of sputtered species from the sample surface. The mass analyser may be a quadrupole mass analyser (with unit mass resolution), but magnetic sector mass analysers or time-of-flight (TOF) analysers are also often employed (for higher sensitivity and mass resolution).

Static SIMS is a highly surface sensitive mode used for probing the uppermost monolayer of the material by employing very low ion fluxes (around $10^{12}\,cm^{-2}$). The output data of a static SIMS experiment is a mass spectrum showing which elements and functional groups are present.

While static SIMS concentrates on the first top monolayer, in dynamic SIMS mode, the ion dose is increased and bulk composition and in-depth distribution of trace elements are investigated with a depth resolution ranging from sub-nm to tens of nm. If specific masses are chosen and their signals followed as a function of sputter time, a depth profile of their concentration will be produced. Dynamic SIMS instruments are equipped with oxygen and caesium primary ion beams in order to enhance, respectively, positive and negative secondary ion intensities. One of the main applications of dynamic SIMS is the in-depth distribution analysis of trace elements (for example, dopants or contaminants in semiconductors, as shown in Fig. 3.17). Dynamic SIMS is also frequently used for high resolution imaging analyses and high precision isotope ratio measurements. In general, TOF analysers are preferred for static SIMS, whilst quadrupole and magnetic sector analysers are preferred for dynamic SIMS.
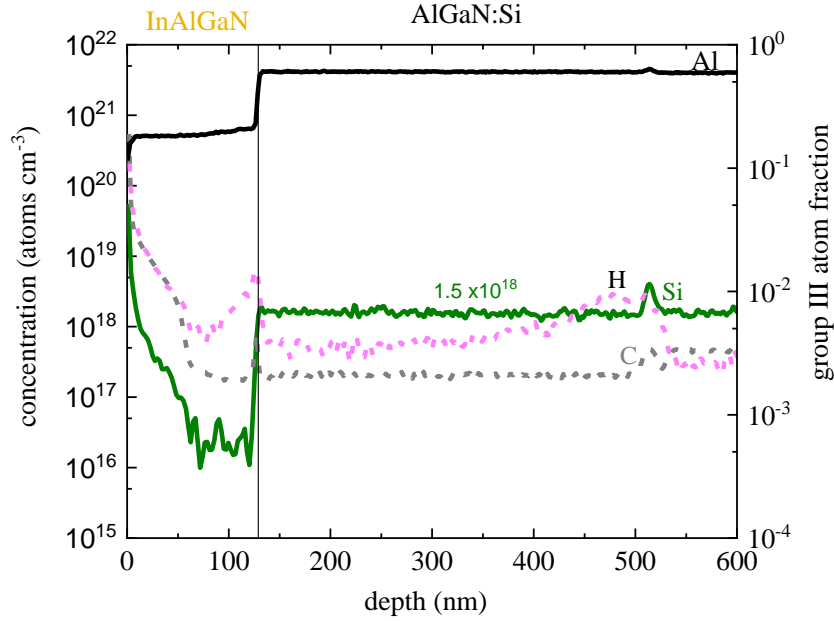
Figure 3.17: SIMS depth profiles for Si, Al, H and O. The sample consists of 150 nm InAlGaN on top of a thick AlGaN:Si layer grown in two steps, with a change of reactors at a depth of approximately 500 nm.

The depth resolution in SIMS is measured in terms of the decay length (λ_d), the distance over which the signal falls by a factor e, the natural log base. It is also sometimes described in nm/decade as it is easy to estimate it from a graph. SIMS depth profiles are usually presented with logarithmic concentration axis due to their high dynamic range.

The SIMS technique cannot reliably estimate quantity based on relative intensities. Secondary ion yield varies depending on the elements and can also vary from matrix to matrix. Therefore, the relative sensitivity factors (RSFs) derived from ion implanted or bulk doped samples have been widely used for SIMS depth profile quantification. The quantitation is based on equation:

$$\rho_i = (I_i/I_m)/(RSF) \tag{1.3}$$

where ρ_i is the impurity concentration (atomic density) in atoms/cm^3, I_i is the impurity isotope secondary ion intensity in counts/s, I_m is the matrix isotope secondary ion intensity in counts/s and RSF has units of atoms/cm^3, and the RSF of the matrix element is equal to the atomic density of the matrix.

3.5 Atomic force microscopy (AFM)

In this thesis the morphology of AlGaN alloys is presented in Chapter 4 (data obtained from Ohio University) and Chapter 6 (from the Tyndall National Institute) they were investigated using an atomic force microscope (AFM) in tapping mode. More details about the technique can be found in [26], [27] and [28].

Atomic force microscopy is a type of scanning probe microscopy with nano-scale resolution (5−10 nm laterally and sub-nanometer vertically). It is mostly employed to characterize different material properties. AFM is one of the few tools that is able to quantitatively measure all 3 dimensions of a surface: lateral (x and y) and height (z). The AFM probe consists of a very sharp tip (typical radius of curvature at the end 5−10 nm) that hangs off the bottom of a long and narrow cantilever (made of silicon or silicon nitride). The information is gathered by "feeling" or "touching" the surface with a mechanical probe. Piezoelectric elements that facilitate small but accurate and precise movements on (electronic) command enable precise scanning. The motion of the AFM tip as it scans along the surface is monitored through a laser beam reflected off the cantilever. This reflected laser beam is tracked by a position sensitive photo-detector (PSPD) that picks up the vertical and lateral motion of the probe. The mechanical interactions with the surface make it possible to acquire the surface topography and to position the tip in specific locations. The AFM tip can also be used as a probe of electrical properties which allows determination of resistivity, surface potential and capacitance simultaneously with acquiring topographic information.

In contact mode, the simplest mode of operation, the AFM tip is in constant contact with the sample. As the probe is scanned over the surface the deflection of the cantilever is measured and maintained, which is directly proportional to the force on the cantilever. A feedback loop on the z piezo in the instrument keeps the cantilever deflection constant throughout the image.

Topographic imaging is usually performed in intermittent contact (IC) mode, often referred to as tapping mode, where the AFM cantilever is oscillated near its resonance frequency, and the probe tip only contacts the sample during part

of the oscillation cycle. In tapping mode, the probe is mounted into a holder with a shaker piezo and a constant cantilever vibration amplitude is maintained rather than a constant cantilever deflection. This mode protects the sample from damage and reduces tip wear.

The roughness value can be calculated from either a cross-sectional profile (line) or a surface (area). The most common roughness parameters rely on calculation of the vertical deviation from a mean line or plane. Surface structure such as roughness and texture are often closely related to a semiconductor behaviour. For instance, control of the surface roughness can improve the efficiency of LEDs.
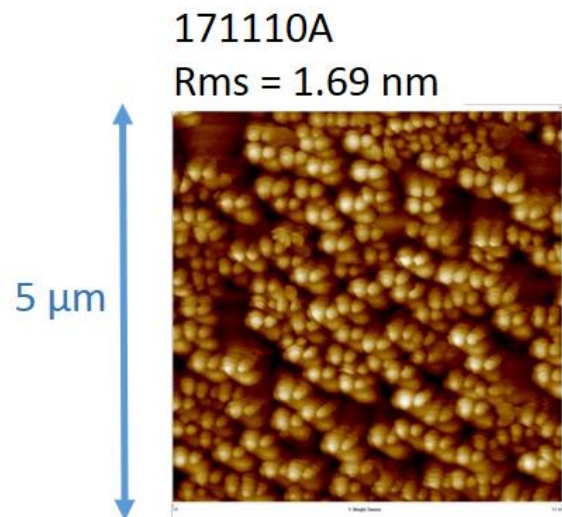
Figure 3.18: Topography imaging of AlGaN alloy using AFM.

Roughness parameters summarize the complex 3D information of topography images. Surface roughness is most commonly described by the root mean square R_{RMS}, defined by:

$$R_{RMS} = \frac{1}{N} \sum_{i=1}^{N} z_i^2 \qquad (1.4)$$

Where z_i is the height at a given pixel i, and N is the total number of pixels in the image.

3.6 Growth techniques

Samples presented in this thesis were grown by metal organic chemical vapour deposition (MOCVD) or molecular beam epitaxy (MBE) methods. These are the most widely used methods for III-V epitaxy, although other techniques are available. In this section an overview of the techniques will be presented. The choice of the best growth technology is based on the precise details of the grown structure and end application. More details about MOCVD growth techniques can be found in Ref. [29], [30] and [31] and about the MBE technique in Ref. [32], [33], [34].

3.6.1 MOCVD

A breakthrough in the development of MOCVD of the GaN-based material system was achieved due to work from Amano, Akasaki et al. [35], and Nakamura et al.[36], which led to reliable and efficient InGaN based blue light emitting diodes (LEDs) and laser diodes (LDs)[37]. Today, most of the epitaxially grown AlGaN-based optoelectronic and electronic device structures on the market are produced using MOCVD. In general, the MOCVD method is used to grow bulk layers with high grow rates. As well as becoming a popular method due the possibility of growing almost all compound semiconductors, it also provides excellent controllability of growth parameters to achieve good uniformity and doping levels with sharp layer interfaces.

In the MOCVD method, very thin layers of atoms are deposited onto a heated semiconductor wafer in a pressure regime of 15 to 750 Torr. To produce compound semiconductors (such as GaN, InP, GaAs and related alloys) chemicals are vaporized and transported into the reactor together with other gases where they react resulting in epitaxial growth. MOCVD uses more complex compound sources, namely metal-organic sources (e.g. trimethyl- or triethyl- Ga, In, Al) as group III precursors, hydrides (e.g. AsH_3 or NH_3) as group V precursors, and other gas sources used for doping (e.g., disilane). The metal-organic precursors are diluted in large flows of purified hydrogen (H_2) and/or nitrogen (N_2) that act as carrier gases and deliver the metal-organic

precursors to the heated growth zone. The whole process consists of the following steps: (i) transport of precursors to the growth zone; (ii) gas-phase reactions of the precursors in the hot zone to form reactive by-products; (iii) transport of the precursors and the reactants to the substrate; (iv) adsorption of reactants on the substrate; (v) surface diffusion, nucleation and surface reactions on the surface leading to the growth; and (vi) desorption and transport of by-products away from the surface.

The overall chemical reaction in MOCVD of III-nitrides can be described by:

$(CH_3)M + NH_3 \rightarrow MN + 3CH_4$, with M= group III metal element Al, Ga, In

Parasitic reactions are also possible between the metalorganic molecules and ammonia leading to formation of $(CH_3)_xM-NH_x$ adducts.
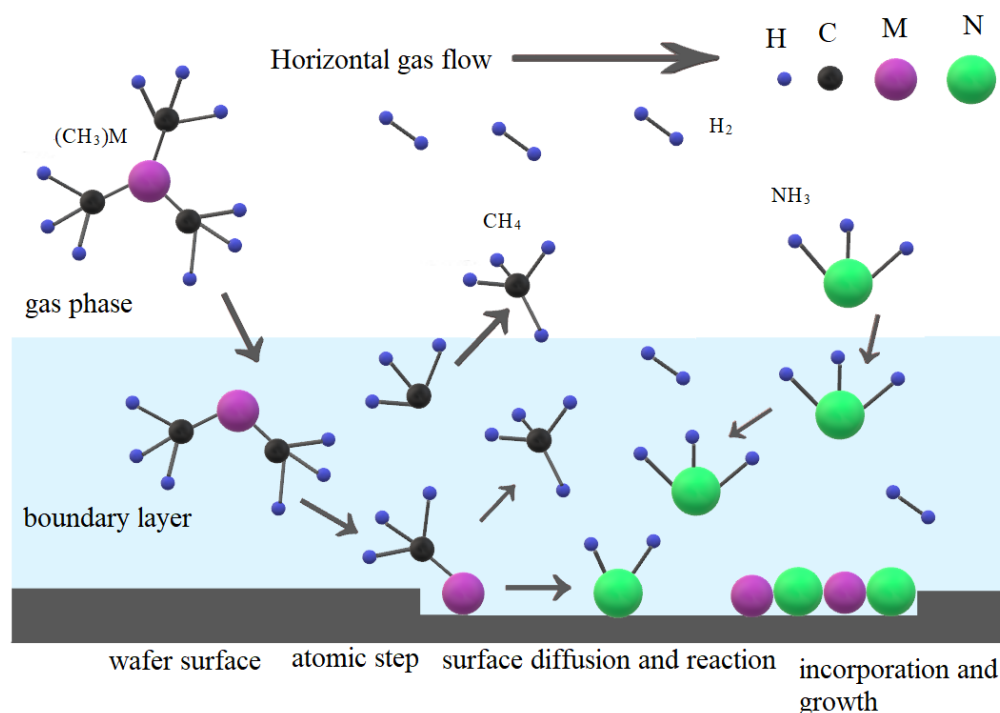
Figure 3.19: Schematic diagram of the relevant growth steps. Redrawn after original from [38].

For MOCVD growth two different reactor designs are available: the horizontal reactor, where the gas flows horizontally over the substrate, and the shower head reactor, in which the gas inlet is vertical over the substrate. The MOCVD growth of AlGaN requires high growth temperatures to facilitate adequate surface diffusion due to the strong Al–N bond energy of 2.88 eV. Heteroepitaxial GaN

layers with atomically smooth surfaces have been obtained using a growth temperature ~1000−1100 °C while the optimized growth temperature for AlN is much higher (>1200 °C). Pulsed-flow growth, a variant of MOCVD, is used to enhance adatom surface mobility.

In this work, growth was performed on both sapphire and AlN substrates. Properties of the common substrates used for AlGaN epitaxy are summarized in Table 3.1.

3.6.2. MBE

Molecular beam epitaxy MBE has made important contribution to more fundamental studies and to the growth of nitrides for high power and microwave devices, but the growth of group III nitrides has been dominated by MOCVD. Some of the AlGaN samples studied in this thesis are produced using MBE. In the MBE method growth is also performed on a heated substrate but in an ultra-high vacuum (UHV) (10^{-8}−10^{-12} Torr) environment and rather than complex compound sources used in MOCVD, MBE employs elemental sources and a plasma source (e.g. N plasma for nitride applications). The UHV environment is necessary due to material purity and to ensure highly directional elemental beams, thus avoiding carrier gas. In solid source MBE, elements such as gallium and aluminium are heated in separate effusion cells or electron-beam evaporators until they begin to slowly sublime. The molecules land on the surface of the substrate, condense, and build up very slowly and systematically ultra-thin layers. Controlling the temperature of the source will control the rate of material impinging on the substrate surface and the temperature of the substrate will affect the rate of hopping or desorption. One of the in-situ analytical techniques used in MBE is reflection high-energy electron diffraction (RHEED) used for determination of surface structure and growth rates.

MBE is normally regarded as an epitaxial technique for the growth of very thin layers with monolayer control of their thickness. Some of the advantages of the method are: no need of hydrogen passivation, relatively low growth

temperature, precise control of growth to less than a monolayer thickness and range of analytical techniques compatible with the UHV environment.
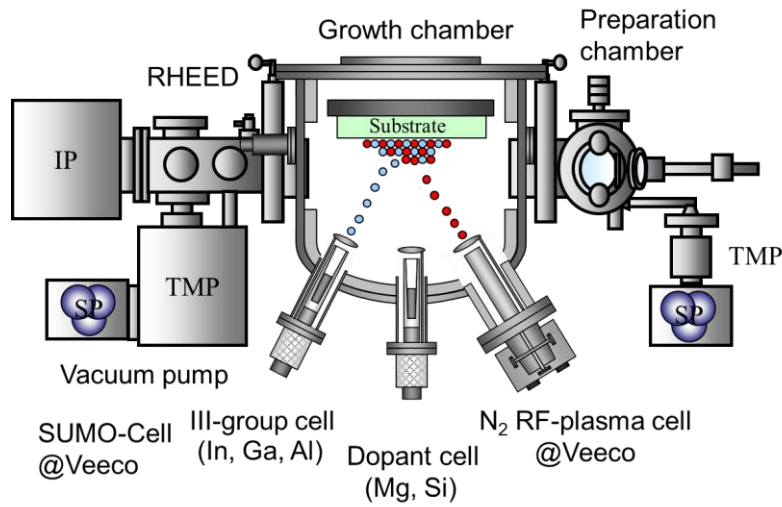
Figure 3.20: Schematic diagram of an MBE growth chamber, provided by Dr Ke Wang from Nanjing University, used to grow AlGaN samples characterised in Chapter 4.

3.7 Substrates

In this work, growth was performed on both sapphire and AlN substrates. Properties of the common substrates used for group-III nitrides epitaxy are summarized in Table 3.1. When choosing a substrate, important parameters are the mismatch in lattice parameter and thermal expansion between the substrate and the material grown on top of it. These should match as closely as possible. Thermal conductivity is also an important parameter because substrates with a higher thermal conductivity can be used in applications where the circuit generates a large amount of heat. To achieve high crystalline quality of the semiconductor alloy the choice of the right substrate is crucial. Homoepitaxy is always the best choice in terms of crystalline quality (e.g. GaN on GaN or AlN on AlN), but is not always feasible due to the high price of bulk GaN or AlN substrates and the limited availability of wafers with different orientations and sizes.

Sapphire substrates (α-Al$_2$O$_3$) are the most commonly used for the group-III nitride growth due to their high availability, affordable price, and good thermal and chemical stability. The disadvantage of using sapphire substrates is the large

lattice mismatch compared to AlN which is 13% (Table 3.1). When growing AlGaN on a sapphire substrate a high dislocation density is expected (10^7 to 10^{10} cm^{-2}) due to the large lattice mismatch between the substrate and film. When growing epitaxial films on a large lattice mismatch substrate, additional buffer layers or transition layers are required. If we compare the growth of AlGaN alloys on native AlN substrates, it is evident that the lattice mismatch is significantly reduced and the thermal conductivity is improved, which is important for high power devices. With the growth of AlGaN on AlN substrate, a reduction in the densities of dislocations and compensating defects is therefore expected. In this case no buffer or transition layers are needed. It is also crucial to obtain atomically smooth AlGaN layers in quantum well structures that require compositional uniformity, or to achieve efficient electron transport properties in high electron mobility transistors which are directly dependent on the interface roughness.

While the most common type of substrates are c-plane substrates, substrate misorientation from the c-axis plays an important role in the semiconductor properties (more details in Chapter 1).

Table 3.1: Lattice parameters and thermal properties of commonly used substrates for AlGaN growth.

substrate	structure	a_0 (Å)	c_0 (Å)	lattice mismatch with AlN (%)	Thermal expansion coefficient α_a(10^{-6}/°C)	Thermal conductivity (Wcm^{-1}K^{-1})
Si	diamond	5.431[a]	-		3.9[a]	1.3[a]
Al$_2$O$_3$	rhombohedral	4.759[a]	12.991[a]	-13	8.31[a]	0.25[c]
4H-SiC	hexagonal	3.080[a]	10.083[a]	1	4.75[a]	4.9[b]
GaN	wurtzite	3.189[d]	5.186[d]	2.4	5.00[a]	1.3[b]
AlN	wurtzite	3.112[b]	4.981[d]	0	5.41[a]	2.85[b]

a [39], b[40], c[41] and d [42]

3.8 III-nitrides growth parameters

Ever since H. Amano et al. in 1986 made a breakthrough in achieving high-quality GaN due to addition of low-temperature AlN growth optimisation of III-nitride layers have become a significant research topic [43].

In the traditional two step heteroepitaxial growth of III-nitrides, a low temperature (LT) GaN or AlN buffer layer is usually deposited to achieve high quality materials. For example, when growing c-plane GaN on sapphire with a LT GaN buffer layer, a thin GaN nucleation layer is first deposited on the substrate at the low temperature (around 550^0C), followed by a high temperature annealing. After increasing the temperature to around 1000^0C the GaN growth is started. In first stage the LT GaN buffer layer is in polycrystalline phase. In second stage when high temperature annealing is applied GaN layer will start to decompose and multiple islands will be formed (recrystallization). With further annealing less GaN island will be left on the surface. Next step is the lateral growth of GaN islands which will completely coalesce and quasi-2D growth will occur. The high quality GaN epilayers are grown due to significant reduction in threading dislocation density during the lateral growth and coalescence process [44].

The growth of AlGaN layers has become a focus of attention in recent years due to its wide applicability in optoelectronic devices and microwave devices at high temperature and power. Epitaxial process for obtaining AlGaN is more complicated compared to GaN growth, common issues are related to low growth efficiency, non-ideal surface morphology and high dislocation density. Since MOCVD is most commonly employed for its growth, we will discuss how its growth mechanism may be optimized. At the moment AlN buffer layer is widely used as the substrate, first impurities are removed of substrate at high temperature (>1000 °C) in H_2 atmosphere, following low temperature GaN layer at about 520 °C, and temperature is continuously raised to about 1000 °C to grow the high temperature GaN layer also with an AlN or AlGaN interlayer,11–15 and in final step AlGaN film is grown. Some of the obstacle encountered in AlGaN growth are related to strong parasitic reaction between the Group III

precursor TMAl and the V group precursor NH$_3$ which will result in lower Al content in AlGaN film [45]. These unwanted reactions will also make AlGaN film growth strongly dependent on temperature and pressure. Due to this dependence there will only be a narrow growth window and the growth process will be difficult to control. Another difficulty is the bond strength of Al–N, the strongest among the three nitrides which decreases the lateral growth rate, also AlGaN layer grown with higher Al content exhibit strong defect formation, high impurity incorporation and become more insulating (explored in further chapters). Difficulties with achieving n- ore p-type doping of this material is discussed in Chapter 2. Due to all mentioned obstacles it is still difficult to grow a high quality AlGaN layers for commercial applications.

Now we will reflect on how growers are trying to improve AlGaN growth process.

3.8.1 Substrate temperature

The substrate temperature of the AlGaN layer grown by MOCVD was usually about 1050 °C or higher, but Coltrin et al.[46] and Dauelsberg et al. [47] succeed in growing an AlGaN layer at 933 °C and 945 °C by using the rotating disk reactor (RDR) reactor and the horizontal reactor respectively. It was concluded that temperature had a significant effect on the growth rate of AlGaN and the Al content of the epitaxial layer. Experimental work from Ng et el. [48] indicated that in the case of low temperature or increased amount of NH$_3$ (N-rich conditions) the growth rate was higher until saturation point. The growth rate of the layer was as high as 3.2 μm h^{-1} when the partial pressure of NH$_3$ was 0.4 and the temperature was 1040 °Cm (low temperature and "N-rich" atmosphere). They assigned high growth rates to the weak parasitic reaction at low temperature. Different groups reported different growth rates also due to the different reactor configurations. Ikenaga et al. [49] found in the horizontal reactor that temperature change has little effect on the growth rate of AlGaN, and the V/III ratio at the same temperature was a key parameter affecting the growth rate. It was found that when using moderate temperature and increasing the partial pressure of the Group III gas by reducing the V/III ratio can increase the growth rate to a certain extent when the temperature increases. The growth rate was greatly reduced as the growth temperature was over 1200 °C[50] even

though some researcher showed a weak degradation of growth rate as the growth temperature was less than 1100 °C[46].

Basically, there are three different temperature growth regions. At low growth temperatures, the growth rate decreases with the temperature, the growth rate is limited by the reaction kinetics, namely the slowest reaction in the gas phase or at the surface. At medium growth temperatures, the growth rate is insensitive to the temperature but it will be limited by the transport of the reactants to the surface (diffusion-limited growth). Last temperature region is very high growth temperatures, where the growth rate decreases possibly due decomposition of the film, parasitic reactions between the precursors in gas phase and desorption of precursors from the surface [51]. What we can conclude is that temperature reduction can enhance the growth rate of AlGaN, but it is practical to achieve higher rates at high temperature just by changing the reactor structure and other growth parameters such as TMAl/III and gas flow. Temperature doesn't only affect the growth rate but also Al content. Keller et al. [52] together with many other groups documented that the Al component increased with temperature. With their research on AlGaN growth Coltrin et al.[46] came to conclusion that at low temperature only a few parasitic reactions occur and since the parasitic reaction energy barrier of the substance with Al was smaller than the one with Ga, when the temperature rose, and the parasitic reaction of the substance with Al consumed a part of the Al source result was a decrease in the Al content in the layer. It was also found that the temperature had little effect on the Al incorporation with small TMAl/III ratio, while the effect was larger with higher TMAl/III. Okada et al.[53] and Kato et al. [54] studied high temperature range growth (1236 °C ~ 1450 °C) and found that the Al component in the layer increased rapidly with the rise of temperature. Explanation was that although there were parasitic reactions, GaN was more easily desorbed and etched than AlN, which would decrease the Ga content and increase the Al content in the layer, conclusively temperature rise resulted in higher Al content. Lobanova et al. controlled the Al content by varying the TMAl/III ratio at the inlet [55]. When growing AlGaN with MOCVD, the growth rate decreased and the Al content increases with the temperature rise. Keller et al. [52] also reported that the surface morphology of the layer deteriorated with the increase of the Al content. Almogbel et al.[56] observed a strong anticorrelation between

AlGaN:Si conductivity and growth temperature, suggesting increased silicon donor compensation at elevated temperatures. They also observed dependence of the unintentional carbon and oxygen impurity incorporation on growth temperature, with the temperatures >1050 °C yielded the lowest concentrations. It was expected that carbon incorporation would decrease as the growth temperature increased due to the decomposition of carbon containing reaction by-products at higher temperatures. The oxygen impurity concentration was insensitive to the growth temperature in the range 900–1175 °C, which may be attributed to the low water vapour content in the precursors, chamber, and carrier gas.

3.8.2 The operating pressure

Due to the common parasitic reaction during the growth of AlN and AlGaN they are usually grown in low pressure regime and the higher the pressure it is more difficult to grow. Usually the reactor pressure is set to about 76 torr pressure [51]. For example, Lobanova et al. [55] found that growth rate and efficiency both decreased with increasing pressure, the pressure affected both the growth rate and the Al component in the layer. The Al content decreased with pressure, due to the increased parasitic reaction of TMAl and NH_3 that led to a large consumption of Al source due to rising pressure. Importantly, under the low pressure range (<150 torr), the Al content decreased rapidly with increasing pressure, which was reported by Touzi et al. [57] while the decline was slow under middle and high pressure range (>150 torr). It was explained that the growth of AlGaN under low pressure was favorable for increasing the growth rate and the Al component in the layer

3.8.3 The gas flow

The III-nitride (TMAl+TMGa) flow rate, the TMAl/III group flow rate ratio and the V/III ratio have a tremendous effect on the growth rate of the layer and the Al content. Choi et al. [58] and Allerman et al. [59] studied the effect of III-nitride (TMAl +TMGa) flow rate on the Al incorporation. They concluded how Al content and growth efficiency decreased with the rise of the III-nitride flow rate due to enhanced parasitic reactions caused by increasing flow rate of III-nitride. Lundin et al. also found that although the Al content decreased with the

rise of III-nitride, the rate of decrease in the high ammonia atmosphere was significantly faster than that in the low, also with the raise of the ratio of the III-nitride flow rate in the total gas, the growth rate also grew. Concussively it was difficult to achieve rapid growth of the AlGaN layer and obtain a high Al content simultaneously by adjusting the III-nitride flow rate. Coltrin et al. [46] found that the growth rate decreased with the rise of TMAl/III, same funding was reported by Tokunaga et al. [60]. Stellmach et al. reported different findings: the growth rate of AlGaN was almost free from effect of TMAl/III with certain reaction chamber height, with a different height by raising TMAl/III by increasing the flow rate of TMAl and keeping the rate of TMGa constant, the growth rate increased faster. Also when kept TMAl flow rate constant and TMAl/III was increased by decreasing TMGa flow rate, the growth rate turned slow.

 From all these different findings there is no clear correlation between the effect of TMAl/III on the growth rate of AlGaN, which might be related to the total flow rate of the III-nitride or the reactor structure. The correlation between the Al content of AlGaN and TMAl/III at the inlet is used to indicate growth efficiency. When the Al content is larger than the TMAl/III at the inlet or they have a linear relation, it indicated that the parasitic reaction is suppressed, and the growth efficiency is high, opposite finding will indicate that parasite reaction was strong.

In general, there are two ways to increase TMAl/III: maintained TMGa flow rate constant and increased TMAl flow rate, or keep TMAl flow rate constant and decreased TMGa flow rate. When TMAl flow rateis increased due to the parasitic reaction between TMAl and NH_3 being stronger than TMGa, more consumption of TMAl is caused by parasitic reaction, without effect on the layer growth so lowering the TMGa flux is more effective than increasing the TMAl flow rate to raise the Al content in the layer [51].

Additionally, NH_3 flow rate will also affect growth rate. Choi et al. [58]found that Al content and growth rate in the layer decreased with the increase of NH_3 flow rate. But Lundin et al. [61] observed that the growth rate increased with rise of ammonia flow in the low ammonia atmosphere, but decreased in the high. With medium ammonia atmosphere the growth rate tended to saturate when the

III-nitride flow rate was low, in atmosphere with high ammonia, the Al content also tended to saturate when III-nitride flow rate was low. The reason for it is that the parasitic reaction is weak when the gas-phase ammonia content is small. However, when the ammonia content is high, the strong parasitic reaction enhances the gas-phase scavenging effect of the Al source on the Ga source and

the etching effect of H_2 on GaN by NH_3 decomposition eventually resulting in the consumption of the source gas. Lundin et al. [61]found that the Al content in the layer increased with the rise of carrier gas flow rate and saturate at high flow rate. Increasing the gas flow rate was favourable for suppressing the parasitic reaction and increasing the growth rate.

3.8.4 Disilane flow

Almogbel et al. [56] found that the disilane flow have a weaker influence on the AlGaN conductivity at lower growth temperatures. At 1175 $^\circ$C, optimization of silicon doping reduced the resistivity from >300 to 87 mΩ cm, while at lower temperatures, a wider variation in disilane flow did not result in an abrupt change in resistivity. A further decrease in growth temperature from 1115 to 1050°C reduced the minimum resistivity from 18.5 to 7.5 mΩ cm. In addition, for the same [Si] of 1.5–2 $\times$ 10^{19}/cm^3 the decrease in growth temperature correlates with the increase in the maximum electron concentration n. For example, n doubled from 7.5×10^{18}/cm^3 to 1.6×10^{19}/cm^3 upon reducing T from 1115 to 1050 $^\circ$C. Confirming higher doping efficiency at lower growth temperatures. A further increase in the Si concentration did not result in higher n, suggesting that n saturates at a certain growth-temperature-dependent limit.

From all these findings we can conclude that the growth of AlGaN layers it is hard to achieve growth of high efficiency and high rate, high AlN incorporation and layer quality. A lot of work still remains for growers to identify optimal growth parameters.

3.9 Conclusion

This chapter presents a general overview of the experimental methods employed in this thesis. The explained techniques include scanning electron microscopy, cathodoluminescence spectroscopy and electron probe microanalysis. Additional techniques not employed directly in this thesis but whose data has been used include secondary ion mass spectrometry and atomic force microscopy. Different growth techniques employed to grow the studied AlGaN layers are discussed: metal organic chemical vapour deposition and molecular beam epitaxy. Since growth was performed on both sapphire and AlN substrates, the choice of substrates is also briefly reviewed. Chapter included short discussion of the growth of III-nitrides explaining the different parameters available to the growers to optimize the material properties.

Bibliography

[1] P.J. Goodhew, F.J. Humphreys, R. Beanland, Electron Microscopy and Analysis, CRC Press, Boca Raton, 2017.

[2] P.R. Edwards, M.R. Lee, Cathodoluminescence hyperspectral imaging in geoscience, in: I.M. Coulson (Ed.), Mineralogical Association of Canada, 2014.

[3] P.R. Edwards, R.W. Martin, Cathodoluminescence nano-characterization of semiconductors, DOI (2011).

[4] https://www.jeol.co.jp/en/science/epma.html.

[5] J. Ltd., Scanning Electron Microscope A to Z, Basic Knowledge for using the SEM

[6] Electron–specimen interactions, in: S.J.B. Reed (Ed.) Electron Microprobe Analysis and Scanning Electron Microscopy in Geology, Cambridge University Press, Cambridge, 2005, pp. 7-20.

[7] https://blog.phenom-world.com/sem-electrons.

[8] C. Trager-Cowan, A. Alasmari, W. Avis, J. Bruckbauer, P.R. Edwards, B. Hourahine, S. Kraeusel, G. Kusch, R. Johnston, G. Naresh-Kumar, R.W. Martin, M. Nouf-Allehiani, E. Pascal, L. Spasevski, D. Thomson, S. Vespucci, P.J. Parbrook, M.D. Smith, J. Enslin, F. Mehnke, M. Kneissl, C. Kuhn, T. Wernicke, S. Hagedorn, A. Knauer, V. Kueller, S. Walde, M. Weyers, P.M. Coulon, P.A. Shields, Y. Zhang, L. Jiu, Y. Gong, R.M. Smith, T. Wang, A. Winkelmann, Scanning electron microscopy as a flexible technique for investigating the properties of UV-emitting nitride semiconductor thin films, Photon. Res., 7 (2019) B73-B82.

[9] M.T. Postek, A.E. Vladár, Does Your SEM Really Tell the Truth?-How Would You Know? Part 4: Charging and its Mitigation, Proc SPIE Int Soc Opt Eng, 9636 (2015) 963605 (October 963621, 962015); doi:963610.961117/963612.2195344 Text Size: A A A.

[10] Scanning Electron Microscopy, Materials Characterization, pp. 127-161.

[11] K.W. Böer, U.W. Pohl, Carrier Recombination and Noise, Semiconductor Physics, Springer International Publishing, Cham, 2018, pp. 1125-1179.

[12] http://ssd.phys.strath.ac.uk/techniques/scanning-electron-microscopy/cathodoluminescence/, Cathodoluminescence.

[13] C. Colliex, The "father" of microanalysis: Raymond Castaing, creator of a generation of scientific instruments, still in worldwide operation, Comptes Rendus Physique, 20 (2019) 746-755.

[14] J.I. Goldstein, D.E. Newbury, J.R. Michael, N.W.M. Ritchie, J.H.J. Scott, D.C. Joy, X-Rays, in: J.I. Goldstein, D.E. Newbury, J.R. Michael, N.W.M. Ritchie, J.H.J. Scott, D.C. Joy (Eds.) Scanning Electron Microscopy and X-Ray Microanalysis, Springer New York, New York, NY, 2018, pp. 39-63.

[15] D. Shindo, T. Oikawa, Energy Dispersive X-ray Spectroscopy, 2002, pp. 81-102.

[16] J.C. Russ, Chapter 3 - Energy Dispersive Spectrometers, in: J.C. Russ (Ed.) Fundamentals of Energy Dispersive X-ray Analysis, Butterworth-Heinemann1984, pp. 17-41.

[17] N. Chatterjee, Electron Microprobe Analysis, Course 12.141, in: M.E.M. Facility (Ed.)2012.

[18] X-Ray Spectroscopy for Elemental Analysis, Weinheim, Germany: Wiley-VCH Verlag GmbH & Co. KGaA, Weinheim, Germany, 2013, pp. 191-219.

[19] J.C. Russ, Chapter 2 - Wavelength Dispersive Spectrometers, in: J.C. Russ (Ed.) Fundamentals of Energy Dispersive X-ray Analysis, Butterworth-Heinemann1984, pp. 10-16.

[20] C.E. Lyman, J.I. Goldstein, A.D. Romig, P. Echlin, D.C. Joy, D.E. Newbury, D.B. Williams, J.T. Armstrong, C.E. Fiori, E. Lifshin, K.-R. Peters, Wavelength-Dispersive X-Ray Spectrometry and Microanalysis, in: C.E. Lyman, J.I. Goldstein, A.D. Romig, P. Echlin, D.C. Joy, D.E. Newbury, D.B. Williams, J.T. Armstrong, C.E. Fiori, E. Lifshin, K.-R. Peters (Eds.) Scanning Electron Microscopy, X-Ray Microanalysis, and Analytical Electron Microscopy: A Laboratory Workbook, Springer US, Boston, MA, 1990, pp. 42-47.

[21] P. Lanari, A. Vho, T. Bovay, L. Airaghi, S. Centrella, Quantitative compositional mapping of mineral phases by electron probe micro-analyser, Geological Society, London, Special Publications, 478 (2019) 39-63.

[22] D.E. Newbury, C.E. Fiori, R.B. Marinenko, R.L. Myklebust, C.R. Swyt, D.S. Bright, Compositional mapping with the electron probe microanalyzer: Part II, Analytical Chemistry, 62 (1990) 1245A-1254A.

[23] D. Drouin, A.R. Couture, Joly Dany, X. Tastet, V. Aimez, R. Gauvin, CASINO V2.42—A Fast and Easy-to-use Modeling Tool for Scanning Electron Microscopy and Microanalysis Users, Scanning, 29 (2007) 92-101.

[24] G.E. McGuire, Y. Strausser, Characterization in Compound Semiconductor Processing, Momentum Press, New York, 1995.

[25] F.A. Stevie, Secondary Ion Mass Spectrometry : Applications for Depth Profiling and Surface Characterization, Momentum Press, New York, [New York] [222 East 46th Street, New York, NY 10017], 2016.

[26] R.A. Oliver, Advances in AFM for the electrical characterization of semiconductors, Reports on Progress in Physics, 71 (2008) 076501.

[27] Industry News, Microscopy Today, 23 (2015) 44-45.

[28] G.J. Simpson, D.L. Sedin, K.L. Rowlen, Surface Roughness by Contact versus Tapping Mode Atomic Force Microscopy, Langmuir, 15 (1999) 1429-1434.

[29] G. Malandrino, Chemical Vapour Deposition. Precursors, Processes and Applications. Edited by Anthony C. Jones and Michael L. Hitchman, Angewandte Chemie International Edition, 48 (2009) 7478-7479.

[30] S. Keller, S.P. DenBaars, Metalorganic chemical vapor deposition of group III nitrides—a discussion of critical issues, Journal of Crystal Growth, 248 (2003) 479-486.

[31] X.-T. Yan, Chemical Vapour Deposition, Dordrecht: Springer2010.

[32] S.V. Novikov, A.J. Kent, C.T. Foxon, Molecular beam epitaxy as a growth technique for achieving free-standing zinc-blende GaN and wurtzite AlxGa1-xN, Progress in Crystal Growth and Characterization of Materials, 63 (2017) 25-39.

[33] R. Pelzel, A comparison of MOVPE and MBE growth technologies for III-V epitaxial structures, CS MANTECH Conference, Citeseer, 2013, pp. 105-108.

[34] P. Capper, S. Irvine, T. Joyce, Epitaxial Crystal Growth: Methods and Materials, in: S. Kasap, P. Capper (Eds.) Springer Handbook of Electronic and Photonic Materials, Springer US, Boston, MA, 2007, pp. 271-301.

[35] H. Amano, M. Kito, K. Hiramatsu, I. Akasaki, P-Type Conduction in Mg-Doped GaN Treated with Low-Energy Electron Beam Irradiation (LEEBI), Japanese Journal of Applied Physics, 28 (1989) L2112-L2114.

[36] S. Nakamura, T. Mukai, M. Senoh, N. Iwasa, Thermal Annealing Effects on P-Type Mg-Doped GaN Films, Japanese Journal of Applied Physics, 31 (1992) L139-L142.

[37] S. Nakamura, M. Senoh, S.-i. Nagahama, N. Iwasa, T. Yamada, T. Matsushita, H. Kiyoku, Y. Sugimoto, InGaN-Based Multi-Quantum-Well-Structure Laser Diodes, Japanese Journal of Applied Physics, 35 (1996) L74-L76.

[38] F.H. Yang, 2 - Modern metal-organic chemical vapor deposition (MOCVD) reactors and growing nitride-based materials, in: J. Huang, H.-C. Kuo, S.-C. Shen (Eds.) Nitride Semiconductor Light-Emitting Diodes (LEDs), Woodhead Publishing2014, pp. 27-65.

[39] L. Liu, B. Liu, J.H. Edgar, S. Rajasingam, M. Kuball, Raman characterization and stress analysis of AlN grown on SiC by sublimation, Journal of Applied Physics, 92 (2002) 5183-5188.

[40] V. Cimalla, J. Pezoldt, O. Ambacher, Group III nitride and SiC based MEMS and NEMS: materials properties, technology and applications, Journal of Physics D: Applied Physics, 40 (2007) 6386-6434.

[41] L. Liu, J.H. Edgar, Substrates for gallium nitride epitaxy, Materials Science and Engineering: R: Reports, 37 (2002) 61-127.

[42] S. Fritze, A. Dadgar, H. Witte, M. Bügler, A. Rohrbeck, J. Bläsing, A. Hoffmann, A. Krost, High Si and Ge n-type doping of GaN doping - Limits and impact on stress, Applied Physics Letters, 100 (2012) 122104.

[43] H. Amano, N. Sawaki, I. Akasaki, Y. Toyoda, Metalorganic vapor phase epitaxial growth of a high quality GaN film using an AlN buffer layer, Applied Physics Letters, 48 (1986) 353-355.

[44] D.D. Koleske, M.E. Coltrin, K.C. Cross, C.C. Mitchell, A.A. Allerman, Understanding GaN nucleation layer evolution on sapphire, Journal of Crystal Growth, 273 (2004) 86-99.

[45] J.R. Creighton, G.T. Wang, Reversible Adduct Formation of Trimethylgallium and Trimethylindium with Ammonia, The Journal of Physical Chemistry A, 109 (2005) 133-137.

[46] M.E. Coltrin, J. Randall Creighton, C.C. Mitchell, Modeling the parasitic chemical reactions of AlGaN organometallic vapor-phase epitaxy, Journal of Crystal Growth, 287 (2006) 566-571.

[47] M. Dauelsberg, D. Brien, H. Rauf, F. Reiher, J. Baumgartl, O. Häberlen, A.S. Segal, A.V. Lobanova, E.V. Yakovlev, R.A. Talalaev, On mechanisms governing AlN and AlGaN growth rate and composition in large substrate size planetary MOVPE reactors, Journal of Crystal Growth, 393 (2014) 103-107.

[48] T.B. Ng, J. Han, R.M. Biefeld, M.V. Weckwerth, In-situ reflectance monitoring during MOCVD of AlGaN, Journal of Electronic Materials, 27 (1998) 190-195.

[49] K. Ikenaga, A. Mishima, Y. Yano, T. Tabuchi, K. Matsumoto, Growth of silicon-doped Al0.6Ga0.4N with low carbon concentration at high growth rate using high-flow-rate metal organic vapor phase epitaxy reactor, Japanese Journal of Applied Physics, 55 (2016) 05FE04.

[50] A. Yamamoto, K. Kanatani, S. Makino, M. Kuzuhara, Metalorganic vapor phase epitaxial growth of AlGaN directly on reactive-ion etching-treated GaN surfaces to prepare AlGaN/GaN heterostructures with high electron mobility (~1500 cm2 V−1 s−1): Impacts of reactive-ion etching-damaged layer removal, Japanese Journal of Applied Physics, 57 (2018) 125501.

[51] L. Tang, B. Tang, H. Zhang, Y. Yuan, Review—Review of Research on AlGaN MOCVD Growth, ECS Journal of Solid State Science and Technology, 9 (2020) 024009.

[52] S. Keller, G. Parish, P.T. Fini, S. Heikman, C.H. Chen, N. Zhang, S.P. DenBaars, U.K. Mishra, Y.F. Wu, Metalorganic chemical vapor deposition of high mobility AlGaN/GaN heterostructures, Journal of Applied Physics, 86 (1999) 5850-5857.

[53] N. Okada, N. Fujimoto, T. Kitano, G. Narita, M. Imura, K. Balakrishnan, M. Iwaya, S. Kamiyama, H. Amano, I. Akasaki, K. Shimono, T. Noro, T. Takagi, A. Bandoh, Thermodynamic Aspects of Growth of AlGaN by High-Temperature Metal Organic Vapor Phase Epitaxy, Japanese Journal of Applied Physics, 45 (2006) 2502-2504.

[54] N. Kato, S. Sato, T. Sumii, N. Fujimoto, N. Okada, M. Imura, K. Balakrishnan, M. Iwaya, S. Kamiyama, H. Amano, I. Akasaki, H. Maruyama, T. Noro, T. Takagi, A. Bandoh, High-speed growth of AlGaN having high-crystalline quality and smooth surface by high-temperature MOVPE, Journal of Crystal Growth, 298 (2007) 215-218.

[55] A. Lobanova, E. Yakovlev, J. Jeschke, A. Knauer, M. Weyers, Kinetics of AlGaN metal–organic vapor phase epitaxy for deep-UV applications, Japanese Journal of Applied Physics, 55 (2016) 05FD07.

[56] A.S. Almogbel, C.J. Zollner, B.K. Saifaddin, M. Iza, J. Wang, Y. Yao, M. Wang, H. Foronda, I. Prozheev, F. Tuomisto, A. Albadri, S. Nakamura, S.P. DenBaars, J.S. Speck, Growth of highly conductive Al-rich AlGaN:Si with low group-III vacancy concentration, AIP Advances, 11 (2021) 095119.

[57] C. Touzi, F. Omnès, B. El Jani, P. Gibart, LP MOVPE growth and characterization of high Al content AlxGa1−xN epilayers, Journal of Crystal Growth, 279 (2005) 31-36.

[58] S.C. Choi, J.-H. Kim, J.Y. Choi, K.J. Lee, K.Y. Lim, G.M. Yang, Al concentration control of epitaxial AlGaN alloys and interface control of GaN/AlGaN quantum well structures, Journal of Applied Physics, 87 (1999) 172-176.

[59] A.A. Allerman, M.H. Crawford, A.J. Fischer, K.H.A. Bogart, S.R. Lee, D.M. Follstaedt, P.P. Provencio, D.D. Koleske, Growth and design of deep-UV (240–290nm) light emitting diodes using AlGaN alloys, Journal of Crystal Growth, 272 (2004) 227-241.

[60] H. Tokunaga, A. Ubukata, Y. Yano, A. Yamaguchi, N. Akutsu, T. Yamasaki, K. Matsumoto, Effects of growth pressure on AlGaN and Mg-doped GaN grown using multiwafer metal organic vapor phase epitaxy system, Journal of Crystal Growth, 272 (2004) 348-352.

[61] W.V. Lundin, A.V. Sakharov, A.F. Tsatsul'nikov, E.E. Zavarin, A.I. Besyul'kin, A.V. Fomin, D.S. Sizov, Growth of AlGaN epitaxial layers and AlGaN/GaN superlattices by metal-organic chemical vapor deposition, Semiconductors, 38 (2004) 678-682.

Chapter 4

4. AlGaN samples

4.1 Introduction

AlGaN based alloys are desirable due to their wide applicability in different areas, like UV LED-s and transistors, that were presented in more details within Chapter 2 [1]. The basis for the development of this alloy is its successful production by either metal-organic chemical vapour deposition (MOCVD) or molecular beam epitaxy (MBE). The choice between the different growth methods depends on the precise details of the grown structure and the end application. The growth methods were introduced in the introductory Chapter 3 of this thesis.

The properties of AlGaN layers grown using MOCVD and MBE techniques on different substrates and with inclusion of different layers, such as buffer layers, are explored in this chapter. Next studied set are MBE samples grown on different substrates, namely AlN/sapphire templates and native AlN substrates.

A lot of effort has been invested into development of AlGaN alloys, but there are still challenges to be overcome. Some of the issues are related to the low availability and high cost of native AlN substrates [2]. These can be circumvented by growth on sapphire substrates, naturally with some penalty due to lattice and thermal mismatch. Even though sapphire substrates are more affordable and transparent in the entire UV spectral region, the resulting epitaxial films have high densities of defects which in turn limit their efficiency. GaN substrates are not adequate for higher AlN content AlGaN due to the lattice mismatch between the epitaxial layers and the GaN substrate [3]. When strained epitaxial layers exceed their critical thickness, threading dislocations can be generated, which will dramatically lower device performance [4]. AlGaN layers grown on GaN can form cracks as a result of the relaxation of tensile stress. There are also limitations due to the high absorption of UV light by GaN layers. As a consequence, AlN substrates are a better alternative, and it is possible to grow higher AlN content AlGaN heterostructures on top of them with relatively low strain. If the stress occurs it will be compressive, not tensile and extended

cracks will not be formed [5]. Epitaxial lateral overgrowth (ELOG) techniques on honeycomb or micro-stripe shape-patterned sapphire and on nanopatterned sapphire substrates (NPSSs) have shown promising results in reducing the defect density of the AlGaN layer [6]. The low defect densities of bulk AlN substrate are attractive and AlN substrates are becoming more popular with multiple commercial suppliers in existence such as HexaTech [7] Crystal IS and CrystAL-N, only drawback is their high price. Some samples investigated in this chapter are grown on AlN substrates from the HexaTech company and AlN-on-sapphire templates from Nitride Solutions Inc. The epitaxial growth of thick, crack-free, high-quality high AlN content AlGaN with a low dislocation density template is crucial in constructing high-performance AlGaN-based optoelectronic devices.

Deep impurity luminescence characteristic for AlGaN material was described in Chapter 2. The relative intensities of the defect peaks give valuable information about the formation energy and incorporation of the different defect centres. Defect emission is a consequence of incorporation of oxygen in AlGaN due to the high chemical affinity of aluminium for oxygen [8], [9]. The origin of the defect peak at 2.7 eV is assumed to be recombination between a shallow donor (Si) and a deep acceptor [10]. The deep acceptor is most likely a triply charged cation vacancy $(V_{III})^{3-}$ [11]. The group III-vacancies are often associated with one or two O_N impurities in adjacent sites, forming different complexes [12]. The impurity transition at $3.3-3.6$ eV is attributed to recombination between a shallow donor (Si) and a doubly-charged deep level acceptor. The doubly-charged deep level acceptor is most likely another acceptor complex $(V_{III}\text{-}O_N)^{2-}$[10]. The energy level of $(V_{III}\text{–}O_N)^{2-}$ locates approximately 1.5 eV above the value of E_v (the top of the valence band) [12]. The defect peak emission at $3.8-3.9$ eV can be assigned to the group III-vacancies that are associated with two O_N impurities in adjacent sites, forming $(V_{III}\text{–}2O_N)^{1-}$ complexes [13]. This transition is associated with recombination between a shallow donor (Si) and a singly-charged deep level acceptor [12], [14].

4.1.1 Methodology

Wavelength dispersive X-ray spectrometry (WDX) enables a fast, non-destructive determination of the AlN content in the top AlGaN layers. All WDX measurements in the EPMA are conducted with the samples placed perpendicular to the incident electron beam. WDX analyses are performed with different analytical conditions, such as accelerating voltage, and with or without carbon coating. The acceleration energy utilized is well above the minimal energy needed to excite the characterized elements while containing the interaction volume in the desired top AlGaN layer. Data resulting in weight totals (wt) closest to 100 % is shown in table 4.1 (data resulting in wt< 95% or wt>105% are rejected). In the quantitative analysis X-ray line intensities emitted from the specimens (L_α for Ga and K_α for Al, N) are compared against the same X-ray line from the standard samples with known concentrations (AlN (for Al and N) and GaN (for Ga)). The measured intensities are then corrected for differences in composition between the standard and main specimens using an iterative procedure to give accurate atomic percentages of the species. Optical characterization at room temperature using cathodoluminescence (CL) permits analysis of near band edge emission in the range 4.7–5.2 eV as well as various deep impurity transition peaks in the range 2.7–3.9 eV. CL mapping and WDX mapping are utilized to correlate optical properties with surface morphology

4.2 MOCVD AlGaN samples

4.2.1 Comparison between MOCVD AlGaN samples: directly on sapphire substrates (B1, B2 and A) and on AlN buffer/ sapphire substrate (USC902)

A series of MOCVD samples are studied; namely samples A, B1 and B2 grown directly on sapphire substrates, and sample USC902 grown on an AlN buffer/sapphire substrate. The AlN buffer layer is used to reduce the density of defects in the epitaxial films. Samples A, B1 and B2 are more than 500 nm thick, and sample USC902 is around 200 nm thick.

CL maps are recorded from uncoated samples in the low-vacuum FEG-SEM with an electron beam voltage of 10 kV, spot size 5.5 at high vacuum conditions (A, B1 and B2) and with beam voltage of 6 kV, spot size 5 and 0.3 mbar low pressure for sample USC902. At 10 kV 90% of the beam energy is being deposited in the first 580 nm, at 6 kV 90% of the beam energy is being deposited in the first 190 nm confining the interaction volume into the top AlGaN layer according to Monte Carlo Casino software [15]. Low vacuum mode was necessary due to charging effects preventing a clear image to be obtained in high vacuum mode.WDX maps are acquired with 15 kV and 40 nA. Samples A and B2 exhibit hexagonal surface features with AlN-rich boundaries confirmed by WDX mapping.

Table 4.1: Description and the schematic representation of the studied samples, originating from Sandia National Laboratories (A, B1), University of South Carolina (B2) and from Ohio State University (USC902).
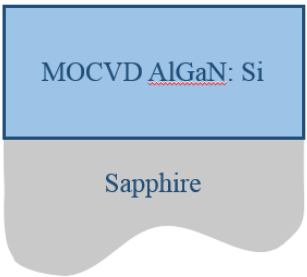
Sample schematic	Sample name (MOCVD AlGaN ~500 nm on sapphire)	AlN at% growers estimate	AlN at% measured with WDX (3 kV uncoated samples)	Total wt% (average of 9 points)	NBE CL peak energy (eV) and intensity (a.u.)*	[Si] cm^{-3} growers estimate
MOCVD AlGaN: Si / Sapphire	A	70 %	69 ± 1%	100%	4.87 (190,000)	~ 3×10^{19}
	B1	60 %	72 ± 1%	101%	5.02 (426,000)	~ 3×10^{19}
	B2	60 %	57 ± 1%	99%	4.74 (593,000)	~ 5×10^{19}

MOCVD AlGaN:Si / MOCVD AlN / Sapphire	(MOCVD AlGaN ~200 nm/AlN on sapphire) USC902	60%	(6 kV coated sample) 62 ± 1%	95%	4.79 (13,300)	5-7×10^{18}

*CL intensity comparison only rough estimate, data extracted from CL maps, sample USC902 CL data acquired with different conditions

In order to investigate the influence of the different AlN composition of the AlGaN layers on the surface morphology and the spatial homogeneity of the luminescence CL hyperspectral maps are collected from different MOCVD samples (A, B1, B2: grown directly on sapphire substrate and USC902 grown with AlN buffer). CL maps contain spectral information in each pixel and therefore make it possible to extract information about intensity variations, changes in peak width and energy shifts. Gaussian functions are fitted to the generated CL hyperspectral data set to extract information about the emission energy as well as the intensity of the peaks.
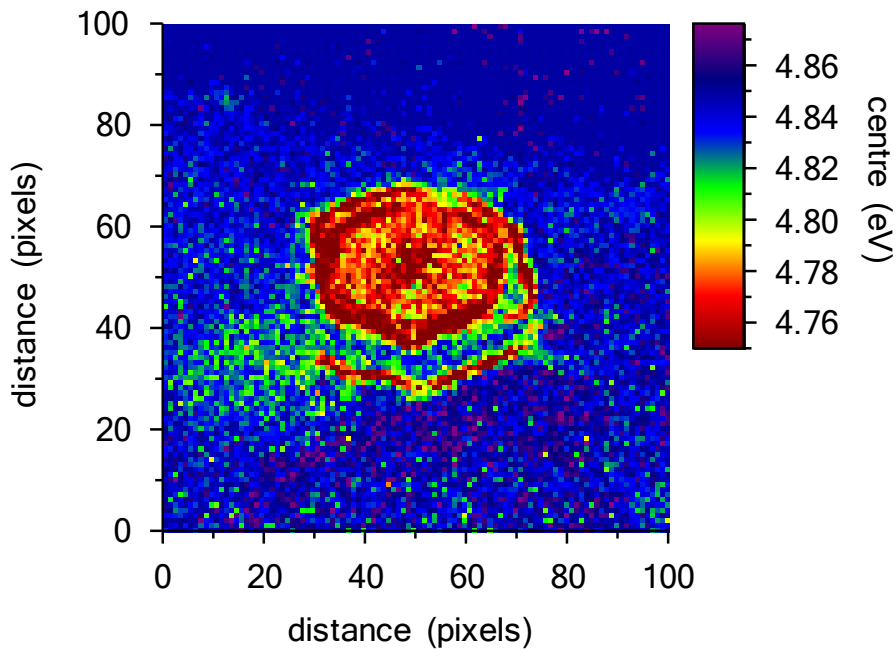
Figure 4.1: RT-CL map of sample A, peak energy map of the fitted 4.0 eV peak.

a)

b)
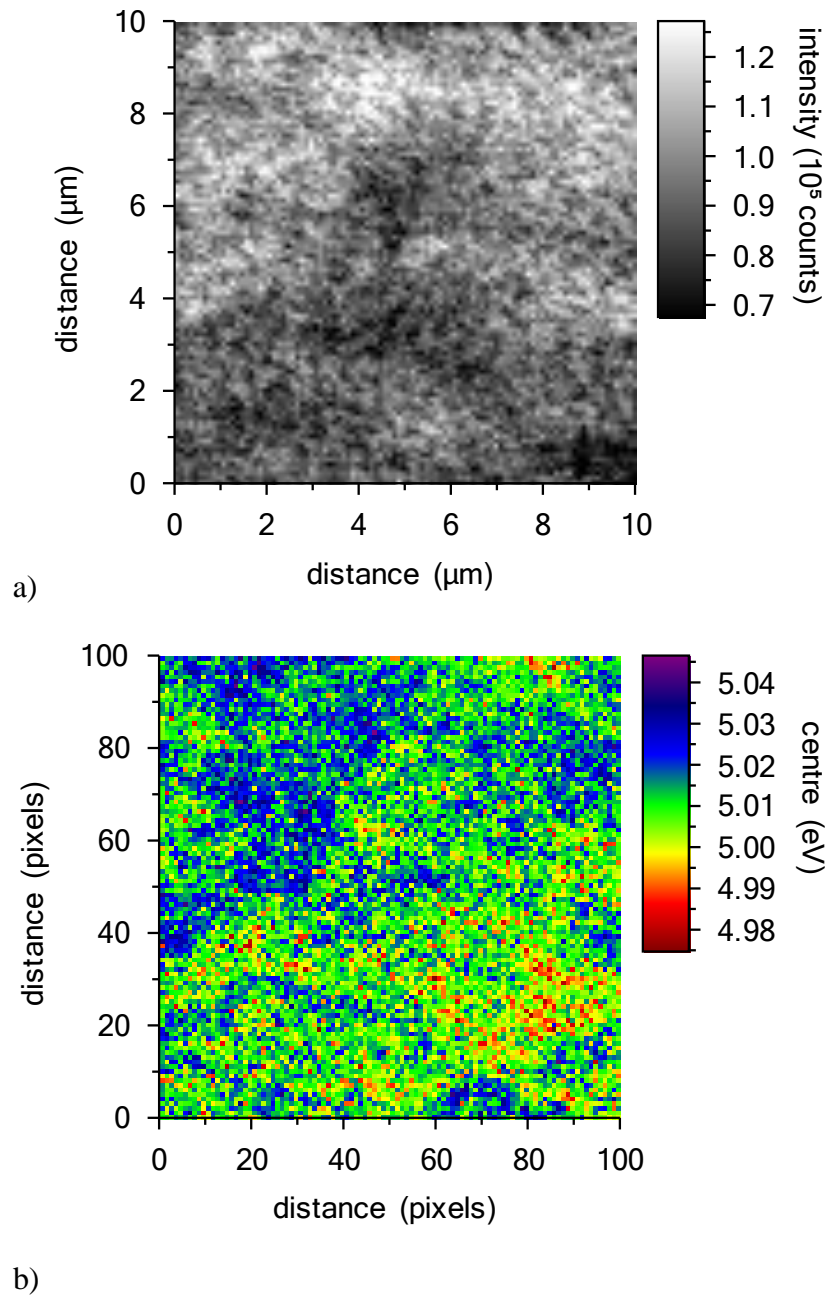
Figure 4.2: RT-CL map of sample B1: a) integrated CL intensity map (4.7−5.2 eV), b) peak energy map of the fitted 5.0 eV peak.

a)

b)
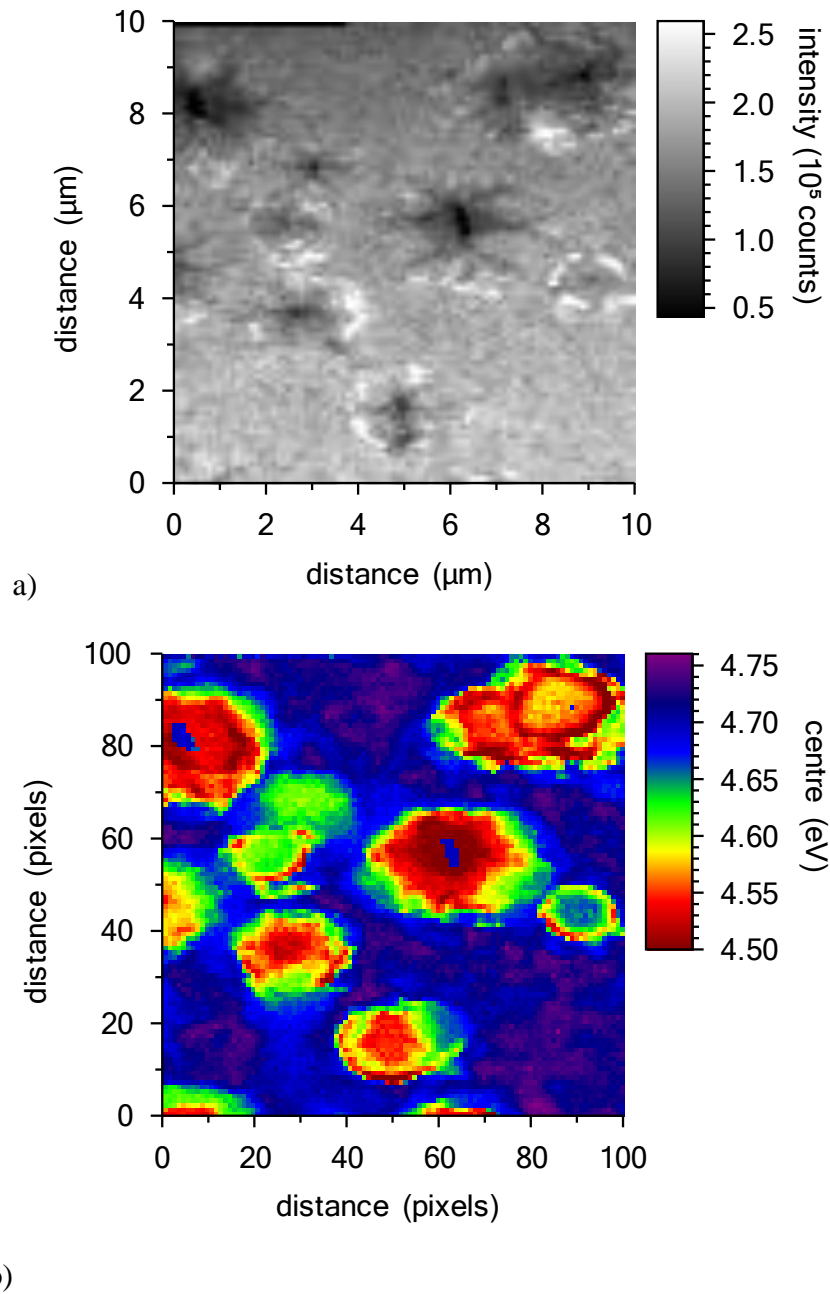
Figure 4.3: RT-CL map of sample B2: a) integrated CL intensity map (4.3−4.5 eV), b) peak energy map of the fitted 4.7 eV peak.

a)

b)

c)
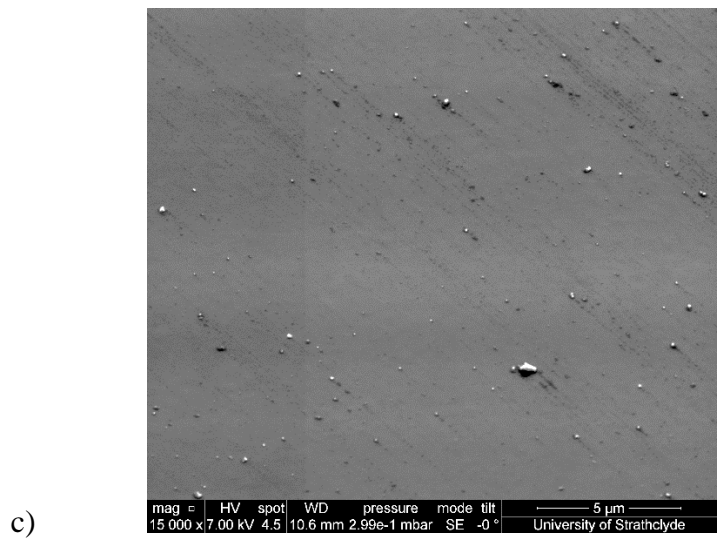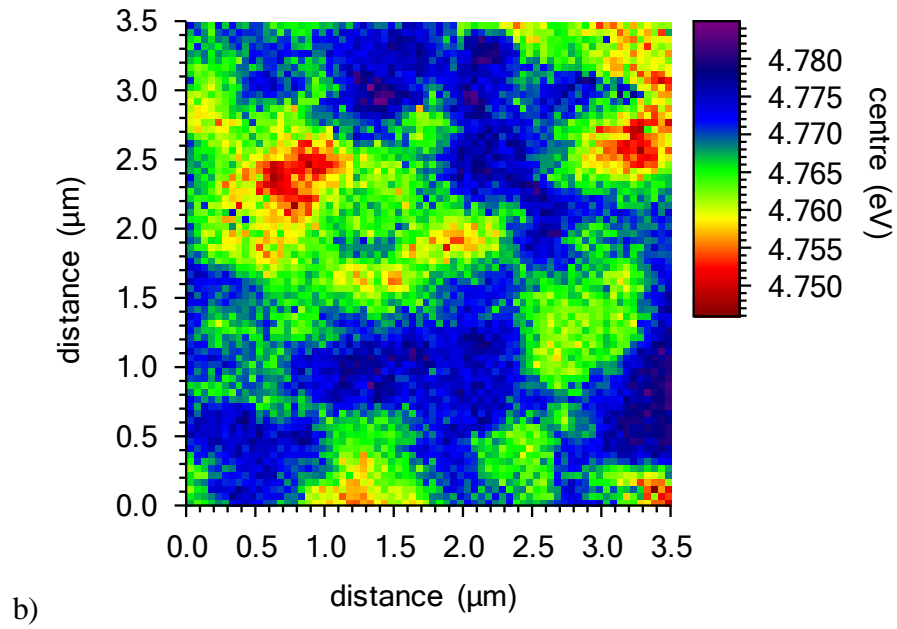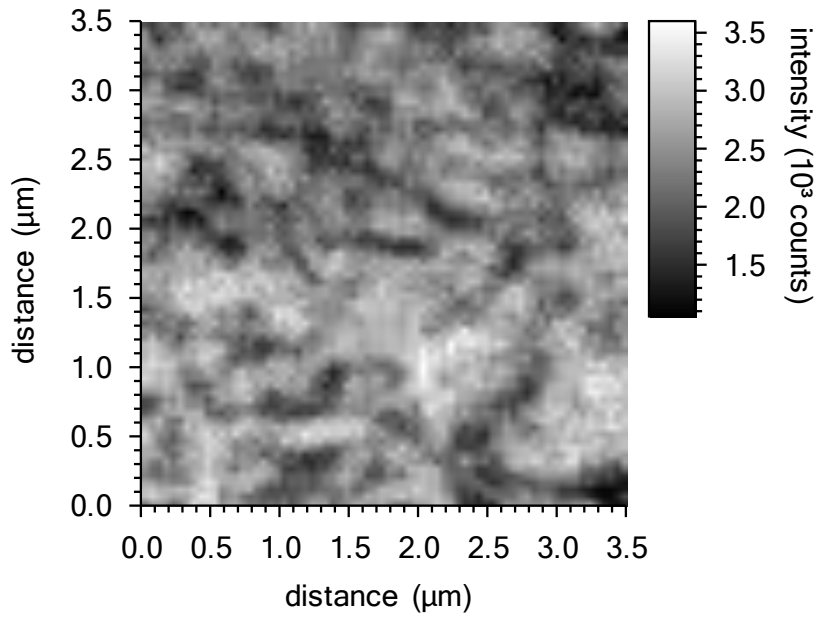
Figure 4.4: RT-CL map of sample USC902: a) integrated CL intensity map (4.5−5 eV), b) peak energy map of the fitted 4.7 eV peak c) SE image of the representative area.

In Figs. 4.2a), 4.3a) and 4.4a) the intensity maps of the NBE emission are depicted, while Figs. 4.1 4.2b), 4.3b) and 4.4b) show the result of fitting Gaussian functions to each spectrum in the data set using a nonlinear least-squares optimisation routine to produce 2D maps showing variations in the peak energy.

In the CL map of sample B1 (Fig.4.2) there are no visible hexagons on the sample surface and the NBE peak energy map reveals more homogeneous emission, with small shifts in peak energy which are not related to any 3D structure appearing on the sample surface. The CL map reveals that the AlN composition is also more homogeneous across the sample surface compared to sample B2.

The surface of sample USC902 (Fig. 4.4b) is free from cracks and hexagons, similar to sample B1(Fig. 4.2b). The peak energy map of sample USC902 (Fig. 4.4b) shows smaller shifts in emission energy over larger micron size areas compared to sample B2 (Fig. 4.3b) and sample A (Fig. 4.1) but larger compared to sample B1 (Fig. 4.2b). In the integrated intensity map of sample USC902 (Fig. 4.4a) dark spots are observed, which can be associated with threading dislocations (TDs) (lower estimate 6×10^8 cm^{-2}) and related to non-radiative recombination centres [12]. The CL map of sample A (Fig. 4.1) is showing hexagon 3D features, similar to sample B2. The middle of the hexagon area exhibits lower emission energy and hence lower AlN content. When compared to sample B2, the concentration of hexagons is significantly reduced in sample A.

From the energy map of sample USC902 it is possible to conclude that the AlN buffer layer helps to keep the surface morphology of the AlGaN layer smooth due to good coalescence and two-dimensional (2D) growth. However, it is not clear if the only reason for the lower NBE intensity compared to other MOCVD samples is the different set of analytical conditions used (such as voltage, current and chamber pressure) to acquire CL data. Due to the large lattice mismatch between sapphire and AlN (~13.3%) as well as the requirement to

use high temperature (> 1250 °C) for growth, the resulting AlN layers can exhibit low emission efficiency which will in turn have an effect on AlGaN layers grown on top, and cause their low NBE intensity [16]. It is also expected for the CL intensities of AlGaN layers to increase with increase in the AlN buffer layer thickness due to reduction in the TDs. The increase of the CL intensity would indicate an improvement of the crystalline quality of the AlGaN epilayer [17]. The energy shift is still visible in the CL map of sample USC902 (Fig. 4.5b) which indicates some degree of heterogeneous composition.

In the case of sample A (Fig. 4.1) and sample B2 (Fig. 4.3b) it is evident that the NBE energies are lower in the more GaN rich regions of the sample. This finding is also confirmed by WDX mapping.
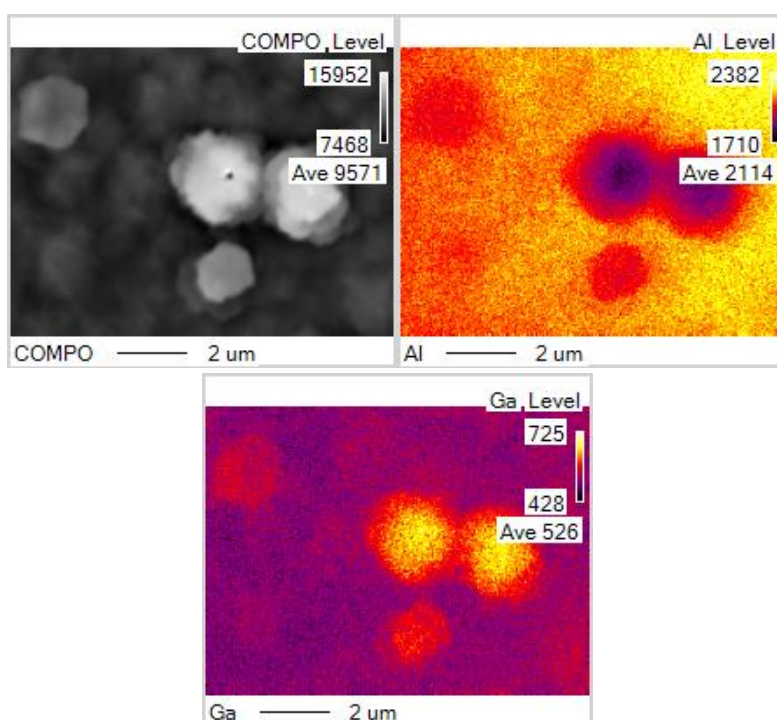
Figure 4.5: Composition mapping of the B2 sample, left BSE image of the measured area, right WDX map of Al K_α intensity map, down WDX map of Ga L_α intensity.

WDX maps in Fig. 4.5 show an opposite correlation between Ga L_α and Al K_α intensity. In the case of sample B2, there is a noticeable shift in the energy and intensity of the NBE emission across the sample. The NBE peak energy map reveals different types of hexagons, some of them are smaller in size and have smaller NBE energy shifts relative to the surrounding area (emission at 4.60 eV). While others are bigger in size and showing higher energy shift (emission

at 4.5 eV). Surprisingly, one of the hexagons exhibits different behaviour and shows higher emission energy from the centre compared to its edges, so in the case of that particular hexagon it is possible to conclude that AlN content is higher in the middle of the feature (emission at 4.7 eV). From the SE image (not shown here) pits coming from the apex of the 3D features are visible, and CL NBE intensity is reduced at the apex of each hillock as seen in Fig. 4.3a, probably due to the screw dislocations [18]. In GaN epitaxy, hexagonal crystallographic pits with a single TD are commonly observed [19]. Electron channelling contrast imaging (ECCI) could be employed on this set of sample to study threading dislocations as in Ref [20] where they confirmed formation of different domains due to spiral growth around a dislocation with a screw component using ECCI technique.

Probably better surface quality can be achieved with thicker AlN buffer layers or by adjusting the growth temperature of the AlN layer [16, 21]. It is important to achieve optimal thickness of AlN buffer layer, because if the buffer is too thick, it can lead to the coalescence of islands too quickly and result in a large dislocation density [22]. In general, the AlN compositional inhomogeneity of the AlGaN epilayer can be attributed to the low lateral mobility of Al adatoms on the growing surface [21].

From the acquired hyperspectral CL maps, the average CL spectra were extracted within flat regions (avoiding any 3D features) in order to compare the energy of the NBE peaks. The emission spectrum has a broad FWHM at room temperature. The map of USC902 was not acquired simultaneously with samples A, B1 and for that reason its mean spectra is shown separately. Sample USC902 was not available at the time when A, B1 and B2 measurements were performed.
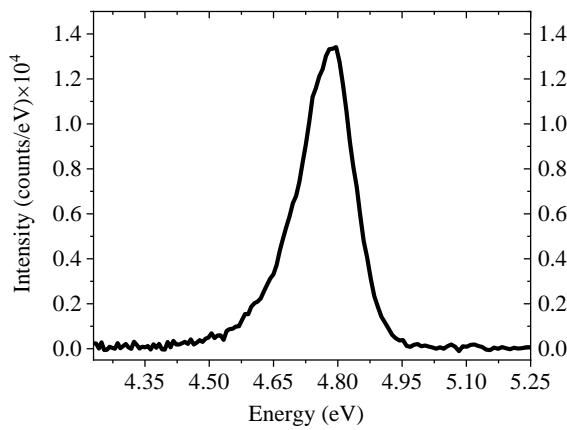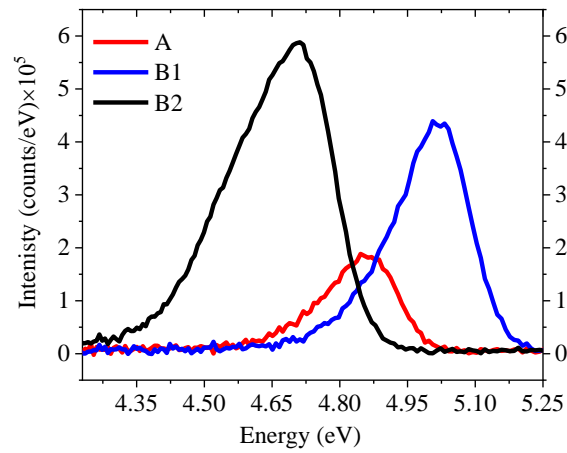
Figure 4.6: Mean RT-CL spectra of the samples A, B1 and B2 (top) and sample USC902 (bottom) extracted from CL maps showing NBE emission region.
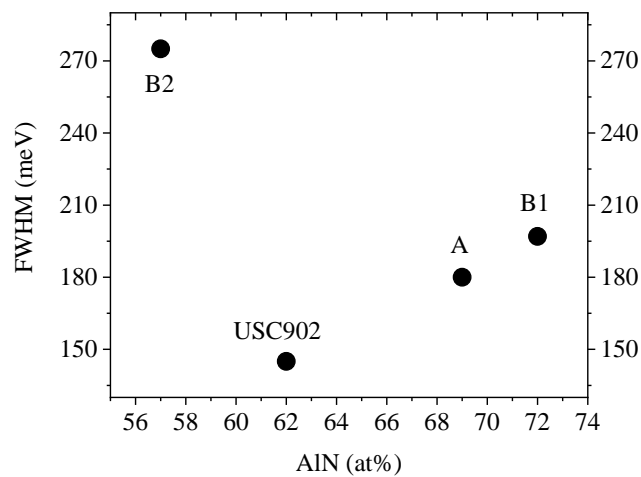
Figure 4.7: Values for the FWHM extracted from RT-CL spectra of the samples A, B1, B2 and USC902 depending on AlN at% measured with WDX.

The mean CL spectra of sample USC902 (Fig. 4.6 bottom) only shows a NBE emission peak near 4.8 eV, with no visible defect peaks. However, the intensity of the NBE emission is lower compared to samples A, B1 and B2 (as explained previously). In Fig. 4.6 (top) the highest intensity of the NBE emission is observed for sample B2 (sample with highest level of Si doping and lowest AlN at%) and the lowest intensity is observed for sample A (lower Si doping). The full width at half maximum (FWHM) of the NBE peak was smallest for the sample with the AlN buffer layer (USC902) measuring 145 meV due to improved surface morphology (Fig 4.7). The measured FWHM value for sample A is 180 meV, for sample B1 197 meV and for sample B2 275 meV. The FWHM value is increasing with measured AlN at% except for the sample B2 due to compositional inhomogeneity caused by morphological effects (3D features).

As expected the $Al_xGa_{1-x}N$ NBE emission energy shifts significantly with the AlN composition. Fig. 4.8 depicts the relation between experimental data for the NBE emission energy and measured AlN content of the alloy. The band gap energy of III–V compound alloys and their dependence on alloy composition can be described by standard quadratic interpolation scheme for the entire range of alloy composition.

The composition dependence of the bandgap can be described by the standard bowing equation,

$$E_g^{AlGaN}(x) = xE_g^{AlN} + (1-x)E_g^{GaN} - bx(1-x) \qquad (4.1)$$

The parameter b is called the bowing or nonlinear parameter [16]. Values for b reported for AlGaN in the literature vary from -0.8 eV to 2.6 eV [17] due to different preparation techniques, different alloy composition ranges, etc.
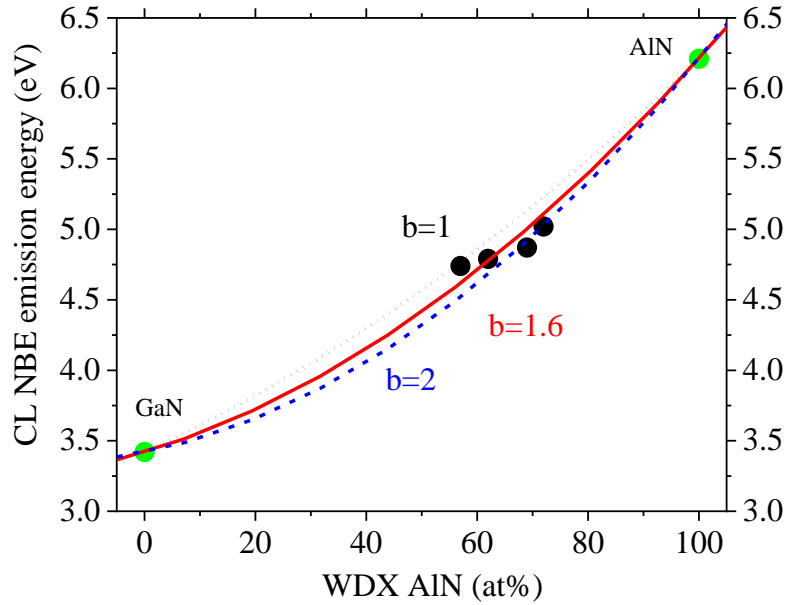
Figure 4.8: Evolution of the near band edge peak energy (NBE) of MOCVD samples (black points) measured with the CL system against the AlN% measured by WDX. Green points represent theoretical RT values for GaN (Madelung (1991)) and AlN respectively (Yamashita et al. (1979)).

From the Fig. 4.8 the trend of increasing NBE emission with increase in AlN at% is evident, as expected. For example, sample B1 with 72 at% AlN exhibits the highest NBE energy at 5 eV. By fitting the experimental data to the polynomial band gap–composition relationship, a bowing parameter of $b = 1.6$ was obtained. Obtained value is within the reported values for the bowing parameter (-0.8−2.6 eV)[23].

In the next section, the occurrence of defect peaks will be discussed (more details in introductory Chapter 2) and the difference between CL point spectra extracted from various regions of the samples in relation to occurrence of 3D features.

In spectra extracted from CL maps of MOCVD samples (Fig. 4.9) the variations in the NBE intensity and the position are noticeable due to occurrence of hexagonal 3D features (sample B2). Also additional deep impurity peaks are visible (Fig. 4.9a), having lower intensity compared to the NBE emission intensity. Observed additional peaks are probably associated with screw dislocations, since they are only visible in the spectrum extracted from the

hexagon apex, and according to Ref [18], a screw dislocation has been reported to emerge from the apex of the hexagon. The observed defect peaks indicate that around screw dislocations the formation of compensating defects and incorporation of oxygen atoms are increased [24].
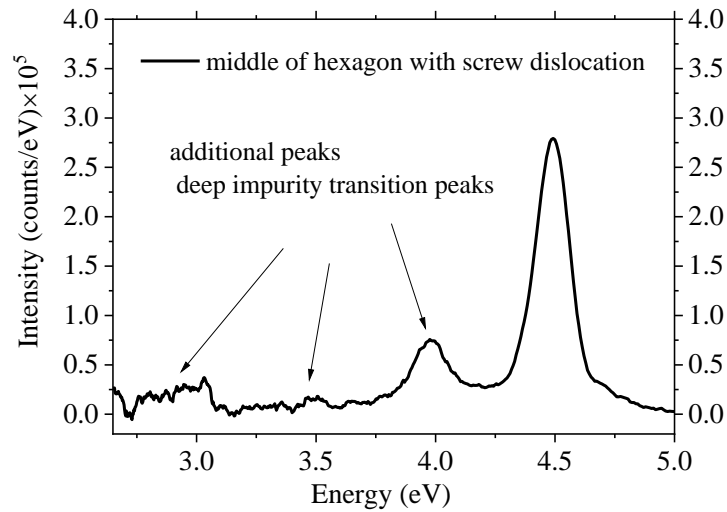
a) Extracted point CL spectra from hexagon apex, sample B2
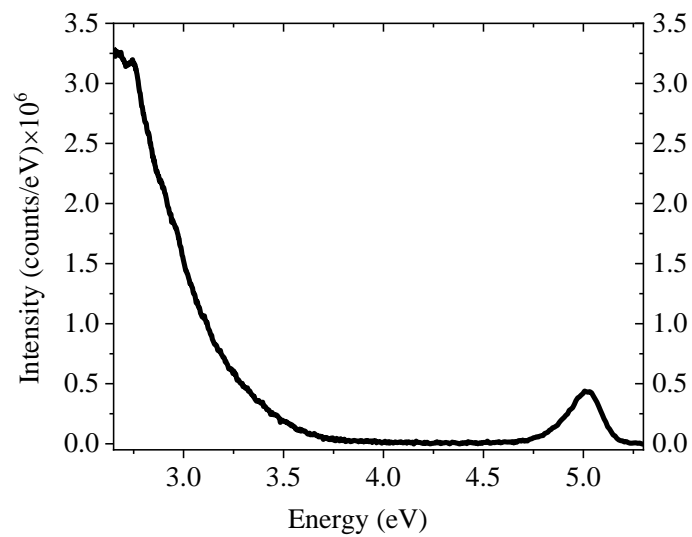
b) Extracted mean CL spectrum, sample B1
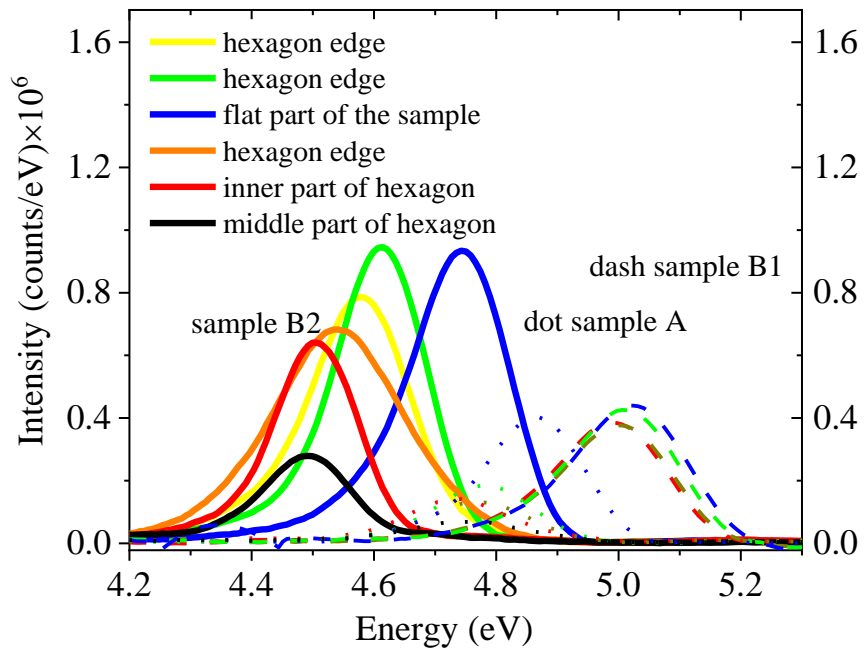
c) Comparison of extracted CL point spectra from sample B1, B2 and A. The spectra are averaged from 4 pixel diameter
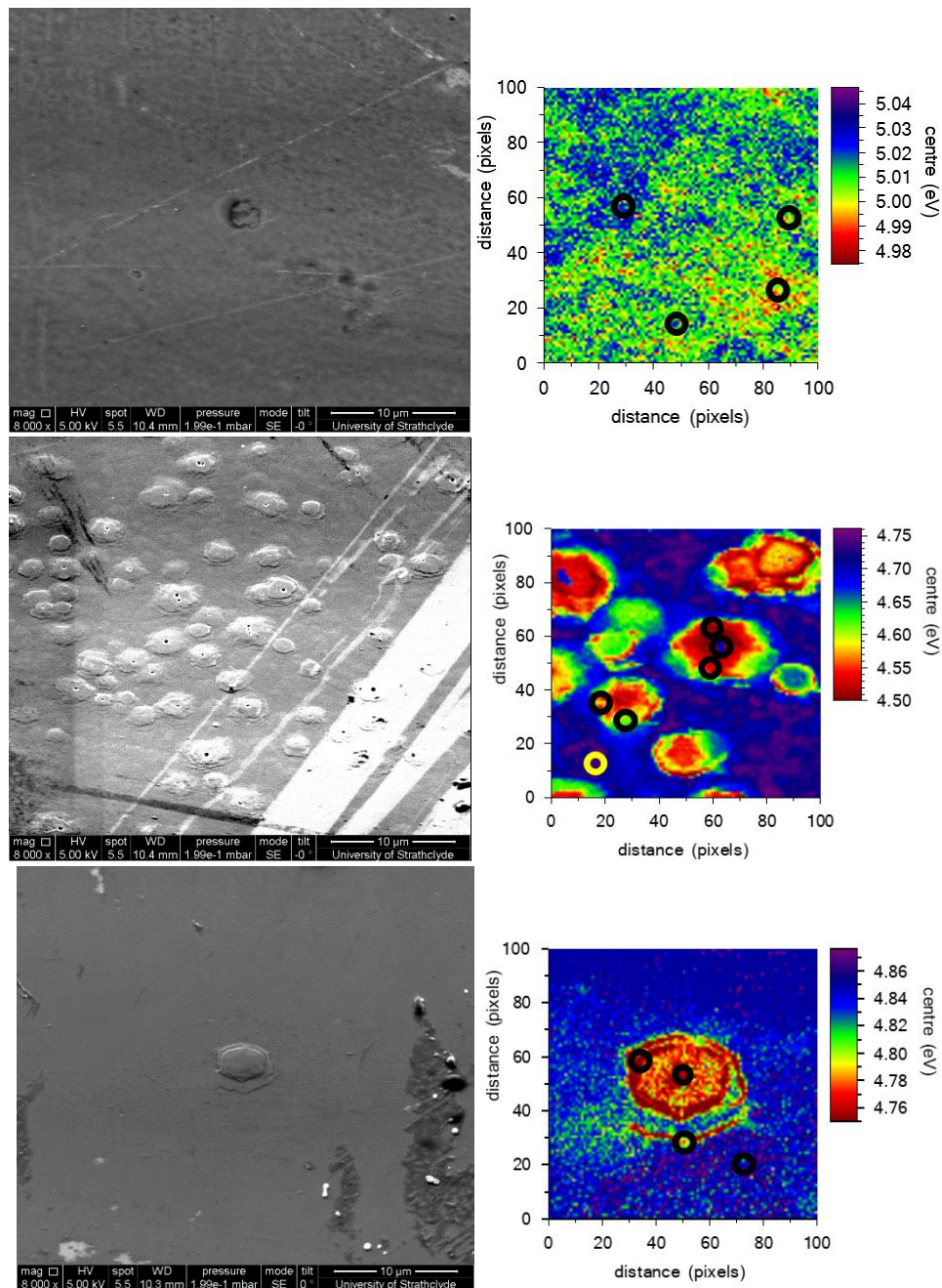
d) The circled parts in the maps represent the areas from which spectra are averaged for sample B1, B2 and A with the SE image of the sample area on the left.

Figure 4.9: Comparison of CL spectra between MOCVD AlGaN on sapphire (B1, B2 and A).

The mean CL spectrum of sample B1 (Fig. 4.9b) shows a small NBE intensity emission peak at 5 eV and a higher intensity peak at 2.7 eV originating from defect luminescence. Strong defect luminescence is suggesting that the excited carriers were mostly trapped and consumed through the presence of impurities,

which would limit the usability of this material as an DUV emitter. Relatively high growth temperature can introduce more V_{III}-relevant defects due to re-evaporation of the III-species from the crystal. Also the high chemical activity of Al-species contributes to the incorporation of oxygen impurities from the growth [12]. The mean spectrum for sample A (not shown) is similar to the B1 spectrum. The mean CL spectra shows a NBE emission peak at 4.8 eV and a peak of slightly lower intensity at 2.7 eV originating from the same type of defect luminescence.

In Fig. 4.9 c) point spectra extracted across different regions from sample B2, B1 and A (Fig. 4.9d) are compared. For sample B1 the shift in NBE emission energy from various regions across the sample is smallest and the measured AlN at% for that sample is highest. The biggest shift in NBE emission energy is observed for sample B2 (lowest measured AlN at%). The sample with highest difference in NBE emission energy and highest intensity is the one containing most hexagons on the surface. Sample B1 does not exhibit hexagons on the surface. While sample A only contains a few hexagons and its intensity is the lowest one (middle AlN % content).

4.3 MBE AlGaN samples

4.3.1 Comparison between samples from Ohio State University: MBE AlGaN on AlN substrate (171110A, 171110B, 171121B and AGBK850) and AlGaN/AlN on sapphire (AGC850)

A series of MBE samples are studied; namely samples 171110A, 171110B, 171121B and AGBK850 grown directly on native AlN substrates, and sample AGC850 grown on AlN/sapphire substrate. The MOCVD and MBE layers are expected to greatly differ due to differences in growth temperature, growth mechanisms, and largely different growth pressures. Samples 171110A, 171110B, 171121B are around 150 nm thick, and samples AGBK850 and AGC850 are around 100 nm thick. The types of measurement performed on the MBE samples are similar to the ones described in MOCVD section. WDX is used to determine the AlN content of the AlGaN layer, with the results shown

in Table 4.2. Optical characterization at room temperature using CL allows analysis of near band edge emission in the range 5.0−5.2 eV as well as deep impurity transition peaks in the range 3.4−3.9 eV. CL maps are recorded from uncoated samples in the low-vacuum FEG-SEM with an electron beam voltage ranging from 4−10 kV, spot size 5.0−5.5 and at a 0.1−0.4 mbar low chamber pressure. Different surface morphology is confirmed compared to the MOCVD samples.

Table 4.2: Sample description and the schematic representation of the studied sample from the Ohio State University (171110A, 171110B, 171121B, AGBK850 and AGC850)

Sample schematic	Sample name (MBE AlGaN ~150 nm on AlN)	AlN at% growers estimate	AlN at% measured with WDX (3 kV uncoated samples)	Total wt% (average of 9 points)	NBE CL peak energy (eV) and intensity (a.u.)*	[Si] cm^{-3} growers estimate
	171110A	85 %	84 ± 1%	104 %	5.2 eV (124,000)	~ 10^{19}
	171110B	~ 98 %	97 ± 1%	100 %	/	~ 10^{19}
	171121B	78 %	80 ± 1%	103 %	5 eV (613,000)	~ 10^{19}
	AGBK850 (AlGaN ~100 nm)	62 %	(coated) 59 ± 1%	102%	/	~ $5-7 \times 10^{18}$
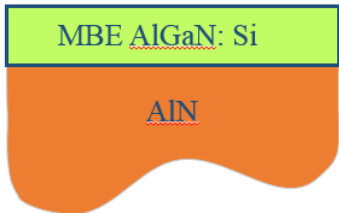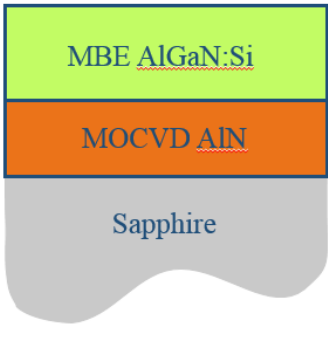
	AGC850 (MBE AlGaN ~100 nm/AlN on sapphire)	65%	67 ± 1%	97%	/	~ 5−7×10^{18}
MBE AlGaN:Si / MOCVD AlN / Sapphire						

As in the case of MOCVD samples, CL hyperspectral maps were collected from the different MBE samples in order to investigate luminescence and defect properties. As shown in MOCVD section, CL hyperspectral imaging offers the ability to map shifts in wavelength or energy, which can be correlated to features on the sample surface. For this set of samples, the influence of the different AlN composition of the AlGaN layers on the surface morphology and the spatial homogeneity of the luminescence was also examined. It will be possible to compare luminescence characteristics between MOCVD and MBE samples. The CL measurements were performed with different sets of analytical conditions (accelerating voltage, current, chamber pressure).

171110A
Rms = 1.69 nm

5 µm

a)

b)

171121B
Rms = 2.46 nm

5 µm

c)

d)

e)

f)
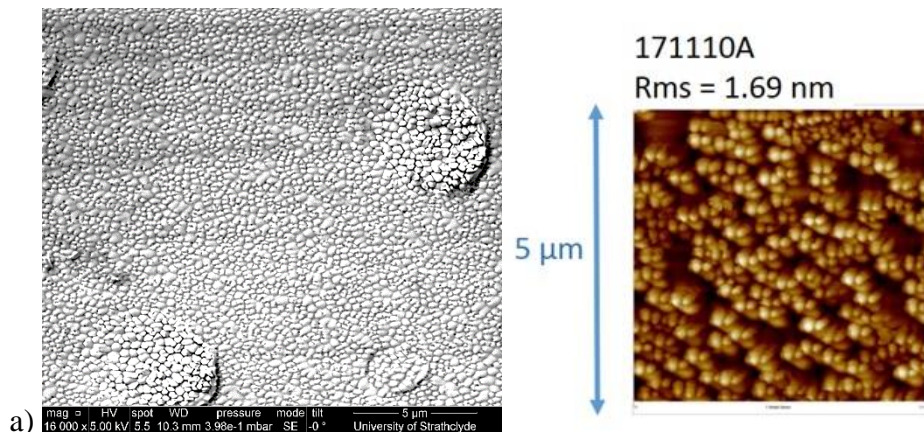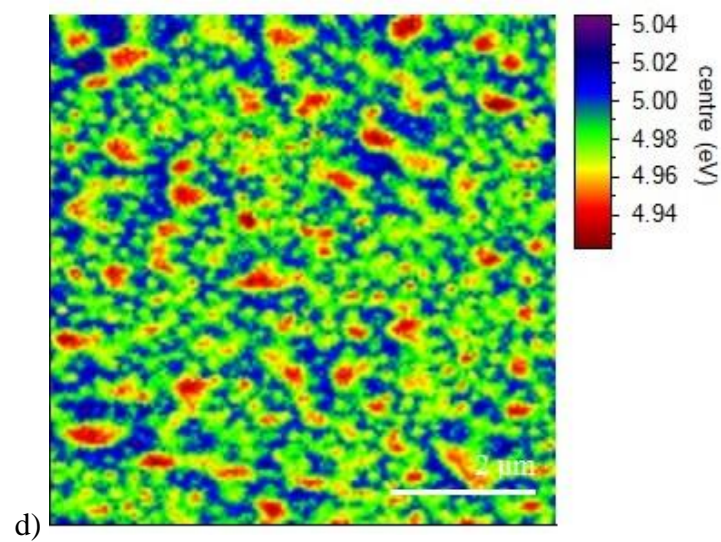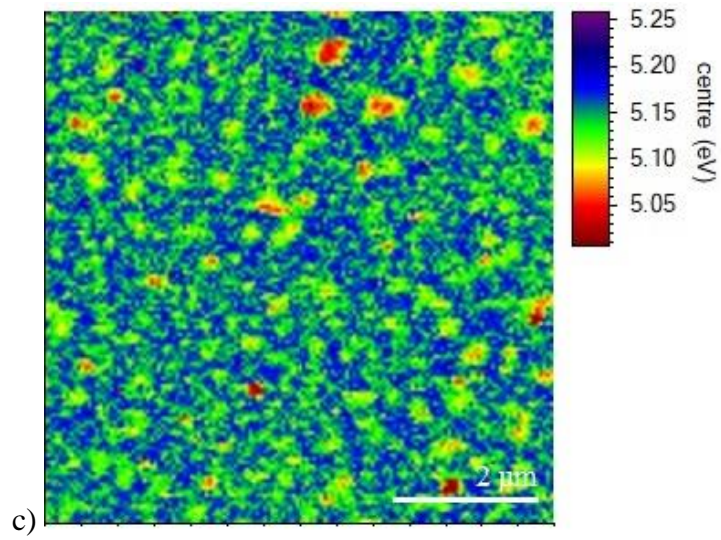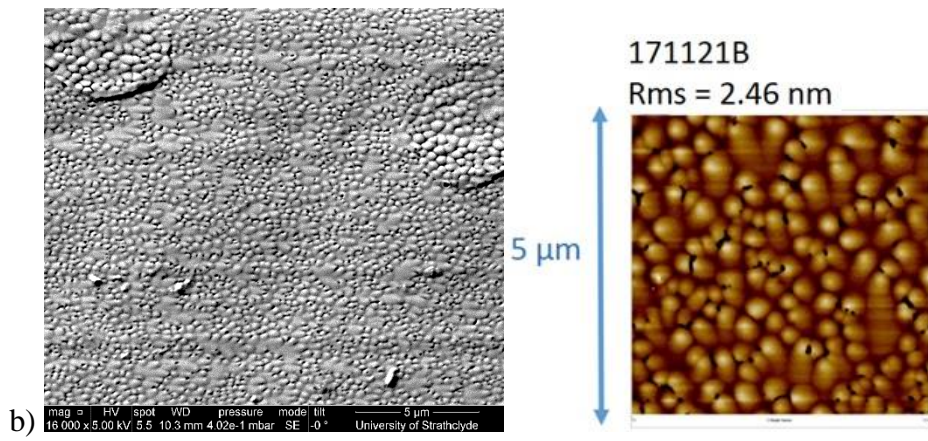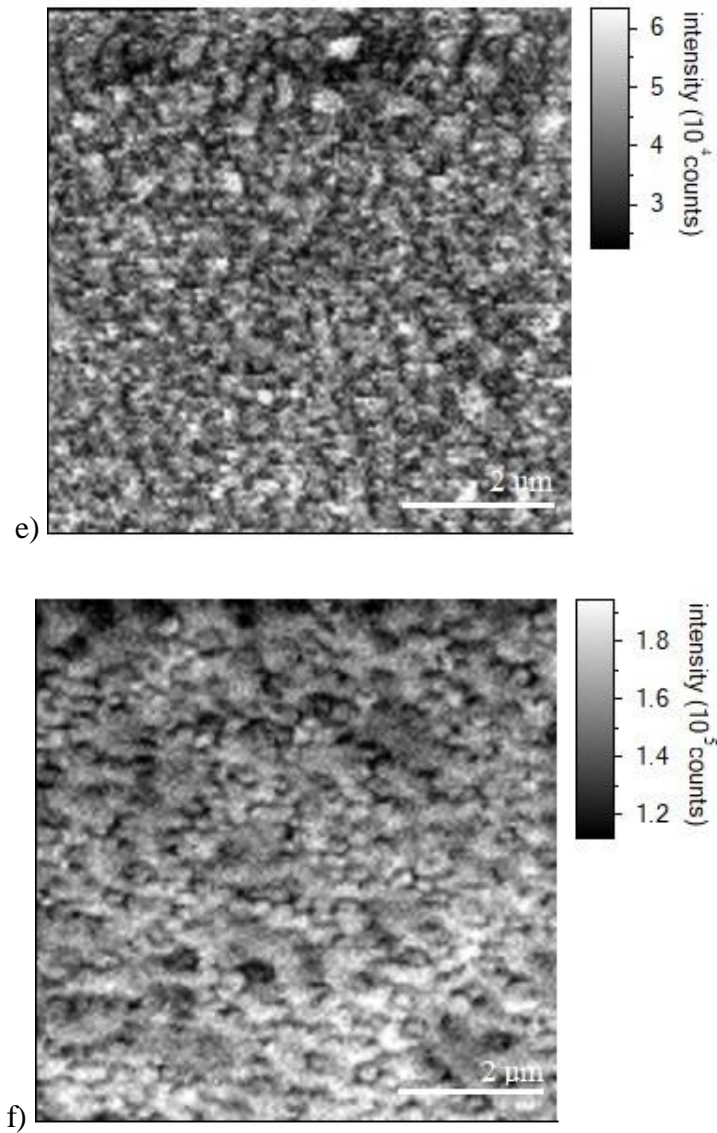
Figure 4.10: AFM and SE image of the typical surface morphology for MBE AlGaN on AlN samples: a) 171110A and b) 171121B and comparison of RT-CL maps for samples: c) 171110A, peak energy map of the fitted 5.15 eV peak, d) 171121B, peak energy map of the fitted 5 eV peak, e) 171110A, integrated CL intensity map (4.8-5.5 eV) f) 171121B integrated CL intensity map (4.7−5.3 eV)

By comparing Fig. 4.10 and Figs. 4.11−4.14 distinctive differences between the MBE and MOCVD CL maps are immediately apparent in terms of different sample texture and appearance. The AFM measurements are performed in the Ohio State University by the group of Prof. Siddharth Rajan over 5×5 μm^2 areas (Fig. 4.10a and b). The corresponding CL maps of samples reflect the same type of topography observed in the AFM measurement. The AFM and CL images of

sample 171110A (84% AlN) reveal a granular surface structure, consisting of small "spots", approximately 20 nm in size (Fig. 4.6a), with an RMS roughness of 1.69 nm.

From the NBE peak energy map of sample 171110A (Fig. 4.10c) is evident how the emission from the spherical spots is red shifted with respect to the surrounding areas. The energy shifts from "spot" to surrounding area being ~60 meV. The shift in emission energy corresponds to a change in the AlN content by about 1 atomic %. The MOCVD samples are not showing this type of granular texture. The observed NBE energy shifts in MBE samples also indicate compositional inhomogeneity, though, in this case, on a nanoscale level.

The AFM and CL images of sample 171121B (80% AlN) (Figs. 4.10b, d, f) reveal the same type of granular morphology as sample 171110A (84% AlN) but with larger "spot" sizes and with an RMS roughness of 2.46 nm. The peak energy map of sample 171121B (Fig. 4.10d) also reveals red shift in the emission from spherical spots with respect to the surrounding areas. NBE energy shift is more pronounced in this sample, being ~130 meV. The shift in emission energy corresponds to a change in the AlN content by about 2 atomic %. The red shift indicates lower AlN content within "spot" region and compositional inhomogeneity, which is more pronounced in sample 171121B.

Even though the NBE intensity of sample 171110A is lower compared to sample 171121B, the sample is showing some improvement in terms of compositional homogeneity. Similar behaviour was observed in the MOCVD set of samples, where sample B2 showed the highest NBE intensity but also the largest compositional inhomogeneity. In general, it is possible to conclude that emission is more homogenous in MBE samples compared to MOCVD samples. The morphological and compositional inhomogeneity's are strengthened in the III-Nitride layers due to the inherent grain structure with typical dimensions of several hundreds of nanometers. The origin of the inhomogeneity is the same as for MOCVD sample, resulting from the limited mobility of Al atoms compared to Ga atoms [25].

Samples AGBK850 and AGC850 are grown on different substrates but with the same thickness of 100 nm and similar AlN at%. The Si concentration in these

two samples is lower compared to the rest of the MBE samples ($\sim 5-7 \times 10^{18}$ compared to 10^{19}). For this reasons they are compared separately from the rest of the MBE samples. Sample AGBK850 has the lowest AlN content among MBE samples (59% AlN) after which comes sample AGC850 with AlN content of 67 at%.

d)
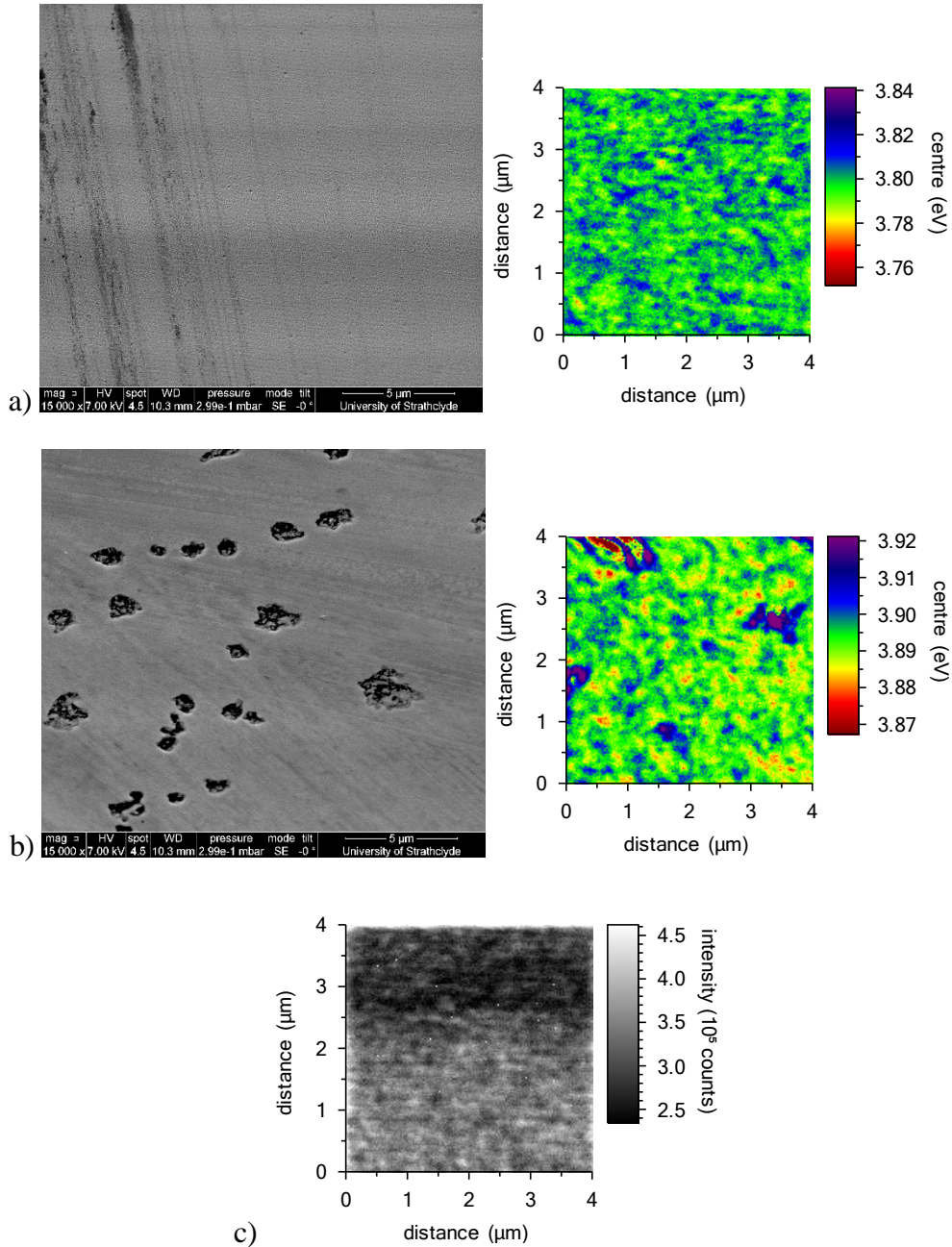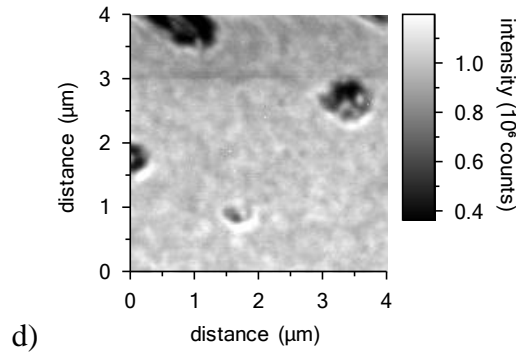
Figure 4.11: Comparison of RT-CL maps for: sample AGBK850 (MBE AlGaN on AlN), a) centroid map and SE image c) integrated CL intensity map (2.21−5.40 eV) and sample AGC850 (MBE AlGaN/AlN on sapphire),: b) peak energy map of the fitted 3.9 eV peak and SE image, d) integrated CL intensity map (2.21-5.40 eV)

The CL maps in Fig. 4.11 of both samples reveal only defect luminescence, originating from $(V_{III}-2O_N)^{1-}$ complexes, with no NBE luminescence as recorded for the rest of the MBE samples (Fig 4.11). The CL map of the defect peak in sample AGBK850 (Fig 4.11a and c) reveals similar granular structure present in other NBE maps of MBE samples 171110A and 171121B (Fig 4.10). In Fig 4.10c) a significantly smaller red shift is observed, compared to the rest of MBE samples. The shift in the emission from spherical "spots" with respect to the surrounding areas being only ~4 meV. For the sample AGC850 (Fig. 4.11b and d) degradation of the material structural quality is also expected due to the occurrence of only defect emission, similar to the case of sample AGBK850. In the CL intensity map of defect peak (Fig 4.11d) large pores are visible in the material caused by the unfinished coalescence of the material. The defect emission is uniform across the sample, with only larger energy shifts coming from the pores.

In the case of MBE AlGaN it is not possible to completely avoid "spots" appearing in the CL maps, because during epitaxial growth active nitrogen reacts instantly with arriving Al atoms on the substrate and limits their diffusivity leading to nucleation of small AlGaN islands (spots) and films with microstructures consisting of small hexagonal columnar domains [26]. Consequently, MBE materials are expected to have high dislocation density,

since the majority of the threading dislocations occur primarily at the boundaries of the hexagonal columnar domains due to their incomplete coalescence [27]. This is even more important in silicon-doped high AlN content AlGaN films, since silicon is an anti-surfactant and thus, it strengthens microstructures with even smaller domains [44]. Seemingly, this is the main reason for MOCVD samples exhibiting higher NBE intensities when compared to MBE samples.

From the acquired hyperspectral CL maps, the mean average CL spectra of MBE samples are extracted (Fig. 4.12) in order to compare the energy of the NBE peaks and appearance of different defect peaks. CL spectra are plotted separately for each sample, due to different conditions employed (accelerating voltages, current and chamber pressure).

a) sample 171110A
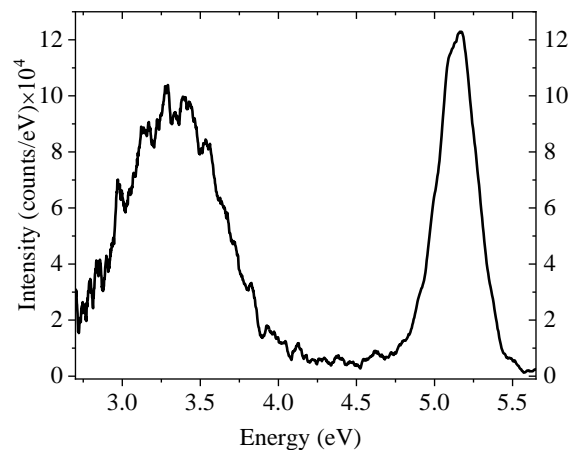
b) sample 171121B
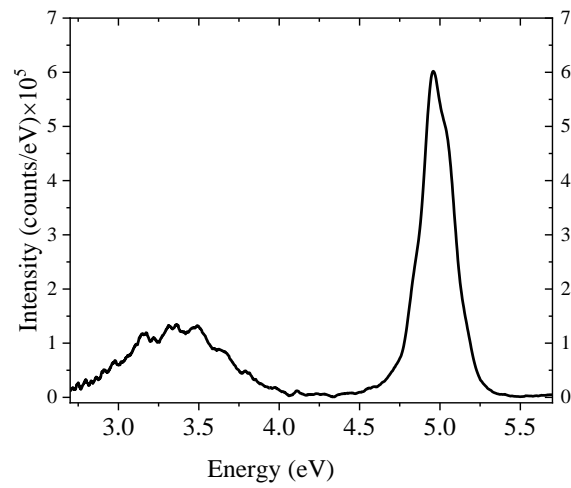
c) sample 171110B
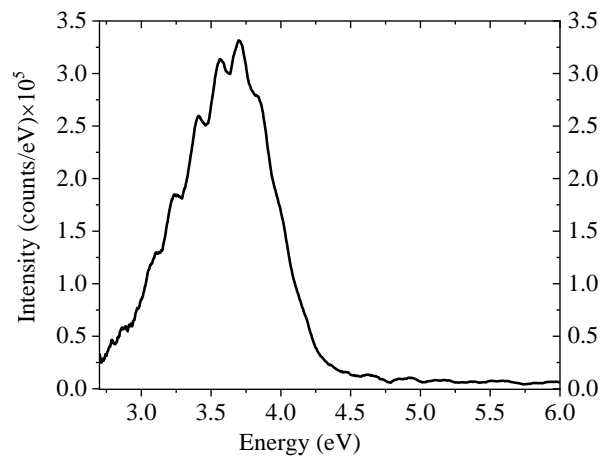
d) sample AGBK850
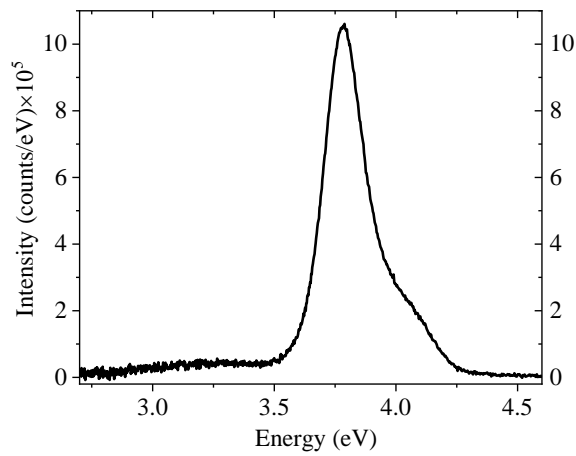
e) sample AGC850
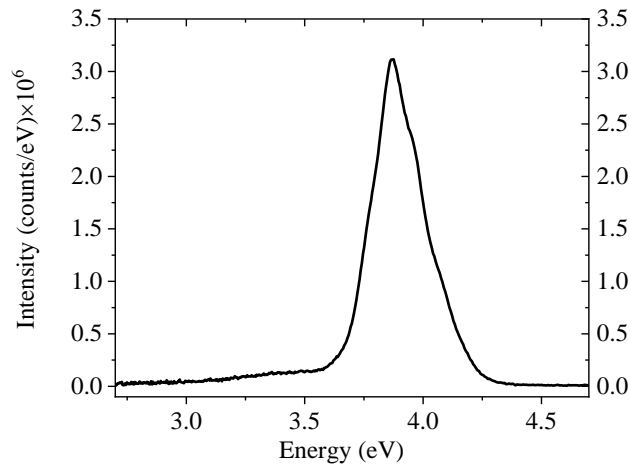
Figure 4.12: Comparison of mean CL spectra between MBE AlGaN on AlN (171110A, 171110B, 171121B and AGBK850) and MBE AlGaN/AlN on sapphire (AGC850) sample.

The mean CL spectrum of sample 171110A (Fig. 4.12a) reveals two emission peaks: a peak at 5.2 eV corresponding to NBE emission and a broad defect peak at 3.3 eV. The defect peak at 3.3 eV corresponds to $(V_{III}–O_N)^{2-}$ complex [10]. The same type of emission peaks are present in sample 171121B (Fig. 4.12b), with an NBE emission peak at 5.0 eV and a defect emission appearing at 3.3 eV. For sample 171121B the intensity of the NBE peak is significantly higher compared to defect peak intensity, while for sample 171110A difference between NBE and defect peak intensity is significantly reduced. Both of these samples are grown with same level of Si doping, with sample 171121B having lower AlN content (80 vs 84 at%). The FWHM of the NBE peak is smaller for sample 171121B (225 meV) compared to sample 171110A (287 meV).

The mean CL spectrum of sample 171110B (Fig. 4.12c) reveals only one broad defect peak at 3.6 eV. This defect peak corresponds to the same type of defect emission observed in samples 171110A and 171121B. In this sample the NBE emission peak (which should appear close to 6 eV) is absent. It is possible that the NBE is present but that the spectral response of employed CL system is weaker in this wavelength range [28]. With decrease in AlN content from 97 to 80 AlN at% the intensity of the NBE peak also increases, but at highest AlN

at% as in the case of sample 171110B (97 at%) NBE emission is possibly absent or undetected. The change in the relative emission intensities of the defect peak can be explained with a change in the formation energy (Fig. 2.10). The reduced formation energy from GaN to AlN of the group-III vacancy explains the increase in luminescence intensity of the defect peaks with increasing AlN concentration. It is evident that for the samples with same Si concentration (171121B, 171110A and 17110B) the observed $(V_{III}-O_N)^{2-}$ complex has the lowest formation energy at 97% AlN. The formation energy of the defect decreases and the intensity of the defect emission increases with increase in AlN at%.

The mean CL spectrum of sample AGBK850 (Fig. 4.12d) shows only one defect peak at 3.8 eV associated with a different type of defect emission, namely the $(V_{III}-2O_N)^{1-}$ complex [10], [17]. In this sample, defect luminescence is of higher intensity and smaller FWHM compared to defect luminescence originating from the $(V_{III}-O_N)^{2-}$ complex. It is expected that the low dislocation density of the AlN translates into lower density of non-radiative recombination centres in the epitaxial material [29], which is not the case for this sample. This sample differs from other characterised MBE samples in the group; having the lowest AlN at% (62% compared to 80, 84 and 97%) and lowest Si content ($5-7\times10^{18}$ compared to 10^{19}). Also, it is thinner compared to other samples (100 vs 150 nm). The changes in AlN content, Si doping level and thickness of the sample resulted in only defect emission from this sample.

As observed earlier for sample AGBK850, the mean spectrum of sample AGC850 (Fig. 4.12e) also shows only defect emission peak at 3.9 eV assigned to $(V_{III}-2O_N)^{1-}$ complex [12], [14]. In this sample defect luminescence is of higher intensity (3×10^6 vs 10^5) compared to sample AGBK850 and peaks have similar FWHM values (250 vs 210 meV). This sample differs from other samples in the group also by having lower AlN content (65%), lower Si content ($5-7\times10^{18}$ compared to 10^{19}) and thickness (100 vs 150 nm). The formation energy of the $(V_{III}-2O_N)^{1-}$ complex is lower in higher AlN content sample (67%) compared to sample AGBK850 (62%).

Since lower AlN content MBE samples are showing different defect luminescence ($(V_{III}-2O_N)^{1-}$ complex) compared to higher AlN content MBE

samples ((V_{III}–O_N)$^{2-}$ complex) it is possible to conclude that the formation energy of the (V_{III}–$2O_N$)$^{1-}$ complex is lower in lower AlN content samples opposite to the findings for the (V_{III}–O_N)$^{2-}$ complex) whose formation energy is lower in higher AlN content MBE samples. Defect luminescence associated with triply charged cation vacancy (V_{III})$^{3-}$ is not observed for MBE set of samples.

The disappearance of the NBE emission can be explained by inadequate crystallographic quality of the material, possibly due to sub-optimal growth parameters. It is possible to compare MOCVD sample USC902 grown on the same template as the MBE sample AGC850. Insertion of an AlN buffer layer in sample USC902 (compared to MOCVD samples A, B1 and B2) resulted in better compositional homogeneity but the NBE intensity was reduced. Because sample USC902 exhibits a reduction of the NBE intensity and not an increase as expected, it is indication of the problem regarding the AlN buffer layer. Since samples USC902 and AGC850 are grown on the same template, probably the same problem is occurring again in sample AGC850. The quality of the AlN buffer layer will depend on the grain sizes, that are proportional to the time available for nucleation of the AlN nanoislands. Enhancement in grain size of the AlN nucleation layers plays a significant role in lowering the densities of both screw and edge TDs [30]. The most effective way to reduce the dislocation density in AlN buffer layers is to achieve quick island nucleation and a fast transition to two-dimensional growth mode [31]. However, by growing an AlN epilayer directly at high temperature, without a LT-BL (Low temperature AlN buffer layer) the formation of inversion domains from Al-polar to N-polar domains can be induced [32]. Also, without the sapphire substrate pre-treatment with trimethylaluminum (TMAl), the AlN films nucleated will result in rough AlN film surfaces. Pre-treatment can reduce mixed crystallographic Al- (N-) polarity [33]. Overall, for successful growth of AlN template layer the key factors are optimum thickness and an optimum growth temperature. It is possible to conclude that deficiencies in the AlN buffer layer for samples USC902 and AGC850 have potentially caused disappearance of the NBE emission completely.

Extracted spectra from various regions for samples 171110A and 171121B are depicted in Fig. 4.13a. Relation of the NBE emission energy regards to the AlN content of the alloy is depicted in Fig. 4.13b.
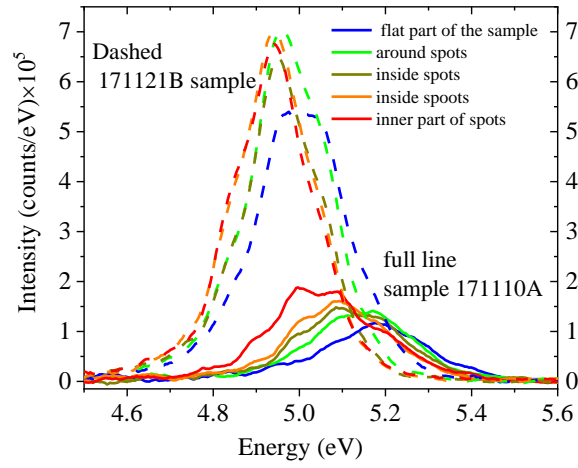
a)
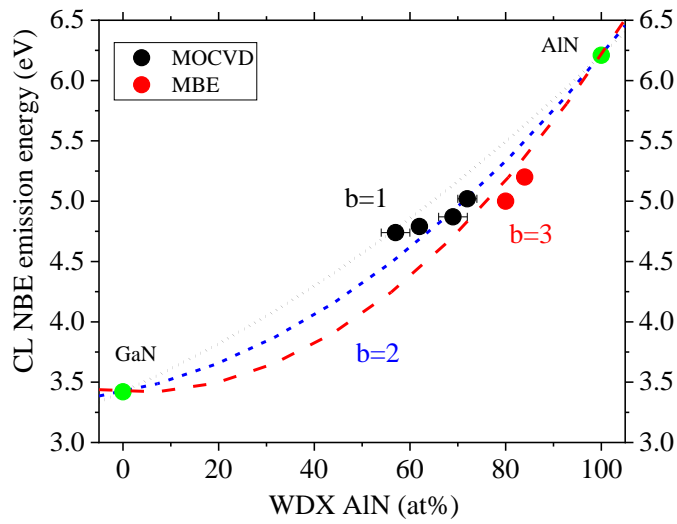
b)
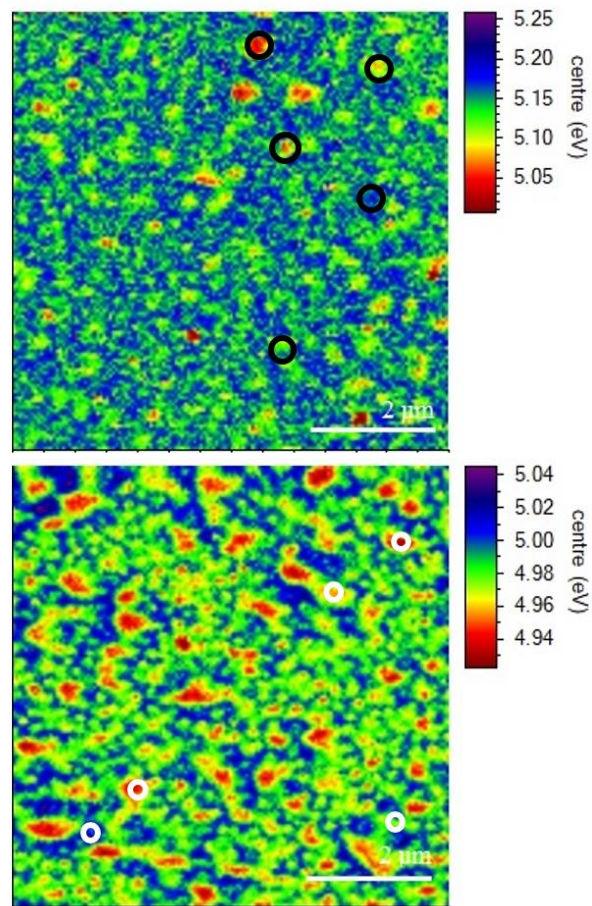
c)

Figure 4.13: a) Comparison of extracted CL point spectra from sample 171121B and 171110A, spectra averaged from 4-pixel diameter b) evolution of NBE CL emission energy for the MOCVD (black points) and MBE (red points) samples, AlN% measured by WDX c) the circled parts in the maps represent the areas from which spectra are averaged for sample 171110A (top) and 171121B (bottom).

Values for MBE samples are now plotted together with MOCVD ones (Fig. 4.14b). The overall behaviour does not look quadratic anymore, as was the case in the Fig. 4.8 just for the MOCVD samples. Plot depicts how the near band edge peak energy blue-shifts with increasing AlN% from 4.74 eV (57% AlN) to 5.2 eV (84% AlN).

Similar variation in peaks intensities and energies are present in both samples, but not as prominent as in case of the MOCVD samples (Fig. 4.9c). Intensity of the NBE emission is lower for higher AlN content sample 171110A, but it has to be evident that in this case a higher voltage is employed for the collection of

140

CL data. Within this set of samples, optimum growing conditions are achieved for the middle AlN at% sample 171121B, even though defect emission is still present, the NBE intensity was highest within the set.

4.4 Texture comparison between MOCVD and MBE samples

From the acquired peak energy CL maps of MOCVD and MBE samples it is possible to confirm large differences between samples grown using different techniques, in terms of different final sample texture. To better emphasise the observed difference, line profiles are extracted from the maps and compared.

a)   b)
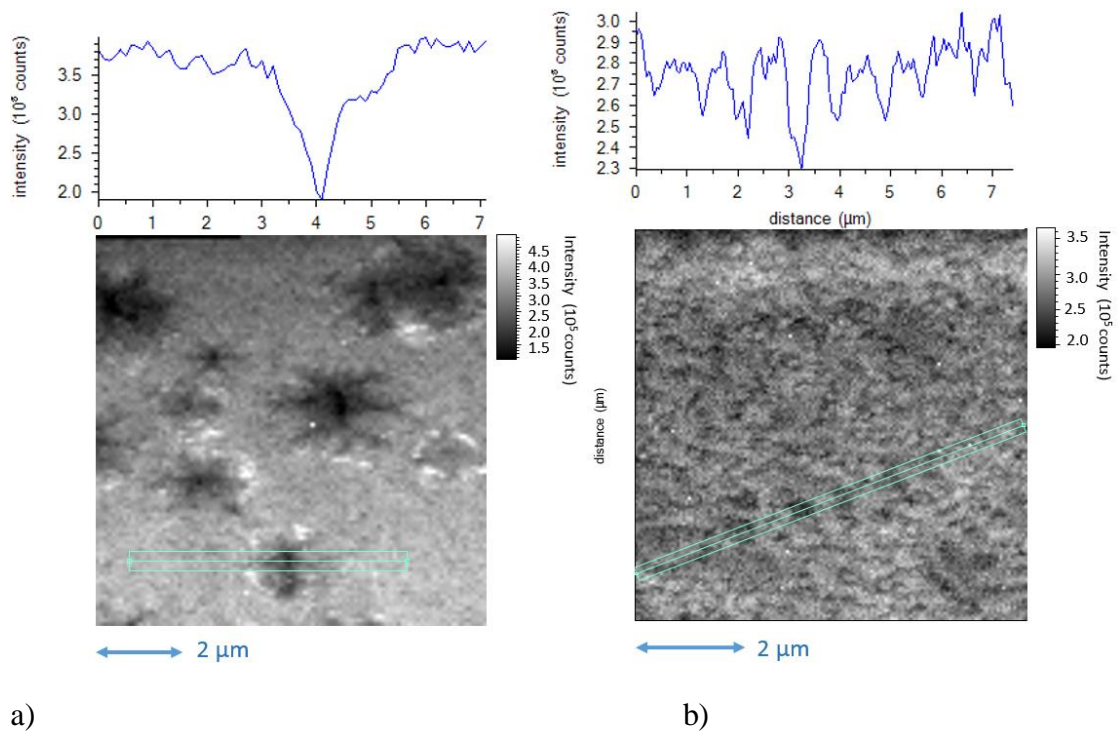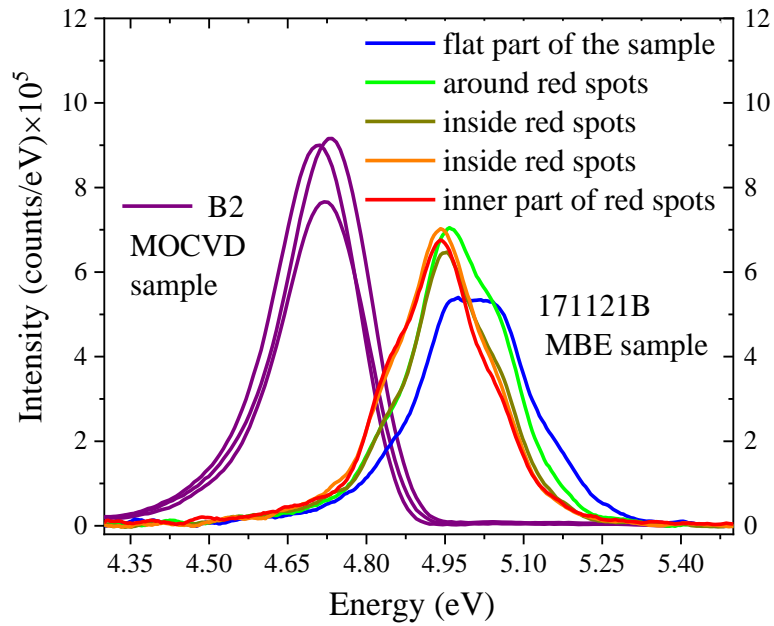
c)

Figure 4.14: Profiles extracted from CL intensity maps of: a) MOCVD sample B2 b) MBE sample 171121B c) comparison of extracted CL point spectra from various regions of samples B2 and 171121B

The profiles extracted from the maps reveal differences in the textures owing to the different growth mode employed. From the spectra extracted from various flat parts of both samples (Fig. 4.14c) it is noticeable how the spectra of the MBE sample still show variation in NBE energy, while for the MOCVD sample there is no significant variation. As showed in the profiles (Fig. 4.14a and b), MOCVD sample contain smooth regions with occurrence of 3D features, and in the case of MBE samples there is a dramatic change in surface texture. The surfaces are featureless but micro-texture is always present.

4.5 WDX mapping

In previous sections different textures between MOCVD and MBE samples were confirmed. Also, it was discussed how in the peak energy maps of MBE samples emission from spherical "spots" is red shifted with respect to the surrounding areas. WDX mapping is therefore employed to estimate the

difference in GaN incorporation between the "spots" which are responsible for the observed texture in the MBE samples.
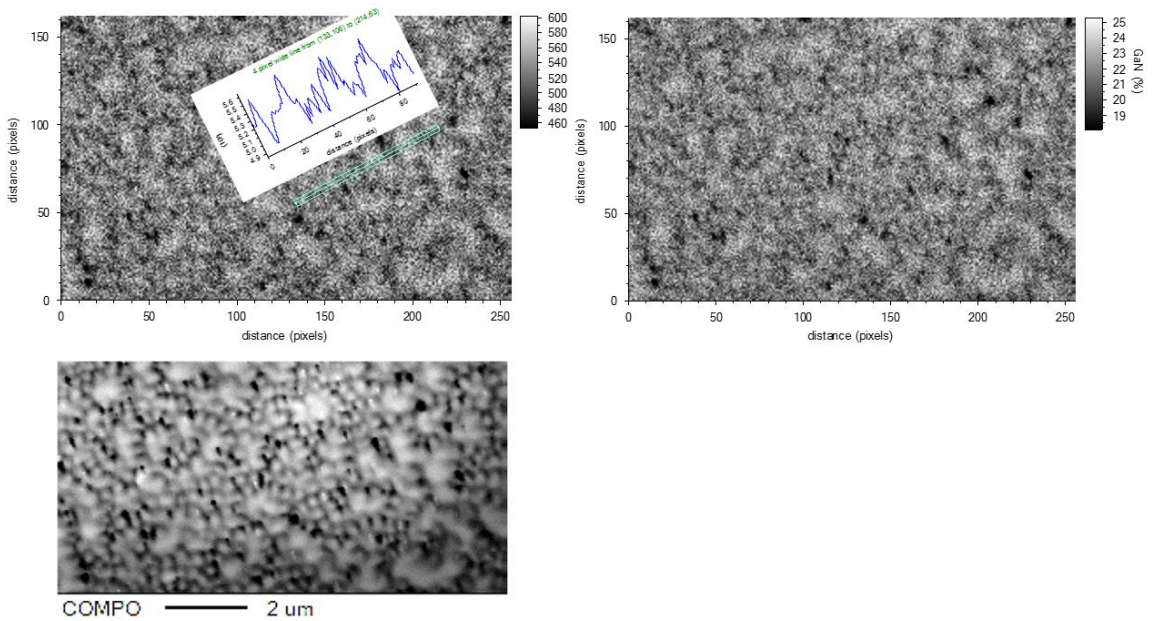
Figure 4.15: WDX map of the Ga L_α X-ray intensity for the MBE sample 171121B with the extracted line scan (upper left), GaN content map (at%) obtained from a WDX map of the Ga L_α X-ray intensity (right) and backscattered electron image (BSE) of the measured area (lower left, compo).

The high resolution X-ray intensity WDX map shows the spatial distribution of elements in a sample and element maps are extremely useful for displaying element distributions in textural context, particularly for showing compositional zonation. The experimental data show a higher (lower) intensity of Ga L_α (Al K_α) X-within the "spots" region, the same behaviour is observed in the compositional BSE image. Comparing the BSE image with maps allows topographic effects to be ruled out as the dominant source of contrast, in which an increased backscatter signal would result in less X-ray counts. Seeing bright spots in both therefore unambiguously points to higher mass regions in a way that either map alone would not. Despite the challenging signal-to-noise ratio, inherent to X-ray counting statistics, clear variations in the Ga distribution on a sub-µm length scale are visible. The measured GaN % composition (from WDX quantitative point measurements) has been assigned to the average intensity value in order to get the estimate for the quantitative map. WDX maps are only

acquired for the Ga L_α X-ray intensity because Ga is only present in the top MBE layer and not in the substrate layer (AlN), while Al is present in both layers. Variation in GaN incorporation is confirmed across the sample, with formation of nanometre sized islands rich in GaN, as demonstrated in the converted WDX quantitative map (Fig. 4.15, right). The GaN content was quantified giving an estimate of 25% GaN coming from the 20 nm-sized spot region and the observed difference between spots and region around them is about 3% GaN. This value is similar to the 2 at % GaN difference estimated from the NBE CL map.

4.6 Different characteristics of MOCVD and MBE devices

The experimental data in this section (Fig. 4.11) have been provided from Ohio State University (Prof. Siddharth Rajan) [34, 35]. Aluminum-rich AlGaN can be used instead of conventional n-GaN channel and it is a promising candidate as a channel material for high power mm-wave transistors due to its large bandgap and high breakdown field. However, it is challenging to make good ohmic contacts to AlGaN with high Al compositions due to its low electron affinity. Other challenges are related to material quality (defects and mobility) [36]. In this example characteristics of a metal-insulator-semiconductor field effect transistor (MISFET) device are demonstrated. Characteristics of devices consisting of AlGaN MBE or MOCVD layers are compared in order to demonstrate how material properties explored in this chapter will affect final device performance.
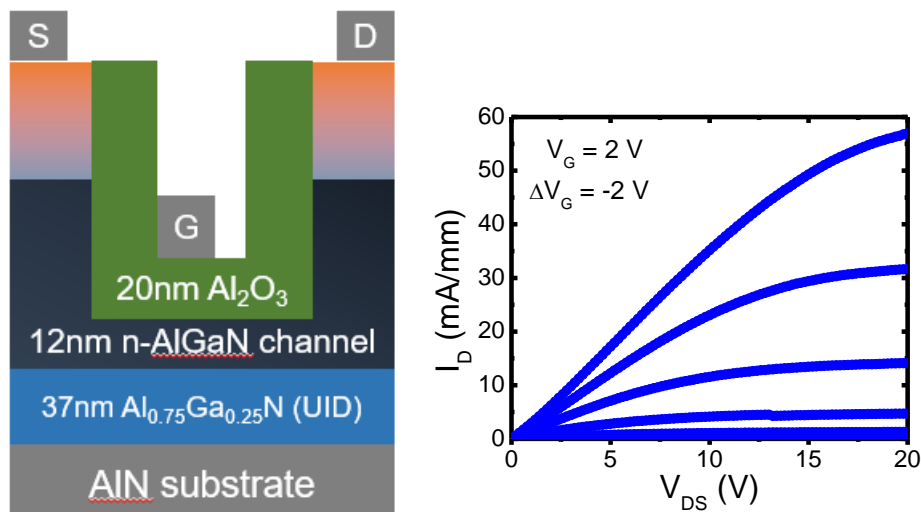
a)
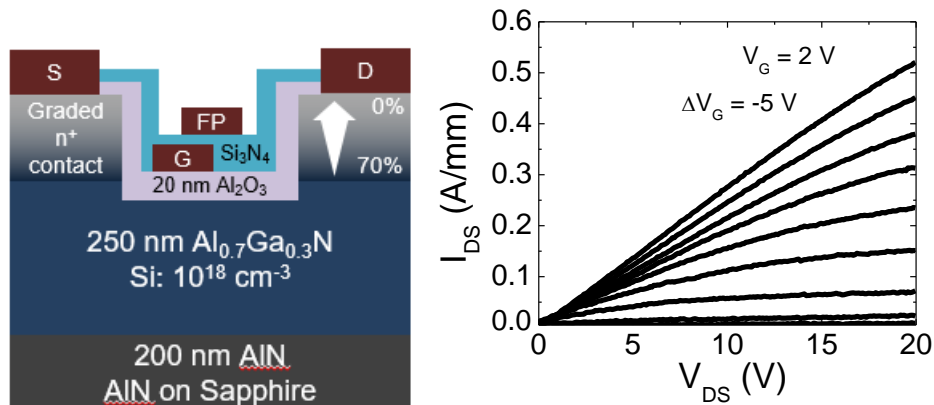
b)

Figure 4.16: a) Device structure schematic and measured family output current-voltage characteristics (I–V) of; a) MBE $Al_{0.75}Ga_{0.25}N$ MISFET b) MOCVD $Al_{0.70}Ga_{0.30}N$ MISFET

Fig.4.16 shows the measured family output I–V characteristics for MBE and MOCVD devices. In the case of the MBE device (Fig. 4.16a) a maximum drain current, I_{DS_MAX}, of ~60 mA/mm at V_{GS} = 2 V (voltage from gate to source) is achievable. For the MOCVD device (Fig. 4.16b) a maximum drain current, I_{DS_MAX}, of ~0.5A/mm at V_{GS} = 2 V is obtained. From the obtained data it is evident how significantly higher current density is achievable with MOCVD device compared to the MBE device. Fig. 4.16 depicts how MBE and MOCVD layers with similar compositions have very different characteristics. The main difference is due to the lower electron mobility in MBE samples (< 20 cm^2/Vs versus ~ 80 cm^2/Vs for MOCVD sample. This leads to almost 10× difference in the transistor current density. The relatively low electron mobility of MESFET MBE device will hinder its performance. In contrast, MOCVD grown high Al-composition AlGaN channels have much higher mobility due to superior compositional uniformity. Since impurity scattering cannot account for the lower mobility in MBE samples, other reasons are responsible for the observed reduction, such as the alloy fluctuation, discussed in more details inside this chapter. Consequently, the higher mobility observed in MOCVD samples leads to the better device performance.

4.7 Conclusion and comparison between MOCVD and MBE samples

The characterization of different sets of MOCVD and MBE samples showed that the type of growth method and choice of the substrate has a great influence on the surface morphology and luminescence homogeneity of the AlGaN layer.

For the MOCVD AlGaN-on-sapphire samples, the highest intensity of NBE emission is observed for sample B2 (sample with highest level of Si doping and lowest AlN content). The CL energy map of the sample B2 reveals the variations in the NBE intensity and energy due to occurrence of hexagonal 3D features, as well as the appearance of an additional deep impurity peak associated with a screw dislocation coming from the middle of the hexagonal feature. WDX and CL mapping of the sample B2 confirmed lower emission energy coming from middle of the hexagon area due to the lower AlN content and thus chemical inhomogeneity of the sample. Sample B1, with highest AlN at%, shows also emission from the $(V_{III})^{3-}$ defect, that is of higher intensity than NBE emission. However, the NBE energy emission is more homogeneous due to lack of 3D features. Sample A, with similar AlN content shows similar emission characteristic to sample B1, except in the appearance of few hexagons on the surface. With the increase of AlN at% in the MOCVD set, the intensity of the NBE emission reduces, but chemical homogeneity improves.

Addition of AlN buffer layer for MOCVD sample (USC902) results in only NBE emission but with reduced intensity compared to samples grown without buffer layer, which was not as expected. FWHM of the NBE peak was smallest within the MOCVD set (145 meV). Sample morphology is improved compared to samples B2 and A1 (lowest and highest AlN at%) but is not better compared to middle AlN at% sample B1. In this case optimum growing condition for the AlN buffer layer were not achieved.

MBE AlGaN/AlN on sapphire sample only shows defect emission peak associated with $(V_{III}-2O_N)^{1-}$ complex. NBE emission is absent probably due to same problem with growth of AlN buffer layer. CL mapping revealed uniform defect emission across the sample.

The last studied set of samples consisted of MBE samples grown on native AlN substrate. Samples of middle AlN at% within the set, 171110A (84%) and 171121B (80%) exhibit NBE and $(V_{III}–O_N)^{2-}$ defect emission. In sample 171121B optimum growing conditions are achieved because the intensity of the NBE peak is significantly higher than the defect peak intensity, while for the sample 171110A the NBE emission was only slightly higher than the defect emission. Samples with highest and lowest AlN at% are exhibiting only defect emissions with 171110B (97%) showing $(V_{III}–O_N)^{2-}$ emission and sample AGBK850 (59%) $(V_{III}–2O_N)^{1-}$ emission. The formation energy of the $(V_{III}–2ON)^{1-}$ complex is lower in lower AlN content samples opposite to the findings for $((V_{III}–ON)^{2-}$ complex) whose formation energy is lower in higher AlN content MBE samples. Defect luminescence associated with triply charged cation vacancy $(V_{III})^{3-}$ is not observed in MBE set of samples.

Overall, chemical homogeneity of MBE samples is improved compared to MOCVD samples. It is possible to conclude that the same type of impurity emission is present in both MOCVD and MBE samples. Even though, all samples are showing variation in energy emission across nano-size regions (~20 nm), with more pronounced energy emission differences in sample 171121B. The different textures of the MOCVD and MBE samples are confirmed, with compositional inhomogeneity of the MBE samples on sub μm level. The MBE emission intensity is also lower compared to MOCVD samples probably due to vast majority of threading dislocations occurring at the boundaries of the nano-size domains (~20 nm). Alloy fluctuations in MBE samples will affect the sample mobility and have negative effects on the device performance, such as transistor current density.

Ultimately, the ability to achieve defect free and atomically smooth surfaces will be made possible by adjusting the growth process according to results of analysis of multiple sets of samples grown at different conditions.

Bibliography

1. Kaplar, R., et al., *Review—Ultra-Wide-Bandgap AlGaN Power Electronic Devices.* ECS Journal of Solid State Science and Technology, 2017. **6**: p. Q3061-Q3066.
2. Novikov, S.V., et al., *Growth of free-standing wurtzite AlGaN by MBE using a highly efficient RF plasma source.* 2016. **34**(2): p. 02L102.
3. Li, D., et al., *AlGaN photonics: Recent advances in materials and ultraviolet devices.* Advances in Optics and Photonics, 2018. **10**: p. 43.
4. Lee, S.R., et al., *In situ measurements of the critical thickness for strain relaxation in AlGaN/GaN heterostructures.* Applied Physics Letters, 2004. **85**(25): p. 6164-6166.
5. Tsao, J.Y., et al., *Ultrawide-Bandgap Semiconductors: Research Opportunities and Challenges.* Advanced Electronic Materials, 2018. **4**(1): p. 1600501.
6. Tasi, C.-T., et al., *Structural and Stress Properties of AlGaN Epilayers Grown on AlN-Nanopatterned Sapphire Templates by Hydride Vapor Phase Epitaxy.* Nanomaterials (Basel, Switzerland), 2018. **8**(9): p. 704.
7. Dalmau, R., et al., *High Quality AlN Single Crystal Substrates for AlGaN-Based Devices.* 2018.
8. Elsass, C.R., et al., *Effects of growth conditions on the incorporation of oxygen in AlGaN layers grown by plasma assisted molecular beam epitaxy.* Applied Physics Letters, 2000. **77**(20): p. 3167-3169.
9. McCluskey, M.D., et al., *Metastability of Oxygen Donors in AlGaN.* Physical Review Letters, 1998. **80**(18): p. 4008-4011.
10. Nam, K.B., et al., *Deep impurity transitions involving cation vacancies and complexes in AlGaN alloys.* Applied Physics Letters, 2005. **86**(22): p. 222108.
11. Yan, Q., et al., *Origins of optical absorption and emission lines in AlN.* Applied Physics Letters, 2014. **105**(11): p. 111104.
12. Huang, C.-Y., et al., *Suppression of "volcano" morphology and parasitic defect luminescence in AlGaN-based deep-UV light-emitting diode epitaxy.* Results in Physics, 2019. **13**: p. 102285.
13. Hevia, D., F. Viñes, and F. Illas, *Microscopic origin of n-type behavior in Si-doped AlN.* Physical Review B, 2013. **88**.
14. Dinh, D.V., P. Pampili, and P.J. Parbrook, *Silicon doping of semipolar (112¯2)AlxGa1−xN(0.50≤x≤0.55).* Journal of Crystal Growth, 2016. **451**: p. 181-187.
15. Dominique, D., et al., *CASINO V2.42—A Fast and Easy-to-use Modeling Tool for Scanning Electron Microscopy and Microanalysis Users.* Scanning, 2007. **29**(3): p. 92-101.
16. Abd Rahman, M.N., et al., *Standard pressure deposition of crack-free AlN buffer layer grown on c-plane sapphire by PALE technique via MOCVD.* Superlattices and Microstructures, 2018. **120**: p. 319-326.
17. Jayasakthi, M., et al., *Influence of AlN thickness on AlGaN epilayer grown by MOCVD.* Superlattices and Microstructures, 2016. **98**: p. 515-521.
18. Kusch, G., et al., *Spatial clustering of defect luminescence centers in Si-doped low resistivity Al0.82Ga0.18N.* Applied Physics Letters, 2015. **107**(7): p. 072103.

19. Huang, C.-Y., et al., *The origin and mitigation of volcano-like morphologies in micron-thick AlGaN/AlN heteroepitaxy.* Applied Physics Letters, 2017. **111**(7): p. 072110.

20. Kusch, G., et al., *Spatial clustering of defect luminescence centers in Si-doped low resistivity Al0.82Ga0.18N.* 2015.

21. Li, X.-H., et al., *Growth of high-quality AlN layers on sapphire substrates at relatively low temperatures by metalorganic chemical vapor deposition.* 2015. **252**(5): p. 1089-1095.

22. Zhao, D.G., et al., *Surface morphology of AlN buffer layer and its effect on GaN growthby metalorganic chemical vapor deposition.* Applied Physics Letters, 2004. **85**(9): p. 1499-1501.

23. Yun, F., et al., *Energy band bowing parameter in AlxGa1−xN alloys.* Journal of Applied Physics, 2002. **92**(8): p. 4837-4839.

24. Belabbas, I., et al., *Local electronic structure of threading screw dislocation in wurtzite GaN.* Computational Materials Science, 2006. **37**(3): p. 410-416.

25. Jmerik, V., D. Nechaev, and S. Ivanov, *Kinetics of Metal-Rich PA Molecular Beam Epitaxy of AlGaN Heterostructures for Mid-UV Photonics.* 2018. p. 135-179.

26. Moustakas, T.D., *Ultraviolet optoelectronic devices based on AlGaN alloys grown by molecular beam epitaxy.* MRS Communications, 2016. **6**(3): p. 247-269.

27. Moustakas, T.D., *The role of extended defects on the performance of optoelectronic devices in nitride semiconductors.* physica status solidi (a), 2013. **210**(1): p. 169-174.

28. Edwards, P.R. and R.W. Martin, *Cathodoluminescence nano-characterization of semiconductors.* 2011.

29. Dalmau, R., et al., *Growth and Characterization of AlN and AlGaN Epitaxial Films on AlN Single Crystal Substrates.* 2010.

30. Nechaev, D.V., et al., *Control of threading dislocation density at the initial growth stage of AlN on c-sapphire in plasma-assisted MBE.* Journal of Crystal Growth, 2013. **378**: p. 319-322.

31. Petrov, S.I., et al., *High temperature ammonia MBE—Real way to improve crystal quality of nitride heterostructures.* Journal of Crystal Growth, 2019. **514**: p. 40-44.

32. Matta, S., et al., *Properties of AlN layers grown on c-sapphire substrate using ammonia assisted MBE.* Journal of Crystal Growth, 2018. **499**: p. 40-46.

33. Sun, H., et al., *Structural properties, crystal quality and growth modes of MOCVD-grown AlN with TMAl pretreatment of sapphire substrate.* Journal of Physics D: Applied Physics, 2017. **50**(39): p. 395101.

34. Bajaj, S., et al., *AlGaN channel field effect transistors with graded heterostructure ohmic contacts.* Appl. Phys. Lett., 2016. **109**(13).

35. Razzak, T., et al., *Design of compositionally graded contact layers for MOCVD grown high Al-content AlGaN transistors.* Appl. Phys. Lett., 2019. **115**(4).

36. Xue, H., et al., *Al0.75Ga0.25N/Al0.6Ga0.4N heterojunction field effect transistor with fT of 40 GHz.* Applied Physics Express, 2019. **12**(6): p. 066502.

Chapter 5

5. Measurement of Si at low concentration

5.1 Introduction to trace element measurements

The main advantage of wavelength-dispersive spectrometer (WDX) over scanning electron microscope-energy-dispersive spectrometer system (SEM-EDX) is the high energy resolution that enables separation of closely spaced lines which would overlap in EDX system. Owing to this it is possible to measure trace and light elements with a WDX system [1, 2]. The EPMA instrument equipped with WDX, is routinely used for quantification of major (concentration>1000 ppm) and minor (100–1000 ppm) elements. Measurement of trace elements (below 100 ppm and down to 10 ppm) is challenging due to multiple factors such as the precision and accuracy of the background measurement [3]. There is no rigorous definition of a trace element, but they can be also defined as those whose concentrations are of a similar order to the detection limit [4]. With the development of EPMA equipment, it has become easier to obtain trace element data due to improvements in the instrumentation, including the use of spectrometers with high X-ray collection efficiencies, high brightness (FEG) electron sources, and overall improved stability, not to forget advances in the software necessary for the acquisition and data analysis. Another necessary technological advancement was improved stability of spectrometers and the electron column when operated at high probe current [5].

Over the years, many research groups have addressed the trace element capabilities of the WDX technique. Some early examples include analysis of Ge distributions in iron meteorites [6], transition elements in ferro-magnesian silicate minerals [7] trace elements in quartz [8] trace elements in glass [9], trace element analysis applied to geochronology [10]. More recent works focus on specific situations or on refinements of the technique and conditions for trace analysis, such as work from John J. Donovan et al. [11] Stephen J. B. Reed et al.[12], M. J. Jercinovic et.al. [13], Julien M. Allaz et al. [14], J.Fournelle et al. [15], V.G. Batanova et al. [5], P. Carpenter et al. [16], B.Buse at al. [17] and

others. Donovan et al. 2011 [8] developed optimum measurement practises for WDX trace analysis which will be applied in the analysis of Si doping.

The aim of this chapter was to explore the use of WDX in a commercial EPMA (JEOL JXA-8530F) to simultaneously measure the concentration of major (alloy) and minor (dopant) elements within semiconductor epilayers at specific points on the sample surface. A new approach is demonstrated to correct for the overestimation in measured Si donor concentration caused by inherent contamination of the sample surfaces with additional Si. The capability of the WDX technique for measuring dopants within semiconductor epilayers has been reported by Deatcher et al. and Kusch et al. [18, 19]. The latter compared WDX data for Si concentration ranges 40–350 ppm ($3 \times 10^{18} - 2.8 \times 10^{19}$ cm^{-3}) in Al$_x$Ga$_{1-x}$N with commercially performed D-SIMS on some of the samples in the study. Both, SIMS and WDX measurement methods showed the same general trend: a linear increase in the Si concentration with increasing SiH$_4$/III (silane to group-III ratio) but the Si concentration measured by WDX was higher by a factor of approximately 2 compared to D-SIMS. The reason for the discrepancy between the different types of measurement was not clarified at the time [19] (Kusch et al., 2017). However, the reports in Deatcher et al., 2006 [18] and Robin et al., 2016 [2] show that it is possible to use X-ray microanalysis to measure doping levels in semiconductor epilayers, with Robin et al. using energy dispersive X-ray (EDX) to address quantitation of dopants. The report of Deatcher et al., 2006 shows that Mg measurement in GaN gives very good agreement between WDX and D-SIMS. The question of why WDX measurement appears to over-estimate values for the Si doping is the subject of the investigation presented in this chapter.

In order to select optimal analytical conditions, knowledge of the behaviour of primary beam electrons, the sample, and the X-rays generated by beam–specimen interactions are required. The analyst has to be aware that changing the beam current and energy will have major consequences for the precision, accuracy, and spatial resolution of analysis [20]. A very important attribute in the trace analysis is the background measurement and it is essential to always keep in mind that background shape and interferences will affect inaccuracies [13].

WDX analysis has several advantages over other analytical methods such as dynamic secondary ion mass spectrometry (D-SIMS), laser ablation inductively coupled plasma mass spectrometry (LA-ICP-MS) and micro particle-induced X-ray emission (μ-PIXE). These include its high lateral spatial resolution (sub μm), non-destructive nature and that it usually doesn't require extensive standards due to the existence of well-developed matrix correction procedures [21]. In addition, the EPMA allows acquisition of other analytical signals simultaneously with the high-resolution composition mapping such as: cathodoluminescence (CL), electron beam-induced current (EBIC) and electron channelling contrast imaging (ECCI) signals [22-28]. Some limitations of the WDX technique are related to the fact that depth resolution is a function of the electron accelerating voltage, which must be high enough to excite all the relevant X-ray lines, preferably with an overvoltage ratio of at least 2 to ensure accurate analysis, particularly when approaching detection limits. These limitations also introduce constraints on the minimum sample thickness [29] and depth profiling, where SIMS performs strongly including for nitride semiconductor structures [30-33]. Two of these works employed time-of-flight SIMS (TOF-SIMS) which has a number of advantages over D-SIMS, including dual source depth profiling where the two ion beams have been optimized for their respective tasks, although work is needed to achieve the same detection limit for dopants [34].

There is still room for improvement regarding the sensitivity of EPMA, which is not adequate for concentration ranges below 10 ppm level [5]. When trying to find the optimal conditions for trace element analysis regarding accelerating voltage, beam current, and counting time certain things should be taken into account as: the size, composition and stability of the sample, the number of trace and minor elements to be analysed and the required detection limits and precision [5].

5.2 Challenges for trace element analysis

With the instrumentation improvement that has enabled high spatial resolution the detection limits have been pushed to lower levels, such that a new realm has been opened for the EPMA or a new challenge, the trace element analysis.

The trace element sensitivity is limited by intrinsic random variation in the X-ray continuum background and weak signals at low concentrations [11]. Also, the problem with trace analysis is that the accuracy of EPMA decreases at low concentrations, due to magnification of most sources of random and systematic errors [13]. Several factors can act as sources of errors, such as: spectral background subtraction, beam damage, secondary fluorescence from phase boundaries, carbon contamination, and to some extent instrumental instability. Fluorescence effects can result in falsely high concentrations and totals. However, in most cases, absorption effects outweigh the fluorescence effects. The background subtraction may be disturbed by the background curvature or by the interference peaks from other elements [35]. Like in other trace analytical techniques, care must be taken to carefully interpolate from off-peak intensity measurements to obtain the background intensity [11].

When using a low kV analysis different new challenges are introduced: because the electrons no longer penetrate deeply into the material and the state of the sample surface becomes more critical. The smoothness of the surface, cleanliness, and the conductive coating will all have significant effects on the analysis [36]. The possibility of the formation of a native oxide layer on the surface of samples and/or standards should be tested as well as the chance of surface contamination. Depending on the sample nature it is possible to have signal drift due to charging and sample destruction during signal acquisition [37].

Trace element analysis is also time consuming process since counting times can be of an order of magnitude greater than those used for major elements in order to achieve statistical confidence in the collected data.

5.3 Quantitative analysis procedure

The general procedure for quantitative analysis is the same for major and trace elements. The elemental concentration is calculated using the ratio of the background-corrected peak intensity for the sample to that obtained from a standard.

The JXA-8530F machine uses ZAF correction method as a standard option. The ZAF correction calculation method consists of atomic number correction (Philibert-Tixier method [38]), absorption correction (Philibert method [39]), and fluorescent excitation correction (Reed method [40]).

The ZAF correction method determines the weight concentration C_A of an element A according to the following equation:

$$C_A^{UNK} = K_A^{UNK} \times Z \times A \times F=$$
$$K_A^{UNK} \times \frac{R_A^{STD} \times P_A^{STD}}{R_A^{UNK} \times P_A^{UNK}} \times \frac{f_A^{STD}(\chi_A)}{f_A^{UNK}(\chi_A)} \times \frac{1}{1 + \frac{I_{A(f)}}{I_A(d)}} \qquad (5.1)$$

Where $K_A^{UNK} = \frac{I_A^{UNK}}{I_A^{STD}}$ and I_A are the X-ray intensities (in cps) per unit current of element A after dead time correction and background correction. *UNK* indicates the unknown sample, *STD* standard sample, *Z, A*, and *F* are atomic number correction coefficient, absorption correction coefficient and fluorescence correction coefficient, respectively. Atomic number correction (*Z*) deals with differences in the degree of X-ray absorption between an unknown sample and a standard sample. It accounts for the fact that heavier elements produce and absorb more X-rays than lighter elements. This correction entails mass absorption coefficient, incident electron energy and X-ray take off angle. The absorption correction (*A*), is required to account for absorption of primary, characteristic X-rays that are being measured on their way out of a sample. Without it, the intensities of certain X-rays will be apparently reduced, giving anomalously low concentration results. Fluorescence correction (*F*) needs to be considered if the characteristic X-rays from an element B are at the high energy side of the absorption edge of element of interest A. In this case, the X-rays from element B may excite element A. Same principle applies to fluorescent excitation by continuous X-ray, but effect is usually negligible. The

fluorescence effects cause the measured X-ray intensities to be higher than expected, and result in falsely high concentrations and totals. In most cases, absorption effects outweigh fluorescence effects [41].

The X-ray intensity I_{net}, due to background correction, is obtained from the equation:

$$I_{net} = I_{peak} - \frac{I_{PBH}\overline{PB_L} + I_{PBL}\overline{PB_H}}{\overline{PB_L} + \overline{PB_H}}$$

(5.2)

Where I_{peak} is the X-ray intensity at peak position, I_{PBL} and I_{PBH} are the X-ray intensities of the background on low-angle side and high-angle side. $\overline{PB_L}$ and $\overline{PB_H}$ are the distances between the peak position and background measurement positions, example shown in Figure 5.1
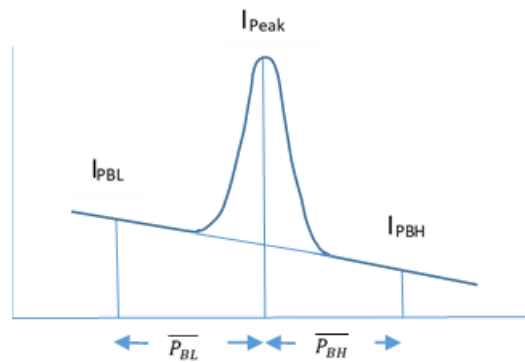
Figure 5.1: X ray peak and background position. Redrawn after original from [42].

The relative intensity K is calculated according to:

$$K = \frac{I^{UNK} CUR^{STD}}{I^{STD} CUR^{UNK}} C^{STD}$$

(5.3)

Where I^{UNK}, I^{STD} are the X-ray intensities of the unknown and standard specimen. CUR^{UNK}, CUR^{STD} are total specimen current of unknown and standard specimen during measurement (A). C^{STD} is the weight concentration of standard specimen.

At the beginning of the calculation process, the relative intensity measured is assumed to be equal to the weight concentration:

$$C_A^{UNK} = K_A^{UNK} \qquad\qquad \text{initial assumption} \qquad\qquad (5.4)$$

$$K_A^{UNK\prime} = \frac{K_A^{UNK}}{K_A^{UNK}+K_B^{UNK}+\cdots K_N^{UNK}} \quad \text{normalisation} \qquad\qquad (5.5)$$

$$C_A^{UNK} = K_A^{UNK} \times G_Z \times G_A \times G_F =$$

$$K_A^{UNK} \times \frac{R_A^{STD}\times P_A^{STD}}{R_A^{UNK}\times P_A^{UNK}} \times \frac{f_A^{STD}(\chi_A)}{f_A^{UNK}(\chi_A)} \times \frac{1}{1+\frac{I_{A(f)}}{I_A(d)}} \qquad (5.6)$$

$$C_A^{UNK\prime} = K_A^{UNK} \left\{ \left(\frac{R_A^{STD} \times P_A^{STD}}{R_A^{UNK\prime} \times P_A^{UNK\prime}} \right) \times \left(\frac{f_A^{STD}(\chi_A)}{f_A^{UNK\prime}(\chi_A)} \right) \times \left(\frac{1}{1 + \frac{I_{A(f)}}{I_A(d)}} \right) \right\} \qquad (5.7)$$

First calculation

$$C_A^{UNK\prime\prime} = K_A^{UNK} \left\{ \left(\frac{R_A^{STD} \times P_A^{STD}}{R_A^{UNK\prime\prime} \times P_A^{UNK\prime\prime}} \right) \times \left(\frac{f_A^{STD}(\chi_A)}{f_A^{UNK\prime\prime}(\chi_A)} \right) \times \left(\frac{1}{1 + \frac{I_{A(f)}}{I_A(d)}} \right) \right\} \qquad (5.8)$$

Second calculation

Where term $\frac{R^{STD}}{R^{UNK}} \times \frac{P^{STD}}{P^{UNK}}$ represent the atomic number correction (Z), R is the backscattering factor, P is the penetration factor. Absorption correction (A) is presented in the term $\frac{f_A^{STD}(\chi_A)}{f_A^{UNK}(\chi_A)}$ where $\chi = (\mu/\rho)\ \mathrm{cosec}\ \theta$, θ being the X-Ray take-off angle and μ/ρ mass absorption coefficient. Finally the term $\frac{1}{1+\frac{I_{A(f)}}{I_{A(d)}}}$ represents the fluorescence correction (F), with $I_A(d)$ being the intensity of primary X-rays of element A subject to direct excitation and $I_A(f)$ the intensity of X-rays due to fluorescence excitation of the other element B.

The whole procedure is started with the concept that this quantitative method will give a linear correction curve. However, the multiplicative factors (Z, A, F)

correct for deviations from ideal model. However, the values of the correction factors depend on the composition of the specimen, which is unknown. As an initial assumption of the specimen composition it is assumed that the weight fractions of the elements are proportional to the experimentally obtained X-ray intensity ratios. This estimate, as well as further estimates, is normalised so as to keep the sum of mass fractions equal to unity. The solution is to use an estimate of the composition to calculate the correction factors (first calculation) and afterwards to employ resulting mass fraction as a new estimate of composition (second calculation) and iterating until convergence of the results is obtained [43]. The ZAF correction procedure is iterated until the calculation converges, in other words is iterated until the result stabilises to within 0.001 mass%, or until the tenth calculation.

5.3.1 Choice of Line and Crystal

For a given element, sometimes there is a choice between multiple analytical lines and different spectrometers and crystals that can be used for the analysis. Different criteria are used to choose a line and crystal depending on element abundance in the sample. For major elements, the peak intensity is much greater than background and the choice of X-ray line and of spectrometer crystal is governed by the maximum intensity as well as the minimum counting time for given statistical uncertainty.

In the case of trace elements, the peak intensity differs only by a small amount from the background and the statistical uncertainty is governed by the expression (P^2/B) where P is the peak count-rate for the measured element, and B is the background count-rate on the sample. The peak-to-background ratio is much more important when choosing line and crystal for the trace element [12]. In the end the observed intensities are affected both by generated X-ray intensity and by spectrometer efficiency, so when performing trace analysis the optimum line/crystal combination is that which gives the maximum (P^2/B).

For elements of atomic number less than approximately 30, the K_α line is nearly always the best choice [12]. However, in order to stay within the doped

semiconductor layer, the accelerating voltage often must be reduced from 15–20 to ≤10 kV in order to reduce the electron interaction volume. At these low voltages, critical K_α X-ray lines of atoms such as Ga are no longer generated, so L X-ray lines must be used. One should also consider using the L lines for quantitative analyses involving minor or trace elements, because they are less likely to be produced by secondary fluorescence, and a better resolution can be obtained if the intensity is satisfactory [44]. However, applying the necessary matrix corrections to these L lines is complicated by bonding and chemical peak shifts for soft X-ray transitions such as those producing the Ga L_α X-ray line [36].

If there is a choice of crystal for a given X-ray line, the one with larger interplanar spacing (and hence lower Bragg angle) usually gives higher intensity. However, on the other hand, the peak-to-background ratio is greater for the crystal of smaller spacing, owing to the better resolution and consequently narrower band of X-ray continuum detected. In our study, when measuring low concentrations, one has to make sure that any possible gain in intensity is not counteracted by a decrease in peak to background ratio. In some cases the first choice X-ray line and crystal may not be adequate because of the existence of an overlapping line [12].

5.3.2 Background measurement

If the background is not properly estimated, it can become an important source of error for the trace element analysis. In the case of trace elements, the peak-to-background ratio is significantly lower than for major elements. It is therefore necessary to accurately estimate the background using a detailed WD intensity scan on the both sides of the peak of interest, with an example given in Fig. 5.2 [5]. It is important to evaluate the background spectrum at similar precision to the peak measurement. For that purpose WDS scanning is used in order to account for any possible interferences, existence of the absorption edges from other elements, existence of higher order lines, lines due to fluorescence and the curvature of the background [13]. It is usually wisest to slowly scan the spectrometer over the range of interest to characterise the shape and slope of the

continuum. From the Figure 5.2 it is possible to determine that there are not any interference peaks around Si K_α position or at the positions used for measuring backgrounds that could hinder quantitation of trace Si dopant. Background offsets should be chosen so that no absorption edges lie between the peak and the positions used for measuring background. It is necessary to be conscious about discontinuities in the background due to absorption edges. Absorption edges of major elements in the sample can cause steps due to the change in the absorption of the emerging continuum X-rays. Another thing to be careful about are "holes" in the background, such as the one occuring for LiF crystals at 0.1271 nm where the lattice planes in the WDX crystal reflect X-rays away from the counter [4]. This can result in nonlinearity of the continuum in the peak region [5]. Also, if possible, it is better to avoid peak or background positions close to spectrometer drive limit. With the help of detailed WD intensity scans it is possible to select positions for background measurement and the appropriate method of background interpolation like classic linear or for example exponential [5].
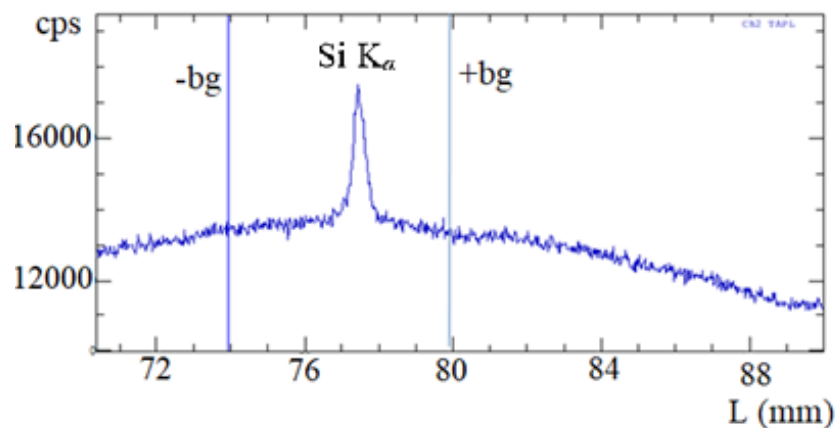
Figure 5.2: High count precision WD intensity scans on both sides of Si K_α on TAPL crystal spectrometer (Rowland circle 140 mm) in GaN:Si sample, counter differential mode employed (base level 0.7 V, window 9.3 V). -bg and +bg indicate possible positions of background measurements for two points of linear interpolation.

The scans for Si K_α in AlGaN/GaN do not reveal crystal diffraction artefacts but show a significant convex curvature of the X-ray continuum. At this scale, even

though the curvature is present, linear fit still seem acceptable. The background curvature can be modelled by appropriate exponential, polynomial regression. or using linear fit. An exponential fit did not result in any significant changes when measuring Si concentration. The problem with the two-point interpolation is that it does not account for background curvature. There are numerous reasons for the specific curvature of the X-ray spectrum near the peak of interest. One of them is the spectrometer efficiency, the degree to which the cone of X-rays entering a spectrometer is diffracted and counted at the particular spectrometer position. For example, at low diffraction angles, the diffracting crystal is closer to sample, and the detector is closer to the diffracting crystal, therefore a larger proportion of the X-rays will be diffracted and counted. Another source is the detector quantum efficiency, wavelength dependence of absorption through a detector window, and the natural bremsstrahlung emission which are expected to cause a positive-sloping curvature. All of the above factors make the exact shape of the background highly complex, including the hardware factors such as: counter gas composition and pressure, pulse-height discriminator window width, detector bias, dimensions of the monochromator, the presence or absence (and width) of collimating slits, and Rowland circle radius [10]. It is expected that the compositional effect on curvature is minimal [20]. Finally, it is possible to conclude that when measuring trace Si doping levels curvature is generally small over the relevant wavelength interval and the best method for background interpolation is linear fit.

5.3.3. Different standards for trace measurements

When considering the analysis error, the error on the peak and background measurements must be considered for both the unknown and the standard. For the trace elements it is important to consider the basic relationships for the precision of X-ray emission. The variance of the raw k-ratio (net intensity sample/net intensity std.) can be expressed as [13]:

$$\sigma_k^2 = k^2 \left[\frac{\bar{N} + \bar{N}(B)}{n(\bar{N} - \bar{N}(B))^2} + \frac{\bar{N}_S + \bar{N}_S(B)}{n'(\bar{N}_S - \bar{N}_S(B))^2} \right] \qquad (5.9)$$

Where σ_k is the standard deviation, $\bar{N}$ and, $\bar{N}(B)$ are the measured peak counts for the peak and background on the sample. $\bar{N}_S$ and $\bar{N}_S(B)$ are the mean counts

for the peak and background on the standard and n and n' are the number of measured points on sample and standard. The variance of the concentration can be expressed as [13]:

$$\sigma_c^2 = C^2 \left[\frac{\overline{N} + \overline{N}(B)}{n(\overline{N} - \overline{N(B)})^2} + \frac{\overline{N}_S + \overline{N}_S(B)}{n'(\overline{N}_S - \overline{N}_S(B))^2} \right] * \left[1 - \frac{(a-1)C}{a} \right]^2 \qquad (5.10)$$

Where σ_c is the concentration standard deviation. C is the concentration, and a is the correction factor that relates the k-ratio to the concentration. From that relationship it is possible to conclude that precision for the trace element analysis is highly dependent on the precision of the sample analysis and less upon the precision of the standard measurements (if the standard data was acquired on sample with high concentration of element of interest). From the Eqs. (5.9) it is evident that when using a standard with low concentration of element of interest and therefore low intensity will result in large errors in the analysis of trace elements compared to using standards with high concentration of element of interest [13]. The standard measurement is then subject to the inaccuracies associated with measuring small peaks. Another problem is that is generally hard to find homogeneous trace-element standards [4].

For the trace measurements, it is important to notice that for the major elements, the accuracy depends on the peak counts for sample and standard (P-B) whereas for the trace elements the largest source of errors is the determination of net counts for the unknown.

In addition to choice of standard, matrix corrections have to be considered as well, for example uncertainty in the matrix corrections is reduced if the standard resembles the sample in composition. When tested different matrix procedures for major elements errors are generally less than ± 5% (relative), which is usually smaller than the errors associated with measurements of trace elements. The compositional similarity of standards is thus less important in the case of trace element measurements [4].

5.3.4 Blank standards

How can one be sure that the analysis is correct? Correct answer would be to analyse a secondary standard, but the problem is that is very difficult to find or make a homogeneous trace element secondary standard and that is the reason why a blank standard is needed. Blank standards containing none of the trace elements of interest can be helpful for correction of continuum artefacts such as the holes in the spectrum or the curved background [4]. The main purpose of the blank measurement is an accuracy reference. Of course the blank correction is only the last step in properly optimizing the measurement. That is after obtaining a primary standard with a high concentration of the element of interest (because that improves the standard statistics and overall analytical sensitivity), proper placement of the background measurement positions (and correcting for curvature in the background) and careful treatment of possible spectral interferences.

The term blank standard has been adopted from other trace element techniques, such as ICP-MS, where the absolute accuracy of the measurement is characterised by analysing the sample with a matrix as close possible to the unknown but which contains none of the trace element of interest. The blank measurement has to be performed with the same conditions as for the unknown. The idea is to accurately measure the background at zero concentration and then to subtract the measured X-ray intensity from the net X-ray intensity of the trace element during matrix correction procedure, as in equation 5.11. Where I_{corr} is the blank corrected unknown net intensity, I_{unk} is the measured unknown net intensity, I_{std} is the measured primary standard net intensity. C_{meas} is the measured concentration in the blank standard, C_{level} is the zero or the known concentration in the blank standard, C_{std} is the concentration in the primary standard, ZAF_{std} is the matrix correction factor for the primary standard and the ZAF_{unk} for the unknown sample [45].

$$I_{corr} = I_{unk} - I_{std} \frac{(C_{meas} - C_{level})\lfloor ZAF_{std} \rfloor}{C_{std}\lfloor ZAF_{unk} \rfloor} \qquad (5.11)$$

In order to find a suitable blank standard for my work, qualitative scans are performed on different GaN and AlGaN samples (Mg doped or undoped) to check for the existence of Si peak. However, every measured sample showed significant Si peak and therefore none of the available non-Si-doped samples could be used as a blank standard, with an example shown in Figure 5.3 and later within result section in Figure 5.9. If the possible blank samples are not tested for the trace element of interest, they may contain a significantly higher "value" compared to what is expected for blank "level", if this measurement where to been applied to the actual unknown, it will result in over correction of the measured intensity and a negative *k*-ratio. This a common problem that occurs for the trace measurement - namely not being able to find a suitable blank standard.
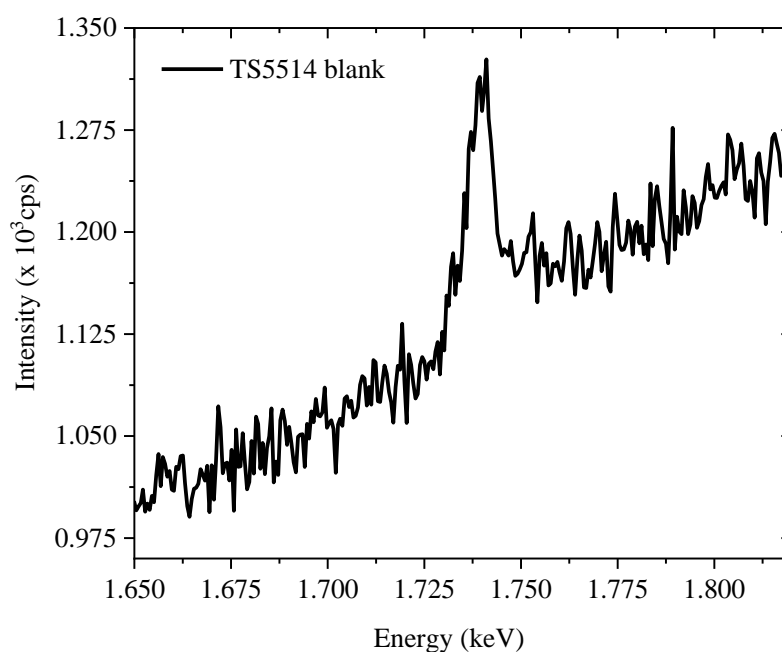
Figure 5.3: Long qualitative scan for the Si peak on GaN: Si samples: sample TS5514 "blank" AlGaN sample using a TAPL crystal at 10 kV, 100 nA.

5.3.5 Pulse height analysis (PHA)

The background shape will depend upon the Bremsstrahlung characteristics of the sample and other factors due to the spectrometers and collection efficiency. It is important to being able to separate signal from the noise in background [13]. The detector gain and bias settings are adjusted so that when the spectrometer is tuned to a particular X-ray line, the voltage pulse produced by X-ray ionization of the detector gas is centred in the (single channel analyser) SCA voltage window [46]. With the pulse-height analysis it is possible to supress the high-order reflections of characteristic X-ray lines if there is interference with the first order lines, but another advantage is to reduce the background by removing the contribution of high-order continuum X-rays and to remove the background produced by scattered X-rays and electrons [4].

When setting pulse-height analysis settings, care must be taken not to constrain the energy windows too much such to prevent counts from being cut off. Also, it is necessary to check for possible pulse shifts. For this reason, it is recommended that PHA parameters are set based on counter energy distributions for the peaks of interest on standards with relatively high concentrations [10]. When setting a PHA for the trace element analysis, there is potential for the peak to shift to a higher voltage compared to that for a standard with a high concentration. The shift occurs because each time a photon enters the proportional detector it creates an ionization trail and that causes the high voltage bias on the detector to discharge. This is the signal that is processed by the preamp and then counted. However, at very high count rates, the detector doesn't have quite enough time to re-charge back to full bias voltage before the next photon enters and causes another discharge cycle. This generated discharge is observed as a shift towards lowers PHA voltages with high count rates.

Therefore, the analyst has to be careful not to set too tight windows due to potential to cutoff of high-voltage pulses. The peak shift can be minimized by performing pulse height analysis (PHA) on standards using lower current (e.g 10 nA). The voltage windows should be sufficiently narrow, yet wide enough to absorb possible pulse shifts without clipping signal. Setting voltage windows

164

requires prior knowledge of the expected count rate range [46]. Example of setting PHA parameters is shown in Figs. 5.4 and 5.5.

Mode: High Voltage Scan CH-2
Voltage: 1850.00 V 37 count
Peak: 1724.00 V
Base Length: 1.60V
Window Width: 3.90 V
High Voltage: 1724 V
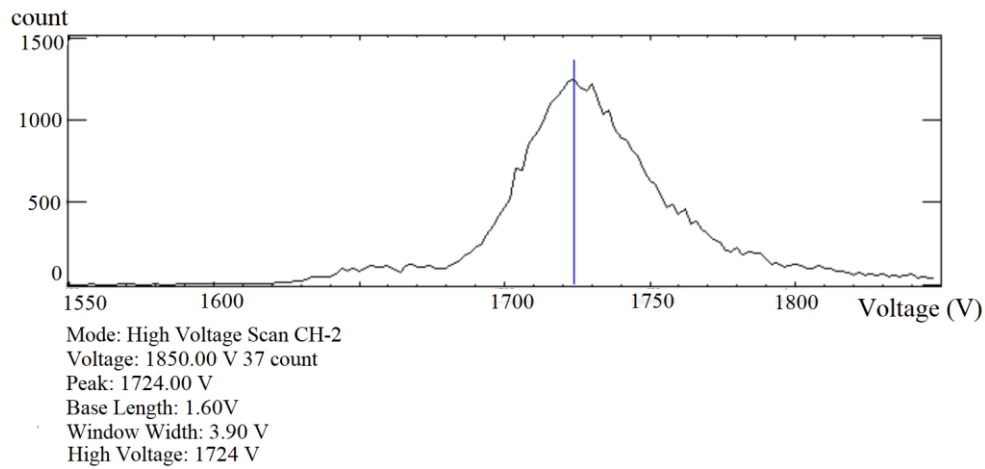
Figure 5.4: High voltage scan on Si standard at 15kV and 20 nA.

Mode: Base Length Scan CH-2
Voltage: 9.80 V 3 count
Peak: 4.00 V 1231 count
Base Length: 1.15 V
Window Width: 5.40 V
High Voltage: 1724 V
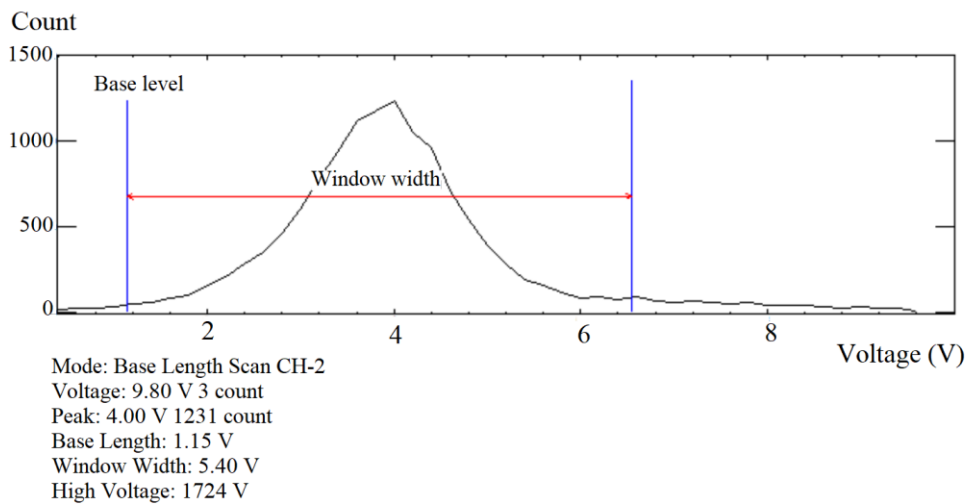
Figure 5.5: Single-channel analyzer (SCA) scans of Si standard with spectrometer PETL at Si K$_\alpha$ position.

Scan in the differential mode, which is used in quantitative analysis and in WD scans (Figure 5.2) is very different from the integral mode and it clearly demonstrates the power of pulse height analysis. In the differential mode, background intensities are significantly lower throughout the whole scan, mainly due to an elimination of contributions from various higher order X-rays from the continuous spectrum.

5.3.6 Measurement statistics

The main source of random errors in EPMA is the statistical fluctuations in the measured X-ray intensities. Other minor sources include, for example, beam current instability. If the counting rate is known in EPMA then the expression for statistical relative uncertainty (of one standard deviation) $n^{-1/2}$, where n is the number of counts accumulated in the measurement of an X-ray peak intensity, can be used to evaluate either the counting time required to obtain a given uncertainty or the uncertainty obtainable for a given counting time [12].

For the high analytical sensitivity in ppm range a high count precision is a requisite. The biggest problem is still the measurement accuracy because all sources of errors will be magnified in trace analysis. With longer counting times and with increasing current it is possible to increase the precision and sensitivity without sacrificing spatial resolution. Precision in EPMA depends on number of photons counted, counting time, X-ray production efficiency (fluorescence yields, ionization cross sections), and collection efficiency. Counts can be increased either with current or with using higher overvoltage, but if a higher overvoltage is used, inevitably the spatial resolution will be worsened due to increases in electron path length and the number of ionizations per unit time. Another thing to consider is that with the increase in current and time there is a potential in instrumental drift and beam damage [13]. With the increase of beam current there will be some degradation in the beam diameter, but beam diameter is usually increased during high current analysis to counteract the beam damage [12].

5.3.7 Separate measurements of major and trace elements

The best solution for trace element measurements is to use separate routines with different set of analytical conditions for trace and major element analysis owing to their different requirements [4, 13]. The best practise is to use the same accelerating voltages when measuring major and trace elements and only change the current in order to ensure trace and major element data will refer to same volumes within the sample [4]. The elemental detection limit is ultimately governed by counting statistics. By using appropriate conditions, such as high beam current and long counting times, it is possible to detect elements in the concentrations of the order of 10 ppm [4]. The detector saturation is not a factor in WDX technique, because unlike in the EDX technique, the WD spectrometers in the EPMA are designed to record only one wavelength at a time so there is not a risk to oversaturate detector with major element counts when measuring trace elements with high current [4]. If the detector is overloaded that will result in pulse height depression and possible errors in dead-time corrections [12]. In WDX technique, contrary to EDX technique, much longer acquisition time and probe current are employed, therefore instrumental and sample stability is obligatory and needs to be checked in order to obtain accurte trace element analysis [5].

5.3.8 Errors in trace element analysis

Contribution to errors in trace analysis can be split into different categories:

a) short-term random errors (counting statistics, instrument noise, surface imperfections, deviations from ideal homogenity);

b) short-term systematic error (session to session, beyond a single set of analyses: background estimation, sample coating and calibration effects); and

c) long-term systematic errors affecting accuracy (effects stemming from quality of standards, evolving algorithms for interferences, background

regression, dead-time corrections, ZAF factors, physical constants [47]). Larger errors are connected with background subtraction and interferences [4]. For trace element analysis it would be beneficial to assess the accuracy by using a secondary standard but as previously mentioned, it is problematic to find a standard with a homogeneous trace element concentration of the elements of interest.

In the Figure 5.6. the percent counting error for trace elements (Si and Mg) intensity is presented for measurements performed at different accelerating voltages. From the figure it is evident that the highest counting errors are obtained when using current of 40 nA for measuring trace elements (green points), even with high accelerating voltage. In general, errors are lower when measuring Mg opposed to measuring Si. The lowest obtained errors are around 1% when measuring Mg in GaN. Even when it is necessary to us low accelerating voltage of 3 or 4 kV, the resulting errors are not too high and range from $3-5\%$. The choice of voltage is assessed based on the spatial requirements, and is chosen according to Monte Carlo simulations using CASINO software [48] with the beam energy being sufficient to efficiently excite X-ray lines of interest and to contain the interaction volume within the semiconductor layer.
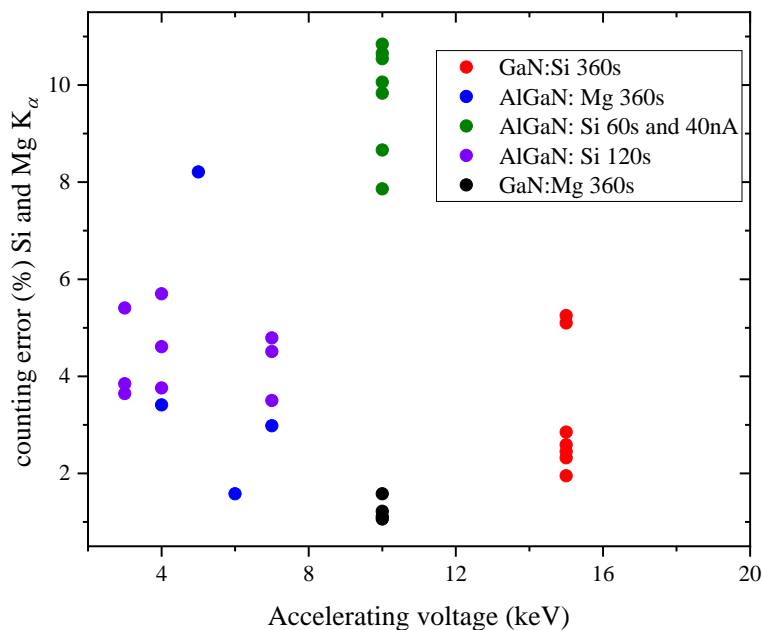
Figure 5.6: The percent counting error for trace element intensity (Si or Mg) resulting from prolonged beam exposure at varying kV.

Prior to trace analysis it is necessary to obtain quality standard data. The quality of the data can be checked via the percentage of statistical fluctuation in X-ray counting (S.D %) and specially via the percentage for the standard variance (S.V %). The smaller the relative standard deviation is, the higher the precision. Multiple measurements of a single point are necessary when acquiring standard data, and variance percentage is related to the degree of standard homogeneity, also smaller S.V indicates better homogeneity [49].

Example of standard data required for analysis of GaN: Si sample is given in Table 5.1, showing all relevant data necessary to check the quality of the performed measurement.

Statistical fluctuation in X-ray counting is obtained as the value corresponding to 1σ using the following equation:

$$S.D.\% = \frac{100}{I_{net}} \sqrt{\frac{I_{peak}}{t_{peak}} + \left(\frac{\overline{L_{PBH}}}{L}\right)^2 \frac{I_{PBL}}{t_{PBL}} + \left(\frac{\overline{L_{PBL}}}{L}\right)^2 \frac{I_{PBH}}{t_{PBH}}} \qquad (5.12)$$

Where t_{peak}, t_{PBL}, t_{PBH} is counting time (in seconds) at the peak, and of the

background signal at low and high angles and $L = L_{PBH} + L_{PBL}$

$$I_{net} = I_{peak} - \frac{I_{PBH}\overline{L_{PBL}} + I_{PBL}\overline{L_{PBH}}}{\overline{L_{PBl}} + \overline{L_{PBH}}} \qquad (5.13)$$

I_{net}, I_{peak} represent intensities of net X-rays and measured X-rays at the peak position, I_{PBH}, I_{PBL} represent intensities of background X-rays measured at high and low angles.

When measurement of X-rays at multiple points is performed using accumulation, standard variation is calculated using the following equation:

$$S.V.(\%) = \frac{100}{I_{net}} \sqrt{\frac{\overline{(Ii-\bar{I})}^2}{n-1}} \qquad (5.14)$$

I_i represent intensities of X-rays on each measuremnet, $\bar{I}$ average intensity of net X-rays, n number of accumulation. It is necessary to check if there are any possible interferences on peaks and background positions, which could contribute to the analytical error. For the trace elements values for the Pk-Bkg will be low and in that even small errors in the net intensity can result in large accuracy errors.

From Table 5.1, it is noticeable that S.V% is in order 0.05−0.6% and the value is consider acceptable. For the coated samples S.V is usually higher compared to uncoated samples.

Table 5.1: Data for standard measurement that are used for the analysis of GaN:
Si sample.

UNCOATED STANDARDS									
Pure silicon wafer, 15 kV Curr.(nA) : 20									
Element	Crys-tal	Cha-nnel	L (mm)	Net (cps)	Bg– (cps)	Bg+ (cps)	S.D. (%)	S.V. (%)	D.L. (ppm)
Si	TAP	3	77.483	67793.6	161.4	105.7	0.02	0.10	10
GaN standard, 15 kV Curr.(nA) : 40									
Ga	TAPH	1	122.751	19252.7	169.4	215.2	0.03	0.12	37
N	LDE1L	2	149.563	811.5	64.9	36.8	0.16	0.50	91
COATED STANDARDS									
Pure silicon wafer, 15 kV Curr.(nA) : 20									
Si	TAP	3	77.473	48063.4	115.7	73.8	0.02	0.05	12
GaN standard, 15 kV Curr.(nA) : 40									
Ga	TAPH	1	122.739	19073.0	166.1	212.9	0.03	0.13	37
N	LDE1L	2	149.563	751.2	61.9	34.6	0.17	0.64	95

5.3.9 Final recipe for quantitative analysis

After consideration of all the factors involved in quantitative analysis procedure described in section 5.3, this subsection describes the quantitative analysis procedure employed for analysis of the Si-doped GaN and AlGaN samples of interest, whose growth parameters are listed in Tables 5.2 and 5.4.

WDX measurements are performed in the EPMA with the incident electron beam normal to the sample surface, and an acceleration voltage of 10 kV. Under these conditions, the electron interaction volume is kept within the first 500-800 nm of the $Al_xGa_{1-x}N$ layer (samples listed in Table 5.4) according to Monte Carlo simulations using CASINO software [50] and dependent on the AlN molar content. In all samples the interaction volume is contained within the topmost $Al_xGa_{1-x}N$ layer and the beam energy is sufficient to efficiently excite the selected X-ray lines. The beam current of 40 nA is used for analysis of the major elements (Al, Ga, N) and increased to 400−500 nA for the minor elements (Si). The beam was defocused to 10 or 20 μm to improve sample averaging and avoid damaging the sample. The samples and standards are carbon coated to remove charging effects, with a thickness of approximate 15 nm (as determined by the interference-colour method [51]). This becomes

increasingly important for AlN-rich $Al_xGa_{1-x}N$ for which the conductivity decreases. Measurements are also performed on two of the GaN:Si without coatings (and using uncoated standards) to confirm that the coating is not a source of Si.

According to best practice for trace analysis the pulse height analysis (PHA) parameters (such as voltage window, baseline, electronic bias and gain on the detector) are adjusted before measuring the Si K_α peak, using energy distributions of the peak on a pure Si standard with a beam current of 20 nA [12]. The Si peak has a tendency to shift due to valence and coordination change depending on sample the matrix [52], but in this case the shifts in the Si K_α peak position between the pure Si standard and the unknown samples are insignificant (Si K_α peak position on TAPL crystal: GaN: Si 77.302 mm, Si standard: 77.344 mm). Differential mode is employed simply to exclude noise peaks and no higher order interferences are observed in the region of the Si K_α peak [53, 54].

Two methods are employed for analysing the Si doping: qualitative and quantitative measurement. In the qualitative scan the information on the element concentration is present in the height of the peak, extracted as peak maximum minus interpolated background. For the quantitative measurements the EPMA's standard ZAF correction procedure is used in the usual way to determine the Si concentration and the results are included in Table 5.2. The quantitative procedure improves counting statistics due to the extended time spent acquiring peak and background X-rays, compared to the qualitative scan. The concentration of the major elements is quantified using the ratios of the background-corrected peak intensities for the sample to the corresponding ones obtained from AlN, GaN and Si standards (k-ratios). Signals were acquired for 60 s on the peak positions and for 30 s on the background positions with a beam current of 20 nA. Ga L_α and Al K_α signals are recorded using a TAPH crystal (thallium acid phthalate, 100 mm Rowland circle) while for the N K_α signal a synthetic layered LDE1L crystal (140 mm Rowland circle) is used. For quantification of the minor element the Si K_α X-rays are recorded using a large TAP crystal (140 mm Rowland circle). The measured intensities are corrected

for differences in composition between standard and specimen using the standard ZAF correction procedures in the JEOL EPMA software. The low silicon concentrations necessitate a separate measurement routine to that for the major elements, due to different requirements for the counting statistics between major and minor elements [1]. Therefore, in order to improve counting statistics longer measurement times and higher currents were employed: $400-500$ nA, and 360 s and 180 s counting times for the peak and background respectively. The accelerating voltage and measurement positions are kept unchanged in order to ensure that the data for the silicon and major elements will refer to the same volumes within the sample. With the new measurement condition the counting statistics are significantly improved for silicon and the counting error was reduced to 1–3% relative, with detection limit (DL) reduced to 1 ppm. Before the optimisation of the measurement condition same current of 40 nA was used for trace and major elements, resulting in large counting error for Si 7–10% relative, and high Si DL of around 30 ppm. Despite the new smaller errors in the silicon signal, the final silicon concentration in the sample still resulted in higher concentrations (($0.6-4)\times10^{19}$ cm^{-3} levels) than expected when compared to SIMS data available for the same samples. In order to check the accuracy of measured results an inter-laboratory study was conducted and some samples were also measured on the EPMA (JEOL JXA-8530F) at the University of Bristol.

5.4 Measurement optimisation and inherent contamination

A range of Si-doped GaN and $Al_xGa_{1-x}N$ samples, grown by MOCVD by different groups, were used to clarify the best way to measure Si [55-60]. GaN:Si material (sample EU2000894) was provided by IQE Europe Ltd. A series of $Al_xGa_{1-x}N$ samples with different crystal polarities and different AlN contents were provided by the Tyndall Institute. These $Al_xGa_{1-x}N$ samples included polar oriented [0001] (samples AP, BP, CP) and semi-polar oriented layers [112-2] orientations (samples ASP, CSP). More details on the growth of the $Al_xGa_{1-x}N$:Si layers from the Tyndall Institute are given elsewhere [55, 58, 60, 61]. Samples labelled TS are $Al_xGa_{1-x}N$ layers with various AlN contents and crystal polarities grown at the Technische Universität Berlin[56, 57, 59, 62].

The "blank" $Al_xGa_{1-x}N$ TS5541 was grown with no Si doping and shipped, immediately after growth, in a sealed container filled with N_2 gas in order to minimise contamination. On receipt it was immediately placed under vacuum within the EPMA chamber. Information on the three sets of samples are given in Tables 5.2 and 5.4. Attempts were made to remove inherent surface contamination by oxygen plasma cleaning treatments. Traditionally, plasma cleaning is employed to remove hydrocarbon contamination [63]. Apart from contamination, the samples can also suffer from oxidation. To investigate the effect of oxidation of the Si standard, cleaning with HF solution is employed.

D-SIMS data were provided by three different companies: RTG Mikroanalyse GmbH Berlin [64] , Loughborough Surface Analysis Ltd. (using a Cameca 7f) and Evans Analytical Group (EAG). All samples were analysed in depth profile mode, using areas typically 100×100 μm. RTG used ion implanted AlGaN samples to produce absolute and relative sensitivity factors for Si in AlGaN, with further details given in Jörchel et al. 2016. The same approach was used for data from Loughborough. EAG used a proprietary formulation that calculates the change in sensitivity factors with respect to the AlN fraction in AlGaN.

Another challenge is the inherent contamination of the sample surfaces with additional Si incorporation is known to be a contaminant during metal-organic chemical vapour deposition (MOCVD) growth of GaN and $Al_xGa_{1-x}N$ [33, 65]. Typical growth temperatures are in the region of 1100°C, in order to promote the break-up of the ammonia molecules and adatom mobility on the growing surface, and it should be noted that the graphite susceptors used to heat and support the substrate wafer during growth are often coated with SiC to provide robustness. It typically takes about 30 minutes for the samples to cool down from the growth temperature and possible sources of Si contamination during that period include the reactor walls, precursors, substrates or quartz liners (as molten Ga can etch the quartz to produce gallium oxide and free silicon). It is possible that there is a constant background source of Si within the reactor and the incorporation of Si has been shown to increase sharply when the ammonia flow drops [65]. After removing a sample from the growth chamber silicate dust

in the air and silicone oils are a likely source of Si contamination of the surfaces. SIMS data for samples where there has been a growth interruption to allow transfer between reactors reveal contamination with Si is illustrated in Figure 5.7 for an AlGaN:Si layer grown in two stages. The spike in the Si trace at a depth of approximately 500 nm shows a significant increase in its concentration at the interruption interface. Such a spike has also been observed in samples where there is no Si doping as well as ones where there was simply a pause in epitaxy, with no change in reactor, to allow changes in growth parameters such as temperature and pressure. SIMS profiles from Pickrell et al. 2019 reveal significantly greater Si concentration in GaN due to air contamination when compared to growth interruptions with temperature ramps. In both cases the oxygen trace remained at the detection limit.

Furthermore, a number of groups fabricating GaN-based nanowires have discussed Si-rich layers forming on the surface of nanowires grown with high silane flows and which impact the lateral-to-vertical growth rates [66, 67]. These layers are clearly visible in EDX maps obtained using transmission electron microscopy and although only a few nm thick but contain high concentrations of Si.
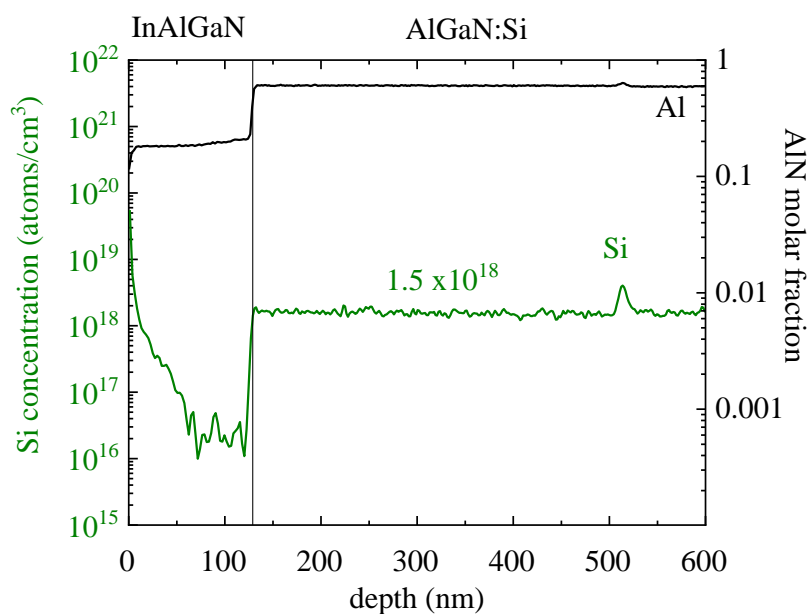
Figure 5.7: SIMS profiles for Si and Al for a sample for which there was an interruption during the MOCVD growth. The sample consists of 150 nm

InAlGaN on top of a thick AlGaN:Si layer grown in two parts, with a change of reactors at a depth of approximately 500 nm.

5.4.1 Detection limit

The precision and detection limits of EPMA are typically 1−2% relative for major elements with detection limits of 100s of ppm, although 10s of ppm can be achieved using multiple spectrometers and/or high beam currents.

The sensitivity of analysis can be quantified by calculation of the minimum detectability limit. Expression that describes the concentration at the limit of detection is:

$$C_{DL} = \frac{3\sqrt{\overline{N}(B)}}{\overline{P_{std}} - \overline{N}(B)} C_{std}$$

(5.15)

Where C_{DL} is the detection limit (mas%) C_{std} is the concentration of the element of interest (mass%) in the standard, $\overline{N}(B)$ are the measured peak counts for the background, and $\overline{P}_{Std}$ are the counts for measured peak [13]. This equation enables to distinguish the peak from the background with 99.7% confidence level [1].

If the peak and background intensity is converted in Eqs 5.15 into count rate per unit time and unit probe current, the following equation can be obtained:

$$C_{DL} = \frac{3\sqrt{(B)}}{(P - B)\sqrt{i\,x\,t}} C_{std}$$

(5.16)

Where i is current in μA and t is time in seconds. Eqs. 5.16 shows that the detection limit improves in proportion to the square root of the probe current and the measurement time [1].

Various definitions of detection limit are used, Eqs. 5.15 is often simplified into the form `3 standard deviations of background' (3sdbg), obtained by dividing 3 times the square root of the background count by the peak count for the pure

element (corrected for absorption in the sample). The 3sdbg detection limit is thus the concentration for which the presence of the element can be affirmed with 96.6% confidence. In EPMA the presence of the X-ray continuum will always limit the detectability of small peaks as defined by statistical criteria [4].

Eq. 5.16, allows estimation of a detection limit in the order of 10 ppm, corresponding to 10^{18} cm^{-3} of Si in GaN. The test was performed on two GaN: Si samples (TS4142 and TS4137) with low silicon contents that were also characterised by SIMS (Table 5.2), and on one "blank" AlGaN sample TS5541. Figure 5.8 shows long qualitative WDX scans (dwell time 12 s, 505 points, total time: 1h 36 min), which were performed to check for the existence of the Si K_α peak. A Si peak is clearly visible above the background level in all of the above mentioned samples (even in the "blank" sample, referred from now on as a control sample) and much greater than error/detection limit. It is possible to conclude that sample TS5541 is not actually blank and has accrued Si either during growth or in the time before measurement. From the qualitative scans it is also evident that there are no signs of any interference close to the Si K_α peak that could be a serious source of error in quantitative microanalysis and peak position is the same in tested samples [68]. There are differences in the shape of the background for the samples shown in Figure 2, with the main difference being the high Al content in TS5541 which could be responsible for the increased background on the high energy side for this sample.

Since the SIMS measurements (for the GaN samples) gave values below or close to the detection limit, the silicon doping should have been unmeasurable in these cases. However, the WDX data shows clear Si X-ray peaks and high apparent Si content ($> 6\times10^{18}$ cm^{-3} compared to $< 7\times10^{17}$ cm^{-3} from the SIMS value in Table 5.2). Furthermore, the WDX analysis returned a similar value for Si concentration from the control sample. Measurements performed at the University of Bristol for GaN samples (TS4142 and TS4137, Table 1) gave similar Si concentrations ($\times1.6$ and $\times2$ higher, respectively). A different set of analytical conditions was used for the measurement, with a 400 nA current and 10 μm spot size.

Table 5.2: Reference GaN and Al$_x$Ga$_{1-x}$N samples for which independent measurement of the Si concentration is available.

Sample name	AlN at%	Si net (Peak intensity-background intensity) (cps/µA)	WDX concentration (×10^{18} cm^{-3})	SIMS concentration (×10^{18} cm^{-3})	WDX concentration (×10^{18} cm^{-3}) from University of Bristol EPMA lab
TS4142 (GaN)	0	188 ± 16	6.2 ± 0.6 (coated) / 6.5 ± 0.7 (uncoated)	0.743	10.0 ± 2.0
TS4137 (GaN)	0	208 ± 19	6.3 ± 0.4 (coated) / 10 ± 2 (uncoated)	0.212	20.0 ± 0.9
TS5541 ("blank" Al$_x$Ga$_{1-x}$N), control sample	76*	192 ± 44	7.0 ± 2.0	0*	-
TS2039 (Al$_x$Ga$_{1-x}$N)	94 ± 3‡	220 ± 22	9.0 ± 0.3	3.6 ± 0.7	7.0 ± 0.6
TS1860 (Al$_x$Ga$_{1-x}$N)	80 ± 3‡§	306 ± 27	9.0 ± 0.4	4.1 ± 0.8 / 7.0 ± 4.0	10.0 ± 2.0
EU2000894 (GaN)	0 §	857 ± 44	40.0 ± 3.0	12.0 ± 0.6 / 13	-
TS5565 (Al$_x$Ga$_{1-x}$N)	57	634 ± 5	21.4 ± 0.5 (uncoated)	8.3	-
TS5587 (Al$_x$Ga$_{1-x}$N)	62	1062 ± 15	27.3 ± 2.0 (uncoated)	13.4	-
TS5712 (Al$_x$Ga$_{1-x}$N)	79	506 ± 10	14.8 ± 0.5 (uncoated)	4.0	-
TS5770 (Al$_x$Ga$_{1-x}$N)	80	260 ± 11	7.6 ± 0.9 (uncoated)	1.4	-
TS5602 (Al$_x$Ga$_{1-x}$N)	60	1700 ± 36	37.1 ± 3.7 (uncoated)	20.8	-

* sample TS5541 has not been measured by SIMS, but it was grown undoped, so the SIMS concentration is assigned to be 0; AlN at% as estimated from the growth conditions, § samples TS1860 and EU2000894 were measured by two of the three SIMS companies ‡[19]
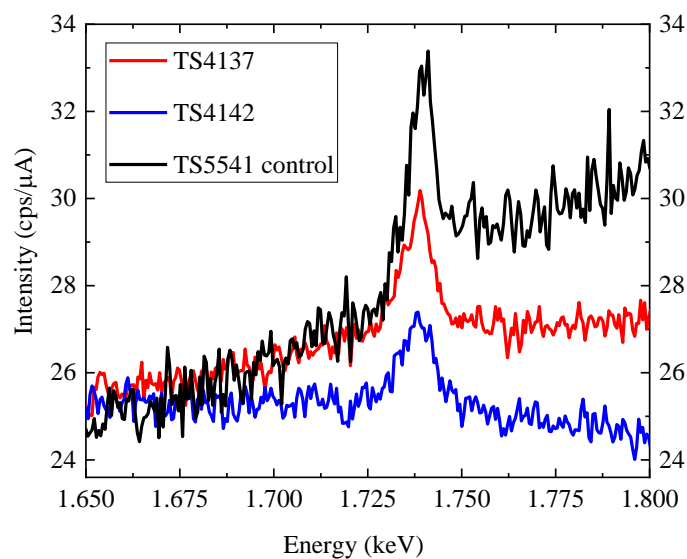
Figure 5.8: Long qualitative scan (dwell time 12 s) for the Si K$_\alpha$ peak from GaN:Si samples: TS4142 (blue), TS4137 (red) and Al$_x$Ga$_{1-x}$N control sample TS5541 (black) using a TAPL crystal at 10 kV, 400 nA, (100 nA for the control sample).

The above results appear to confirm that inherent contamination of the sample surfaces with additional Si is the cause of the discrepancy between the results from D-SIMS and WDX and it prevents convergence of the WDX and SIMS results by any simple adjustment of the analysis conditions. Attempts were therefore made to remove the contamination by cleaning treatments.

5.4.2 Plasma treatment

Attempts were made to remove inherent surface contamination by oxygen plasma cleaning treatments. Traditionally, plasma cleaning is employed to remove hydrocarbon contamination [69]. Ex-situ plasma cleaning did not result in any conclusive results when comparing Si content before and after cleaning (not shown).

5.4.3 Si standard before and after cleaning

The silicon standard will form native layers of oxygen on the surface. Therefore, cleaning in HF solution was employed to remove the oxide layer from the Si standard. When electrons pass through an oxide film layer on the surface following will happen: attenuation of the electron beam current, attenuation of the electron energy, deflection of the electron beam, and X-ray attenuation [70]. Oxidation of the standard will reduce the standard intensity due to the native oxygen layer and cause an overestimate of the concentration in the unknown [71]. Qualitative scans around the Si peak were performed before and after cleaning (not shown here), with no change in Si peak intensity after the treatment. Additionaly. Si K_α intensity data were acquired on the Si standard before and after the cleaning to check the difference, presented in Table 5.3.

Table 5.3: Si K_α intensities acquired for pure Si standard, before and after removal of native oxide layer.

TAPL crystal, 20 nA, 10 kV	Before cleaning (counts)	After cleaning (counts)	Percentage difference (%)
uncoated	76,313	79,353	4%
coated	78,596	80,823	3%

Qualitative scans on a pure metal Si standard were used to check that the Si concentration was not underestimated in standard and that the intensity of Si measured from the standard remains the same before and after removal of native oxygen (Table 5.3). Table 5.3 shows that removal of the oxidation layer from the standard did not produce any significant changes (only $3-4\%$) in the intensity of Si K_α peak. It is possible to assume that the native oxygen layer is thinner than 10 nm [72].
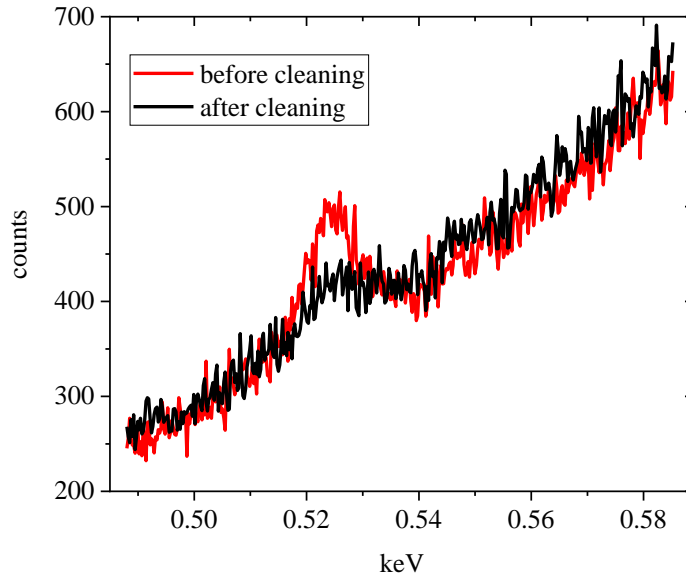
Figure 5.9. Qualitative scan for oxygen peak on LDE2H crystal, comparison before and after cleaning.

From the qualitative scan for the oxygen peak, Fig 5.9, reduction in the oxygen peak is observable, while for the Si peak there was not any noticeable reduction in the intensity.

Thus, it is possible to conclude that cleaning treatments did not remove possible Si contamination and that oxidation of the sample or standard is not the reason for the large discrepancy between SIMS and WDX results. The data measured from two GaN:Si samples, with and without C-coating, confirm that the C-coat is not the source of extra Si (Table 5.2).

After cleaning the Si standard, calibration data was acquired from it using a very low current of 1nA in order to reduce the count difference between the standard and unknown trace element. This did not result in any difference in the measured concentration for the trace element when compared to calibration data acquired with 20 nA. Subsequently, all calibration data is acquired with a lower beam current of 20 nA compared to the 500 nA employed to measure Si in the

unknowns, in order to avoid detector oversaturation. In doing this we have relied on the current measurement system scaling linearly from 20 to 500 nA.

5.4.4 Time dependent measurement

Due to the long measurement time and high currents used for the silicon analysis, the instrumental and sample stability need to be checked [73]. A sample will generally be stable during analysis with usual operating conditions (10−100 nA), but the high currents (hundreds of nA) required for trace element analysis may cause it to degrade [74]. A generally known example is the anisotropic, time-dependent variation in F K_α and Cl K_α in apatite samples during prolonged electron-beam exposure [75]. It is necessary to assess if the AlGaN: Si samples are stable during measurement time due to potential charge build-up, heating or radiation damage. This was assessed by monitoring the count rate for Si K_α in one of the calibration samples at the same time as the absorbed current. Figure 5.10 shows that the silicon signal remains stable during the long counting times and there is only a very slight decrease of the absorbed current (0.3 %). Since the measured absorbed current is not showing a significant drop or oscillations, it implies that the electrical properties of the coating are sufficient. The time scan was performed with a 10 μm defocused beam to simulate more extreme conditions, while the quantitative analysis sometimes used a beam diameter of 20 μm in order to minimize any absorbed current instability [10].
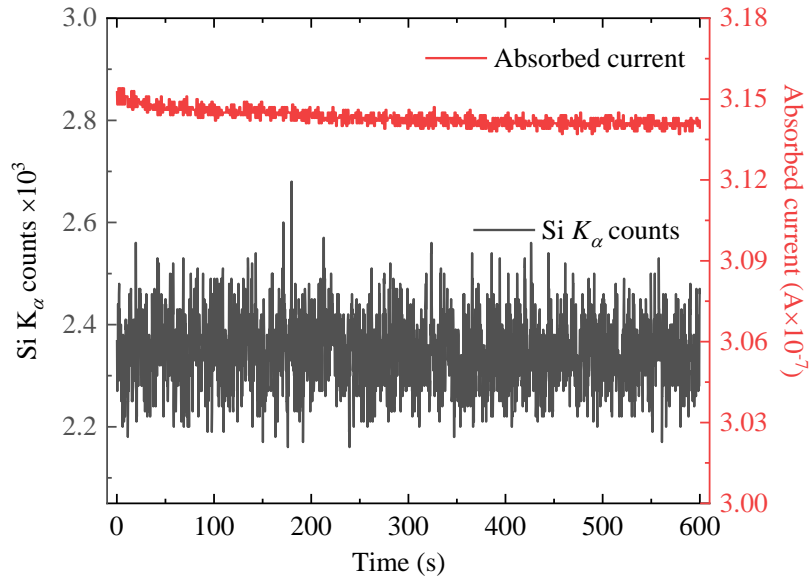
Figure 5.10: Time scan for Si Kα in the GaN: Si calibration sample under "trace analysis" electron-beam operating conditions showing a constant Si Kα count rate and absorbed current as a function of time, showing only minor change in the absorbed current during long counting times.

The measured sample current reflects the proportion of current flowing to ground in conductive specimens. If there was a significant change in the measured sample current during the X-ray acquisition time that would reflect the non-equilibrium build-up of charge within the specimen and/or changing electron emission characteristics. The charge build up can cause a dynamic shape distortion of the excitation and X-ray production volumes, and ultimately lead to unpredictable X-ray emission characteristics [12]. It is important to monitor changes in intensity of the measured element because that can also revel the presence and extent of spectrometer drift, such as that caused by temperature-related changes in diffraction crystal d-spacing [29].

5.5 Other minor effects that were investigated

Since sample contamination with Si was confirmed and cleaning attempts were unsatisfactory it was shown how WDX and SIMS results cannot coincide by any simple adjustment of the analysis conditions. Other minor effects will now be mentioned that could affect the discrepancy between the results from SIMS and WDX are also mentioned. Even though these effects are not fully explored it is worth being aware of them. They include ZAF correction, dead time and crystallographic orientation effects. It is valuable to be able to evaluate the results from several different correction procedures for trace element quantification [76]. In some cases, ZAF correction method may not be the best choice, sometimes φ (ρz) method works better, usually in case of silicates or oxides [41]. As stated previously, analysis of trace elements requires high probe current and long X-ray counting times to measure weak X-ray signals. Since the X-ray count rate of a standard material is much higher compared to trace elements and the effect of the deadtime becomes significant, having same dead time corrections for both measurements can become an issue in the quantification [77]. Due to previously observed changes in F and Cl X-rays intensities of apatite crystals by Stormer et al. [78] and Goldof et al. [79] depending on their orientation related to the incident electron beam, same effect may be observable for the AlGaN:Si smples of different orientations.

5.5.1 ZAF corrections (calcZAF)

By trying different correction routines available in calcZAF software it is possible to check that the error introduced by selection of different ZAF correction routines is no larger than the error associated with the Si statistical uncertainty [46]. The different correction procedures available in CalcZAF software did not produce a noticeable difference in the correction factors. In addition to correction method employed, there are also different tables of physical constants available (e.g. mass absorption coefficients, MAC, however most of them are still empirical and only a few have been obtained experimentally [41].

5.5.2 Dead Time

Each spectrometer in EPMA has a specific deadtime that depends on factors such as electronic circuit design, counter bias, and X-ray energies. The dead time also changes with aging degradation. The dead time of the WDS can be considered to be non-extendable. There is no software available for the measurement of dead time, so it may be only measured manually [77]. The gas proportional counters require certain amount of time to absorb and process each X-ray. Dead time is used to correct for the uncounted time interval of the counter. The correction is more important when dealing with high counts. The dead time constant for gas proportional counters is usually between $1-4$ µs. Incoming X-ray count rate (n) can be calculated for the detected X-ray count rate (n') if the dead time (τ) is known.

$$n = \frac{n'}{1 - n'\tau} \qquad (5.17)$$

The incoming X-ray count rate (n) is expressed as kI_p because it is directly proportional to the beam current I_p. By rewriting Eqs. 5.17 linear from is obtained in Eqs. 5.19 where k is the proportionality constant.

$$Cts_{True} = Cts_{Meas}/(1 - Cts_{Meas}\ DT) \qquad (5.18)$$

$$\frac{n'}{I_p} = (-k\tau)n' + k \qquad (5.19)$$

$$DT = slope/intercept \qquad (5.20)$$

By recording the output count rate (n') using different beam currents (I_p), the time constant can be calculated from the slope ($-k\tau$) and intercept (k). From the plot in Fig. 5.11 it is possible to determine more accurate time constant then those provided by the manufacturer.
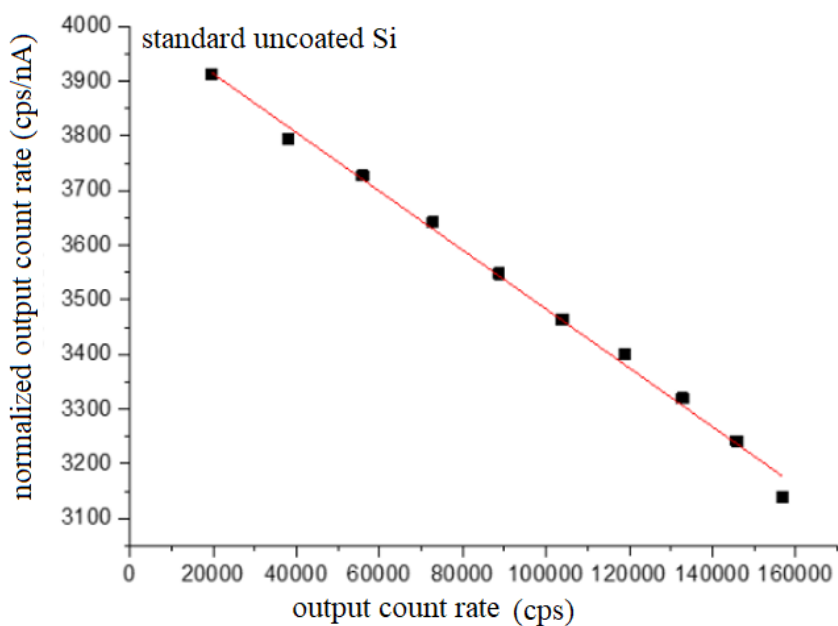
Figure 5.11: Normalised output count rate as a function of the output count rate for the Si K$_\alpha$ on TAPL crystal at 10 kV using Si uncoated standard, spot mode, varying current from 5−50 nA. Red line corresponds to a linear fit.

From the Fig. 5.11 on TAPL spectrometer at 10 kV measured DT is following: DT = 0.00538/4021,2457 = 1.34 μs. The default dead time in Jeol software is 1.1 μs and it cannot be edited, because it would be impractical to measure the dead time whenever quantitative analysis is performed. It is possible that with dead time of 1.1 μs the X-ray intensity of the Si standard might be estimated to be lower than the actual value, with the dead time of 1.4 μs, standard counts would effectively be increased and finally concentration of trace elements would decrease. In practice, the dead time constant only affects measurement of the standard material, but when standard data is employed in quantitative procedure it will affect the trace level results. Possible solution would be to add an pseudo-fixed dead time generator as suggested by Takenori Kato et al. [77] inserted between the SCA/PHA and the pulse counter.

5.5.3 Crystallographic orientation effects

Variation in X–ray intensity can occur not just because of the compositional changes in the sample but due to the electron channelling effects. The effect is the result of the scattering of the electron beam within a crystalline specimen [80]. Electron channelling may be produced when a sample is placed so that a plane or planes are at, or close to, the Bragg angle with respect to the incident electron beam. Any deviation in crystallographic orientation or in lattice constant due to local strain will produce a variation in contrast in the resultant electron channeling contrast imaging (ECCI) micrograph (produced by monitoring the intensity of backscattered or forescattered electrons). [81]. The electron channelling effect is more prominent in low overvoltage analysis [80, 82], and is important to notice that X-ray production rate is a function of the deviation from the exact Bragg condition, and that observed variation in X-ray intensities decrease as specimen thickness increases. Spencer et al. discovered that for medium atomic weight materials and typical microanalysis overvoltages, the orientation dependence of the X-ray signal should be weak— on the order of 1% [83]. The crystallographic effects are not accounted for in the modern quantitative X-ray microanalysis matrix correction schemes ~e.g., Z.A.F. and Phi Rho Z. For example, the atomic number correction does not account for any crystallographic orientation dependence of the backscatter electron yield, and there is no way to correct for variation in the path length over which absorption can occur as a function of crystallographic orientation. The reason why there aren't any corrections for the crystal orientation effect is that the channelling effect is usually negligible.

Figure 5.12 shows an example of a c-plane (0001) AlGaN layer. The BSE image shows contrast not visible in secondary electron topographic images, including grain-to grain and intra-grain variations; these are only partly explained by atomic number contrast caused by Ga-rich areas at grain perimeters (seen also in the WDX and CL maps), with channelling accounting for the smaller scale details [22].
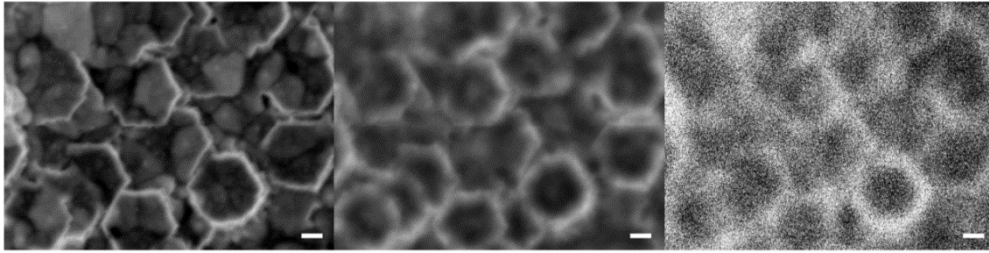
Figure 5.12: (Left) BSE image, (centre) panchromatic CL image and (right) WDX Ga L_α map of a c-plane $Al_{0.82}Ga_{0.18}N$ layer. Acquired at 10 kV; scale bar 1 μm.

Since investigated AlGaN:Si samples consisted of sets with different crystal polarities, polar oriented [0001] and semi-polar oriented layers [11-22], sample orientation may have minor influence on the Si peak X-ray intensity, but since Si peak signal is already weak even a small change due to crystal orientation can have more profound effect on the final trace element concentration. It is possible to have anisotropy in the Si count rate due to sample orientation that can result in overestimation of Si concentrations on samples analysed with the crystallographic c-axis parallel to the electron beam. It can be expected that if the crystal is oriented with the c-axis perpendicular to the electron beam, the count rate of the trace element could increase [84]. More tests have to be performed in order to get conclusive results about influence of sample orientation on dopant X-ray intensity.

5.6 Results

5.6.1 Calibration curve

According to the tests described in the Measurement optimisation, detection limits and inherent contamination sections 5.4 as well in the section describing Minor effects 5.5 all the results appear to confirm that inherent contamination of the sample surfaces with additional Si, that cannot be removed is the cause of the discrepancy between the results from SIMS and WDX. It prevents convergence of the WDX and SIMS results by any simple adjustment of the analysis conditions or with employment of cleaning treatments.

This lead to the proposal that the best solution for using WDX for accurate measurement of doping in $Al_xGa_{1-x}N$ samples is to generate a calibration relation using samples also characterised by D-SIMS. The results listed in Table 5.2 are plotted in Figure 5.13 and show that the Si net intensity value (peak minus background) does not go below about 200 cps/µA even for the samples with very low Si contents, which is attributed to surface contamination with Si (samples TS4142, TS4137, TS5541). These samples (marked by the grey circle) are thus considered not suitable for calibration and so a calibration relation for Si concentrations down to a lower limit defined by a Si net value of 200 cps/µA. Prior to generating this line, the impact of the host material must be accounted for, as these samples consist of $Al_xGa_{1-x}N$ with different AlN% contents (Table 5.4).
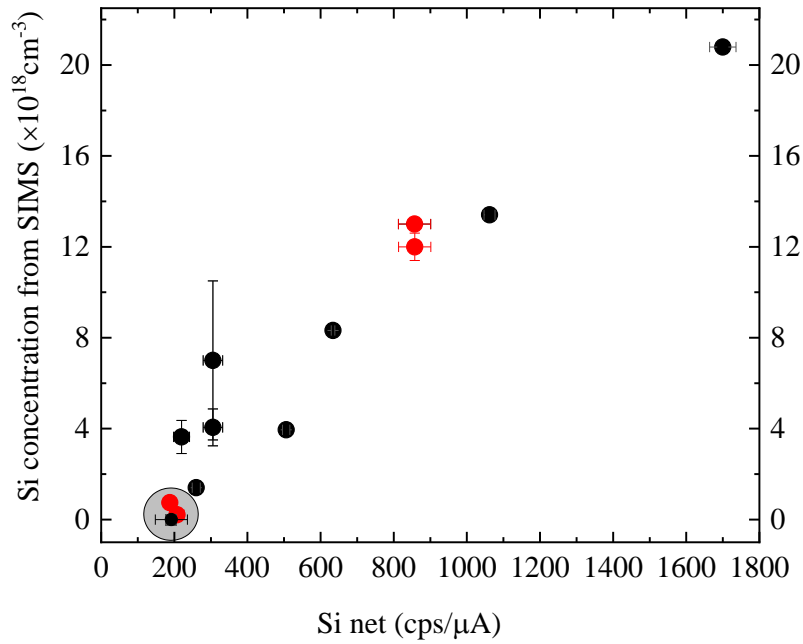
Figure 5.13: Correlation between Si intensity measured by WDX and the concentration from SIMS data for GaN (red points) and $Al_xGa_{1-x}N$ (black points) samples.

5.6.2. ZAF correction

Since, samples mentioned in the Table 5.2 consist of GaN and AlGaN samples of a different AlN% composition and samples of interest (Table 5.4) also have varying AlN content there is a need to develop a unified calibration curve that can be used to measure Si content in samples regardless of varying ZAF correction for Si in the sample (that will vary depending on the AlN content). The change in matrix correction (ZAF correction) for Si for different AlN contents is estimated using the stand-alone CalcZAF software [85] as plotted in Figure 5.16. The different correction procedures available in CalcZAF software did not produce a noticeable difference in the correction factors.

It is important to understand that the ZAF factors are a function of composition, as seen in Figure 5.14. CalcZAF can use composition data to calculate

intensities (*k*-ratios) or calculate composition from intensities using normalised *k*-ratios, raw *k*-ratios or unknown and standard counts [86].
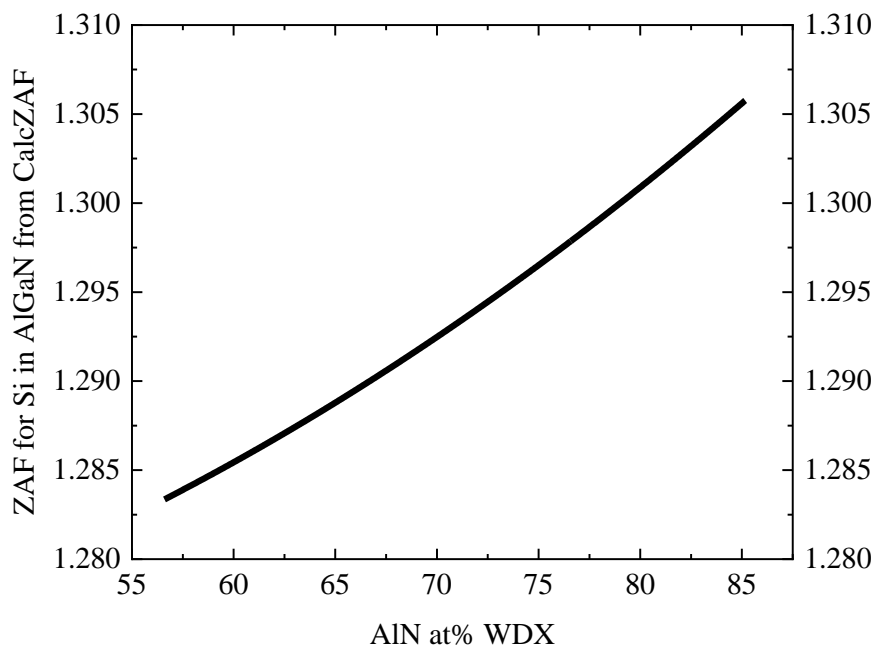
Figure 5.14: Plot of the calculated matrix correction (ZAF correction) factor for Si against AlN at% as measured by WDX for each of the Al$_x$Ga$_{1-x}$N samples.

5.6.3 Calibration curve "GaN" only

The calculated ZAF parameters are then used to adjust all the D-SIMS calibration points to the effective value for a GaN host, as shown in Figure 5.15. This resulting calibration relation allows the Si content to be estimated in samples of all Al$_x$Ga$_{1-x}$N compositions by measuring the Si intensity, afterwards using the GaN calibration curve with the appropriate correction.
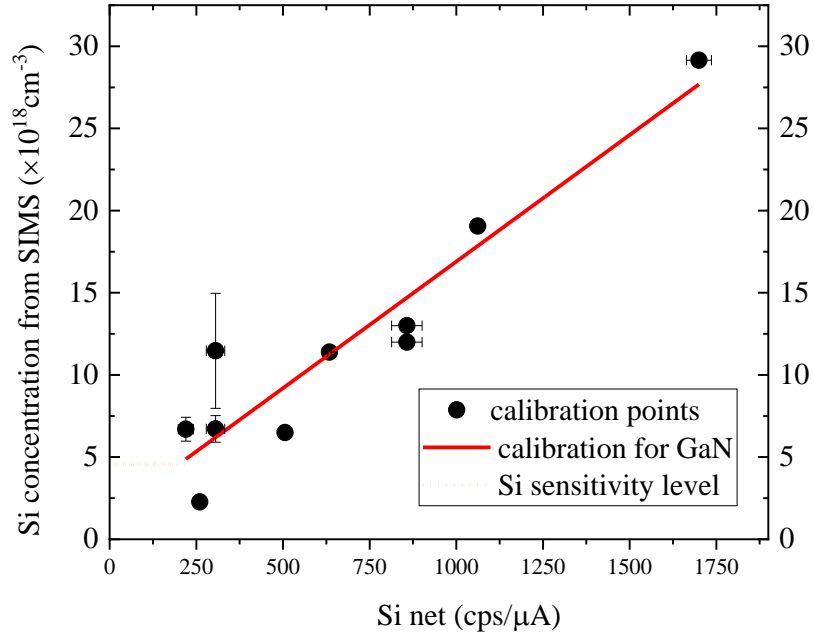
Figure 5.15: Calibration relation with all the points representing Si intensity in GaN (For the Al$_x$Ga$_{1-x}$N points the Si concentration from D-SIMS is converted to its equivalent for GaN using calcZAF software). The orange dotted line represents the Si sensitivity level for GaN.

5.6.4 Si in AlGaN samples

Now it is possible to calculate the Si content in samples of interest by using the measuring Si intensity. Extracting the Si content from the graph and then applying correct ZAF correction obtained with calcZAF software will give concentration of Si in AlGaN sample (Table 5.4), using the following equation.

$$C_i^{unk} = \frac{I_i^{unk}}{I_i^{std}} \frac{ZAF_i^{unk}}{ZAF_i^{std}} C_i^{std} \qquad (5.21)$$

Where C_i^{unk} is the wt% of element i in the sample, I_i^{unk} intensity of element i in the sample, C_i^{std} is the wt% of element i in the standard, I_i^{std} intensity of element

i in the standard, ZAF_i^{unk} matrix correction for sample and ZAF_i^{std} matrix correction for standard [87]. This process is illustrated using the series of $Al_xGa_{1-x}N$ samples listed in Table 5.4. The measured intensity values, Si net (cps/µA), are adjusted to the effective Si net values for GaN, using the ZAF correction procedure, and these are then converted to Si concentration using the calibration curve. The calculated Si concentrations in $Al_xGa_{1-x}N$ are plotted in Figure 5.16, which also shows the calibration line for GaN for comparison. This method enables the Si concentration in $Al_xGa_{1-x}N$ samples of any composition to be estimated by measuring the Si intensity. For samples with Si net ≤ 200 cps/µA (sample A1SP) the equivalent Si concentration is set to the sensitivity limit of 35 ppm, which corresponds to concentrations ranging from 2.4×10^{18} cm^{-3} for AlN or 4.6×10^{18} cm^{-3} for GaN, calculated from the calibration curve in Fig. 5.15).

Table 5.4: List of unknown $Al_xGa_{1-x}N$ samples for which independent constraint on the composition is not available, measured AlN at% using WDX and Si K_α intensity values together with the calculated Si concentration (Crystal orientation [0001] AxP, orientation [11$\bar{2}$2] AxSP).

Sample name	WDX AlN at%	WDX Si net (cps/µA)	Calculated ZAF factor for the Si K_α in $Al_xGa_{1-x}N$	Calculated Si concentration (10^{18} cm^{-3}) using calibration method and calcZAF software	Calculated Si concentration (ppm) using calibration method and calcZAF software
A1SP	56.6 ± 0.6	175 ± 16	1.283	3.1	31
A2SP	65.5 ± 0.7	440 ± 13	1.289	5.7	61
A3SP	61.2 ± 0.7	469 ± 54	1.286	6.2	65
A4SP	59.4 ± 0.7	463 ± 19	1.285	6.2	64
A5SP	59.6 ± 0.7	374 ± 10	1.285	5.2	54
A1P	63.0 ± 0.7	218 ± 33	1.287	3.4	36
A2P	71.7 ± 0.8	253 ± 22	1.294	3.5	40
A3P	68.8 ± 0.7	320 ± 6	1.292	4.3	47
A4P	62.7 ± 0.7	534 ± 9	1.287	6.8	72
A5P	69.3 ± 0.7	743 ± 9	1.292	8.6	96
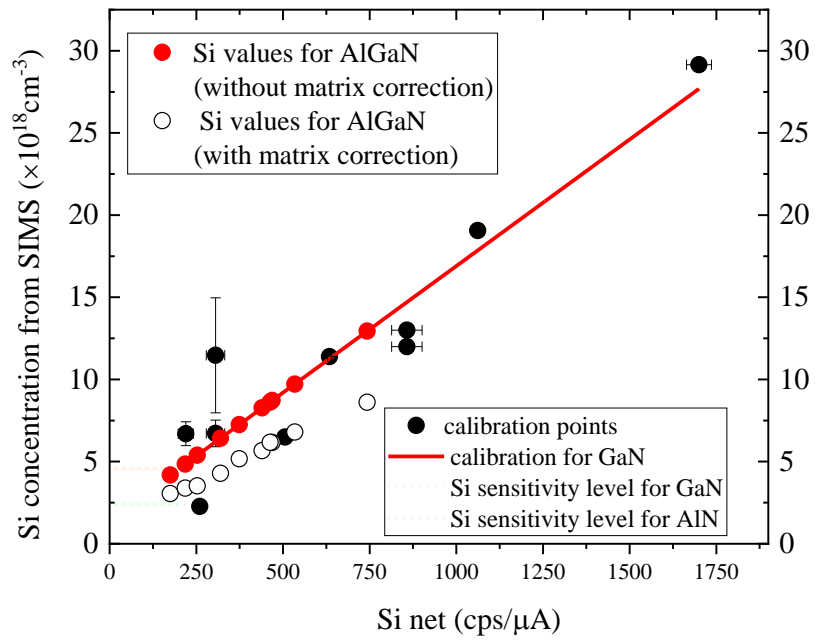
Figure 5.16: Values for Si concentration in $Al_xGa_{1-x}N$:Si layers plotted against the measured Si net signal. The line is the calculated calibration for GaN:Si and the points differ from this line according to the amount of AlN contained in the host material.

These calculated Si concentrations are plotted against the disilane to group-III ratios (Si_2H_6/III-ratios) [55, 60, 61] (Figure 5.17.). More details about the samples can be found in Chapter 6.
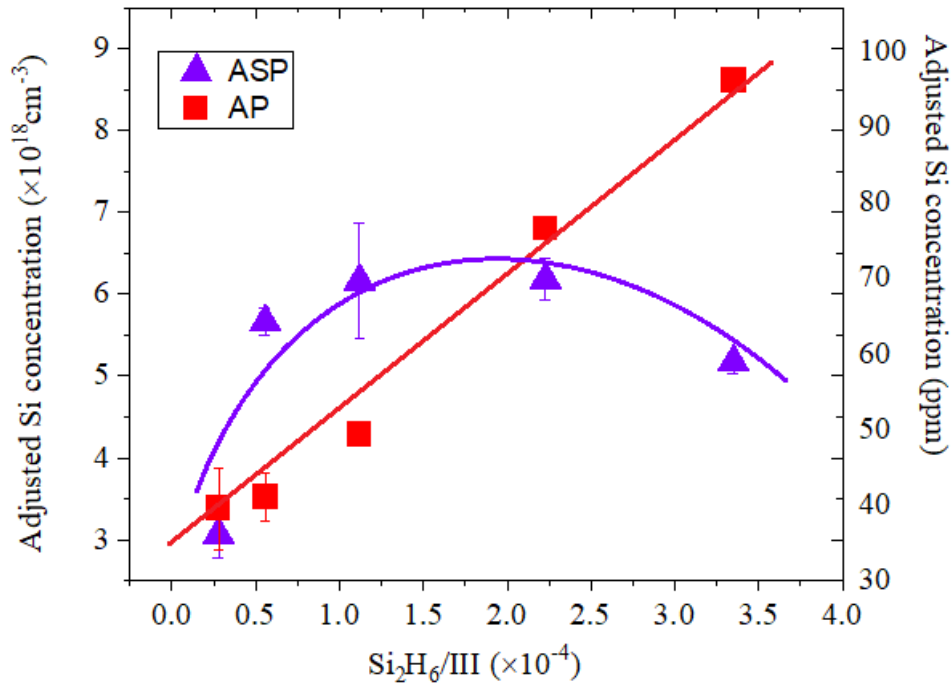
Figure 5.17: Si concentration of the $Al_xGa_{1-x}N$ doped layer as a function of disilane to group-III ratio, as evaluated by WDX. The solid lines provide guides to the eye.

5.6.5 Complementary signals

Finally, a significant strength of electron beam based microanalysis techniques lies in the possibility of combining them with complementary and simultaneously-acquired signals. One example of the complementary data that can be collected is CL, with a spectrum for sample A5P shown in Fig. 5.18, more data is can be found in Chapter 6. The different emission peaks are annotated with their likely origin, including single and doubly charged group III vacancy complexes involving oxygen (V_{III} complex) and near-band edge emission (NBE).
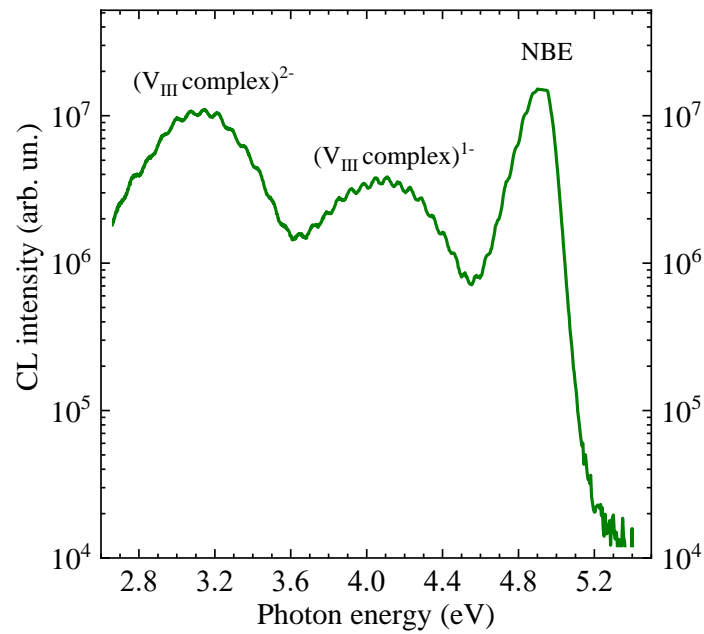
Figure 5.18: The CL spectrum for a polar n-AlGaN sample (A5P), showing emission peaks due to near band-edge (NBE) emission and group III vacancy complexes.

Another recent example of complementary data that can be collected alongside WDX is structural information from electron channelling contrast imaging (ECCI) [27]. In this case standard secondary electron detector is utilised to reveal the influence of incident beam diffraction ("channelling") on the energy and momentum distribution of the backscattered electrons.

5.7 Conclusion

The use of WDX spectroscopy is demonstrated in a commercially available EPMA instrument for the measurement of silicon doping levels in the wide bandgap $Al_xGa_{1-x}N$ layers. A previously reported limitation with over-estimates of the Si contents was thoroughly investigated and was assigned to surface contamination. Various investigations were completed to establish the best conditions for quantitative analysis of Si in $Al_xGa_{1-x}N$. An analytical routine was introduced for measuring the trace Si levels, consisting of separate measurement of Si with high current and long counting times followed by calibration using D-SIMS measurements. By measuring silicon intensities and using a calibration curve method using the SIMS data along with calculated ZAF correction values it was possible to determine doping levels of order $(3–10) \times 10^{18}$ cm^{-3} in $Al_xGa_{1-x}N$ layers with varying AlN contents and polarity. The highest values of Si incorporation were observed for polar samples (100 ppm), whilst saturation of Si incorporation was seen for semipolar samples at high Si/III ratio. Advantages of the WDX approach include high lateral spatial resolution and the ability to determine the alloy composition of the major elements, such as Al, Ga and N, at the same time as the doping levels. The standards used in WDX analysis are more accessible compared to ion-implanted standards required for the D-SIMS analysis. Apart from quantitative abilities of the EPMA instrument, another major advantage in the examination of the semiconductor alloys is the correlation of WDX data with other microscopy techniques such as CL and ECCI as well as the high resolution mapping capabilities.

Bibliography

1. Sato, A., et al., *Examination of Analytical Conditions for Trace Elements Basde on the Detection Limit of EPMA (WDS)*. JEOL News, 2007. **42E**(No.1).
2. Robin, E., Mollard, N., Guilloy, K., Pauc, N., Gentile, P., Fang, Z., Daudin, B., Amichi, L., Jouneau, P., Bougerol, C., Delalande, M. and Bavencove, A., *Quantification of dopants in nanomaterial by SEM/EDS.* . European Microscopy Congress 2016: Proceedings, (Ed.). 2016.
3. Zhao, D., Y. Zhang, and E.J. Essene, *Electron probe microanalysis and microscopy: Principles and applications in characterization of mineral inclusions in chromite from diamond deposit.* Ore Geology Reviews, 2015. **65**: p. 733-748.
4. Reed, S.J.B., *Quantitative Trace Analysis by Wavelength-Dispersive EPMA.* Microchimica Acta, 2000. **132**(2): p. 145-151.
5. Batanova, V.G., A.V. Sobolev, and V. Magnin, *Trace element analysis by EPMA in geosciences: detection limit, precision and accuracy.* IOP Conference Series: Materials Science and Engineering, 2018. **304**: p. 012001.
6. Goldstein, J.I., *Distribution of germanium in the metallic phases of some iron meteorites.* Journal of Geophysical Research (1896-1977), 1967. **72**(18): p. 4689-4696.
7. Merlet, C. and J.-L. Bodinier, *Electron microprobe determination of minor and trace transition elements in silicate minerals: A method and its application to mineral zoning in the peridotite nodule PHN 1611.* Chemical Geology, 1990. **83**(1): p. 55-69.
8. Donovan, J.J., H.A. Lowers, and B.G. Rusk, *Improved electron probe microanalysis of trace elements in quartz.* American Mineralogist, 2011. **96**(2-3): p. 274-282.
9. Fialin, M., et al., *Trace element analysis with the electron microprobe; new data and perspectives.* American Mineralogist, 1999. **84**(1-2): p. 70-77.
10. Jercinovic, M.J. and M.L. Williams, *Analytical perils (and progress) in electron microprobe trace element analysis applied to geochronology: Background acquisition, interferences, and beam irradiation effects.* American Mineralogist, 2005. **90**(4): p. 526-546.
11. Donovan, J.J., J.W. Singer, and J.T. Armstrong, *A new EPMA method for fast trace element analysis in simple matrices.* American Mineralogist, 2016. **101**(8): p. 1839-1853.
12. Reed, S.J.B., *Optimization of Wavelength Dispersive X-Ray Spectrometry Analysis Conditions.* Journal of research of the National Institute of Standards and Technology, 2002. **107**(6): p. 497-502.
13. Jercinovic, M.J., et al., *Trace analysis in EPMA.* IOP Conference Series: Materials Science and Engineering, 2012. **32**: p. 012012.
14. Allaz, J.M., et al., *Electron Microprobe Analysis of Minor and Trace Elements in Beam Sensitive Materials: How Far Can We Go?* Microscopy and Microanalysis, 2019. **25**(S2): p. 2312-2313.
15. Fournelle, J., *Problems in Trace Element EPMA: Modeling Secondary Fluorescence with PENEPMA*, in *AGU Fall Meeting Abstracts*. 2007. p. V51A-0329.

16. Carpenter, P., et al., *Characterization of Corning EPMA Standard Glasses 95IRV, 95IRW, and 95IRX.* Journal of research of the National Institute of Standards and Technology, 2002. **107**(6): p. 703-718.

17. Buse, B., et al., *Secondary Fluorescence in WDS: The Role of Spectrometer Positioning.* Microscopy and Microanalysis, 2018. **24**(6): p. 604-611.

18. Deatcher, C., et al., *Wavelength-dispersive x-ray microanalysis as a novel method for studying magnesium doping in gallium nitride epitaxial films.* Semiconductor Science and Technology, 2006. **21**: p. 1287-1295.

19. Kusch, G., et al., *Analysis of doping concentration and composition in wide bandgap AlGaN:Si by wavelength dispersive x-ray spectroscopy.* Semiconductor Science and Technology, 2017. **32**(3): p. 7.

20. Jercinovic, M., M. Williams, and E. D. Lane, *In-situ trace element analysis of monazite and other fine-grained accessory minerals by EPMA.* Chemical Geology, 2008. **254**: p. 197-215.

21. Batanova, V., A. Sobolev, and V. Magnin, *Trace element analysis by EPMA in geosciences: detection limit, precision and accuracy.* Vol. 304. 2018. 012001.

22. Edwards, P.R., et al., *You Do What in Your Microprobe?! The EPMA as a Multimode Platform for Nitride Semiconductor Characterization.* Microscopy and Microanalysis, 2018. **24**(S1): p. 2026-2027.

23. W., M.R., et al., *Cathodoluminescence spectral mapping of III-nitride structures.* physica status solidi (a), 2004. **201**(4): p. 665-672.

24. Lee, M.R., et al., *Imaging of Cathodoluminescence Zoning in Calcite by Scanning Electron Microscopy and Hyperspectral Mapping.* Journal of Sedimentary Research, 2005. **75**(2): p. 313-322.

25. Edwards, P.R. and R.W. Martin, *Cathodoluminescence nano-characterization of semiconductors.* Semiconductor Science and Technology, 2011. **26**(6): p. 064005.

26. Edwards, P.R., et al., *High-Resolution Cathodoluminescence Hyperspectral Imaging of Nitride Nanostructures.* Microscopy and Microanalysis, 2012. **18**(6): p. 1212-1219.

27. Naresh-Kumar, G., et al., *Metrology of crystal defects through intensity variations in secondary electrons from the diffraction of primary electrons in a scanning electron microscope.* Ultramicroscopy, 2020. **213**: p. 112977.

28. Wallace, M.J., et al., *Bias dependence and correlation of the cathodoluminescence and electron beam induced current from an InGaN/GaN light emitting diode.* Journal of Applied Physics, 2014. **116**(3): p. 033105.

29. Newbury, D.E., *Barriers to quantitative electron microanalysis for low voltage electron microscopy.* Journal of Research of the National Institute of Standards and Technology, 2002. **107**(6): p. 605-619.

30. Michałowski, P.P., S. Złotnik, and M. Rudziński, *Three dimensional localization of unintentional oxygen impurities in gallium nitride.* Chemical Communications, 2019. **55**(77): p. 11539-11542.

31. Martin, R.W., et al., *Depth profiling of ion-implanted AlInN using time-of-flight secondary ion mass spectrometry and cathodoluminescence.* physica status solidi c, 2006. **3**(6): p. 1927-1930.

32. Wei, X., et al., *Characterization of nitride-based LED materials and devices using TOF-SIMS.* Surface and Interface Analysis, 2014. **46**(S1): p. 299-302.

33. Pickrell, G.W., et al., *Regrown Vertical GaN p–n Diodes with Low Reverse Leakage Current.* Journal of Electronic Materials, 2019. **48**(5): p. 3311-3316.

34. Klump, A., et al., *Improvement in detection limit for time-of-flight SIMS analysis of dopants in GaN structures.* Journal of Vacuum Science & Technology B, 2018. **36**(3): p. 03F102.

35. Rinaldi, R. and X. Llovet, *Electron Probe Microanalysis: A Review of the Past, Present, and Future.* Microscopy and Microanalysis, 2015. **21**(5): p. 1053-1069.

36. Moy, A., J.H. Fournelle, and A. von der Handt, *Solving the iron quantification problem in low-kV EPMA: An essential step toward improved analytical spatial resolution in electron probe microanalysis—Olivines.* American Mineralogist, 2019. **104**(8): p. 1131-1142.

37. MüLler, A., et al., *Trace elements in quartz - a combined electron microprobe, secondary ion mass spectrometry, laser-ablation ICP-MS, and cathodoluminescence study.* European Journal of Mineralogy, 2003. **15**(4): p. 747-763.

38. Philibert, J. and R. Tixier, *Electron penetration and the atomic number correction in electron probe microanalysis.* Journal of Physics D: Applied Physics, 1968. **1**(6): p. 685-694.

39. Love, G., M.G.C. Cox, and V.D. Scott, *Assessment of Philibert's absorption correction models in electron-probe microanalysis.* Journal of Physics D: Applied Physics, 1975. **8**(14): p. 1686-1702.

40. Reed, S.J.B., *Characteristic fluorescence corrections in electron-probe microanalysis.* British Journal of Applied Physics, 1965. **16**(7): p. 913-926.

41. https://www.dal.ca/sites/electron-microprobe-lab/analysis.html.

42. Ltd, J., *JEOL JXA-8530F manual.*

43. Heinrich, K.F.J. and R.L. Myklebust, *A simple correction procedure for quantitative electron microprobe analysis.* NBS Technical note 719, 1972(US department of commerce).

44. McSwiggen, P., *Characterisation of sub-micrometre features with the FE-EPMA.* IOP Conference Series: Materials Science and Engineering, 2014. **55**: p. 012009.

45. Donovan, J., H. Lowers, and B. Rusk, *Improved electron probe microanalysis of trace elements in quartz.* American Mineralogist, 2011. **96**: p. 274-282.

46. Pyle, J., et al., *Contributions to precision and accuracy of monazite microprobe ages.* American Mineralogist, 2005. **90**: p. 547-577.

47. Marinenko, R.B. and S. Leigh, *Uncertainties in electron probe microanalysis.* IOP Conference Series: Materials Science and Engineering, 2010. **7**: p. 012017.

48. Drouin, D., et al., *CASINO V2.42—A Fast and Easy-to-use Modeling Tool for Scanning Electron Microscopy and Microanalysis Users.* Scanning, 2007. **29**(3): p. 92-101.

49. Lifshin, E. and R. Gauvin, *Minimizing Errors in Electron Microprobe Analysis.* Microscopy and microanalysis : the official journal of

Microscopy Society of America, Microbeam Analysis Society, Microscopical Society of Canada, 2001. **7**: p. 168-177.

50. Drouin, D., et al., *CASINO V2.42—A Fast and Easy-to-use Modeling Tool for Scanning Electron Microscopy and Microanalysis Users.* Scanning, 2007. **29**(3): p. 92-101.

51. Kerrick, D., L. Eminhizer, and J. Villaume, *The role of carbon film thickness in electron microprobe analysis.* American Mineralogist 1973. **58**: p. 920-925.

52. Fournelle, J., *Silicate Peak Shifts, Spectrometer Peaking Issues and Standard/Specimen Size Discrepancies in EPMA: 3 Bumps in the Road to the Goal of 1% Accuracy.* AGU Spring Meeting Abstracts, 2006.

53. Zhang, C., et al., *A Practical Method for Accurate Measurement of Trace Level Fluorine in Mg- and Fe-Bearing Mineral and Glass Using Electron Probe Microanalysis.* Geostandards and Geoanalytical Research, 2016. **40**: p. 351-363.

54. Geller, J.D. and C. Herrington, *High Count Rate Electron Probe Microanalysis.* Journal of research of the National Institute of Standards and Technology, 2002. **107**(6): p. 503-508.

55. Dinh, D.V., P. Pampili, and P.J. Parbrook, *Silicon doping of semipolar $(11\bar{2}2)Al_xGa_{1-x}N(0.50{\leq}x{\leq}0.55)$.* Journal of Crystal Growth, 2016. **451**: p. 181-187.

56. Knauer, A., et al., *AlGaN layer structures for deep UV emitters on laterally overgrown AlN/sapphire templates.* Physica Status Solidi (A) Applications and Materials Science, 2013. **210**(3): p. 451-454.

57. Kusch, G., et al., *Influence of substrate miscut angle on surface morphology and luminescence properties of AlGaN.* Applied Physics Letters, 2014. **104**(9): p. 092114.

58. Li, H., T.C. Sadler, and P.J. Parbrook, *AlN heteroepitaxy on sapphire by metalorganic vapour phase epitaxy using low temperature nucleation layers.* Journal of Crystal Growth, 2013. **383**: p. 72-78.

59. Mehnke, F., et al., *Electronic properties of Si-doped $Al_x Ga_{1-x}N$ with aluminum mole fractions above 80%.* Journal of Applied Physics, 2016. **120**(14): p. 145702.

60. Pampili, P., et al., *Significant contribution from impurity-band transport to the room temperature conductivity of silicon-doped AlGaN.* Journal of Physics D: Applied Physics, 2018. **51**(6).

61. Dinh, D.V., S.N. Alam, and P.J. Parbrook, *Effect of V/III ratio on the growth of $(11\bar{2}2)$ AlGaN by metalorganic vapour phase epitaxy.* Journal of Crystal Growth, 2016. **435**: p. 12-18.

62. Foronda, H.M., et al., *Electrical properties of (11-22) Si:AlGaN layers at high Al contents grown by metal-organic vapor phase epitaxy.* Applied Physics Letters, 2020. **117**(22): p. 221101.

63. Donovan, J. and M. Rowe, *Techniques for improving quantitative analysis of mineral glasses.* Geochimica et Cosmochimica Acta Supplement, 2005.

64. Jörchel, P., et al., *Quantification of matrix and impurity elements in $Al_xGa_{1-x}N$ compounds by secondary ion mass spectrometry.* Journal of Vacuum Science & Technology B, 2016. **34**(3): p. 03H128.

65. Koleske, D.D., et al., *Influence of MOVPE growth conditions on carbon and silicon concentrations in GaN.* Journal of Crystal Growth, 2002. **242**(1): p. 55-69.

66. Tessarek, C., et al., *The Role of Si during the Growth of GaN Micro- and Nanorods.* Crystal Growth & Design, 2014. **14**(3): p. 1486-1492.

67. Ren, C.X., et al., *Nanoscopic insights into the effect of silicon on core-shell InGaN/GaN nanorods: Luminescence, composition, and structure.* J. Appl. Phys., 2018. **123**(4).

68. Donovan, J.J., D.A. Snyder, and M.L. Rivers, *An Improved Interference Correction for Trace Element Analysis.* Microbeam Analysis, 1993. **2**: p. 23-28.

69. Isabell, T.C., et al., *Plasma Cleaning and Its Applications for Electron Microscopy.* Microscopy and Microanalysis, 1999. **5**(2): p. 126-135.

70. Limandri, S., A. Carreras, and J. Trincavelli, *Effects of the Carbon Coating and the Surface Oxide Layer in Electron Probe Microanalysis.* Vol. 16. 2010. 583-93.

71. Merlet, C. and X. Llovet, *Uncertainty and capability of quantitative EPMA at low voltage – A review.* IOP Conference Series: Materials Science and Engineering, 2012. **32**: p. 012016.

72. Carpenter, P.K., *EPMA Standards: The Good, the Bad, and the Ugly.* Microscopy and Microanalysis, 2008. **14**(S2): p. 530-531.

73. Hughes, E.C., et al., *Low analytical totals in EPMA of hydrous silicate glass due to sub-surface charging: Obtaining accurate volatiles by difference.* Chemical Geology, 2019. **505**: p. 48-56.

74. Carpenter, P., et al., *Characterization of Corning EPMA standard glasses 95IRV, 95IRW, and 95IRX.* Journal of research of the National Institute of Standards and Technology, 2002. **107**.

75. Stock, M.J., et al., *New constraints on electron-beam induced halogen migration in apatite†.* American Mineralogist, 2015. **100**(1): p. 281-293.

76. Marinenko, R.B., *Uncertainties in electron probe microanalysis.* IOP Conference Series: Materials Science and Engineering, 2010. **7**(1): p. 012017.

77. Kato, T., et al., *Pseudo-fixed dead time circuit for designing and implementation of JEOL-type X-ray counting systems.* Chemical Geology, 2018. **484**: p. 16-21.

78. Stormer, J.C., M.L. Pierson, and R.C. Tacker, *Variation of F and Cl X-ray intensity due to anisotropic diffusion in apatite during electron microprobe analysis.* American Mineralogist, 1993. **78**(5-6): p. 641-648.

79. Beth, G., D.W. James, and E.H. Daniel, *Characterization of fluor-chlorapatites by electron probe microanalysis with a focus on time-dependent intensity variation of halogens.* American Mineralogist, 2012. **97**(7): p. 1103-1115.

80. Meisenkothen, F., et al., *Electron Channeling: A Problem for X-Ray Microanalysis in Materials Science.* Microscopy and Microanalysis, 2009. **15**(2): p. 83-92.

81. Trager-Cowan, C., et al., *Scanning electron microscopy as a flexible technique for investigating the properties of UV-emitting nitride semiconductor thin films.* Photonics Research, 2019. **7**(11): p. B73-B82.

82. Miyake, S., K. Hayakawa, and R. Miida, *Variation of emission yield of X-rays from crystals with diffraction condition of exciting electrons.* Vol. 24. 1968. 182-191.

83. *Electron microscopy 1972: proceedings of the Fifth European Congress on Electron Microscopy, University of Manchester, 5-12 September*

1972. Institute of Physics. Conference series no. 14. 1972, London: Institute of Physics. xxvii, 683 p.

84. Goldoff, B., J. Webster, and D. Harlov, *Characterization of fluor-chlorapatite by electron probe microanalysis with a focus on time-dependent intensity variation of halogens.* American Mineralogist, 2012. **97**: p. 1103.

85. Donovan, J., P. Pinard, and H. Demers, *High Speed Matrix Corrections for Quantitative X-ray Microanalysis Based on Monte Carlo Simulated K-Ratio Intensities.* Microsc Microanal, 2019. **25**(3): p. 735-742.

86. Donovan, J., P. Pinard, and H. Demers, *High Speed Matrix Corrections for Quantitative X-ray Microanalysis Based on Monte Carlo Simulated K-Ratio Intensities.* Microscopy and Microanalysis, 2019. **25**(3): p. 735-742.

87. Castaing, R., *Application des Sondes Electroniques a une methode d'analyse ponctuelle chimique et cristallographique.* These Universite de Paris 1951, 1952.

Chapter 6

6. Polar and semipolar Si-doped AlGaN alloys

6.1 Introduction

$Al_xGa_{1-x}N$ is a promising material for optoelectronic devices such as ultraviolet (UV) light-emitting diodes (LEDs) and laser diodes operating in the wavelength range from 210 to 365 nm, depending on the AlN mole fraction x.[1-3] It is also possible to control $Al_xGa_{1-x}N$ properties such as spontaneous and piezoelectric polarization constants, and lattice constants through group-III compositions in order to obtain the optimal characteristics for the target nitride devices.[4] More details about III-nitride properties are presented in Chapter 2. Most $Al_xGa_{1-x}N$ layers are grown on sapphire substrates due to limited availability of native AlN substrates (generally only with small diameters, typically about 1", and at very high cost). Heteroepitaxy on sapphire substrates usually results in growth of $Al_xGa_{1-x}N$ layers with high threading dislocation densities due to the lattice and thermal expansion coefficient mismatches.[5, 6] Detailed discussion about type of substrates in presented with Chapter 3, section 7. These are significant challenges for the production of high quality AlN-rich $Al_xGa_{1-x}N$ films needed for devices.[2] $Al_xGa_{1-x}N$-based LEDs have attracted a lot of attention, with a view to increasing the low emission efficiencies for devices emitting below 300 nm.[3] This lower emission efficiency is a result of various factors, including high dislocation densities, high resistivity and poor light extraction efficiency.[7] $Al_xGa_{1-x}N$-based deep-ultraviolet (DUV) LED bare dies with external quantum efficiencies (EQEs) of 3.5% at 265 nm, over 4.5% at 270 nm, and over 6% between 280 nm and 300 nm without encapsulation and with a p-GaN contact layer have been reported.[7, 8] However, for LEDs emitting around 250 nm, EQEs remain around 2%.[1] UV-LED devices are presented in Chapter 2. One of the major requirements for the device fabrication is successful doping with Si, which is the most common donor for n-type $Al_xGa_{1-x}N$ layers.[9, 10] The Si doping changes the structural, electrical and optical properties of the $Al_xGa_{1-x}N$ material. The main changes are in electric

conductivity,[11] but there are also changes in luminescence efficiency,[12] optical polarization,[13] point defects density,[13, 14] and mechanical strain,[15] particularly through the phenomenon of dislocation inclination.[16] As the AlN fraction increases above 0.8 it becomes increasingly challenging to obtain high conductivity.[10, 17] This effect arises from the self-compensation effects of the Si donor and from a transition of Si from a shallow donor to a DX centre.[18, 19] In turn this leads to an increase in activation energy E_A of Si with increasing AlN fraction.[10, 17] Other factors that influence carrier compensation in the $Al_xGa_{1-x}N$ material are threading dislocations, unintentional impurities and native defects.[20] Challenges associate with Si doping of AlGaN alloys are discussed in more details within Chapter 2.

Trap states introduced by defects in the bandgap often reduce the electrical conductivity.[21] They can be associated with specific luminescence peaks from AlGaN, making it possible to use cathodoluminescence spectroscopy employed in this work and to confirm the existence of different defects. A range of defects are present in AlGaN, including cation vacancies $(V_{III})^{3-}$, defect complexes comprising the cation vacancy plus oxygen, with either one or two negative charges. These defects have small formation energies in AlN-rich AlGaN and are easily formed in undoped and Si-doped AlGaN layers.[22] Mehnke et. al [23] showed how the drop in the resistivity of AlGaN: Si layers is related to the self- compensation effects that may be attributed to the increasing formation of vacancies or vacancy-oxygen complexes with increasing Al content. It has been confirmed that the increase of the resistivity with increasing Al is mainly caused by a decrease in the carrier density.[23, 24] For the set of samples studied, compensation effects were confirmed for semipolar and polar samples, where for the optimised (A4SP) sample a carrier concentration of $\sim 1.2 \times 10^{19} cm^{-3}$ was measured but on further increase in the Si/III ratio (sample A5SP) the carrier concentration and mobility decreased, indicating the beginning of Si over-compensation.[25] For the polar set of samples, a significant amount of the conductivity was due to phonon-assisted hopping among localized states in the impurity band. Free-carrier concentration in the conduction band has already reached its maximum of $1.6 \times 10^{18} cm^{-3}$ at a Si/III ratio of 2.8×10^{-5} cm^{-3} (data provided by growers, sample A1P) and any further increase of dopant

atoms supplied during growth only enhances the impurity-band conduction with concentrations of the carriers participating in this type of transport that increase from 2.1×10^{18} cm^{-3} up to 4.3×10^{18} cm^{-3}. This process eventually stops when a critical Si/III ratio is reached and the band-like channel starts to degrade (i.e. at sample A4P)) and above.[26]

Using CL to identify the suppression of these vacancy complex defects will lead to further improvements in the conductivity.

In the case of the semipolar AlGaN a minimum resistivity of 0.018 Ωcm was reported for the optimised layer with 60% AlN content (A4SP). [25] For semipolar AlGaN samples with 60% AlN content Jo et al. reported resistivity of 0.009 Ω cm.[27] For the polar samples with 60% AlN content the reported resistivity values were much higher, e.g. ~10 Ωcm for sample A1P. [26] The resistivity in high AlN content AlGaN has been shown to increase steeply from 0.026 Ω cm to 2.62 Ω cm as AlN content increased from 82 to 95%.[23]

Traditionally, $Al_xGa_{1-x}N$ is grown in the polar (0001) c-plane orientation because it is relatively easy to obtain higher material quality in this orientation. The drawback of this orientation is that the corresponding structures suffer from a strong polarization-induced quantum confined Stark effect and exciton localization.[28, 29] Growth in semipolar directions can significantly reduce the polarization-induced electrical fields. Furthermore, exciton localization in semipolar $Al_xGa_{1-x}N$ is significantly reduced compared to c-plane $Al_xGa_{1-x}N$ due to a reduction in alloy compositional fluctuations.[30, 31] As a consequence, semipolar $Al_xGa_{1-x}N$ has significant potential in terms of improving the performance of DUV LEDs. Different growing orientations are reviewed in Chapter 2.

This chapter reports on a systematic study of polar and semipolar n-type doped $Al_xGa_{1-x}N$:Si/AlN layers grown on sapphire by metalorganic chemical vapour deposition (MOCVD) with varied Si/group-III ratios in the gas phase. The samples studied were 0.8–1.1 μm-thick layers with Si concentrations ([Si]) in the range from 2×10^{18} cm^{-3} to 1×10^{19} cm^{-3}, grown along polar (0001) and semipolar (11-22) planes. Different planes are described in Figure 2.5, Chapter 2. High AlN alloy fraction samples were investigated because the difference in the lattice constants between

the $Al_xGa_{1-x}N$ and the AlN layer decreases with increasing AlN alloy fraction, reducing the density of misfit dislocations.[32] Systematic reports comparing the optical properties of semipolar and polar $Al_xGa_{1-x}N$ materials should be valuable with a view to guiding improvements in material quality. This study has been designed to determine how the different $Al_xGa_{1-x}N$ crystal orientations (polar (0001) and semipolar (11-22)) affect group-III composition and Si incorporation.

Wavelength dispersive X-ray (WDX) microanalysis and cathodoluminescence (CL) spectroscopy were used to evaluate the doping characteristics and optical properties of a wide range of Si-doped $Al_xGa_{1-x}N$ layers (n-$Al_xGa_{1-x}N$). More details about both experimental technique scan be found in Chapter 3. Optical characterization using cathodoluminescence (CL) spectroscopy allowed analysis of near band edge emission in the range 4.0–5.4 eV as well as various deep impurity transition peaks in the range 2.7–4.8 eV. The combination of spatially-resolved characterization techniques, including CL and WDX, has provided detailed information on how the crystal growth direction affects the alloy and dopant concentrations.

6.2 Experimental details

The $Al_xGa_{1-x}N$ films were grown in an Aixtron 3×2 inch close-coupled showerhead MOCVD reactor on (0001)- and (11-22)-oriented AlN/sapphire templates for polar and semipolar samples, respectively. The templates were prepared as described in Refs. [33] and [34] for polar and semipolar orientations, respectively. Trimethylgallium (TMGa) and trimethylaluminum (TMAl) were used as group-III precursors, and ammonia (NH3) was used as the nitrogen precursor. H_2 was used as the carrier gas and disilane (Si_2H_6) as the doping source. The AlN fraction was controlled by varying TMAl/(TMGa + TMAl) ratio, V/III ratios and growth rate. Three series of experiments were performed at different growth conditions, varying the Si_2H_6/III ratio while keeping all other parameters nominally fixed. Detailed description of MOCVD growth technique can be found in Chapter 3. In the first series, polar (A1P to A5P) and semipolar (A1SP to A5SP) samples were grown

simultaneously with the reactor pressure of 50 mbar, and growth temperature of 1100 °C. In the second series, only polar samples (B1P B5P) were grown at 50 mbar and 1115 °C. Finally, polar (C1P C5P) and semipolar (C1SP C5SP) samples were grown simultaneously at 200 mbar and 1100°C. For each group of the samples V/III ratio and TMAl/(TMGa + TMAl) ratio are listed in Table 6.1. These quite significantly different conditions resulted in variations between the series in terms of average compositions and growth rates; the latter were found to be about 0.23, 0.66 and 0.31 nm/s for series A, B and C, respectively. The thickness of the doped films in all experiments was kept within the range of 800–1100 nm. More details on the growth of polar samples in series A and B are also given in Ref. [28] and for semipolar samples in the series A in Ref. [29]. The AlN alloy fraction and the dopant concentration were determined using WDX measurements. Note that the AlN fractions quoted in Ref. [29] were measured by X-ray diffraction, which results in slight differences. Before the WDX examination, all samples and composition standards (AlN, GaN and Si) were carbon-coated to reduce the effect of charging. WDX measurements were performed with an electron probe microanalyser (EPMA, JEOL JXA-8530F) at an acceleration voltage of 10 kV and a beam current of 40 nA. At these conditions, the interaction volume is kept within the first 800 nm of the $Al_xGa_{1-x}N$ layers according to Monte Carlo simulations using CASINO software.[35] For WDX point measurements quantitative data is an average of 9 independent measurements selected away from larger 3D features across the sample surface. Any longer range compositional variations in the bulk film were below the detection limit of the WDX measurements. In the quantitative analysis X-ray line intensities emitted from the main specimens (L_α for Ga and K_α for Al, N, Si) were compared against the same X-ray line from the standard samples with known concentrations (AlN, GaN and Si). The measured intensities were then corrected for differences in composition between the standard and main specimens using an iterative procedure to give accurate atomic percentages of the species.[36] The calibration method, described in detail in Chapter 5 was used to estimate the Si concentration. The method involves measuring the Si intensity of all samples and comparing with $Al_xGa_{1-x}N$ and GaN reference samples for which Si concentration was known from secondary ion mass spectrometry (SIMS) analysis.[37, 38] Basic

principle of SIMS analysis are presented in Chapter 3. Doping densities evaluated by this method are in the of range 10^{17}–10^{19} cm^{-3}. The concentration determined directly from the WDX are over-estimated, likely as a result of surface contamination.[38]

The surface quality was examined using secondary electron (SE) imaging in a low-vacuum field emission gun scanning electron microscope (SEM, FEI Quanta 250 FEG). The morphology was also investigated using a Veeco multimode V atomic force microscope (AFM) in tapping mode. Images were also acquired in backscattered electron (BSE) mode, yielding compositional contrast dependent on the average atomic number of the material (Z). Mentioned imaging methods are discussed in Chapter 3.

CL spectra were recorded from uncoated samples in the low-vacuum FEG-SEM with a chamber pressure of 1 mbar, electron beam voltage of 15 kV and a beam current of 14 nA. Spectra were recorded with a spectral resolution of 0.8 nm, using a spectrometer with a 600 lines/mm grating blazed at 200 nm, a 50 μm slit, a focal length of 125 mm, and a 1600-element charge-coupled device. CL maps were recorded with the same spectrometer at 0.5 mbar chamber pressure.[39] The optical information obtained using CL was combined with the SE imaging to provide highly spatially resolved correlation of topography and optical properties.[12]

Table 6.1: Sample series details.

Label	Crystal orientation	*	Approx. growth rate (nm/s)	Si_2H_6/III ratio ($\times 10^{-7}$)	V/III ratio	WDX Si content (10^{18} cm^{-3})	AlN fraction x
A1P				279		4	0.63
A2P				558		4	0.72
A3P	(0001)	0.5	0.23	1120	600	5	0.69
A4P				2230		8	0.63
A5P				3350		10	0.70
A1SP				279		3	0.57
A2SP				558		7	0.65
A3SP	(11-22)	0.5	0.23	1120	600	7	0.61
A4SP				2230		8	0.60
A5SP				3350		6	0.60
B1P				131		3	0.85
B2P				219		5	0.84
B3P	(0001)	0.824	0.66	328	460	10	0.85
B4P				437		4	0.85
B5P				656		5	0.84
C1P				112		3	0.81
C2P				299		5	0.82
C3P	(0001)	0.333	0.31	449	23	4	0.82
C4P				561		4	0.82
C5P				749		6	0.82
C1SP				112		4	0.75
C2SP				299		3	0.78
C3SP	(11-22)	0.333	0.31	449	23	3	0.77
C4SP				561		7	0.75
C5SP				749		3	0.76

*
$$\frac{\text{TMAl}}{\text{TMGa}+\text{TMAl}} \text{ratio}$$

6.3 Results and discussion

6.3.1 Surface morphology of the n-Al$_x$Ga$_{1-x}$N films

The surface morphology was examined by AFM for samples grown with different Si$_2$H$_6$ flow rates (1 and 3 sccm). The root mean square (RMS) roughness values were examined for 2μm × 2 μm scan areas, giving average values of 4.35 and 3.76 nm for the polar and semipolar samples, respectively. The semipolar samples were found to have smoother surfaces than their polar counterparts, with an approximate 15% reduction in RMS. The surfaces of the semipolar samples are stable and not changed with different Si$_2$H$_6$ flow rates.[40, 41]

Figure 6.1 shows BSE micrographs of representative n-Al$_x$Ga$_{1-x}$N films grown on AlN/sapphire. The surface of polar sample C4P reveals brighter regions around hexagon edges (Figure 6.1 c), which is indication of a locally lower AlN alloy fraction.[12] These are less clear in the lower AlN alloy fraction polar layer (A1P) shown in Figure 6.1 a, but become apparent using the WDX mapping, which is discussed later. The surfaces of semipolar samples A4SP and C4SP reveal considerably less three-dimensional (3D) features (Figures 6.1 b and d, respectively).

In general, due to the lattice mismatch between Al$_x$Ga$_{1-x}$N and the underlying AlN layer, the resulting compressive strain can be relaxed either through formation of additional dislocations (favored for Al$_x$Ga$_{1-x}$N with high x) or through enhanced surface roughening (preferable for low x).[42] However in the case of n-Al$_x$Ga$_{1-x}$N with high doping levels ($> 10^{18}$ cm^{-3}) and typical crystal quality (total dislocation density ~10^9-10^{10} cm^{-2}), tensile strain gradually builds-up during the n-Al$_x$Ga$_{1-x}$N growth.[43]
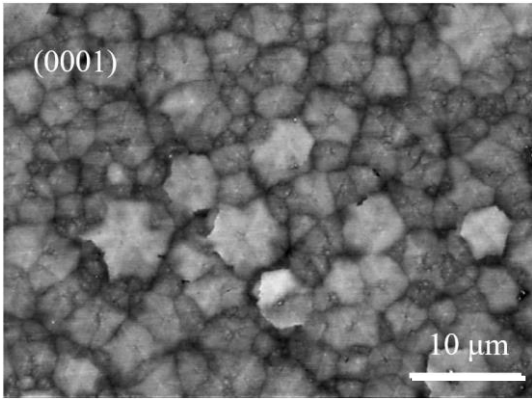
(*a*) A1P (x=0.57, [Si]= 4×10^{18} cm^{-3})
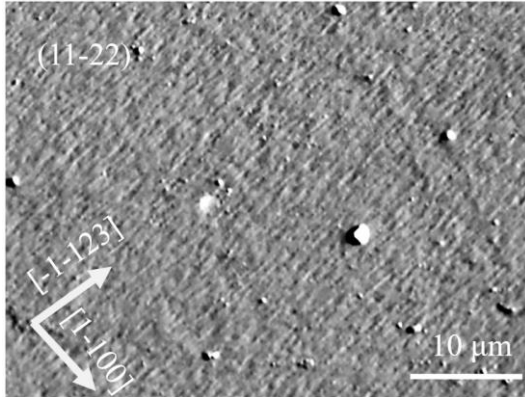
(*b*) A4SP (x=0.63, [Si]= 8×10^{18} cm^{-3})
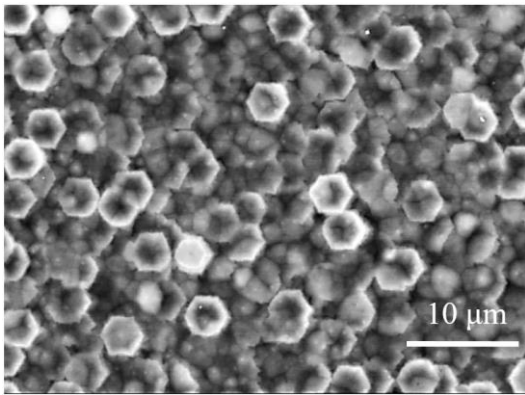
(*c*) C4P (x=0.82, [Si]= 4×10^{18} cm^{-3})
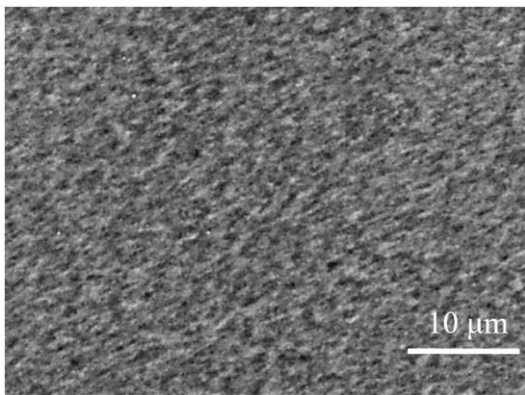
(*d*) C4SP (x=0.75, [Si]= 7×10^{18} cm^{-3})
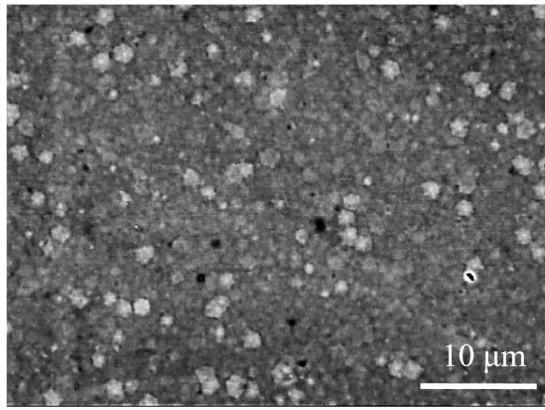
(*e*) B5P (*x*=0.84, [Si]= 5×10^{18} cm^{-3})

Figure 6.1: BSE micrographs of the Al$_x$Ga$_{1-x}$N layers with polar and semipolar orientations, details in Table 1.

All the *c*-plane samples show hexagonal platelet structures and small hillock grains, additionally differently oriented crystallites are observed on their surfaces with no visible pits. The suppression of 3D nucleation for higher AlN alloy fraction *c*-plane samples is expected, due to the lower diffusion length of Ga adatoms at the higher TMAl flux necessary for their growth.[44] Also, compressive stress is reduced with increasing AlN alloy fraction in Al$_x$Ga$_{1-x}$N/AlN and thus reduced defect formation is expected.[42] However, neither of the above effects are observed in our samples, as shown later in Figures 6.5 *c*, *d* and *e*.

There is no clear correlation between the diameter of the hexagonal platelets and the Si$_2$H$_6$ flow rate. The average hexagon diameter varies between 3.5 and 7 µm. Some similar samples have been assumed to be free from stress due to the occurrence of 3D growth [45] but in the present case the layers are smooth on a macroscopic scale and still under stress, as shown by X-ray diffraction measurements (not shown here). The polar layer deposited at a high V/III ratio of 600 (Figure 6.1, *a*) shows a rough surface morphology with some pyramidal hillocks of different sizes. On the other hand, the layer deposited at a lower V/III ratio of 23 (Figure 6.1, *c*) shows a similar morphology, but with similarly sized hexagons on the surface. For the *c*-plane samples in the B series, the surface morphology seems to be optimal with the intermediate V/III ratio of 460

(Figure 6.1, *e*). For the polar samples in the series C, there is a trend of increasing diameter of hexagonal platelets with increasing Si concentration. It may be possible that Si doping favors the stabilization and development of crystallographic facets.[46] There is no obvious correlation between Si concentration and the smoothness of surface morphology due to the enhanced mobility of the adatoms.

The set of semipolar samples (A and C) appears to have formed a continuous film, as seen in Figures 6.1 *b* and *d*. For the same V/III ratio, their AlN fraction is lower compared to the polar samples grown at the same time, as shown in Table 6.1. Some triangular, dot-like and small hillock-like features can be observed on the surface of the semipolar samples (Figures 6.1, *b* and *d*).[41] The samples with the highest Si_2H_6 flow rate have the roughest surface (i.e., samples A4SP and A5SP).

6.3.2 WDX measurements

Table 6.1 presents the WDX measured compositions and doping levels for all the samples. Each of the reported values is the mean of nine measurements, chosen arbitrarily across the sample surface. The standard errors calculated for the AlN atomic fractions are 0.02–0.05, likely caused by compositional inhomogeneities on the samples, as they are too large to be purely caused by the technique limitations. The overall weight total for each of the samples investigated, (the sum of mass percentages for all independently measured elements) was (100 ± 2) %, confirming a successful WDX analysis for the major elements.

Comparing the measured AlN alloy fraction for the samples within the same series but of different crystal orientations, one can see that AlN alloy fraction is lower in the semipolar samples, in agreement with Ref. [40], although there are reports of different relationships between AlN alloy fraction and orientation.[41, 47] For the samples with high V/III ratios, the AlN alloy fraction values are also lower due to increased $TMAl:NH_3$ pre-reactions and the suppression of GaN decomposition at increased ammonia fluxes. [26, 48] For example, for the semipolar samples in series A, grown with a V/III ratio of 600 and TMAl/(TMGa + TMAl) ratio of 0.5, the AlN

alloy fraction is estimated to be 0.57–0.65 as compared with the samples in the series C, grown with the lower V/III ratio of 23 and TMAl/(TMGa + TMAl) ratio of 0.333, where it is estimated to be 0.75–0.78 (Table 6.1).

Figure 6.2 shows the measured Si concentration of the n-Al$_x$Ga$_{1-x}$N layers as a function of Si$_2$H$_6$ to group-III ratio. There is a general trend of linearly increasing Si concentration with increasing Si/III ratio, although with a significant scattering of data. At a Si/III ratio above 2.3×10^{-4} a saturation of the Si concentration is observed for the semipolar samples in series A (ASP). The semipolar samples in series C (CSP) have lower Si/III ratios and although it is harder to be definitive about saturation, it is noted that the Si concentration drops for the highest Si/III ratio.

The saturation point is consistent with the work from Dinh et al.,[25] who used Hall data to show that the carrier concentration and mobility of the semipolar ASP layers reach a maximum at a similar Si/III ratio. The polar samples in series A (AP) exhibit an almost linear increase of [Si] with increasing Si$_2$H$_6$ flow rate, with no evidence of saturation. Interestingly, the trend is very different from the co-loaded semipolar samples (series ASP) with a much higher Si incorporation for A2SP (compared to A2P) followed by a saturation for A4SP. The polar samples in series B (BP) lie on a line parallel to the samples in series A, with the exception of B3P, which has a much higher Si incorporation. Hall-effect measurements for the polar samples in series B show a monotonic decrease of the Hall coefficient with increasing Si$_2$H$_6$ flow rate, [26] strongly indicating that sample B3P is anomalous. For the polar samples in series C (CP), [Si] seems to lie roughly on the same line as the A and B sets. The polar C series shows an approximate linear increase with Si/III ratio. However, the Si/III ratios do not extend above 0.75×10^{-4} in both C series and the [Si] measurements for the semipolar CSP samples show significant scatter.
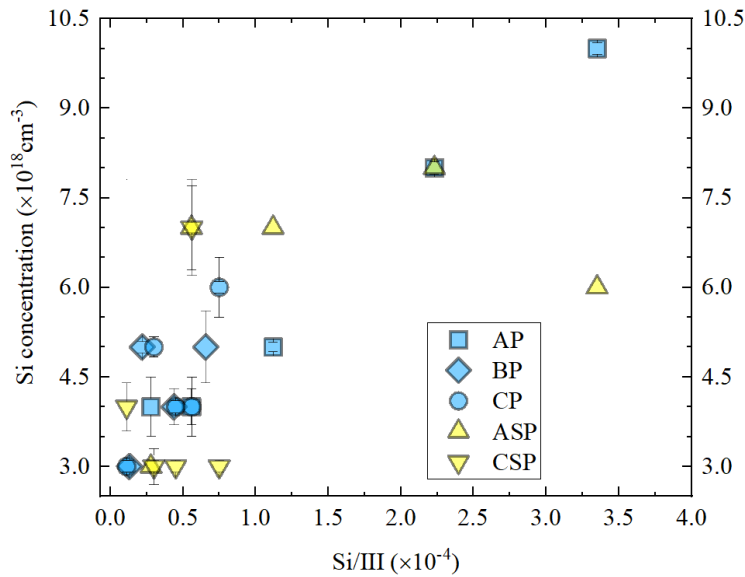
Figure 6.2: Si concentration of the n-Al$_x$Ga$_{1-x}$N layers as a function of Si$_2$H$_6$ to group-III ratio. The anomalous sample, B3P, has not been included in this plot.

6.3.3 WDX mapping

According to Mogilatenko et.al.[42] the difference in AlN fraction of the Al$_x$Ga$_{1-x}$N regions on planar c-plane terraces and on the side facets of the surface macrosteps corresponds to at least 0.1 (10% AlN fraction) for x=0.6 and around 0.04 (4% AlN fraction) for x=0.8.

Due to difference in surface mobility between Al and Ga adatoms the lowest Ga incorporation happens on the top facets of the hexagons.[45] While Al adatoms are readily incorporated onto any Al$_x$Ga$_{1-x}$N surface, due to their lower surface diffusion length.[49] Ga adatoms have longer diffusion length increasing the chance of incorporating at a energetically more favorable site or being irreversibly desorbed to the ambient. From our observations, it is clear that with hexagonal features in sample C1P, Ga will be trapped around the feature edges, resulting in an increased Ga incorporation. However, on the feature top surfaces, effective areas are larger and smoother, leading to a faster Ga diffusion. That is one of the reasons why a GaN-rich phase is noticeable at the boundaries of 3D surface features.[45, 50] A possible explanation for this observation is that island boundaries provide

additional chemical bonds where Ga can be retained, resulting in Ga accumulation.[50]

The experimental data for the polar sample C1P in Figure 6.3 show a higher (lower) intensity of Ga L_α (Al K_α) X-rays around the hexagon edges; the same behavior is observed in the compositional BSE image. Comparing these maps allows us to rule out topographic effects as the dominant source of contrast, in which an increased backscatter signal would result in less X-ray counts. Seeing bright edges in both therefore unambiguously points to higher mass regions in a way that either map alone would not. Despite the challenging signal-to-noise ratio, inherent to X-ray counting statistics, we can see clear variations in the Ga distribution on a sub-µm length scale. The GaN alloy fraction was quantified using the measured GaN at% from WDX quantitative point data giving an estimate of 18% GaN at the middle of the map (Figure 6.3 *b*). The observed difference from centre to edge of a hexagon is about 2% GaN. In contrast, a WDX map of a semipolar sample (A5SP), whose surface is free from hexagons, does not reveal any observable variation between Ga L_α and Al K_α X-rays (therefore not presented), indicating better compositional homogeneity compared to polar samples.

(*a*)   (*b*)
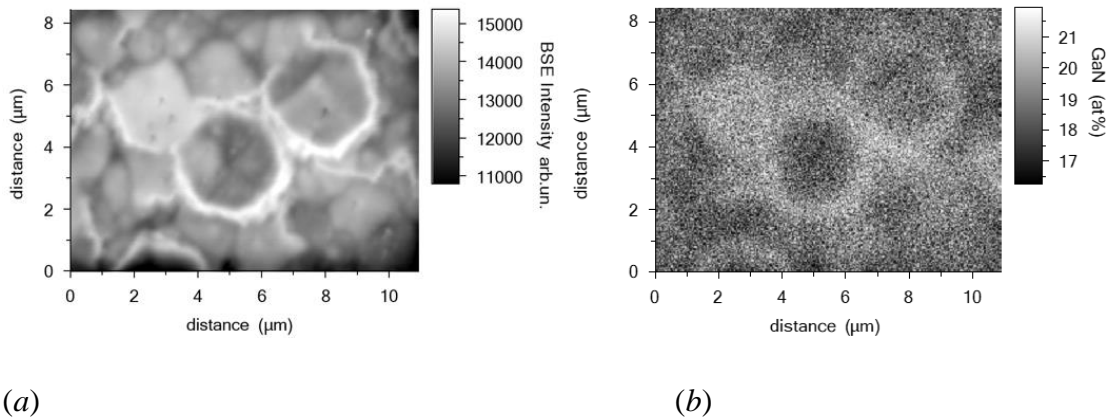
Figure 6.3: Composition mapping of the *c*-plane sample C1P (81% AlN mole fraction). a) BSE image of the measured area, b) GaN content map (at%) obtained from a WDX map of the Ga L_α X-ray intensity.

6.3.4 CL mapping

CL hyperspectral mapping enables us to correlate optical properties with surface morphology by mapping variations in spectral luminescence across a sample.[51, 52] The acquired CL images can be simultaneously or sequentially (as in this work) correlated with WDX spot analyses or maps, thus enabling specific CL characteristics to be related to semiconductor composition.[52]

CL spectra were measured for all samples, and maps collected for selected polar samples. The spectra revealed near-band edge (NBE) peaks in the photon energy range of 4.0–5.4 eV and impurity transition peaks in the range of 2.7–4.8 eV. An example of a typical CL spectrum is shown in (Figure 6.4 b), for the sample C1P. Different impurity transitions are introduced in Chapter 2.

The impurity transitions are assigned to recombination between shallow donors and deep level acceptors including cation vacancies $(V_{III})^{3-}$ and V_{III} complexes (e.g. $(V_{III}^-O)^{2-}$) [53]. One of the explanations for the introduction of the vacancy type defects is related to the transition of the growth mode from 2D growth to 3D growth.[14] Cation vacancies act as non-radiative recombination centres in $Al_xGa_{1-x}N$, and it is possible that they are introduced by Si doping due to a decrease in their formation energy as the Fermi level moves towards the conduction band.[20]

The CL intensity maps (Figure 6.4 $c-f$), extracted from the hyperspectral data set, reveal domains between which there are shifts in the $Al_xGa_{1-x}N$ NBE emission energy. The 2D CL intensity maps were extracted from the 3D data cube by integrating over a given spectral window, while calculating a centroid over the same range generates a map of emission energy.[54] Regions of higher CL intensity in the NBE peak intensity map (Figure 6.4 c) correlate with lower emission energy in the corresponding NBE energy map (Figure 6.4 d), following the same trend as compositional variations revealed by the WDX mapping (Figure 6.3 b). While these alloy variations are likely the dominant cause of the observed peak shift, additional contributions from non-uniform elastic strain and carrier concentrations cannot be discounted.

Figure 6.4 *c* reveals an increase in the NBE intensity all the way along the edges of the hexagons compared to the middle of the feature. The intensity map of the (V_{III} complex)$^{1-}$ defect peak, Figure 6.4 *e*, seems to be more localized and higher intensity spots are observable along the edges of the hexagon. Oxygen can possibly be more easily incorporated at the semipolar facets of the hexagons.[12] For the other two defect peaks ((V_{III} complex)$^{2-}$ and (V_{cation})$^{3-}$) a higher intensity is measured from the middle of hexagon, Figure 6.4 *f*, which contrasts with the behavior of the other peaks. A screw dislocation has been reported to emerge at the middle of the hexagon,[12] with which the defect complex (V_{cation})$^{3-}$ could be related, additionally we found that the AlN composition is higher in the middle of the hexagons which could lead to a locally lower formation energy of these defects. At the edges of the hexagon, the growth conditions differ from the rest of the sample, as discussed above. In the case of the *c*-plane sample C1P (81% AlN), the hexagon centre shows 98% of the mean whole map intensity and the edge 101%. For sample A1P (63% AlN), the difference in NBE intensity from different parts of the sample is larger (the centre of hexagon shows 95% of the mean map intensity and the edge 109 %). Also, the shift in the NBE emission energy from centre to edge is found to be larger in this case of 110 meV compared to 60 meV for C1P (Figure 6.4 *d*). The CL map of sample A1P not presented as it demonstrates exactly the same type of luminescence behavior as seen in sample C1P. This shift for sample C1P corresponds to a difference of about 1.5% in GaN content, which compares well with the 2 at% GaN difference estimated from the WDX map. From these observations, it is apparent that the sample grown with the highest V/III ratio of 600 and with $x < 0.63$ (A1P) shows higher compositional inhomogeneity compared to the sample grown at lower V/III ratio of 23 and with $x > 0.81$ (C1P).
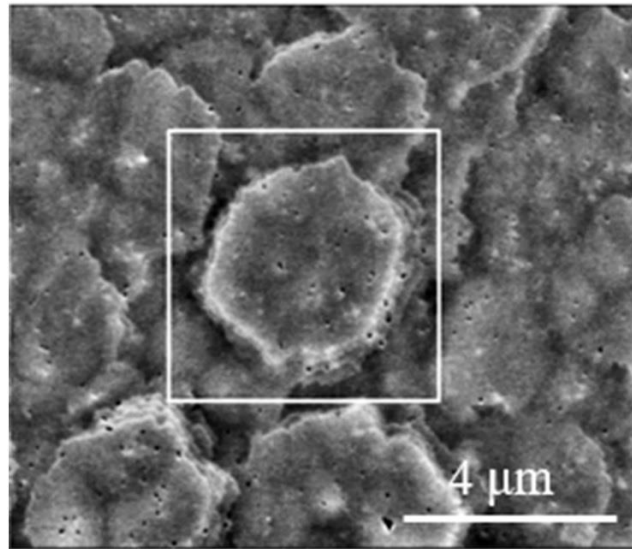
(*a*) SE image, area measured by CL in rectangle
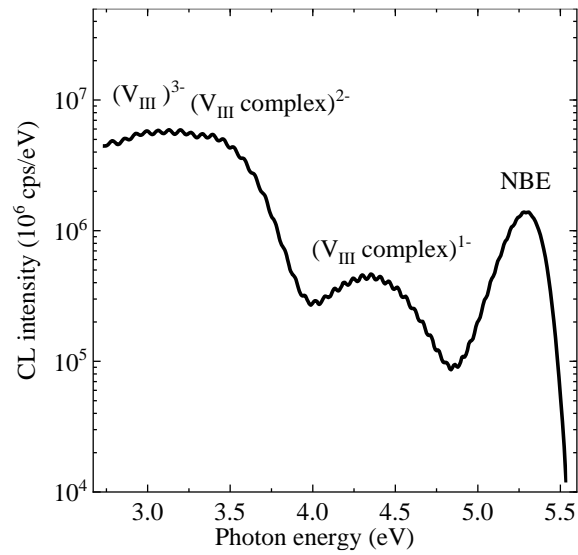
(*b*) A typical mean CL spectrum for a polar n-Al$_x$Ga$_{1-x}$N sample (C1P)
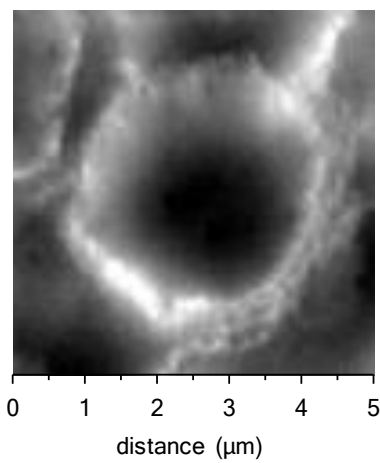
(*c*) 5.3 eV; NBE intensity

(*d*) NBE centroid energy

(e) 4.4 eV; (V$_{III}$ complex)$^{1-}$

(f) 3.11 eV; (V$_{III}$ complex)$^{2-}$ and (V$_{cation}$)$^{3-}$
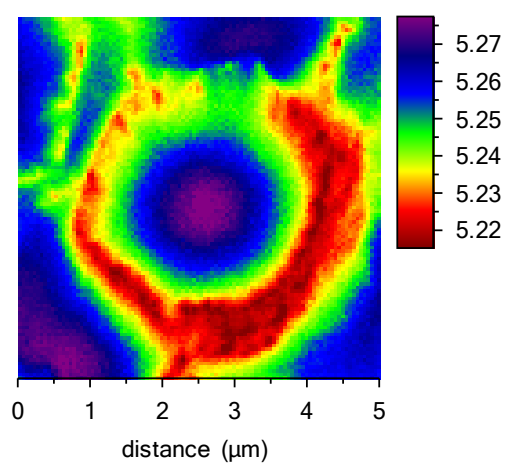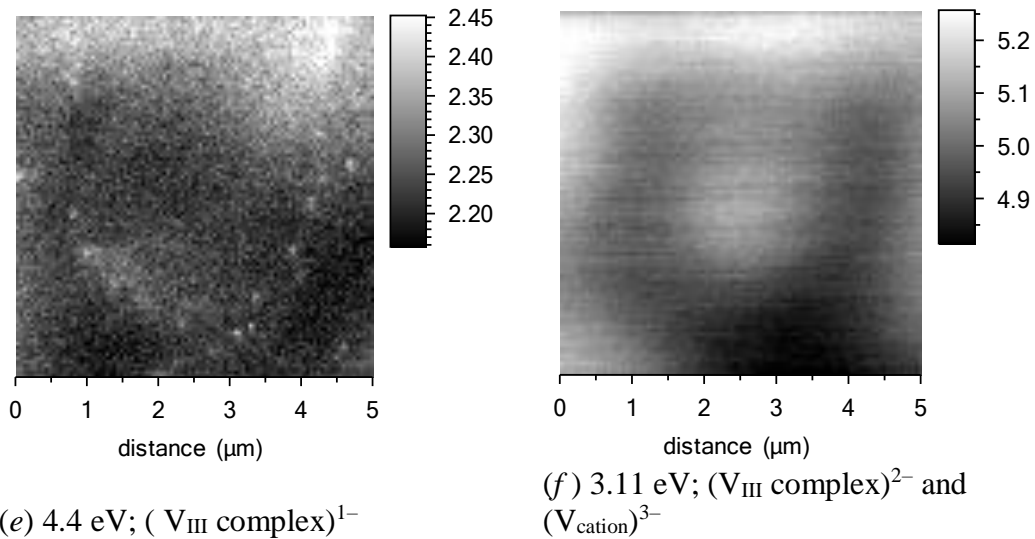
Figure 6.4: CL imaging of the *c*-plane C1P sample: including SE image (a), mean Cl spectrum (b) and 5×5 μm^2 CL maps of the sample (*c−f*).

6.3.5 CL spectra

Figure 6.5 shows mean CL spectra for all *c*-plane and semipolar sample series. It is noticeable that the intensities of the deep impurity transitions are on the same order or higher than those of the band-edge transitions. Each set of CL spectra (Figures 5 *a−e*) represents samples with a particular V/III ratio and orientation, and shows how the relative intensity of the NBE peaks and impurity transitions, depend strongly on the growth conditions. Similar behavior was reported in Refs. [12, 25]. Figure 6.6 plots the peak wavelengths of the impurity transitions observed in the spectra as a function of AlN content, alongside previously published data (Ref. 29), in order to clarify the origins of the peaks.

(a)

(b)
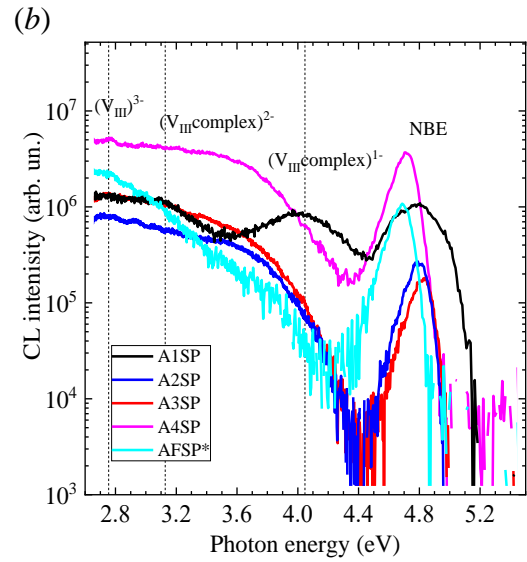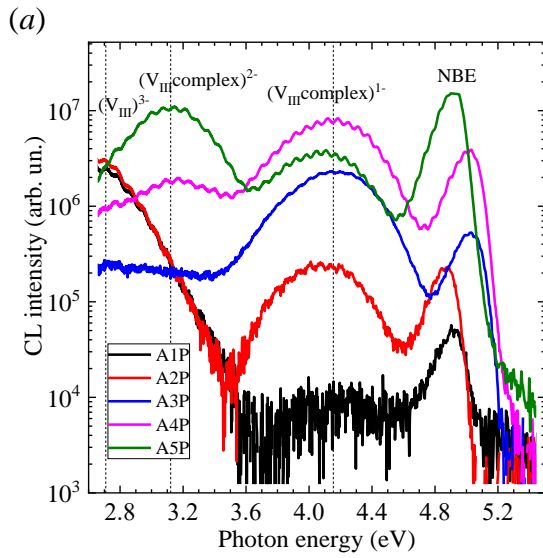
*AFSP not shown in Table 1. Si$_2$H$_6$/III ratio 558 (used the same growth parameters of sample A2SP, but different growth experiment)

(c)

(d)

(*e*)
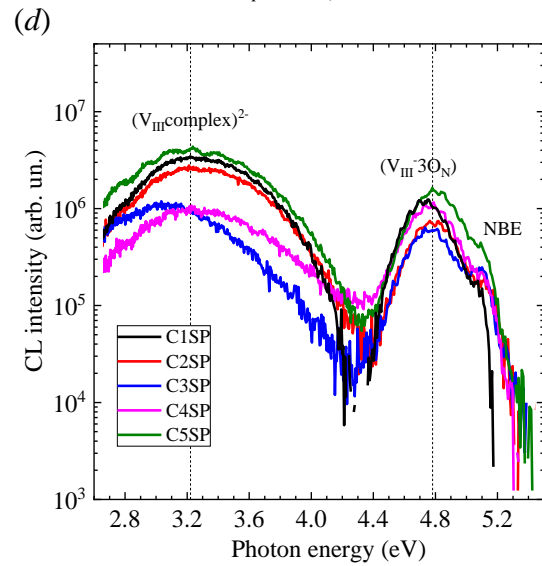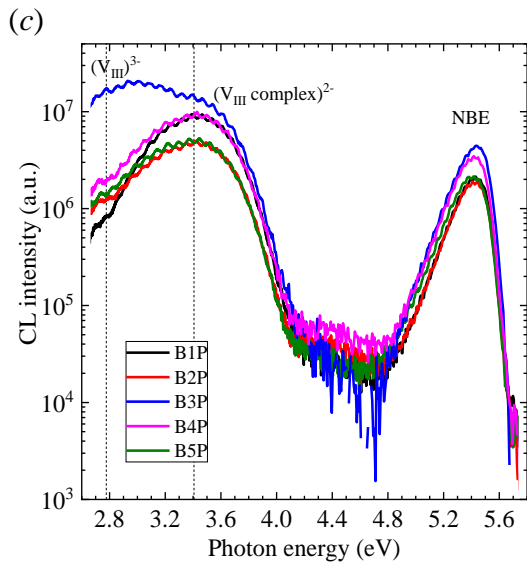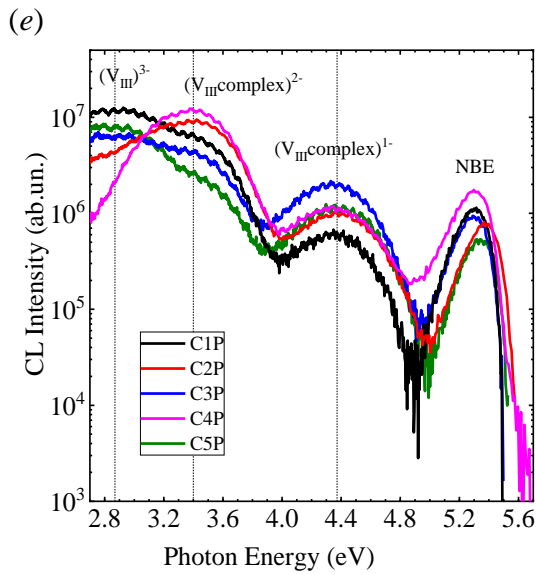
Figure 6.5: CL point spectra of the different AlGaN layers

a) *c*-plane layers (series A), $x = 0.63–0.72$,

b) semipolar layers (series A), $x = 0.57–0.65$,

c) *c*-plane layers (series B), $x = 0.84–0.85$,

d) semipolar layers (series C), $x = 0.75–0.78$,

e) *c*-plane layers (series C), $x = 0.81–0.82$.

The spectra in Figures 6.5 *a*, *b* and *e* (which correspond to the polar and semipolar samples in the series A, and polar samples in the series C, respectively) reveal $(V_{III})^{3-}$, $(V_{III}$ complex$)^{2-}$, $(V_{III}$ complex$)^{1-}$ impurity peaks and NBE peaks. For the polar samples in the series A, the intensity of the NBE peak increases with Si content, as well as the intensity of the $(V_{III}$ complex$)^{1-}$ peak for A1P-A4P samples. $(V_{III}$ complex$)^{1-}$ peak decreases again for A5P where the $(V_{III}$ complex$)^{2-}$ becomes strongest. The $(V_{III}$ complex$)^{2-}$ peak becomes visible in higher Si content samples (A3P-A5P) and follows the same trend, with the intensity of the peak increasing with Si content. The $(V_{III})^{3-}$ intensity is highest for lowest Si content samples (A1P and A2P). As described earlier, WDX and Hall data indicate that the Si incorporation saturated in the semipolar ASP series and it is notable that the $(V_{III}$ complex$)^{1-}$ and $(V_{III}$ complex$)^{2-}$ peaks are hardly present in the CL spectra from the more highly doped samples in this series. This may be related to a low solubility limit for Si in the semipolar samples, although further research is needed to confirm this.

For the polar samples in series C, the intensity of the NBE decreases with increasing [Si], as well as the intensity of the $(V_{III}$ complex$)^{2-}$ peak as seen in Figure 6.5 *e*. For the polar samples in the series B and the semipolar samples in the series C the $(V_{III}$ complex$)^{1-}$ is not present, as shown in Figures 6.5 *c* and *d*. The V_{III} complex with

oxygen is only visible in Figure 6.5, *d* for the semipolar samples in the series C. Oxygen can behave as an electron acceptor in $Al_xGa_{1-x}N$ and hinder *n*-type behavior achieved with Si doping, similar to cation vacancies.[19, 20, 55] The aforementioned complex could be associated also with N vacancies, since the growth was performed at very low V/III ratio of 23.[48]
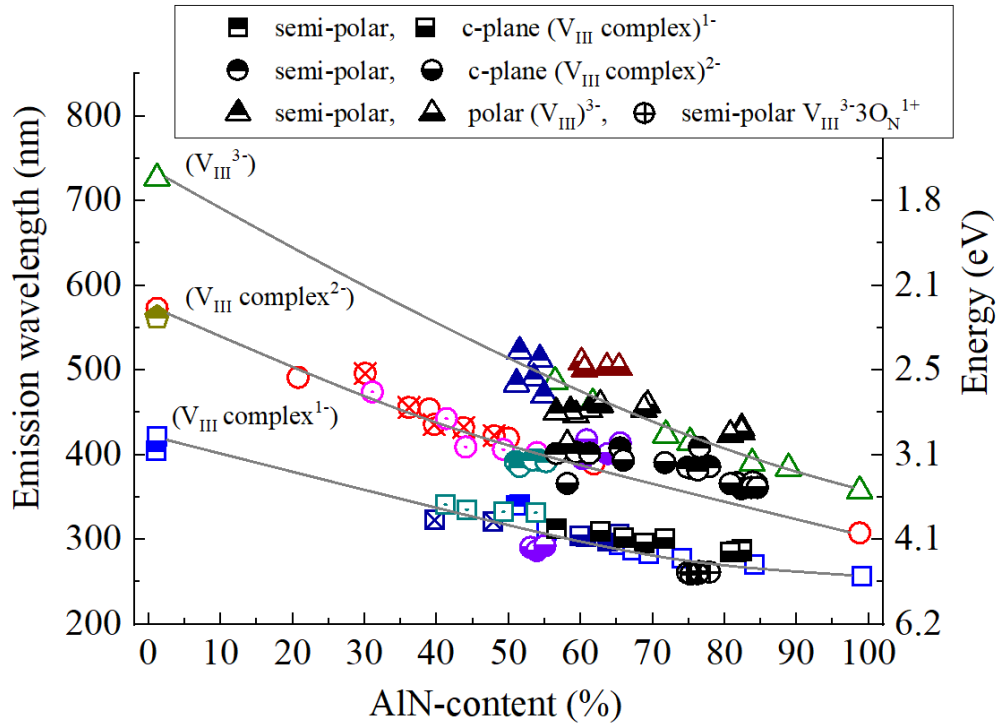
Figure 6.6: CL peak positions of deep impurity transitions obtained from Figure 6.5 as a function of AlN- alloy fraction. The results from this work (black and white symbols) are plotted against previously published data (coloured symbols) from Ref. 29 for comparison. The solid lines provide guides to the eye.

6.4 Conclusion

The compositional and optical properties of semipolar (11-22) and polar (0001) n-Al$_x$Ga$_{1-x}$N films have been systematically investigated using WDX and CL measurements. The Si-doping concentration was measured by WDX, using calibration data from SIMS. Comparison of the measured AlN alloy fraction for samples with different crystal orientations showed that the AlN incorporation was higher in the polar samples. The highest values of Si incorporations were observed for the polar samples with the highest Si/III ratios, while saturation of Si incorporation was seen for the semipolar samples at higher Si/III ratios. CL hyperspectral imaging of the polar samples revealed significant reductions in near-band-edge luminescence intensity from the middle of surface hexagonal features where a threading dislocation is expected to be terminated. WDX mapping confirmed higher Ga incorporation around the hexagon edges. The semipolar samples showed no such features, corresponding to a better compositional homogeneity. CL point spectra showed how changes in the relative intensity of the NBE peaks and impurity transitions depend strongly on the growth conditions and surface orientations.

The main implications of this work for LED research is the use of the CL technique to identify the suppression of impurity defects, which will lead to further improvements in the layer conductivity since they act as recombination centres. The analysis of CL data can therefore help reduce point defect densities by guiding the optimisation of growth parameters. The technique is potentially also informative for other layers grown under similar conditions where point defects cannot be directly measured, such as quantum wells (QWs). The CL and WDX results presented in this paper provide information on how point defect incorporation in the doped AlGaN contact layers is influenced by crystal orientation, alloy composition, and Si incorporation, as well as on the existence of different compensating defects. This paper also highlights challenges associated with growth of high AlN content AlGaN layers such as occurrence of hexagonal platelet structures in c-plane samples and compositional inhomogeneity.

Bibliography

1. Kneissl, M., et al., *Advances in group III-nitride-based deep UV light-emitting diode technology*. Semiconductor Science and Technology, 2011. **26**(1): p. 014036.

2. Ding, K., et al., *Status of Growth of Group III-Nitride Heterostructures for Deep Ultraviolet Light-Emitting Diodes*. Crystals, 2017. **7**(10): p. 300.

3. Kneissl, M., et al., *The emergence and prospects of deep-ultraviolet light-emitting diode technologies*. Nature Photonics, 2019. **13**(4): p. 233-244.

4. Yu, E.T., et al., *Spontaneous and piezoelectric polarization effects in III–V nitride heterostructures*. Journal of Vacuum Science & Technology B: Microelectronics and Nanometer Structures Processing, Measurement, and Phenomena, 1999. **17**(4): p. 1742-1749.

5. Hakamata, J., et al., *Growth of High-Quality AlN and AlGaN Films on Sputtered AlN/Sapphire Templates via High-Temperature Annealing*. Physica Status Solidi (B) Basic Research, 2018. **255**(5).

6. Cho, H.K., et al., *Structural properties of Si and Mg doped and undoped Al0.13Ga0.87N layers grown by metalorganic chemical vapor deposition*. Journal of Crystal Growth, 2001. **233**(4): p. 667-672.

7. Inoue, S.-i., N. Tamari, and M. Taniguchi, *150 mW deep-ultraviolet light-emitting diodes with large-area AlN nanophotonic light-extraction structure emitting at 265 nm*. Applied Physics Letters, 2017. **110**(14): p. 141106.

8. Kaneda, M., et al., *Uneven AlGaN multiple quantum well for deep-ultraviolet LEDs grown on macrosteps and impact on electroluminescence spectral output*. Japanese Journal of Applied Physics, 2017. **56**(6): p. 061002.

9. Zhu, K., et al., *Silicon doping dependence of highly conductive n-type Al0.7Ga0.3N*. Applied Physics Letters, 2004. **85**(20): p. 4669-4671.

10. Pampili, P. and P.J. Parbrook, *Doping of III-nitride materials*. Materials Science in Semiconductor Processing, 2017. **62**: p. 180-191.

11. Taniyasu, Y., M. Kasu, and N. Kobayashi, *Intentional control of n-type conduction for Si-doped AlN and AlXGa1−XN (0.42⩽x<1)*. Applied Physics Letters, 2002. **81**(7): p. 1255-1257.

12. Kusch, G., et al., *Spatial clustering of defect luminescence centers in Si-doped low resistivity Al0.82Ga0.18N*. Applied Physics Letters, 2015. **107**(7): p. 072103.

13. Kurai, S., et al., *Inhomogeneous distribution of defect-related emission in Si-doped AlGaN epitaxial layers with different Al content and Si concentration*. Journal of Applied Physics, 2014. **115**(5): p. 053509.

14. Uedono, A., et al., *Native cation vacancies in Si-doped AlGaN studied by monoenergetic positron beams*. Journal of Applied Physics, 2012. **111**(1): p. 013512.

15. Murotani, H., et al., *Silicon concentration dependence of optical polarization in AlGaN epitaxial layers*. Applied Physics Letters, 2011. **98**(2): p. 021910.

16. Cantu, P., et al., *Si doping effect on strain reduction in compressively strained Al0.49Ga0.51N thin films.* Applied Physics Letters, 2003. **83**(4): p. 674-676.

17. Mehnke, F., et al., *Electronic properties of Si-doped Alx Ga1−xN with aluminum mole fractions above 80%.* Journal of Applied Physics, 2016. **120**(14): p. 145702.

18. Harris, J.S., et al., *Oxygen and silicon point defects in Al0.65Ga0.35N.* Physical Review Materials, 2019. **3**(5).

19. Thonke, K., et al., *Optical signatures of silicon and oxygen related DX centers in AlN.* physica status solidi (a), 2017. **214**: p. e201600749.

20. Stampfl, C. and C.G.V.d. Walle, *Doping of AlxGa1−xN.* Applied Physics Letters, 1998. **72**(4): p. 459-461.

21. Amano, H., et al., *The 2020 UV Emitter Roadmap.* Journal of Physics D: Applied Physics, 2020.

22. Bryan, Z., et al., *Fermi level control of compensating point defects during metalorganic chemical vapor deposition growth of Si-doped AlGaN.* Applied Physics Letters, 2014. **105**(22): p. 222101.

23. Mehnke, F., et al., *Highly conductive n-AlxGa1−xN layers with aluminum mole fractions above 80%.* Applied Physics Letters, 2013. **103**(21): p. 212109.

24. Nakarmi, M.L., et al., *Transport properties of highly conductive n-type Al-rich AlxGa1−xN(x⩾0.7).* Applied Physics Letters, 2004. **85**(17): p. 3769-3771.

25. Dinh, D.V., P. Pampili, and P.J. Parbrook, *Silicon doping of semipolar (112̄2)AlxGa1−xN(0.50≤x≤0.55).* Journal of Crystal Growth, 2016. **451**: p. 181-187.

26. Pampili, P., et al., *Significant contribution from impurity-band transport to the room temperature conductivity of silicon-doped AlGaN.* Journal of Physics D: Applied Physics, 2018. **51**(6).

27. Jo, M., et al., *Structural and electrical properties of semipolar (11-22) AlGaN grown on m-plane (1-100) sapphire substrates.* physica status solidi c, 2017. **14**(8): p. 1600248.

28. Nepal, N., et al., *Exciton localization in AlGaN alloys.* Applied Physics Letters, 2006. **88**(6).

29. Bryan, Z., et al., *High internal quantum efficiency in AlGaN multiple quantum wells grown on bulk AlN substrates.* Applied Physics Letters, 2015. **106**(14): p. 142107.

30. Li, Z., et al., *Optical investigation of semi-polar (11-22) AlxGa1-xN with high Al composition.* Applied Physics Letters, 2017. **110**(9).

31. Huakai, L., et al., *Epitaxial growth of semi-polar (11-22) plane AlGaN epi-layers on m-plane (10-10) sapphire substrates.* physica status solidi (a), 2017. **214**(5): p. 1600802.

32. Dridi, Z., B. Bouhafs, and P. Ruterana, *First-principles investigation of lattice constants and bowing parameters in wurtzite AlxGa1xN, InxGa1xN and InxAl1xN alloys.* Semiconductor Science and Technology, 2003. **18**(9): p. 850-856.

33. Li, H., T.C. Sadler, and P.J. Parbrook, *AlN heteroepitaxy on sapphire by metalorganic vapour phase epitaxy using low temperature nucleation layers.* Journal of Crystal Growth, 2013. **383**: p. 72-78.

34. Dinh, D.V., et al., *Single phase (112¯2) AlN grown on (101¯0) sapphire by metalorganic vapour phase epitaxy.* Journal of Crystal Growth, 2015. **414**: p. 94-99.

35. Drouin, D., et al., *CASINO V2.42—A Fast and Easy-to-use Modeling Tool for Scanning Electron Microscopy and Microanalysis Users.* Scanning, 2007. **29**(3): p. 92-101.

36. Kusch, G., et al., *Analysis of doping concentration and composition in wide bandgap AlGaN:Si by wavelength dispersive x-ray spectroscopy.* Semiconductor Science and Technology, 2017. **32**(3): p. 7.

37. Trager-Cowan, C., et al., *Scanning electron microscopy as a flexible technique for investigating the properties of UV-emitting nitride semiconductor thin films.* Photonics Research, 2019. **7**(11): p. B73-B82.

38. Spasevski, L., et al., *Quantification of Trace-Level Silicon Doping in $Al_xGa_{1-x}N$ Films Using Wavelength-Dispersive X-Ray Microanalysis.* Microscopy and Microanalysis, 2021: p. 1-9.

39. Edwards, P.R. and R.W. Martin, *Cathodoluminescence nano-characterization of semiconductors.* Semiconductor Science and Technology, 2011. **26**(6): p. 064005.

40. Dinh, D.V., S.N. Alam, and P.J. Parbrook, *Effect of V/III ratio on the growth of (11 2¯ 2) AlGaN by metalorganic vapour phase epitaxy.* Journal of Crystal Growth, 2016. **435**: p. 12-18.

41. Stellmach, J., et al., *Structural and optical properties of semipolar (112¯2) AlGaN grown on (101¯0) sapphire by metal–organic vapor phase epitaxy.* Journal of Crystal Growth, 2013. **367**: p. 42-47.

42. Mogilatenko, A., et al., *Defect analysis in AlGaN layers on AlN templates obtained by epitaxial lateral overgrowth.* Journal of Crystal Growth, 2014. **402**: p. 222-229.

43. Forghani, K., et al., *Strain and defects in Si-doped (Al)GaN epitaxial layers.* Journal of Applied Physics, 2012. **112**(9): p. 093102.

44. Zeimer, U., et al., *High quality AlGaN grown on ELO AlN/sapphire templates.* Journal of Crystal Growth, 2013. **377**: p. 32-36.

45. Kusch, G., et al., *Influence of substrate miscut angle on surface morphology and luminescence properties of AlGaN.* Applied Physics Letters, 2014. **104**(9): p. 092114.

46. Nilsson, D., E. Janzén, and A. Kakanakova-Georgieva, *Strain and morphology compliance during the intentional doping of high-Al-content AlGaN layers.* Applied Physics Letters, 2014. **105**(8): p. 082106.

47. Dinh, D.V., et al., *Aluminium incorporation in polar, semi- and non-polar AlGaN layers: a comparative study of x-ray diffraction and optical properties.* Scientific Reports, 2019. **9**(1): p. 15802.

48. Dinh, D.V., et al., *Pulsed-flow growth of polar, semipolar and nonpolar AlGaN.* Journal of Materials Chemistry C, 2020.

49. Heying, B., et al., *Dislocation mediated surface morphology of GaN.* Journal of Applied Physics, 1999. **85**(9): p. 6470-6476.

50. Mayboroda, I.O., et al., *Growth of AlGaN under the conditions of significant gallium evaporation: Phase separation and enhanced lateral growth.* Journal of Applied Physics, 2017. **122**(10): p. 11.

51. Martin, R.W., et al., *Cathodoluminescence spectral mapping of III-nitride structures.* physica status solidi (a), 2004. **201**(4): p. 665-672.

52. Edwards, P.R., et al., *You Do What in Your Microprobe?! The EPMA as a Multimode Platform for Nitride Semiconductor Characterization.* Microscopy and Microanalysis, 2018. **24**(S1): p. 2026-2027.

53. Nepal, N., et al., *Photoluminescence studies of impurity transitions in AlGaN alloys.* Applied Physics Letters, 2006. **89**(9): p. 092107.

54. Edwards, P.R., et al., *High-Resolution Cathodoluminescence Hyperspectral Imaging of Nitride Nanostructures.* Microscopy and Microanalysis, 2012. **18**(6): p. 1212-1219.

55. Van de Walle, C.G., et al., *Doping of AlGaN Alloys.* MRS Internet Journal of Nitride Semiconductor Research, 1999. **4**(S1): p. 890-901.

Chapter 7

7. Measurement of Mg at low concentration at low concentration in Ga(Al)N

7.1. Introduction to p-doping

P-type GaN is essential for both GaN-based electronic and optical devices [1]. The Mg impurity in GaN is important because it is the only viable dopant available for the production of p-type GaN [1]. Other possible dopants as Zn, Hg, C, Be, Li result in compensated, high-resistivity material, with no measurable hole concentration [2].

In the 1970s and 1980s light-emitting diodes (LEDs) were limited to a just a few of the visible colours. There were green (GaP, AlGaInP, AlGaP), yellow (GaAsP, AlGaInP, GaP) and red (AlGaS, GaAsP, AlGaInP, GaP) LEDs fabricated from widely studied semiconductor compounds. The blue LEDs were still missing and gallium nitride (GaN) was one possible candidate. Gallium nitride films finally appeared out of the laboratories of the Radio Corporation of America (RCA) starting in 1968. One of the researchers from that laboratory, Herbert Maruska was working on p-type doping of GaN but he did not succeed in making a standard pn junction LED. After him, Edward Miller, took over the growth of the gallium nitride films collaborating with Jacque Pankove. Pankove was the first one to report electroluminescence from a GaN:Zn film in 1971. Soon Miller fabricated a blue LED (475 nm) as well and Pankove applied for a patent for GaN LEDs in 1971. Maruska decided to substitute magnesium for zinc to create a novel acceptor, but the resultant GaN films doped with magnesium were electrically insulating. Several device structures were prepared by Maruska based on a thick undoped (n-type) GaN film topped with a thin Mg-doped insulating film. The first functioning GaN:Mg LED was demonstrated in 1972. After Maruska finished his PhD studies in Stanford he returned in 1974 to RCA Labs with a functioning blue LED. The RCA devices suffered from relatively low efficiency from imperfections and defects and they were far from being ready for commercial production [3].

A first breakthrough in growth technology came in 1986, when Isamu Akasaki and Hiroshi Amano from Nagoya University in Japan developed a suitable growth method and device structure based on a chemical vapour deposition technique. However, another unresolved complication was the growth of the p-type layer [4]. The issue was related to neutralization of dopants (usually zinc or magnesium) which would hamper the efficiency of the LEDs. Akasaki and Amano noticed that when GaN doped with zinc was measured in an electron microscope, the brightness of their LEDs is improved. This suggested that electron irradiation improved the p-doping – an effect that was later explained by Nakamura [5]. This breakthrough invention enabled conversion of compensated Mg doped GaN to conductive p-type material.

In 1993 Nakamura developed the thermal annealing technique to remove the detrimental hydrogen that deactivated the p-type dopants, leading on to the first high-efficiency blue LED presented in 1994 [6]. For their invention Nakamura, Akasaki, and Amano were awarded with the Nobel Prize in Physics in 2014 [7].

In general, the challenge in obtaining p-type doped GaN is related to the high activation energy, 160–180meV, for the acceptor state. Furthermore, in the case of MOCVD or HVPE grown layers with the doping concentrations higher than 10^{18} cm^{-3}, Mg has been observed to segregate into a variety of defects including inversion polarity, and pyramidal inversion domains. Also in the MOCVD growth Mg will be incorporated together with H_2 in the form of a Mg-H complex. In contrast, Mg: GaN grown by MBE is p-conductive as grown and does not require annealing. Also for the MBE-grown doped layers a higher concentration of Mg causes clustering or incorporation in interstitial sites [8]. GaN:Mg presents a further challenge in device applications due to low hole mobilities.

Even though the Mg_{Ga} acceptor has been studied for many years, its electronic structure and the attribution of the photoluminescence (PL) bands in Mg-doped GaN are still sometimes debated. Low doping of GaN with Mg (order of 10^{17}-10^{18} cm^{-3}) will result in n doping due to background shallow donors such as O_N and Si_{Ga}. P-type doping can be achieved when the Mg concentration exceeds 10^{19} cm^{-3} with annealing for the MOCVD method and without for the MBE method [9].

According to theoretical calculations by Neugebauer and Van de Walle [10] Mg incorporation in GaN is limited by formation of Mg_3N_2 complexes. Also Mg concentration at high growth temperatures (>1000K) is limited by the formation of nitrogen vacancies (V_N) and Mg-H complexes, which compensate the acceptors (Fig. 7.1). The presence of hydrogen will enhance the solubility of the acceptor species (Mg), and suppresses native defect compensation (V_N).

In the case of AlGaN material, p-type doping is even more demanding, with more details given in section 2.4.2. Obtaining p-type high AlN content AlGaN alloys is a major challenge for development of AlGaN-based deep ultraviolet optoelectronics devices [11].

Measurement of Mg concentration in GaN or AlGaN samples is crucial for optimization of growth and processing procedures, as well as clarifying the impact on the structural and optical properties.
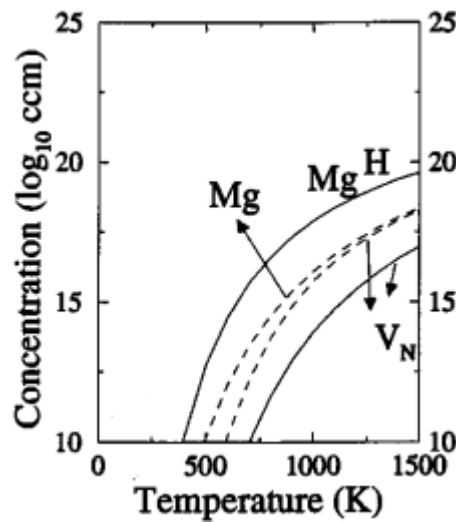
Figure 7.1: Equilibrium concentrations of [Mg] and nitrogen vacancy (V_N), H-rich limit solid lines and H-free limit dashed lines. From Ref. [10].

Figure 7.1 shows how in the H-rich case the Mg and H concentrations are identical indicating that H completely compensates the Mg acceptors. In the hydrogen-free case, the Mg concentration is increased and the V_N concentration decreased, which is beneficial for doping.

7.1.2 Background to measuring magnesium in p-GaN

In this work two Mg:GaN bilayer samples were studied, which will be referred to as A and B. The samples were grown by Drs. Chris Deatcher and Ian Watson by MOVPE at Strathclyde University. A Mg:GaN layer of 1μm thickness was grown on a nid-GaN buffer layer (1 μm), grown heteroepitaxially on sapphire. More details are in Ref. [11]. The samples were activated post growth by the use of a rapid thermal annealing (RTA) treatment.

To confirm the accuracy of the WDX technique for the analysis of Mg concentration the data are compared to SIMS results, provided by the sample growers. Consideration of this complementary technique allows verification of the results and analysis of the reliability for measuring of dopant concentration.

Secondary Ion Mass Spectrometry (SIMS) is the analysis of the mass-to-charge ratio of of molecular or atomic species which are emitted when a surface is bombarded by energetic primary particles in a sputtering process. The emitted secondary ions can provide unique information about the chemistry of the surface from which they originated. During SIMS analysis, the sample surface is slowly sputtered away. Continuous analysis while sputtering produces information as a function of depth, called a depth profile (dynamic mode of operation) [12]. SIMS depth profiling is not just used to check the intentional doping profiles but also to detect the residual impurities. When comparing WDX and SIMS data, it is preferable to average the SIMS data to a depth comparable to that probed by WDX. More details about the SIMS technique can be found in Chapter 3.

It is important to know the amount of trace impurities that incorporate in the samples because they can significantly affect the electronic properties [13]. The unintentionally incorporated impurities can act as an energy-loss path by generating defect states inside the bandgap or non-radiative recombination centres [14].

The WDX technique is also applied to characterise the AlN content and Mg concentration in the top layer of a set of multilayer AlGaN samples. This set of samples comprises of LED samples in which different growth techniques as MOCVD and MBE were employed in growing the different layers of the

structures. The structures were grown on AlN substrate, details available in Table 7.2. Samples varied between hybrid MBE and MOCVD samples to all-MBE samples. The main purpose was to confirm that p-AlGaN can be grown by the MBE technique. The samples were grown by Dr. Ke Wang at Nanjing University.

7.1.3 Background to measuring magnesium in p-AlGaN

$Al_xGa_{1-x}N$ alloys have a direct bandgap energy ranging from 3.4 eV (365 nm) for GaN to 6.0 eV (210 nm) for AlN [15]. They are applicable in many areas due to possibility to tune the gap by changing the alloy composition to cover the entire UV spectral region. AlGaN alloys are attractive materials for the UV optoelectronic device applications such as UV light-emitting diodes (LEDs) and laser diodes (LDs). AlGaN MQWs are often used as the active regions of UV-LEDs and lasers. The very low p-type doping efficiency in AlGaN is the main challenge for the improvement of AlGaN-based DUV LEDs.

One of the issues is the magnesium solubility limit. Calculations by Neugebauer and Van de Walle for GaN indicate a saturation [Mg] value under hydrogen-rich conditions of $\sim 1 \times 10^{20}\,cm^{-3}$[16], while for the saturation limit for [Mg] in $Al_xGa_{1-x}N$ alloy Jeon and co-workers reported a value of $\sim 8 \times 10^{19}\,cm^{-3}$[17]. It is still challenging to grow highly conductive p-type $Al_xGa_{1-x}N$ with a high AlN content due to the large activation energy (E_A) of acceptors in AlGaN and lower formation energy of compensation defects in the material with higher AlN mole fraction. When a semiconductor is doped with donor or acceptor impurities, impurity energy levels are introduced in the forbidden band. For each specific impurity in a semiconductor, there is characteristic activation energy. For hydrogen like shallow impurities, the ionization energy is given by the Rydberg constant corrected for the carrier effective mass and the dielectric constant of the semiconductor. C.-Z. Zhao et al. described the composition dependence of the activation energy for Mg acceptor in AlGaN alloys by modifying the effective mass model[18]. They explained the composition dependence of the activation energy for Mg acceptor is caused by different factors. One is the screening of the acceptor potential by compensating donors and the reduction of the binding energy through the coulomb interaction between the holes in the

VBM (valence band maximum) and the ionized Mg acceptors, Another is that the influence of band-tail state effect on the activation energy for Mg acceptor and the different composition dependence of the VBM between InGaN and AlGaN alloys [18].

For any Al-content, E_A can be expressed with modified Vergards lawaccording to M.S. Hasan et el. and they also demonstrated how calculated activation energies using this modified law have been supported by the Hydrogen atom model or modified effective mass model[19]. The E_A of the Mg acceptors rises from 160 to 630 meV with increasing AlN content x from 0 to 1 [15], due to the low formation energy of compensation defects in material with a higher AlN mole fraction [20]. For example, the nitrogen vacancy acts as a compensation center and its formation energy is reduced with increasing AlN mole fraction [21]. At lower AlN content, effective Bohr radius becomes high and the binding energy is lower. Thus, lower energy is required to substitute any atom or occupy interstitial space of the atoms. The lower binding energy will indicates the lower activation energy of Mg-acceptor [19]. Contrary, for higher AlN content AlGaN higher of Mg-acceptor activation energy is required because the effective Bohr radius is reduces which results in the atoms to stay in close and compact position with high binding energy [22]. With the increase in Al mole fraction, the resistivity becomes a major issue. At AlN contents of $x{\sim}0.45$ a low resistivity of 8 Ω cm was obtained at room temperature [23] whereas at higher AlN content $x{\sim}0.7$ the resistivity increased to 100 000 Ω cm [24]. Recently a low resistivity of 47 Ω cm was reported for $Al_{0.7}Ga_{0.3}N$ [21].

In order to produce high-efficiency DUV-LEDs, it is crucial to obtain a highly conductive p-type AlGaN layer with a high AlN mole fraction. The biggest obstacle with the material is the the maximum external quantum efficiency (EQE) of AlGaN-based deep UV-light-emitting diodes (LEDs), emitting below 300 nm, is only 1%–3% [25]. Recently Shatalov et al. reported a UV LED emitting at 278 nm with EQE of about 10% [26]. For comparison, InGaN-based violet–blue LEDs have EQE higher than 50% [27].

AlGaN material is usually grown heteroepitaxially primarily on the c-plane of sapphire and SiC substrates, due to the large lattice mismatch (about 13%) between substrate and AlGaN layer density of the threading dislocations will be

high. Other solution is to grow AlGaN epitaxial layers on single crystalline AlN substrates in order to improve material characteristics [28] .

The majority of UV optoelectronic devices are produced by the MOCVD method [29], but different growth method, such as the PAMBE method (plasma assisted molecular beam epitaxy) under Ga-rich conditions, can address some of the mentioned challenges. PAMBE growth method can introduce band structure potential fluctuations in the active region of the device, which will in turn promote efficient radiative recombination. Another advantage is the reduction in the incorporation of impurities such as oxygen, carbon, and hydrogen and it can also facilitate the incorporation of dopant impurities [25].

New approaches have been developed to achieve a high free hole concentration in p-AlGaN. These include, for example, growth of the superlattice structures or polarization doping schemes [20].

7.1.4 Introduction to LED structure

UV light sources can be used for a wide variety of applications so it is not a surprise how the demand for them is steadily growing. For example, AlGaN-based ultraviolet light-emitting diodes (UV LED) are used in many areas such as water purification, biological analysis, sensing, epoxy curing, high-density optical storage, white light illumination, UV adhesives, 3-dimensional (3D) printing and UV-coating.

A typical AlGaN UV LED structure consists of the following layers: Si-doped n-type AlGaN, an $Al_xGa_{1-x}N/Al_yGa_{1-y}N$ multiple-quantum well (MQW) active region, an AlGaN-based electron-blocking layer (EBL), Mg-doped p-type AlGaN, and Mg-doped p-type GaN [14] (layers shown in Figure 7.2). When growing an LED structure, a thin AlN nucleation layer is first grown on the sapphire substrate followed by a AlN buffer layer to form a 2D film that serves as the template for the following epi-layers. On the template an n-AlGaN layer is grown to supply electrons. The next layer is the MQW region in which UV photons are generated. MQW region consists of the $Al_xGa_{1-x}N/Al_yGa_{1-y}N$ layers with the x and y satisfying (x < y). On the top an EBL layer is grown that enables efficient carrier injection; this is mainly achieved by a magnesium doped AlGaN

EBL that prevents electron leakage into the p-doped top layers without compromising efficient hole injection into the active region of the LED [30]. The AlN content of the p-EBL layer is larger than content of the AlGaN quantum wells. The following interface is a p-AlGaN/p-GaN heterojunction into which holes are injected, the p-GaN layer forming the p-type ohmic contact as well. The AlN content of the p-AlGaN layer is lower than that of the p-EBL [14].

Every layer has different technical issues to be dealt with. The main challenge is the poor crystallinity of AlGaN epilayers that will cause poor internal quantum efficiency (IQE). Another issue is the n-type and p-type doping efficiencies and resistivity of the material. More details on this are given in Chapter 2.

The lack of p-type conductivity in high AlN content AlGaN results in a number of important issues. Firstly, extremely poor ohmic contacts for p-type AlGaN, that cause a high operating voltage and very poor injection of holes into the active region. Another serious issue is the asymmetry in the carrier transport related to both the concentrations (the activation energy of Mg acceptors is much larger than that of Si donors) and the difference in mobility between electrons and holes (the mobility of holes is much slower than that of electrons due to the large effective mass of holes). Finally, the light-extraction efficiency (LEE) of AlGaN UV LEDs grown on c-plane sapphire substrates is limited by strong transverse magnetic (TM)-polarized anisotropic emission due to the unique valence band structure of AlGaN with a Al molar fraction (>about 25%).

The growth of the AlGaN layers is quite difficult due to the large lattice mismatch and thermal expansion mismatch between AlGaN and the sapphire substrate. The tensile stress in AlGaN epitaxial layers can be relaxed via cracks or formation of threading dislocations (TDD) which is in the order of 10^9–10^{10} cm^{-2}. Another available growth method is homoepitaxy, in which high crystal-quality epilayers can be obtained by using a bulk AlN substrate in order to minimize lattice and thermal expansion mismatches, which will result in decrease in the dislocation density of the epitaxial layer.

It is possible to adjust the strain in the hetero-epilayers by inserting AlGaN/AlN or AlGaN/AlGaN superlattice structures. Another common structure associated

with superlattice is the superlattice-EBL with graded Al compositions, known as graded superlattice-EBL (GSL-EBL), that is used to improve the hole transport in the superlattices and increased overall efficiency. In a Al-composition-graded AlGaN layer with increasing Al content, a high-density mobile three dimensional hole gas can be generated and in turn improve the hole transport [31].
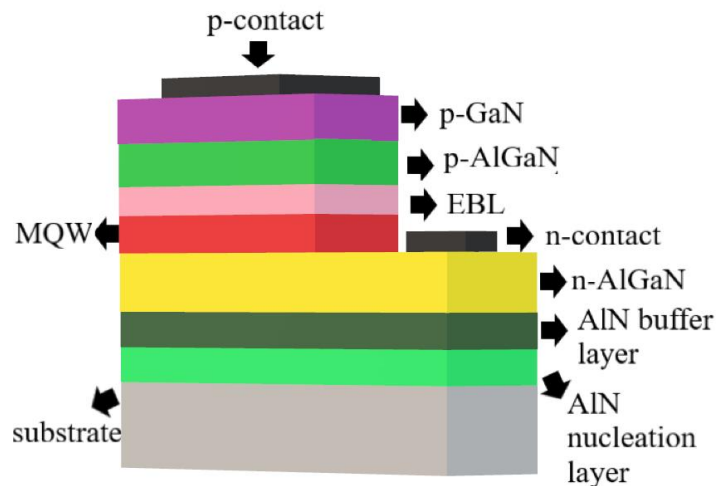
Figure 7.2: Schematic diagram of an AlGaN based UV LED.

7.1.5 Introduction to the WDX technique

The wavelength dispersive X-ray spectroscopy technique that was used to measure the magnesium atom concentration is described in more details in Chapter 3. The usual technique used to measure [Mg] concentration in nitrides are spectrometry techniques such as SIMS and glow discharge mass spectroscopy. However, there are some advantages in using the EPMA method such as: non-destructive nature of the technique, more affordable standards for quantification and possibility to produce quantitative multi-element analysis [32]. It also allows the simultaneous acquisition of luminescence and composition data by combining CL and WDX, and brings high resolution mapping possibilities by scanning the stage or the electron beam [33]. With the adjustment of the accelerating voltage in the EPMA instrument it is possible to control the size of the interaction volume and hence the X-ray spatial resolution and X-ray depth sensitivity. In terms of analysing semiconductor samples, that is particularly useful, because the analyst has a control over the sampling depth

and can be sure which layer has been probed. At low voltages, both the electron range and the interaction volume are significantly reduced, but the voltage has to be high enough to cause X-ray excitation in the material. In turn, that will result in restriction regarding sample thickness, which generally has to exceed around 100 nm.

7.1.6 Methodology for measuring Mg dopants in GaN with WDX

The analysis of magnesium X-rays was performed with a thallium acid phthalate large (TAPL) diffracting crystal at the position of 107.277 mm. Epitaxial layers of GaN from Technische Universität Berlin were used as a standard for Ga and N, while a MgO standard was used for Mg. Mg metal would be an ideal standard, but metallic Mg is prone to oxidation and formation of pits on the surface and it was not available for the performed study.

Mg is present in the measured samples at a trace level (below 1.0 wt. %) [34]. In order to quantify the amount present in the sample a careful choice of analysis conditions such as beam parameters (voltage, current), and other parameters such as spatial resolution, precision, and spectral complexity must be taken into account [35]. With the adjustment of instrumental settings, such as the pulse-height distribution (specifically settings in the gas proportional counter) it is possible to supress the high-order reflections of characteristic X-ray lines if they are producing unwanted interference and to reduce the background signal [36].

When measuring relatively weak magnesium K_α peak careful attention to the background position is crucial in order to avoid any interference. Due to the small signal intensity of the Mg K_α peak, long measurement time is needed in order to improve the counting statistics and signal to noise ratio. The next section illustrates the necessity of a careful background subtraction.
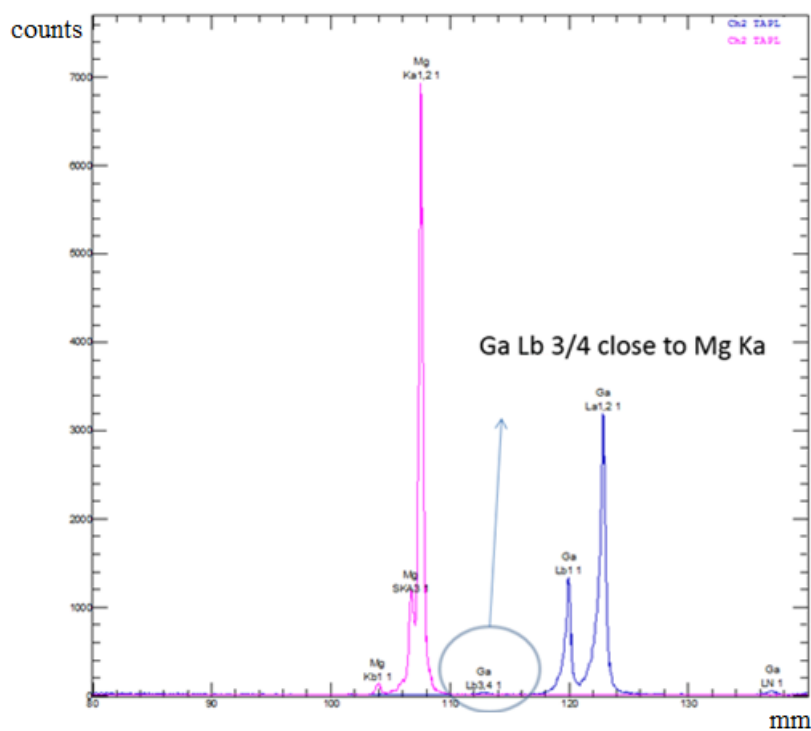
Figure 7.3: Wavelength scan on TAPL crystal for the Mg and Ga peaks, performed on MgO and GaN standards.

Figure 7.3 shows the recorded magnesium X-ray signal from the MgO calibration sample and gallium X-ray signal from the GaN calibration sample. Spectra were superimposed in order to highlight possible overlaps. Both spectra were recorded using a 10 kV accelerating voltage at 100 nA. Besides the Mg K$_\alpha$ peak, there are two additional satellite Mg peaks of the main X-ray line at longer wavelengths, Mg K$_{\beta1}$ and Mg K$_{\alpha2}$.

Care must be taken when choosing background positions for the measurement of Mg due to the Ga L$_{\beta3}$ and L$_{\beta4}$ line in proximity of the Mg K$_\alpha$ line, which is only~60 eV lower than the magnesium K$_\alpha$ photon energy. In the case of Mg doped GaN the Ga L$_{\beta3/4}$ line is more intense than the Mg K$_\alpha$ line. The background position was chosen at 111 mm to avoid interference. In JXA-8530F EPMA distance is defined as distance between the X-ray source and reflecting crystal. Only a negligible change in the position of the Mg peak was observed between the Mg standard and Mg doped samples due to chemical shifts.

Before setting the quantitative analysis, the pulse height distribution always has to be checked for each element on a standard material to avoid any possible

pulse height depression or broadening. The role of the pulse height analysis (PHA) system is set to discriminate between baseline noise and the measured X-ray pulses by adjusting the baseline and window values. Details about WDX principle of work can be found in Chapter 3. Amplification of the detector signal is made applying a detector voltage (referred to as bias) and a gain setting in the electronic amplifier. The bias and gain are set for a particular X-ray of interest, and a single-channel analyzer (SCA) scan is used to inspect the distribution of pulse heights of the X-ray detector. For JEOL instruments the peak in the pulse height distribution is ideally located at 4V [37]. Setting PHA with the differential mode, instead of the commonly used integral mode, is commonly applied to eliminate signals from overlapping elements [38]. When both baseline and window are in use, the PHA is said to be in differential mode.

For the measurement of the Mg, voltage windows are set to differential mode in order to improve signal to noise ratio. The optimal setting of the PHA was found to be a baseline of 1.5 V and window of 5.1 V. An SCA scan (or PHA scan) confirmed the bias value does indeed produce a 4V pulse.


```
Mode          : Base Length Scan    CH-3
Voltage       :   9.80 V          0 count
Peak          :   4.00 V        133 count
Base Length   :      1.50 V
Window Width  :      5.10 V
High Voltage  :   1782 V
```
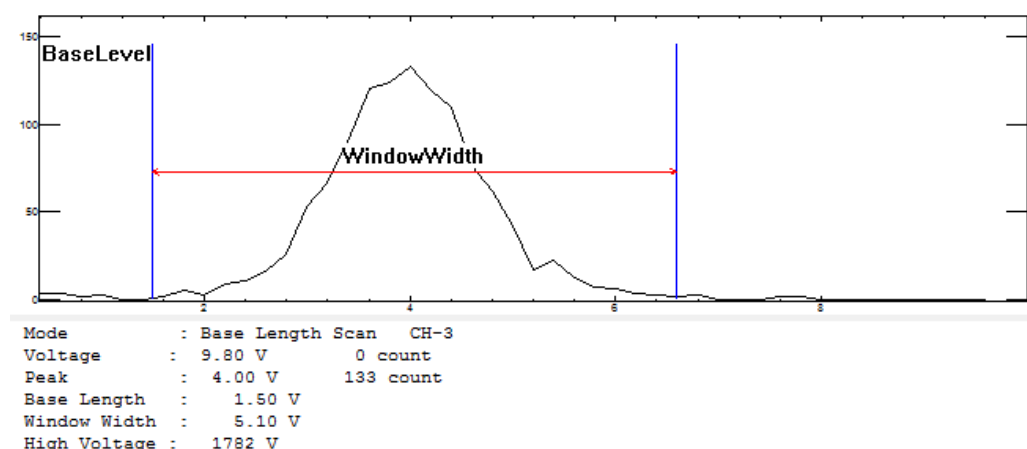
Figure 7.4: PHA scan on Mg standard, used set up for the differential mode. Compositional measurements were performed at an accelerating voltage of 10 kV, and a beam current of 40 nA for Ga and N and 400 nA for Mg. Quantitative analyses on GaN:Mg samples involved signal acquisition for periods of 360 s at the centre of the magnesium peak, while for the Ga and N the measurement time was set to 60 s. The sampling depth was checked with Monte Carlo (MC) simulations using the CASINO software: with the accelerating voltage of 10 kV

used the depth in which 90% of the beam energy is deposited corresponds to ~400 nm in GaN [39].

Mg measurement were performed separately after measurement of the major elements at the same analysis points. Data from the analysis of major elements and Mg is combined in the microprobe software post-analysis in order to perform the ZAF correction.

In order to avoid any possible charging effects on the sample surface, samples were coated with a thin layer of carbon. The effect of the coating could be checked by comparing quantitative results of the coated and uncoated samples. All GaN:Mg epilayer samples were analysed with and without coating (carbon coating thickness ~15 nm). Each sample was measured at nine different analysis points. The MgO standard was carbon coated (25 nm C thickness); an uncoated MgO standard was not available and uncoated MgO would not work as it is too resistive. An uncoated GaN standard was used when analysing coated samples and an uncoated one used when analysing uncoated samples.

7.1.7 Results for p-GaN

The magnesium concentration measured in sample 193 (A), (uncoated) corresponds to a mass percentage of ~0.04%, equivalent to a concentration of 7×10^{19} cm^{-3}, and it is higher than the concentration measured in sample 321 (B) corresponding to a mass percentage of to ~0.03%, and concentration of 5×10^{19} cm^{-3} (Table 7.1). If the obtained WDX values are compared with SIMS for the sample measured, the WDX concentration is 31% lower for sample 193 (A) and 41% lower for sample 321 (B). Note that the analysis points are different for WDX and SIMS measurements. WDX and SIMS quantitative data resulted in the same order of magnitude 10^{19} concentration range and the higher Mg concentration is measured in sample 193 (A) with both techniques.

Next, the effect of the coating will be considered. If the results for the coated and uncoated sample are compared, the measured concentration in sample 193 (A) for the coated sample is 10% lower, while for sample 321 (B) the concentration in coated sample is 31% lower. For the uncoated samples

242

measured Mg concentration is higher, because absorption of Mg X-rays would result in a lower apparent concentration.

Sample 193 (A), which has higher measured Mg concentration also resulted in smaller standard error compared to sample 321 (B) (Figure 7.5). It would be expected to have a larger standard error for the coated samples, due to small discrepancies between the coating thickness of samples and standards and some absorption of the X-ray intensity within the carbon layer. Surprisingly, in sample 193 (A) for the coated sample standard errors are smaller, probably due to the effect of the carbon coating on enhancement of sample conductivity [40].

Overall with the adjusted analysis conditions errors are reduced due to increased measurement time for Mg peak and separate measurement with high current.

Table 7.1: Comparison between [Mg] values determined by SIMS and WDX-EPMA, uncertainty is based on standard error.

Sample name	[Mg] from SIMS (cm^{-3})	[Mg] from WDX-EPMA (cm^{-3})
193 (A)	9.5×10^{19}	$7.0\ (\pm 0.1) \times 10^{19}$
321 (B)	8.1×10^{19}	$5.0\ (\pm 0.2) \times 10^{19}$
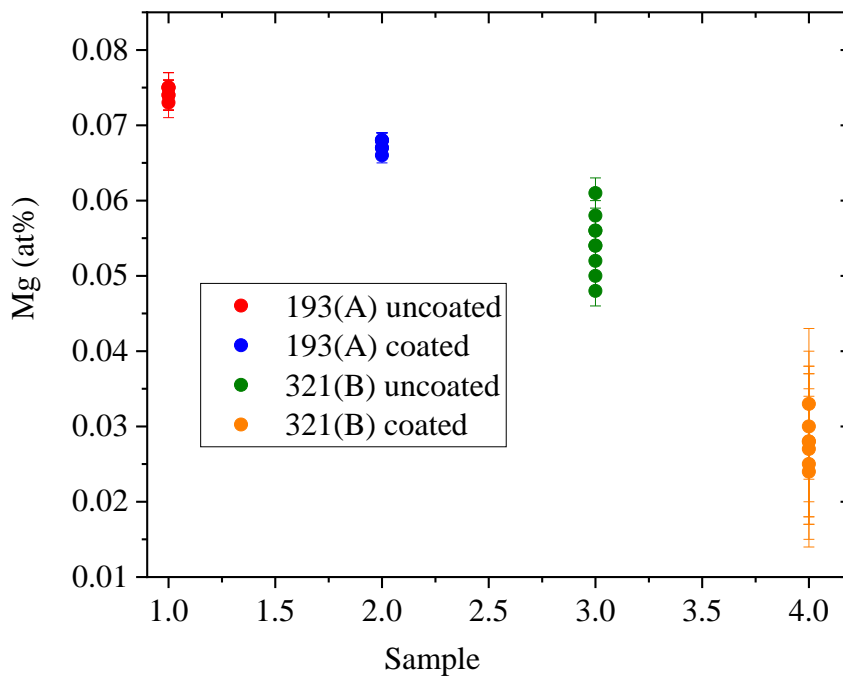
Figure 7.5: Results of the WDX analysis for [Mg] for the uncoated and coated sample 193 (A), and uncoated and coated sample 321 (B).

7.1.8 Methodology for measuring Mg dopants in AlGaN with WDX

All WDX measurements in the EPMA are conducted with the incident electron beam normal to the sample surface, with an varying acceleration voltage depending on the sample structure, ranging from $4-7$ kV (Table 7.2) and a beam current of 40 nA for Ga, Al and N and $500-700$ nA for the Mg. Quantitative analysis on AlGaN:Mg samples involves signal acquisition for periods of 360 s at the centre of the magnesium peak, while for the Ga, Al and N measurement time is set to 60 s. Mg measurement is performed separately, as described in section 7.1.6.

Epitaxial layers of GaN from Technische Universität Berlin are used as a standard for Ga, and AlN sample from Paul Drude Institute for Al and N, while the MgO standard is used for Mg. When analysing higher content AlGaN samples AlN standard has been shown to give better results in terms of stocichometry (measured value for N at% closer to 50%) when compared to GaN standard due to matrix effects.

All AGaN:Mg epilayer samples are analysed without coating, and each sample is measured at nine different analysis points.

The Ga L$_\alpha$, Al K$_\alpha$ and Mg K$_\alpha$ signals are recorded using a large thallium acid phthalate (TAPL) crystals, while for the N K$_\alpha$ signal a synthetic synthetic layered crystal (LDE1L) is used. The signals are recorded with the diffracting crystal at the positions of 90.667 mm, 122.721 mm, 149.667 mm and 107.282 mm for the Al, Ga, N and Mg peaks, respectively. The peak-minus-background signals are compared with those measured from GaN, AlN and MgO standards under the same conditions, to give the experimental k-ratios (sample intensity/standard intensity). The measured k-ratios are then converted to atomic percentages using iterative correction routines [41].

7.1.9 Results for p-AlGaN

AlGaN samples from Nanjing University (more details in Table 7.2), are also analysed to confirm the accuracy of the WDX technique for the analysis of the Mg concentration in ternary alloys. For that purpose, as in the case of the p-GaN

samples, the data is compared to SIMS results provided by the sample growers. Consideration of this complementary technique allows verification of the results and analysis of the reliability for measuring of dopant concentration.

The AlGaN samples analysed are grown using a combination of MBE and MOCVD epitaxial techniques. This is done in order to benefit from the advantages of them both: the high quality of the MBE layer and the fast growth rate offered by MOCVD. At the moment, the MBE method falls behind MOCVD in terms of growth rates or throughput in fabrication, so the combination of methods offers a solution for this concern [42].

Table 7.2: Description of the analysed AlGaN:Mg samples with values of the sampling depth, according to MC simulation [39] as described in section 7.1.8.

Sample name	Sample type	Accelerating voltage (kV)	Sampling depth (nm)	Top layer (probed layer)
N357	MBE p-AlGaN on MOCVD AlN/sapphire template	7	240	MBE p-AlGaN
N361	MBE p-AlGaN on MOCVD: EBL, MQW, n-AlGaN on AlN/sapphire template	6	170	MBE p-AlGaN
N366	MBE p-AlGaN graded on MBE EBL, MOCVD MQW, n-AlGaN on MOCVD AlN/sapphire	5	140	MBE p-AlGaN
N356	MBE p- AlGaN graded on MOCVD AlGaN/ AlN/sapphire template	4	100	MBE p-AlGaN

The beam energy obtained with the help of MC simulation is higher than the minimum energy needed to excite the selected X-ray lines while containing the interaction volume within the desired top p-AlGaN layer of the structure.

Following section provides schematics of the detailed structured of the AlGaN samples described in Table 7.2 and characterised by WDX (same samples are also characterised with CL, results presented in section 7.2).
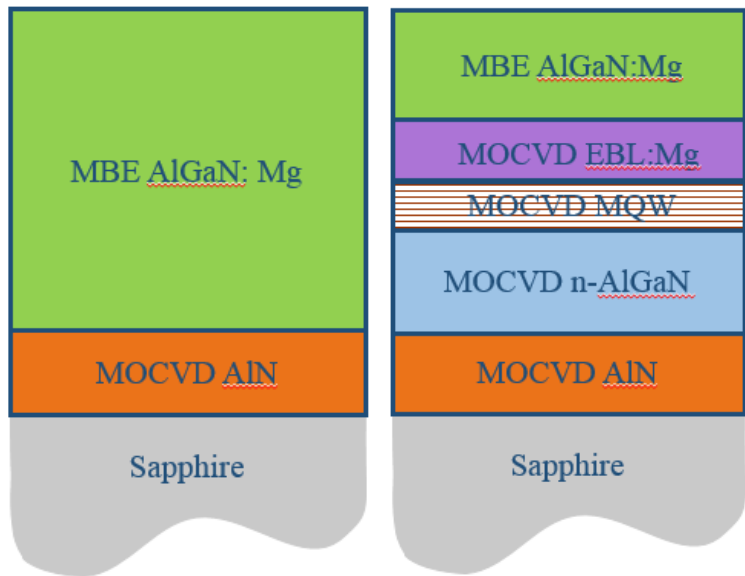
a) Sample N357 non-LED   b) Sample N361 hybrid 1
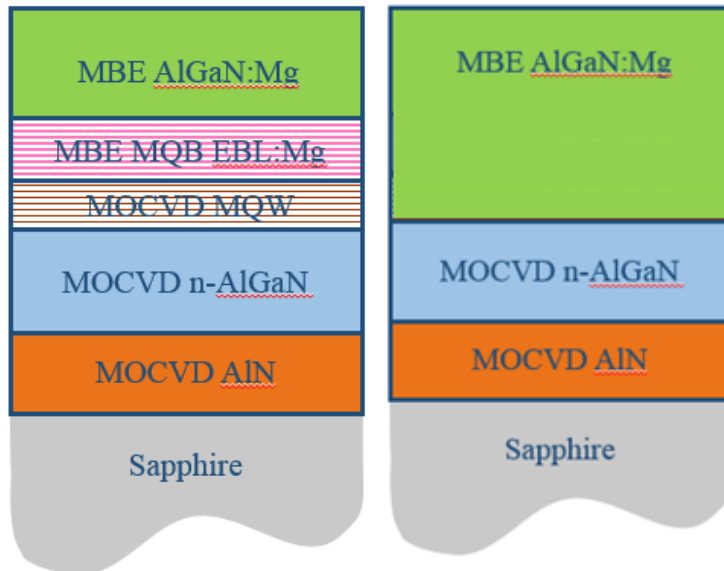
c) Sample N366 hybrid 2   d) sample N356 non-LED

Figure 7.6: Schematic representation of the studied samples: a) and d) epilayer samples: b) and c) LED samples.

Table 7.3: Results of the WDX analysis for the AlGaN:Mg samples measured at different accelerating voltages depending on the thickness of the doped layer.

Sample name	AlN at%	Al standard error at%	GaN at%	Ga standard error at%	Mg at%	Mg standard error at%	N at%	N standard error at%	Mg ($\times 10^{19}$) cm^{-3}	Mg ($\times 10^{17}$) cm^{-3} error	wt total%
N357 (7 kV)	72.52	0.77	27.43	0.29	0.024	0.001	47.38	0.95	2.3	5.5	99.29
N361 (6 kV)	55.84	0.53	43.99	0.42	0.081	0.008	52.42	1.05	7.5	76	101.73
N366 (5 Kv)	56.82	0.58	43.15	0.44	0.015	0.001	48.65	0.97	1.4	5.2	100.65
N356 (4 kV)	88.20	0.88	11.72	0.12	0.037	0.001	50.44	1.01	3.5	9.6	98.13

The composition of the samples is determined by WDX. The AlN concentration increases from 56 to 88% and Mg concentration varies from 1 to 8 $\times 10^{19}$ cm^{-3}. The WDX weight total does not diverge too far from 100%, which is one of the indicators of the successful WDX analysis. At 4 kV, weight total is 98% but at such low overvoltage this value is still acceptable. The ideal atomic percentage of N should be 50% and the measured at% varies from 48−53%. For the sample N361 the N at% is furthest away from the 50%, due to the charging effects that were apparent during SEM observation. All the standard errors are close to 1%, which is another indicator of properly conducted analysis.

Table 7.4: Comparison between [Mg] values determined by SIMS and WDX-EPMA, uncertainty is based on standard error.

Sample name	[Mg] from SIMS (cm^{-3})	[Mg] from WDX (cm^{-3})	Mg cm^{-3} error WDX
N357 (7 kV)	4.5×10^{19}	2.3×10^{19}	6×10^{17}
N361 (6 kV)	8.5×10^{19}	7.5×10^{19}	8×10^{18}
N366 (5 kV)	4.5×10^{19}	1.4×10^{19}	5×10^{17}
N356 (4 kV)	4.5×10^{19}	3.5×10^{19}	1×10^{18}

If the WDX results are compared with SIMS values for the measured samples, the WDX concentration is 50 % lower for sample N357, 12 % lower for sample N361, 70% lower for sample N366 and 23% lower for sample N356. In general

the concentration obtained with WDX measurement is lower than the one obtained with SIMS, the same behaviour observed in the p-GaN samples. Both WDX and SIMS quantitative data resulted in the same order of magnitude 10^{19} concentration range and the highest Mg concentration is measured in sample N361 with both techniques.

7.1.10 SIMS results for p-AlGaN
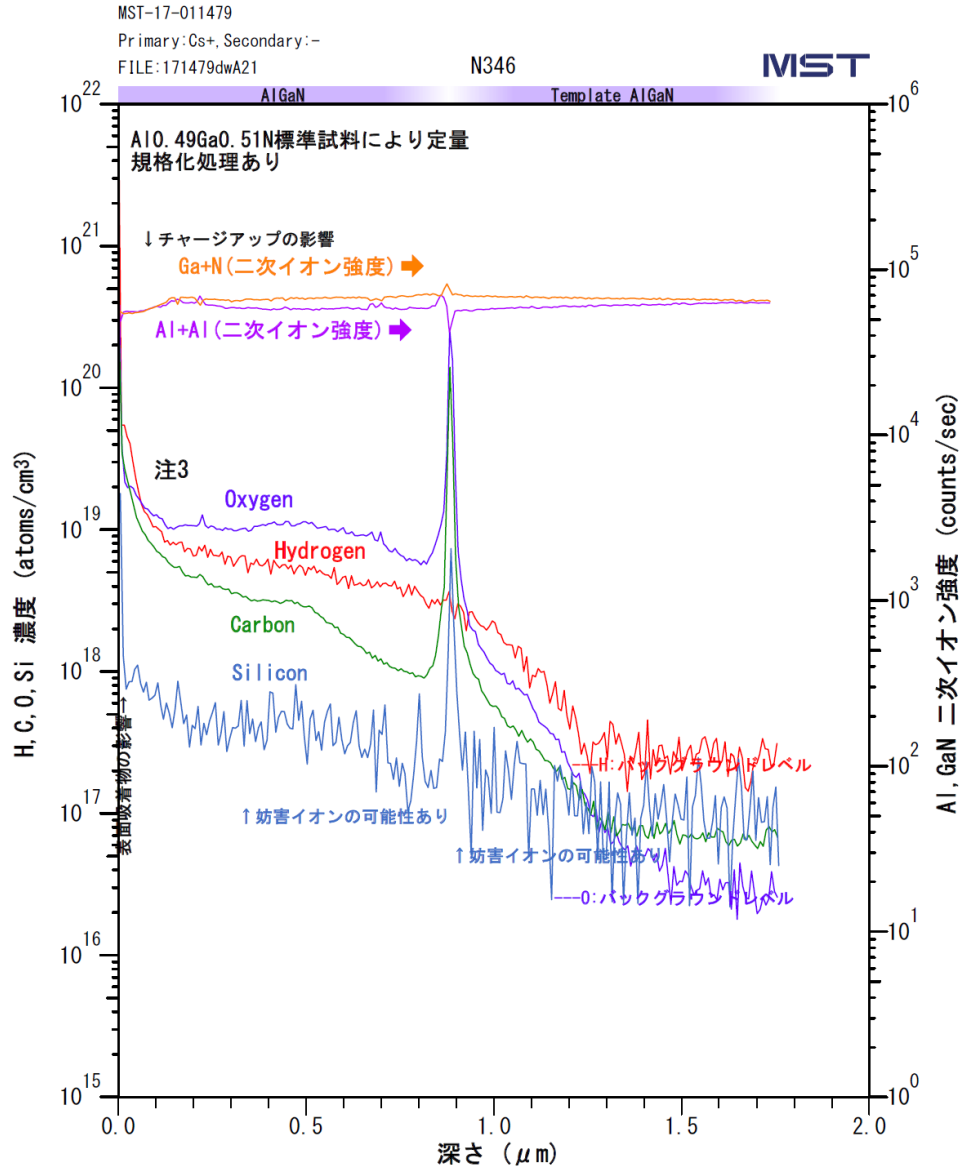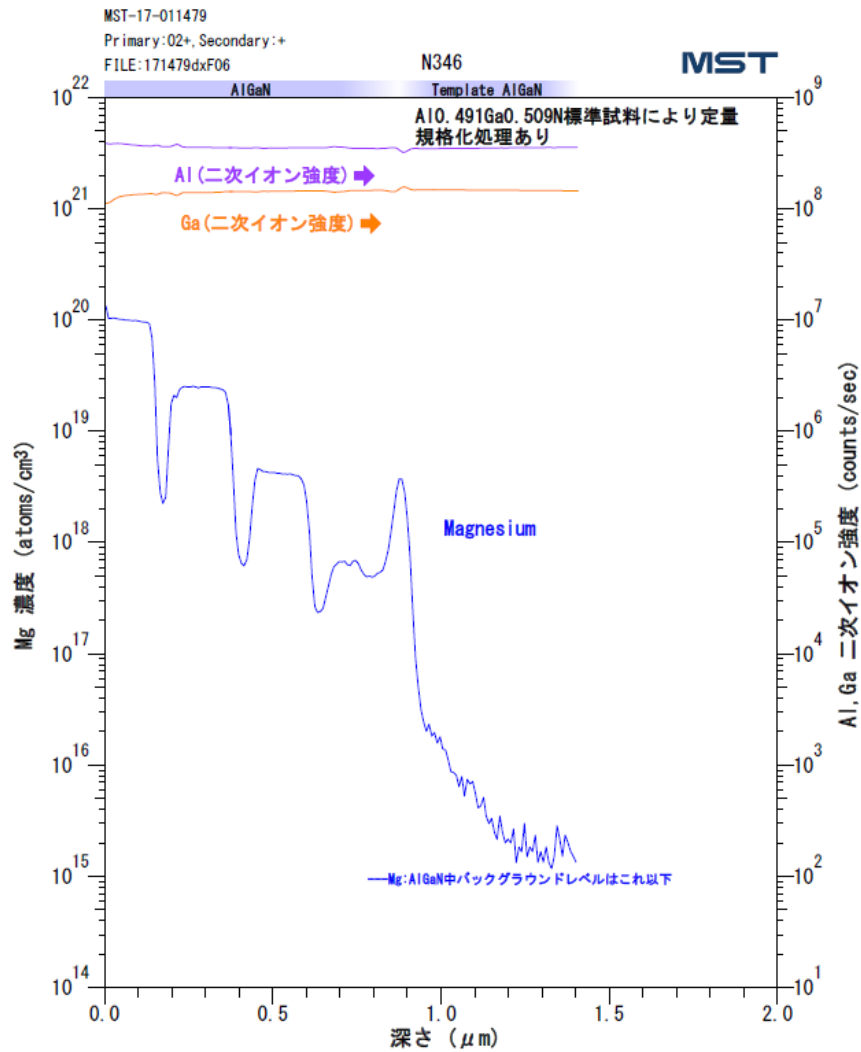
Figure 7.7: The concentration depth profile measured by SIMS for sample N346.

The SIMS measurements shown in Figure 7.7 are performed by the growers. From the concentration depth profile it is evident that the signals from impurities such as C, H, O and Si are quite high. The impurity signals increase significantly at around 900 nm in depth, reaching 10^{19} and 10^{20} cm^{-3} levels. This point of increase corresponds to the interface with the MOCVD AlGaN layer that was grown in a different reactor. This transfer from an MOCVD to an MBE reactor has possibly enabled incorporation of impurities. The impurities signal seems constant through all MBE layer (p-doped AlGaN and undoped AlGaN). Highest signal is for the oxygen and lowest for the silicon. The lowest detection limit is

obtained for oxygen and highest for hydrogen and the impurity signals are lower in the MOCVD layer.

A possible reason for the high incorporation of impurities is the high bond strength of Al with those impurities [43]. Oxygen impurities in AlGaN layers produce impurity related states inside the band gap, causing parasitic emission or phonon generation, which degrade the IQE [14]. From the plots it is possible to interpolate the [Mg] background level being around 10^{17} cm^{-3}, and the detection limit for the [Mg] is around 10^{16} cm^{-3}.

This sample has step Mg concentration and the Mg intensity drops every 160 nm, due to inserted undoped AlGaN layers. The Mg intensity in the doped layers is monotonically decreasing until the interface with the MOCVD layer at 900 nm where the signal increases again. Sample N346 was used as a reference sample to measure Mg concentration in other samples using SIMS technique.

7.1.11 Summary and conclusion

EPMA method has been proven to be a suitable technique for the precise and accurate quantitative chemical analysis chemical of p-GaN and p-AlGaN samples. There are multiple factors that will influence the accuracy and precision of the EPMA analysis. These include the choice of standards, physical condition of the standards and samples, beam stability and effects of the beam on the sample, choice of spectral line and possible background overlaps, counting statistics, matrix correction and sample size relative to the excitation volume.

In this chapter the focus was on getting the best possible results by adjustment of the analytical conditions (e.g., accelerating voltage, beam current, etc.). It is demonstrated how care must be taken to avoid interfering peaks of other elements both on the peak and the background positions and how important is to correctly sett the PHA baseline and window positions.

7.2. Sample structure (CL measurement)

This section provides schematics and tables of the detailed structured of the AlGaN samples from Nanjing University characterised by CL. Non-LED epilayer samples N346 and N357 (samples N357 shown in Figure 7.6) are grown on an MOCVD AlN/sapphire template. Hybrid structure 1 (sample N361, shown in Figure 7.6) consists of a top MBE p-AlGaN layer while the rest of the layers are grown with MOCVD. In hybrid structure 2, an electron-blocking layer (EBL) is also grown with the MBE method (samples N372 and N366). The sample N366 has a special MQB (multi-quantum-barrier) EBL structure developed by Prof. Hirayama (shown in Figure 7.6). The third type of hybrid structure (samples N373 and N374) consists of all MBE layers on top of the template.
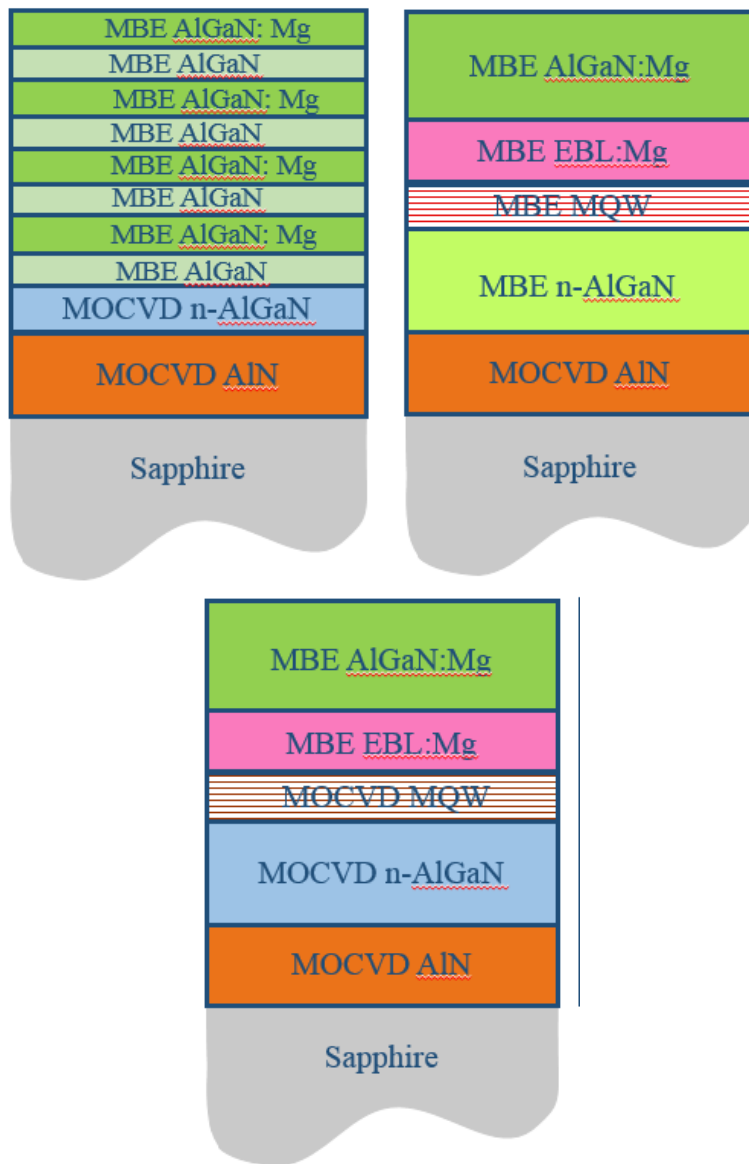
a) Sample N346 non-LED b) Sample N373, N374 hybrid 3 c) Sample N372 hybrid 2

Figure 7.8: Schematic representation of the studied samples: a) epilayer sample: b) and c) LED samples. More details in Tables 7.5 and 7.6, rest of the studied samples are shown in Figure 7.6.

Table 7.5: Sample description of the studied epilayer samples on MOCVD 4 μm AlN/sapphire template (non-LED samples).

Sample layer	p-AlGaN			AlGaN (undoped)				n-AlGaN	
Sample name	Growth method	*(nm)	AlN %	Growth method	*(nm)	AlN %	Growth method	*(nm)	AlN %
N346	MBE	160	70	MBE	80	unknown	MOCVD	1.5 μm	60
N357	MBE	240	70	/	/	/	/	/	/

*thickness

Table 7.6: Sample description of the studied LED samples on MOCVD 4 μm AlN/sapphire template.

Sample layer	p-AlGaN			EBL			MQW				n-AlGaN	
Sample name	Growth method	*(nm)	AlN %	Growth method	*(nm)	AlN%	Growth method	*(nm)	AlN %	Growth method	*(nm)	AlN %
N361 hybrid 1	MBE	200	75	MOCVD	20	90	MOCVD	(10/1.8) × 3	70/60	MOCVD	1500	70
N366 hybrid 2	MBE	160	70	MBE MQB	AlN (12,8,4) AlGaN (6 nm)	3 AlN barriers in AlGaN 70%	MOCVD	(10/1.8) × 3	70/60	MOCVD	1500	70
N372 hybrid 2	MBE	80	70	MBE	20	90	MOCVD	(10/1.8) × 3	70/60	MOCVD	1500	70
N373 hybrid 3	MBE	84	70	MBE	20	100	MBE	(10/1.8) × 4	70/60	MBE	480	70
N374 hybrid 3	MBE	84	70	MBE	20	95	MBE	(10/1.8) × 4	70/55	MBE	480	70

*thickness

7.3 CL data

The emission properties of the described sample (Tables 7.5 and 7.6) are investigated using cathodoluminescence (CL) spectroscopy and hyperspectral imaging using an FEI Quanta 250 using a spectrometer with a with a 600 lines/mm grating blazed at 200 nm, a 50 µm slit, and a 1600-element charge-coupled device. More details about the CL system can be found in Chapter 3. The measurements are performed at room temperature with varying the beam voltage in order to probe the material as a function of depth. different acceleration voltages.

7.3.1 CL from non-LED samples

For the analysed samples, the main purpose of the growers was to confirm that p-AlGaN can be grown by the MBE method. Sample N346 is grown as a "marker" sample for the determination of Mg concentration by the SIMS method. Sample N357, on other hand, is produced in order to confirm whether the p-AlGaN layer can be obtained by the MBE method and if the Mg concentration is within desired range.
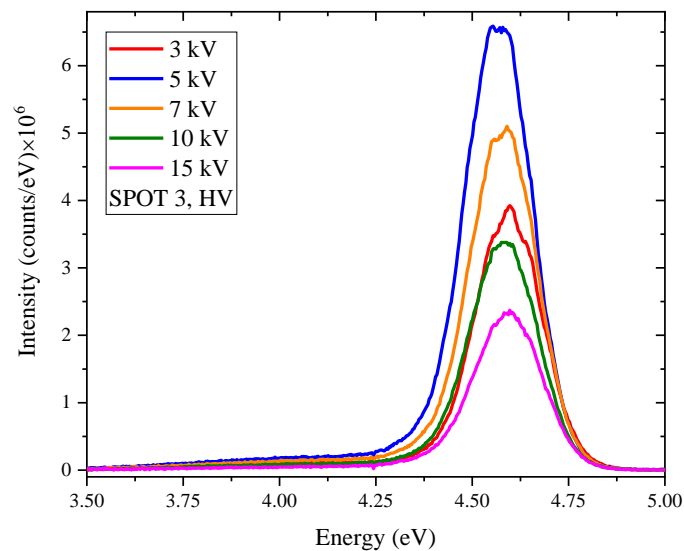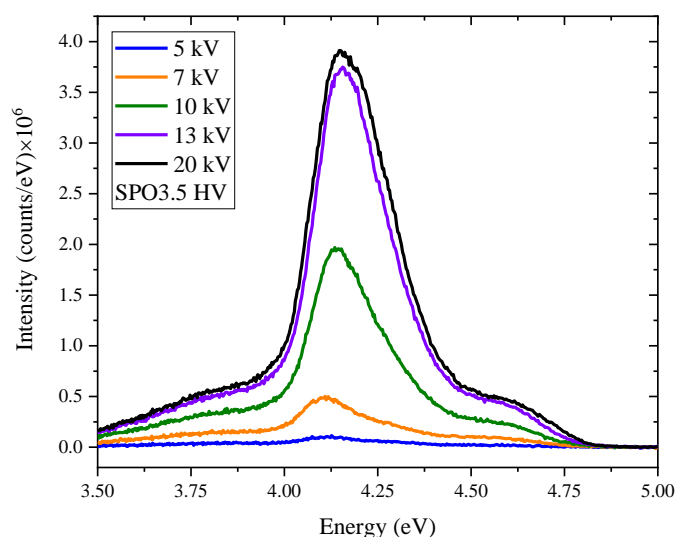
Figure 7.9: CL point spectra of the: on the top N357 MBE grown AlGaN:Mg on MOCVD AlN/sapphire and on the bottom N346 MBE grown AlGaN:Mg with step Mg on MOCVD AlGaN/AlN/sapphire.

In the CL spectra of the sample N357 only one broad peak is visible at 4.6 eV which cannot be attributed to the near-band edge emission (NBE) coming from AlGaN MBE layer due to its low emission energy. The peak can be assigned to defect luminescence corresponding to the III-vacancies often associated with the O_N impurities in adjacent sites, in this case forming the $(V_{III}–O_N)^{1-}$ complex [44]. The intensity of the peak is highest when the beam voltage is at 5 kV, when 90% of the deposited beam energy is contained within first 140 nm of the sample according to MC simulation [39], which is to say beam energy is contained within AlGaN MBE layer. The intensity of the peak increases with increasing voltage from 3 kV to 5 kV, but then decreases at 7 kV when the penetration into template region occurs and drops to its lowest value by 15 kV.

In the point CL spectra of the sample N346 the highest intensity peak is visible at 4.2 eV at each voltage, with its intensity increasing from 3 kV to 20 kV. The peak can be attributed to the V_N defect in Mg doped AlGaN. Nakarmi et al. suggested this emission to be a DAP (donor-acceptor pair) transition between V_N and Mg_{III} [45]. Another peak present in the spectra is positioned at 4.6 eV, which can be attributed to the same defect peak present in sample N357, the $(V_{III}–O_N)^{1-}$ complex. The intensity of the 4.6 eV peak increases with increasing voltage. The presence of this defect peak is consistent with the oxygen observed

in the SIMS data (Figure 7.6). Also in the spectra, an additional peak start to appear at 10 kV and its intensity is increasing with the voltage, it is present on the lower energy side at 3.8 eV and associated with the Mg donors, related to the $Mg_{III}^+H_i$ complex and Mg^{III} defects [46].

Sample N346 has stepped Mg concentration, ranging from 10^{20} at/cm^3 to high 10^{17} at/cm^3 (Figure 7.7) while sample N357 has only single Mg doped level of 4.5×10^{19} at/cm^3 (Table 7.4) according to SIMS measurements. The sample with stepped Mg concentration shows different defect peaks, including ones associated with Mg donors. In contrast, sample N357, which has only single Mg doping, dos not show defect peaks associated with Mg donors. Neither sample is showing NBE emission from MBE AlGaN layer.

7.3.2 CL mapping of the non-LED samples

In order to investigate the luminescence properties of the AlGaN layers CL hyperspectral imaging, as described in Chapter 3, was performed. To ensure that the excitation volume does not penetrate into the MOCVD layers, for sample N346, a 10 kV accelerating voltage was selected (beam energy is contained within 500 nm of AlGaN layers). Sample N357 has thicker top MBE layer so it was possible to use higher voltage of 15 kV. The useful feature of the CL hyperspectral imaging is that, not only does it have the ability to acquire an integrated CL intensity map that is equivalent to a conventionally acquired panchromatic CL intensity map, but it is also possible to map the shifts in wavelength or energy and correlate them to features on the sample surface.

a)
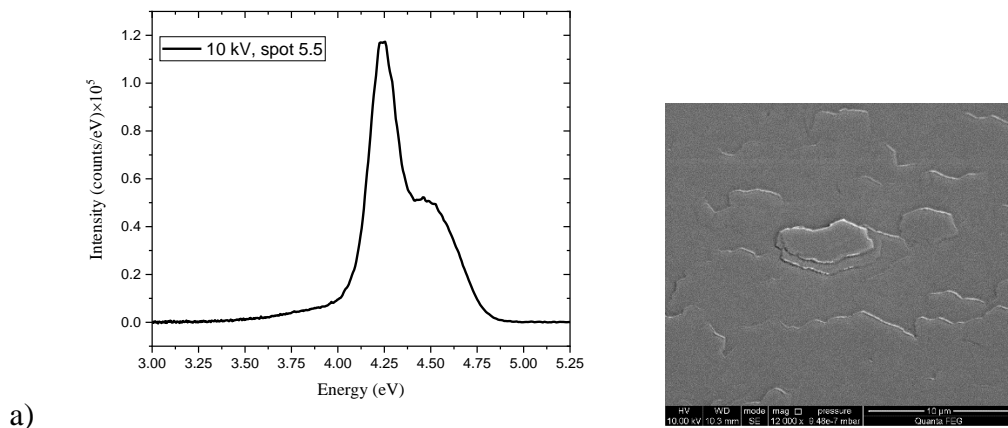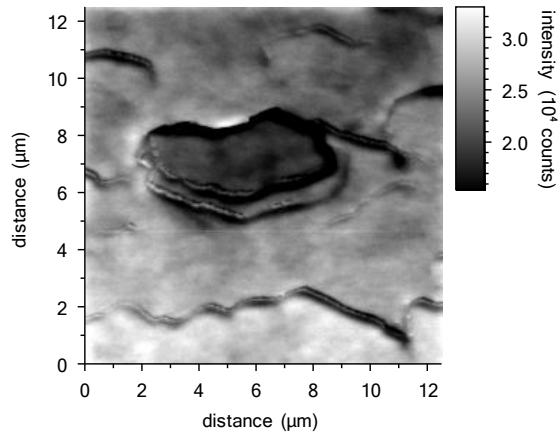
b)
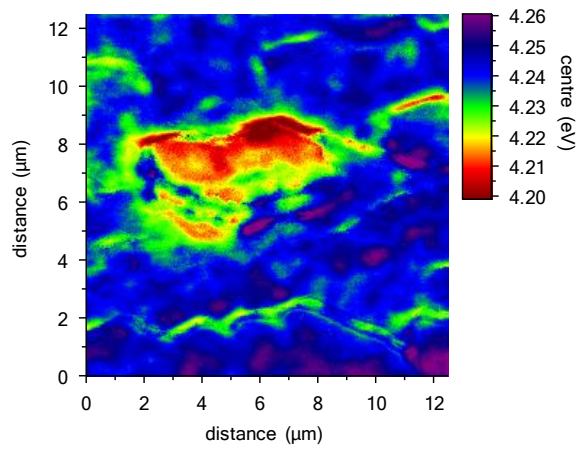
c)
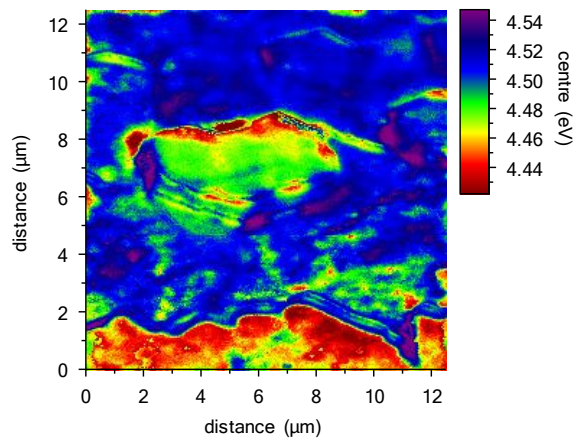
d)
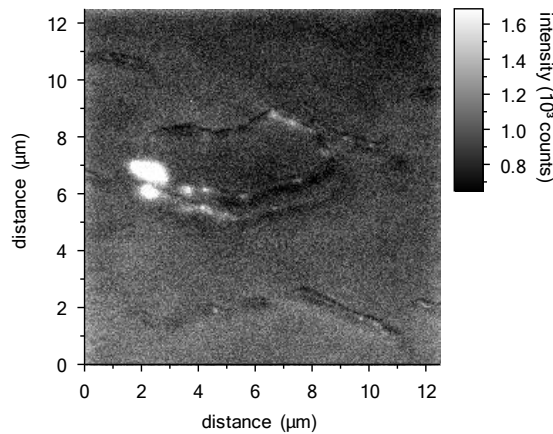
e)

Figure 7.10: Sample N346 map acquired at 10 kV, spot 5.5: a) mean Cl spectrum and SE image; b) integrated CL intensity map (4.0−4.4 eV); peak energy map of the fitted: c) 4.2 eV peak and a d) 4.5 eV peak; and e) integrated CL intensity map (3.8−4.0 eV).

In the mean spectrum extracted from the CL hyperspectral map, two peaks are visible, with the peak at 4.5 eV being of much lower intensity. Similar behaviour was recorded in the CL point spectra. From the CL intensity map larger steps on the surface area are noticeable as well as the bigger hillock-like 3D features. The formation of a hillock-like surface morphology is driven by strain relaxation through the diffusion of surface adatoms [44]. CL imaging reveals two defect peaks at 4.2 eV and 4.5 eV, with the peak at 4.2 eV related to a V_N defect emission and the peak at 4.5 eV corresponding to a $(V_{III}–O_N)^{1-}$ complex [44].

From the peak energy map of the 4.2 eV peak, a lower energy shift along a step edge is visible which would correspond to a Ga rich region along this edge. Also within the 3D structure the emission energy is redshifted, as well as the AlN content being lower compared to the surrounding area. The peak energy map of the 4.5 eV peak looks similar to the 4.2 eV map in terms of lower energy emission within the 3D structure, but the shift is more pronounced at the top edges of the 3D platelet structure as well as the area alongside the step edges. Some additional nanosize areas of lower emission energy are also present in 4.5 eV peak energy map, situated between the platelet structure and the step edges. In the 4.2 eV peak energy map, the area below the step edge is not red shifted. From the energy map it is possible to conclude that different defect

luminescence is concentrated at particular areas within the sample. The CL intensity maps of the defect peak at 3.8 eV (associated with the Mg donors) revels spots of higher intensity which are only present along the edges of platelet structure and therefore possibly indicate localised regions of defect emission.
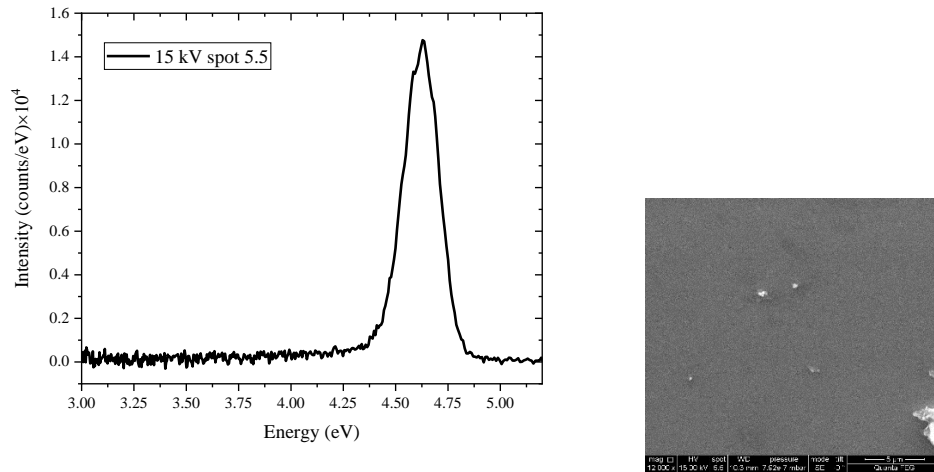
a)
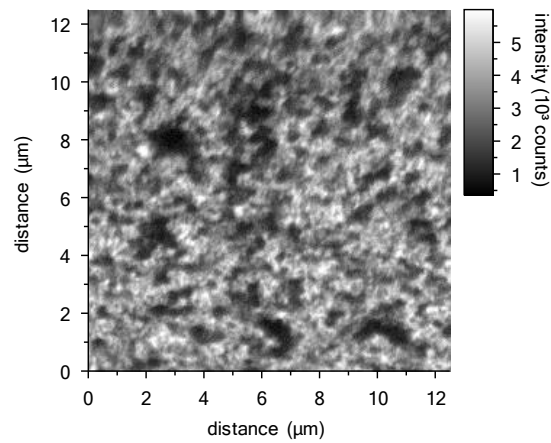
b)
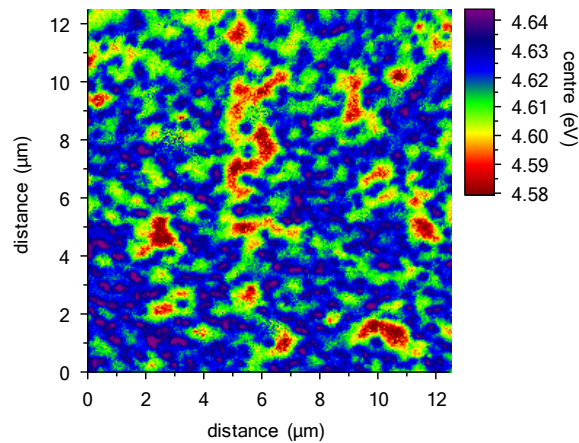
c)

Figure 7.11: Sample N357 map acquired at 15 kV, spot 5.5: a) mean Cl spectrum and SE image, b) integrated CL intensity map (4.4-4.9 eV), c) peak energy map of the fitted 4.6 eV peak.

In the mean spectrum extracted from the CL hyperspectral map, only one peak is visible at 4.6 eV, the same as for the CL point spectra. In the CL intensity map of the peak, small domains of circular shape (approximate 35 nm in size) of different emission energies are noticeable. The compositional difference is much smaller compared to sample N346, but still small local compositional variation is present. The surface is free from hillock features.

7.3.3 WDX mapping of the non-LED samples

By measuring CL in the hyperspectral imaging mode, spatial variations were observed in both emission intensity and wavelength; to compliment these findings, EPMA mapping is used to acquire compositional information like alloy fluctuations by collecting X-ray element distribution maps [47]. While BSE images can show variations in composition in a sample, X-ray maps can show which elements are responsible for the variation [48].
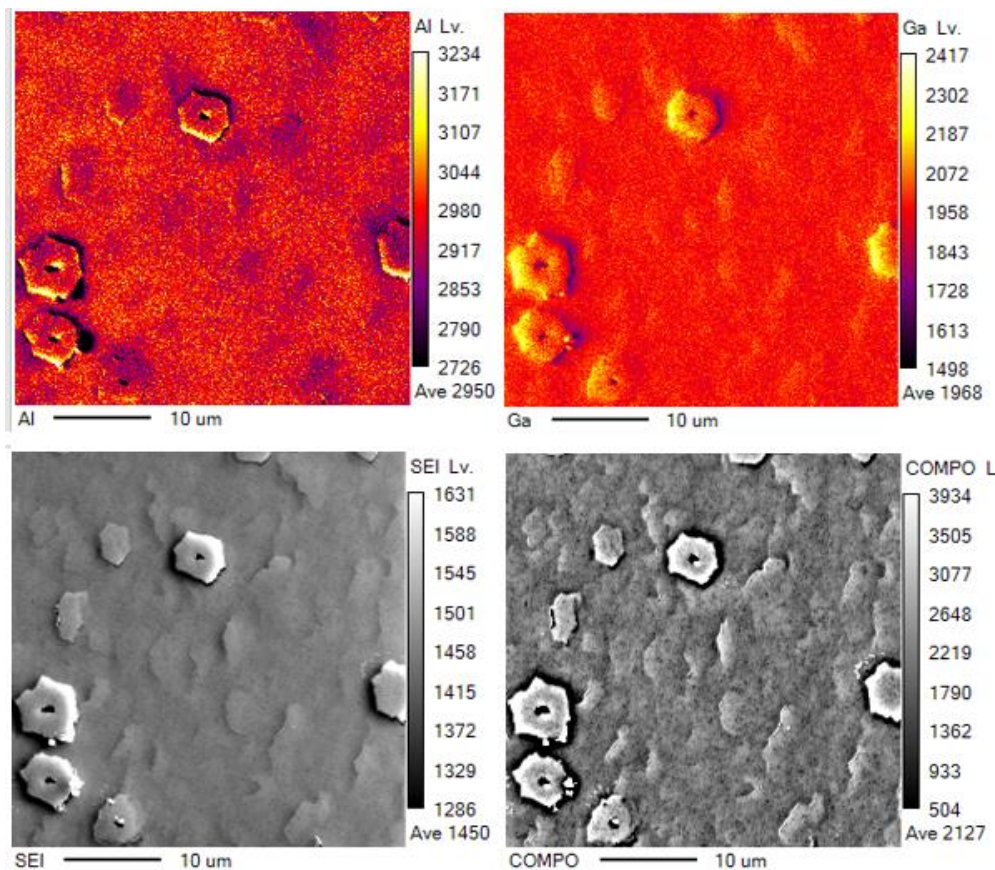
Figure 7.12: N346 WDX map with accompany secondary electron (SE) and backscattered electron (BSE) images acquired with 20 kV, 100 nA.

The AlGaN layers are mapped using an acceleration voltage of 20 kV (voltage was increased compared to CL measurement in order to increase the X-ray signal) and a beam current of 100 nA, by stepping the sample underneath a focused electron beam at normal incidence and using individual spectrometers to measure the intensities of Ga L_α and Al K_α X-rays at each point.

The presence of topography at the specimen surface affects the measurements during X-ray mapping. It can have a significant effect on the produced X-ray intensities. The local topography introduces variable absorption path-lengths in different directions, so that the intensity emitted varies according to the spectrometer position [49]. In order to check the effect of different spectrometer positions, Ga L_α and Al K_α X-ray maps are recorded with different spectrometers, but the produced maps showed the same effect in signal intensity variations.

The local topography affects the angle of incidence between the beam and the specimen surface, and hence the number and trajectories of the measured BSE

(compositional contrast -COMPO) and SE depends on the local orientation [50]. From the SE and BSE images the increase in the signal intensity of the hexagonal features is noticeable due to their 3D nature.

From the WDX map of Al K$_\alpha$ and Ga L$_\alpha$ X-ray intensities, it is clear that parts of the sample with hexagonal features (hexagon edges) have lower Al X-ray intensity, which would correspond to the lower emission energies observed in CL peak energy maps in Figure 7.10. In the WDX maps, a negative correlation between Ga and Al X-ray intensities is confirmed.
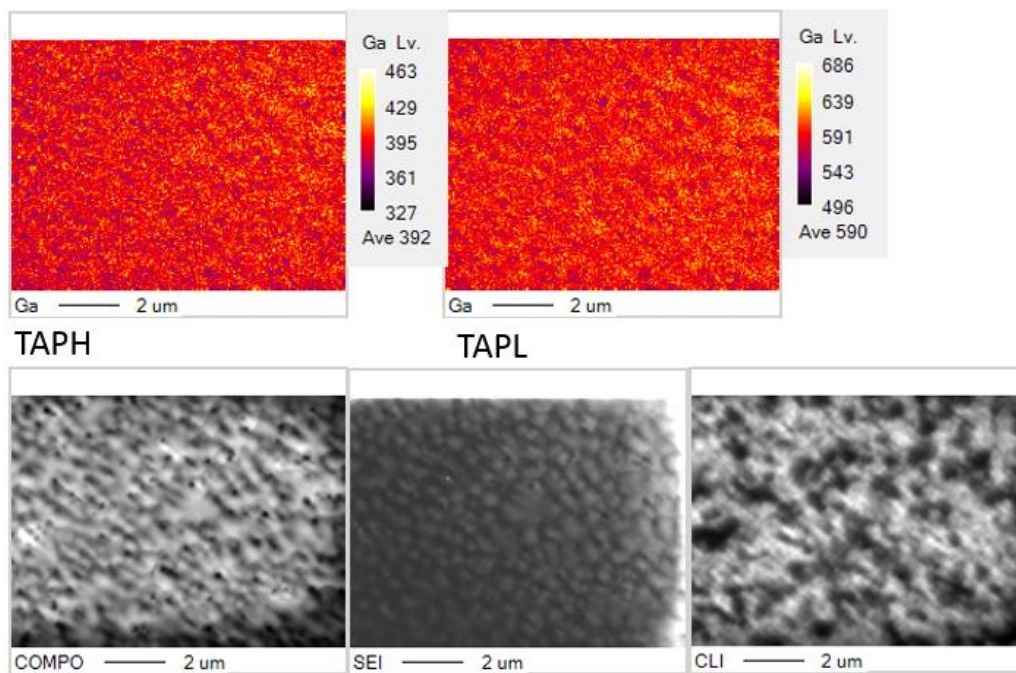
Figure 7.13: N357 WDX map with accompany secondary electron (SE) backscattered electron (BSE) and CL (cathodoluminscence) images acquired with with 15 kV, 40 nA.

Figure 7.13 shows the high resolution WDX map of the Ga L$_\alpha$ X-ray intensity for the sample N357 (acquired from two different spectrometers with different azimuthal take-off angle) as well the BSE (COMPO), SE and CL images. In this case the accelerating voltage was reduced in order to reduce interaction volume and increase spatial resolution, which was necessary due to different surface morphology. From the WDX maps it is possible to see the spatial distribution of Ga in a sample; although it is a bit harder in this case due to the challenging signal-to-noise ratio, it is still possible to notice a variation in the Ga distribution

on sub-µm length scale. Overall, it can be concluded that there is a higher Ga concentration in the middle of round nano-size features. Having acquired WDX intensity maps, it is possible to confirm that the energy variation observed in CL maps is caused by different element distribution.

7.4 CL from LED samples

In the next section, light emission properties of different AlGaN LED samples is studied. The most important difference between the studied samples is the different growth method used for individual layers in the structure. CL will be used to investigate the occurrence of defect peaks in the material, possible variation in composition or changes in intensity of NBE emission.

7.4.1 CL from hybrid 1 and 2 type LEDs

Hybrid 1 structure consists of top MBE p-AlGaN layer and hybrid 2 structure consists of top MBE p-AlGaN layer and MBE p-EBL layer, rest of the layers are MOCVD.
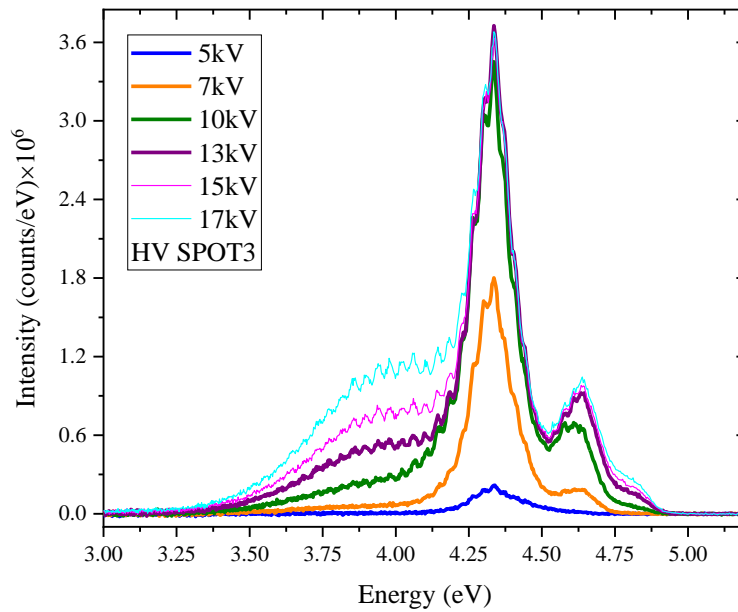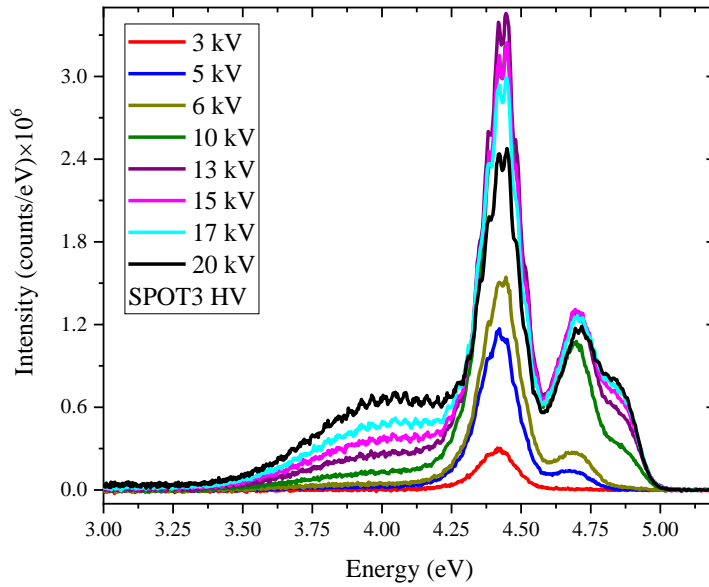
Figure 7.14: Top: sample N361 200 nm of 75% MBE AlGaN on top of MOCVD MQW+LED Bottom: sample N366 MBE grown p-AlGaN EBL on MOCVD MQWs – 160 nm p-GaN.

In the CL spectra of sample N361 the highest intensity peak appears at 4.4 eV, while in sample N366 it is at 4.3 eV. The peak can be attributed to the quantum wells emission or AlGaN MBE layer, more likely QW emission due to the slightly lower emission energy that corresponds to the lower average AlN

content of QW compared to p-AlGaN layer. Surprisingly in sample N361 the peak is already visible at 3kV when 90% of the deposited electron beam energy is confined within first 65 nm of the sample due to the fact that the CL signal results from the recombination of charge carriers, and so the resolution is not depending directly on the spatial distribution of their generation, but on their steady state distribution after carrier transport has been taken into consideration [33]. In sample N366 at 5 kV sampling depth equals to 140 nm. In sample N361 the intensity of the 4.4 eV (N366 at 4.3 eV) peak is increasing with the increase in accelerating voltage from 3 kV to 13. At 15 kV the intensity decreases due to penetration into template region, same behaviour is observed in sample N366. In both samples the maximum peak intensity is achieved at 13 kV, when the electron penetration range is contained within the active LED layers. From 13 kV and above a broad additional peak appears at 3.9 eV associated with the Mg donors [46]. Its intensity is increasing with the increase in voltage from 10 to 20 kV reaching the maximum intensity at 20 kV (17 kV in sample N366). On the high energy side of the spectra another peak appears for accelerating voltages above 5 kV (7 kV for sample N366) at 4.7 eV (sample N366 at 4.6 eV), associated with the NBE emission coming from the n-AlGaN MOCVD layer. The intensity of the peak increases from 5 to 13 kV after which it plateaus around 17 kV before decreasing slightly at 20 kV. The last peak visible in both samples is situated at 4.8 eV and corresponds to emission coming from p-EBL layer, identifiable by the higher peak energy which corresponds to the higher AlN content of the layer. This peak appears at an accelerating voltage of 10 kV and above and its intensity increases with increasing voltage.

The spectrum of sample N372 is not shown here but it shows same peak evolution as in the sample N366, the only difference being the slight blue shift for the quantum well emission at 4.4 eV, with the 4.7 eV NBE emission coming from n-AlGaN MOCVD layer and 4.8 eV from p-EBL layer remaining unchanged. The overall intensity of emission of sample N372 was lower compared to samples N361 and N366. The biggest difference between sample N361 and samples (N366, N372) is in the intensity of the peaks. Sample N361 shows higher intensity for NBE emission peak coming from n-AlGaN MOCVD layer at 4.7 eV and peak from p-EBL layer at 4.8 eV. While sample N366 shows

higher intensity for the 3.9 eV associated with the Mg donors and 4.3 eV peak NBE emission coming from the quantum wells or AlGaN MBE layer.

The change from an MOCVD EBL layer in sample N361 to an MBE EBL layer in sample N366 has resulted in a higher QW intensity. In sample N361 a higher intensity is observed for the MOCVD EBL peak at 4.8 eV, compared to the MBE EBL in sample N366. Higher intensity of the 3.9 eV peak associated with the Mg donors is observed in sample N366 for which Mg concentration is smaller compared to sample N361. It seems that MQB EBL layer in sample N366 compared to single EBL MBE layer in sample N372 has improved the overall emission characteristics of the sample.

7.4.2 CL mapping of LED samples, hybrid 1 and 2 type
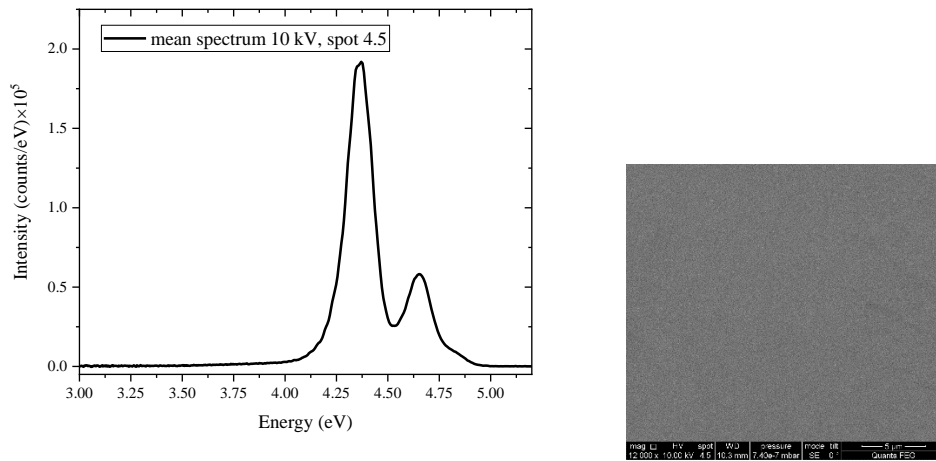
a)
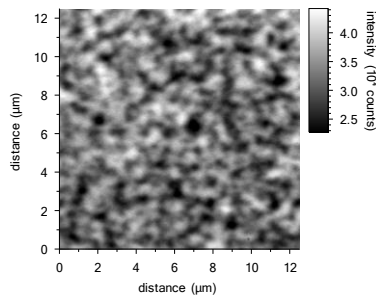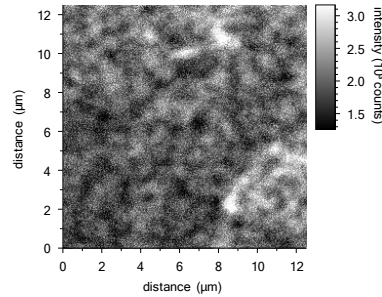
b)   c)
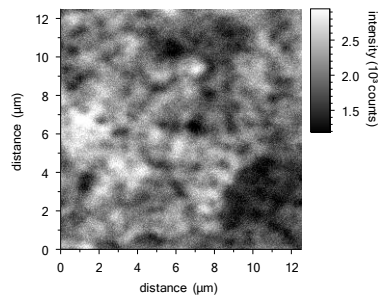
d)
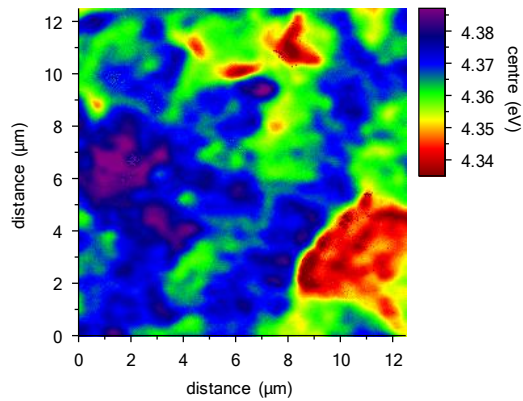
e)
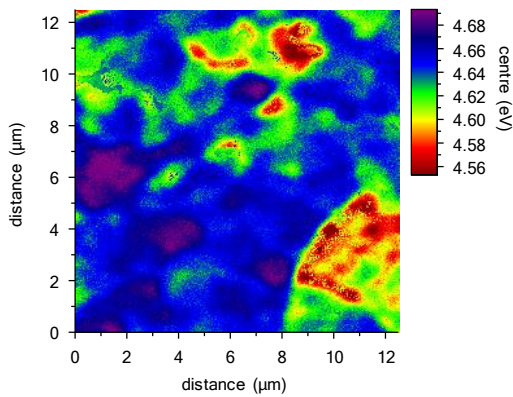
f)

Figure 7.15: Sample N361 map acquired at 10 kV, spot 4.5: a) mean Cl spectrum and SE image; integrated CL intensity maps: b) (4.1−4.5 eV), c) (3.7−4.2 eV) d) (4.7−5.1 eV); fitted peak energy maps: e) 4.4 eV peak f) 4.7 eV peak.

In the mean spectrum extracted from the CL hyperspectral map, two higher intensity peaks are visible: a peak at 4.4 eV, the highest intensity peak, and a peak centred at 4.7 eV of much lower intensity. The lowest intensity peak is also

observable at 4.8 eV. Similar behaviour is observed in the point spectra. The intensity maps of the 4.4 and 4.7 eV peaks (maps b and d) show similar emission characteristics with smaller nanosize regions, but also some larger scale intensity variance.

Even though the integrated intensity map shows smaller nano size regions of higher intensity, similar to those in sample N357, in the peak energy maps of the 4.4 eV (QW emission) and 4.7 eV (MOCVD n-AlGaN) peaks, it seems that the small nano-size regions are indistinguishable in terms of energy and energy variation is confined to larger micron regions. Energy maps of both peaks show similar characteristics, with some small differences. The energy shifts in the energy map of the 4.7 eV peak large shifts occurs over small distances, while for the energy map of the 4.4 eV peak a smaller energy shift occurs over larger regions. The variation in AlN content within micron size regions is also present in the sample due to the energy shifts observed in the maps. Hexagonal features were not observed on the sample surface.
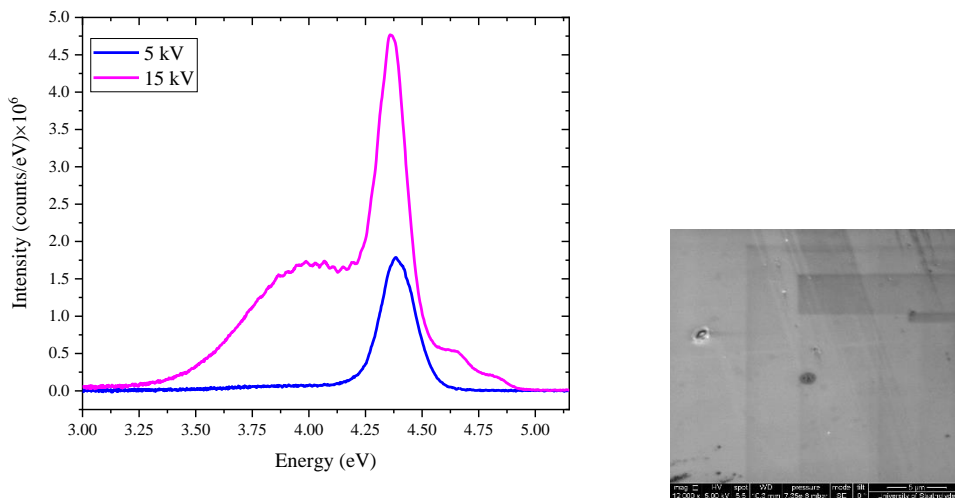
Figure 7.16: Mean CL spectrum from and SE image from sample N366 at 5 and 15 kV.

From the mean spectra extracted from the hyperspectral maps (Figure 7.16) the same behaviour is evident as in the point CL spectra. At 5 kV only one emission peak is present at 4.4 eV assigned to QW emission, while at 15 kV other peaks appear as: the peak at 4.0 eV that is associated with the Mg donors; a 4.6 eV

peak associated with the NBE emission coming from the n-AlGaN MBE layer; and a peak at 4.8 eV that corresponds to emission coming from p-EBL layer.
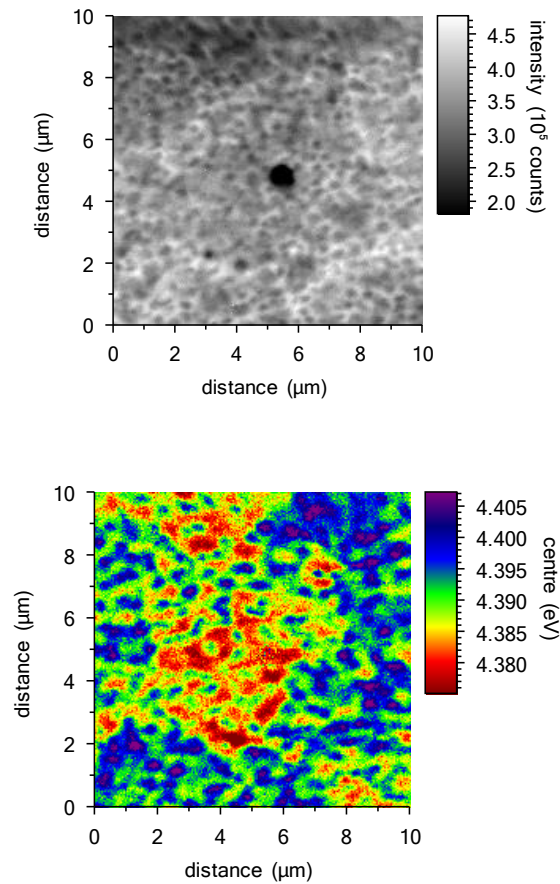
Figure 7.17: Sample N366 map acquired at 5 kV, spot 5.5: integrated CL intensity map (4.2−4.6 eV), peak energy map of the 4.4 eV peak.

Since the peak at 4.4 eV was of the highest intensity in CL point spectra, and it was the only visible peak at 5 kV it is not surprising that is the only peak present in the CL map at 5 kV. In the integrated CL intensity map of the peak, small domains of circular shapes are noticeable, as in the peak energy map (approximately 45 nm in size). The observed shift in the emission energy will correspond to changes in the AlN content, which is restricted to small nano size regions within the sample. In the middle of the map there is quite large pit in the sample and it seems that around it a small nano-size red shifted regions are concentrated. Due to the lattice mismatch between the substrate and the epilayer, threading dislocations occur in the material and they in turn will

introduce the formation of the nanometre size pits in the material [51]. The pit is visible in the CL intensity map as a dark intensity spot.
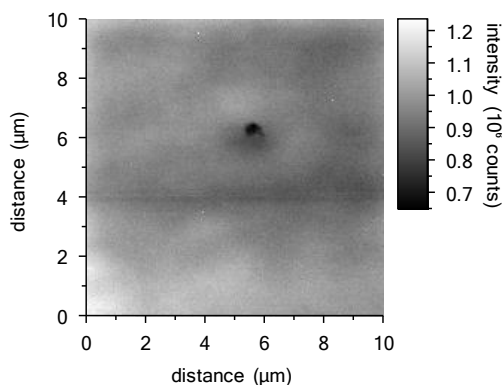
a)
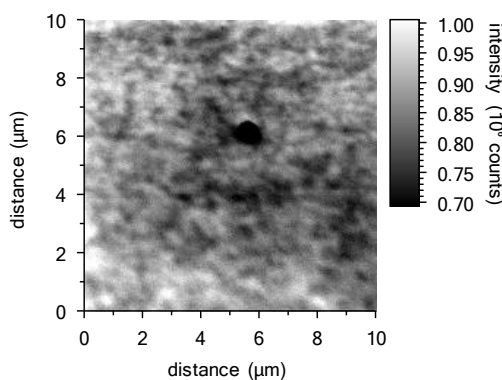
b)
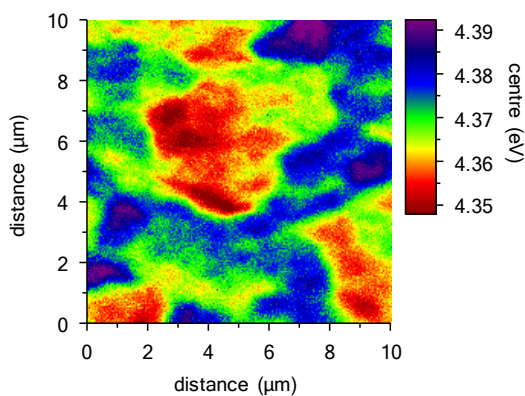
c)

Figure 7.18: CL map acquired from sample N366 at 15 kV, spot 4.5: integrated intensity maps: a) (3.1−4.2 eV) and b) (4.2−4.5 eV); c) peak energy map of the 4.4 eV peak.

The integrated intensity maps acquired at 15 kV (Figure 7.18) and 5 kV (Figure 7.17) show the same emission characteristics, with small domains of circular

shapes present. At 15 kV the integrated intensity maps of the 4.0 eV peak and 4.4 peak are different: while for the 4.4 eV peak (QW emission) small domains are visible, in the 4.0 eV peak (Mg defect), the intensity seems to be of similar intensity along the whole sample surface with a slight increase around the features that appear to be hexagon edges.

The energy map of the 4.4 eV peak shows different emission characteristics at 5 and 15 kV due to the probing of different layers within the LED structure. At 15 kV it is possible to recognise hexagonal features in the map; within the features the energy is redshifted, indicating higher GaN content. Since the hexagonal features are not visible at 5 kV it is possible that n-AlGaN layer contains this 3D features, which could be probed by using a higher accelerating voltage and hence increased penetration depth. At 5 kV the interaction volume is restricted to the MBE top p-AlGaN layer and a small local compositional variation is present, confirmed by a peak energy map of the 4.4 eV peak that exhibits small red shifts within circular domains. From the peak energy maps it is possible to conclude that the compositional difference is smaller for the MBE layers of LED structure when compared to the MOCVD layers.

7.5.1 CL from hybrid 3 type LEDs

Hybrid 3 structure consists of top MBE p-AlGaN layer, MBE p-EBL layer, MBE MQW layers, MBE n-AlGaN layer on the template
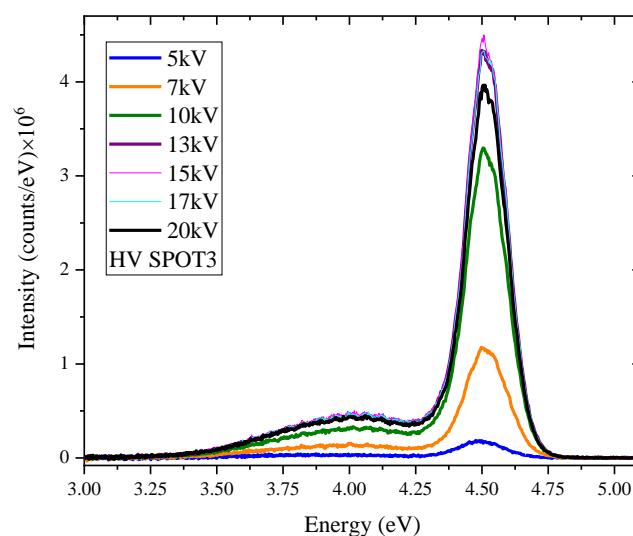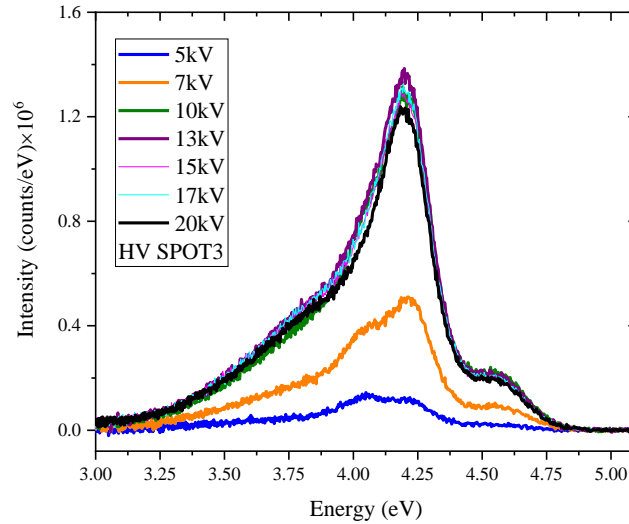
Figure 7.19: CL point spectra from all-MBE LEDs on MOCVD AlN templates: (top) N373 and (bottom) N374.

In the CL spectra of the sample N373 the highest intensity peak appears at 4.5 eV, which can be attributed to the quantum well emisson. The intensity of this peak increases with increasing accelerating voltage from 3 kV to 15 kV after which the intensity decreases due to penetration into template region. Maximum peak intensity is achieved at 15 kV, when the electron penetration range is contained within MBE layers of the LED. From 7 kV and higher, a broad additional peak appears at 3.9 eV associated with the Mg donors (related to the $Mg_{III}^{+}H_i$ complex [46] and Mg^{III} defects) its intensity increasing with the increase in voltage from 3 to 15 kV reaching the maximum intensity at 15, almost the same intensity at 17 kV, and further smaller reduction at 20 kV. Peaks present in hybrid 2 LED samples, such as peaks related to emission from the n-AlGaN MOCVD layer or p-EBL layer are eliminated. The intensity of the QW emission is even higher than in sample N366 (hybrid 2 type structure) and N361 (hybrid 1) but the intensity of the defect Mg donor emission is of lower intensity compared to sample N366 and sample N361. Transition from just the top MBE layer to having MBE layers all the way to the template region has increased overall QW emission and eliminated undesirable luminescence from other layers within the structure.

In the CL spectra of sample N374 the highest intensity peak appears at 4.2 eV, which can be attributed to V_N defect. At 5 and 7 kV accelerating voltages the peak is broad and has two shoulders at 4.05 eV and 4.2 eV. The intensity of the peak increases with increasing accelerating voltage from 5 kV to 13 kV. Above 7 kV a broad shoulder peak appears at 3.8 kV associated with the Mg donors [46]. On the high energy side of the spectrum another peak appears from 7 kV accelerating voltage and above at 4.6 eV, associated with the defect peak luminescence of a $(V_{III}–O_N)^{1-}$ complex [44]. The intensity of the peak increases from 5 to 10 kV, but remains almost the same with further increase in the voltage. Unlike in the case of sample N373, QW emission is not present and the only peak appearing in both samples is the defect peak associated with Mg donors. Samples N373 and N374 are of the same structure, so the difference in their CL spectra is quite surprising. The only differencs are that for the sample N374 the AlN content of the EBL layer is lower (95% compared to pure AlN layer) as well as the AlN content of the MQW layer (70/55 vs 70/60). It is possible that further unintentional differences occurred during the growth of the sample.

7.6 Summary and conclusion

RT-CL spectroscopy was employed to study the impurity transitions and luminescence properties in Mg-doped AlGaN alloy structures.

The first set of samples studied were non-LED samples. One of the samples had stepped Mg concentration and was grown as sample for the determination of Mg concentration by SIMS method. Sample was showing defect peaks associated with Mg donors. By contrast, sample N357 which has only single Mg doping level (not stepped Mg concentration) was free from that defect peak. Surprisingly all of the non-LED samples did not exhibit emission peak from the MBE p-AlGaN layer.

From the SIMS data for the sample with stepped Mg concentration it was evident that the interface between MBE and MOCVD AlGaN layer will be accompanied by an increased level of impurities due to the transfer between reactors. Another conclusion drawn from the SIMS data is that the impurity

signal seems constant through all MBE layers and is lower in MOCVD layers. From the CL hyperspectral maps of the two samples it was determined that the compositional difference is much smaller in the sample with a single Mg level compared to sample grown with stepped Mg concentration, but small local compositional variation was still present, as confirmed with the WDX mapping. The surface of sample with single Mg doping level was free from any hillock features unlike sample with stepped Mg concentration. In that sample the steps formation and step bunching is present, as are a large hexagonal shaped defects. For the sample with single Mg doping level only the surface roughening is present, in terms of small islands formation (2D nucleation growth mode). Sample with single Mg doping has higher AlN content so it seems that with the increase in the AlN mole fraction, phase separation is also reduced [52].

More complicated LED structures were also studied; these are split into three categories, according to the number of MBE layers within the structure. A hybrid 1 structure (sample N361) consisted of a top MBE p-AlGaN layer with the rest of the layers grown with MOCVD. In hybrid 2 structures, the EBL layer is also grown by MBE (samples N372 and N366). Hybrid 2 structures resulted in higher QW intensity. The sample N366 has a special MQB (multiquantum-barrier) EBL structure developed by Prof Hirayama. Comparing the two samples with hybrid 2 structures, this MQB layer has improved the overall emission characteristics of the sample. CL mapping of sample N361 revealed energy shifts due to the variation in AlN content within micron size regions. From the CL maps acquired with different accelerating voltages from sample N366 it was possible to conclude that the compositional difference is smaller for the MBE layers of the LED structure when compared to the MOCVD layers. The third type of hybrid structure (sample N373 and N374) consisted of all-MBE layers on top of the template. Sample N373 has increased overall QW emission and undesirable luminescence from other layers within the structure were eliminated. In general, the presence of the multiple emissions peaks is usually not desirable for optoelectronic applications. For sample N374, the emission properties were surprisingly different: QW emission was absent and the only emission present was from a defect peak, probably because of occurrence of some problems during the growth. Even in hybrid 3, all-MBE sample N373, the defect peak associated with the Mg donors was still present.

Overall, it is possible conclude that emission properties of all MBE sample are superior to other combinations of MBE and MOCVD structures. The main problem with the combination of different growth techniques is the transfer of the sample from one reactor to other and introduction of impurities that will form different defects within material.

MBE layers are compositionally more homogeneous compared to MOCVD layers. A problem with compositional inhomogeneities is that they can lead to band-structure potential fluctuations, but on the positive note they are sufficiently deep that they lead to exciton localization even at room temperature and prevent the carriers from diffusing to point or extended defects in order to recombine non-radiatively [22]. It is not possible to completely eliminate this inhomogeneity, due to the different surface kinetics of Al and Ga adatoms that leads to non-uniform compositions. The local variations in alloy composition observed in rough surfaces are also not desirable since these variations can scatter carriers, broaden emission, and shift threshold voltages. It is therefore necessary to control the surface morphology during the growth of the AlGaN alloys in order to improve the device performance.

Bibliography

1. Chen, J., et al., *Cathodoluminescene study of Mg implanted GaN: the impact of dislocation on Mg diffusion.* Applied Physics Express, 2019. **12**(5): p. 051010.
2. Sheu, J.K. and G.C. Chi, *The doping process and dopant characteristics of GaN.* Journal of Physics: Condensed Matter, 2002. **14**(22): p. R657-R702.
3. Maruska, H.P. and W.C. Rhines, *A modern perspective on the history of semiconductor nitride blue light sources.* Solid-State Electronics, 2015. **111**: p. 32-41.
4. Heber, J., *Nobel Prize 2014: Akasaki, Amano & Nakamura.* Nature Physics, 2014. **10**(11): p. 791-791.
5. Nakamura, S., et al., *Hole Compensation Mechanism of P-Type GaN Films.* Japanese Journal of Applied Physics, 1992. **31**(Part 1, No. 5A): p. 1258-1266.
6. Nakamura, S., T. Mukai, and M. Senoh, *Candela-class high-brightness InGaN/AlGaN double-heterostructure blue-light-emitting diodes.* Applied Physics Letters, 1994. **64**(13): p. 1687-1689.
7. Nakamura, S., *Background Story of the Invention of Efficient InGaN Blue-Light-Emitting Diodes (Nobel Lecture).* Angewandte Chemie International Edition, 2015. **54**(27): p. 7770-7788.
8. *Quantifying Mg doping in AlGaN layers*, in *European Microscopy Congress 2016: Proceedings*. p. 602-603.
9. Reshchikov, M.A., P. Ghimire, and D.O. Demchenko, *Magnesium acceptor in gallium nitride. I. Photoluminescence from Mg-doped GaN.* Physical Review B, 2018. **97**(20): p. 205204.
10. Neugebauer, J. and C.G. Van de wallei, *Role Of Hydrogen And Hydrogen Complexes In Doping Of Gan.* MRS Proceedings, 1996. **423**: p. 619.
11. Deatcher, C., et al., *Wavelength-dispersive x-ray microanalysis as a novel method for studying magnesium doping in gallium nitride epitaxial films.* Semiconductor Science and Technology, 2006. **21**: p. 1287-1295.
12. Johnson, D. and S. Hibbert, *Applications of secondary ion mass spectrometry (SIMS) for the analysis of electronic materials.* Semiconductor Science and Technology, 1992. **7**(1A): p. A180-A184.
13. Klump, A., et al., *Improvement in detection limit for time-of-flight SIMS analysis of dopants in GaN structures.* Journal of Vacuum Science & Technology B, 2018. **36**(3): p. 03F102.
14. Park, J.-S., et al., *Review—Group III-Nitride-Based Ultraviolet Light-Emitting Diodes: Ways of Increasing External Quantum Efficiency.* ECS Journal of Solid State Science and Technology, 2017. **6**: p. Q42-Q52.
15. Ebata, K., et al., *High hole concentration in Mg-doped AlN/AlGaN superlattices with high Al content.* Japanese Journal of Applied Physics, 2018. **57**(4S): p. 04FH09.
16. Neugebauer, J. and C.G. Van de Walle, *Role of hydrogen in doping of GaN.* Applied Physics Letters, 1996. **68**(13): p. 1829-1831.
17. Jeon, S.R., et al., *Investigation of Mg doping in high-Al content p-type AlxGa1−xN (0.3<x<0.5).* Applied Physics Letters, 2005. **86**(8): p. 082107.

18. Zhao, C.-Z., et al., *The activation energy for Mg acceptor in AlxGa1-xN alloys in the whole composition range.* Superlattices and Microstructures, 2017. **109**: p. 758-762.

19. Hasan, M., et al., *Analytical investigation of activation energy for Mg-doped p-AlGaN.* Optical and Quantum Electronics, 2020. **52**: p. 348.

20. Sarkar, B., et al., *N- and P- type Doping in Al-rich AlGaN and AlN.* ECS Transactions, 2018. **86**: p. 25-30.

21. Kinoshita, T., et al., *High p-type conduction in high-Al content Mg-doped AlGaN.* Applied Physics Letters, 2013. **102**(1): p. 012105.

22. Khan, N., et al., *Mg acceptor level in InN epilayers probed by photoluminescence.* Applied Physics Letters, 2007. **91**(1): p. 012101.

23. Imura, M., et al., *Impact of high-temperature growth by metal-organic vapor phase epitaxy on microstructure of AlN on 6H-SiC substrates.* Journal of Crystal Growth, 2008. **310**(7): p. 2308-2313.

24. Nakarmi, M.L., et al., *Electrical and optical properties of Mg-doped Al0.7Ga0.3N alloys.* Applied Physics Letters, 2005. **86**(9): p. 092108.

25. Moustakas, T.D., *Ultraviolet optoelectronic devices based on AlGaN alloys grown by molecular beam epitaxy.* MRS Communications, 2016. **6**(3): p. 247-269.

26. Shatalov, M., et al., *AlGaN Deep-Ultraviolet Light-Emitting Diodes with External Quantum Efficiency above 10%.* Applied Physics Express, 2012. **5**(8): p. 082101.

27. Krames, M.R., et al., *Status and Future of High-Power Light-Emitting Diodes for Solid-State Lighting.* Journal of Display Technology, 2007. **3**(2): p. 160-175.

28. Ren, Z., et al., *AlGaN deep ultraviolet LEDs on bulk AlN substrates.* physica status solidi c, 2007. **4**(7): p. 2482-2485.

29. Khan, A., K. Balakrishnan, and T. Katona, *Ultraviolet light-emitting diodes based on group three nitrides.* Nature Photonics, 2008. **2**(2): p. 77-84.

30. Kolbe, T., et al., *Effect of Electron Blocking Layer Doping and Composition on the Performance of 310 nm Light Emitting Diodes.* Materials (Basel, Switzerland), 2017. **10**.

31. Li, L., et al., *On the Hole Injection for III-Nitride Based Deep Ultraviolet Light-Emitting Diodes.* Materials (Basel, Switzerland), 2017. **10**(10): p. 1221.

32. Kusch, G., et al., *Analysis of doping concentration and composition in wide bandgap AlGaN:Si by wavelength dispersive x-ray spectroscopy.* Semiconductor Science and Technology, 2017. **32**(3): p. 7.

33. Edwards, P.R. and R.W. Martin, *Cathodoluminescence nano-characterization of semiconductors.* Semiconductor Science and Technology, 2011. **26**(6): p. 064005.

34. Jercinovic, M., et al., *Trace analysis in EPMA.* Iop Conference Series: Materials Science and Engineering, 2012. **32**.

35. Jercinovic, M.J., M.L. Williams, and E.D. Lane, *In-situ trace element analysis of monazite and other fine-grained accessory minerals by EPMA.* Chemical Geology, 2008. **254**(3): p. 197-215.

36. Reed, S.J.B., *Quantitative Trace Analysis by Wavelength-Dispersive EPMA.* Microchimica Acta, 2000. **132**(2): p. 145-151.

37. Carpenter, P.K., *Calibrated Procedure for Setting Pulse-Height Parameters in Wavelength-Dispersive Spectrometry.* Microscopy and Microanalysis, 2016. **22**(S3): p. 420-421.

38. Jercinovic, M.J. and M.L. Williams, *Analytical perils (and progress) in electron microprobe trace element analysis applied to geochronology: Background acquisition, interferences, and beam irradiation effects.* American Mineralogist, 2005. **90**(4): p. 526-546.

39. Drouin, D., et al., *CASINO V2.42—A Fast and Easy-to-use Modeling Tool for Scanning Electron Microscopy and Microanalysis Users.* Scanning, 2007. **29**(3): p. 92-101.

40. Limandri, S., A. Carreras, and J. Trincavelli, *Effects of the Carbon Coating and the Surface Oxide Layer in Electron Probe Microanalysis.* Microscopy and microanalysis : the official journal of Microscopy Society of America, Microbeam Analysis Society, Microscopical Society of Canada, 2010. **16**: p. 583-93.

41. Trager-Cowan, C., et al., *Scanning electron microscopy as a flexible technique for investigating the properties of UV-emitting nitride semiconductor thin films.* Photonics Research, 2019. **7**(11): p. B73-B82.

42. Tukiainen, A., et al. *Combined MBE-MOCVD process for high-efficiency multijunction solar cells.* 2016.

43. Jang, H.W., et al., *Investigation of oxygen incorporation in AlGaN/GaN heterostructures.* physica status solidi (c), 2003. **0**(7): p. 2456-2459.

44. Huang, C.-Y., et al., *Suppression of "volcano" morphology and parasitic defect luminescence in AlGaN-based deep-UV light-emitting diode epitaxy.* Results in Physics, 2019. **13**: p. 102285.

45. Nakarmi, M.L., et al., *Photoluminescence studies of impurity transitions in Mg-doped AlGaN alloys.* Applied Physics Letters, 2009. **94**(9): p. 091903.

46. Lyons, J.L., A. Janotti, and C.G. Van de Walle, *Shallow versus Deep Nature of Mg Acceptors in Nitride Semiconductors.* Physical Review Letters, 2012. **108**(15): p. 156403.

47. Edwards, P., et al., *You Do What in Your Microprobe?! The EPMA as a Multimode Platform for Nitride Semiconductor Characterization.* Microscopy and Microanalysis, 2018. **24**: p. 2026-2027.

48. Pownceby, M.I., C.M. MacRae, and N.C. Wilson, *Mineral characterisation by EPMA mapping.* Minerals Engineering, 2007. **20**(5): p. 444-451.

49. Newbury, D.E., et al., *COMPOSITIONAL MAPPING WITH THE ELECTRON-PROBE MICROANALYZER .1.* Analytical Chemistry, 1990. **62**: p. A1159-A1166.

50. Lanari, P., et al., *Quantitative compositional mapping of mineral phases by electron probe micro-analyser.* Geological Society London Special Publications, 2019. **478**: p. 39-63.

51. Liu, X., et al., *Effects of p-AlGaN EBL thickness on the performance of InGaN green LEDs with large V-pits.* Semiconductor Science and Technology, 2015. **31**(2): p. 025012.

52. Gao, M., et al., *Compositional modulation and optical emission in AlGaN epitaxial films.* Journal of Applied Physics, 2006. **100**(10): p. 103512.

Chapter 8

8. Conclusions and Future Work

This chapter summarises the experimental work presented in this thesis and the conclusions presented within different experimental chapters. Based on the experimental results possible future work is also discussed.

8.1 Conclusions

8.1.1 Analysis of AlGaN layers

In Chapter 4 the properties of AlGaN layers grown using MOCVD and MBE techniques on different substrates and with inclusion of different layers, such as buffer layers are explored. This samples can be employed instead of conventional n-GaN channel in metal-insulator-semiconductor field effect transistor (MISFET) devices. The studied samples came from from Sandia National Laboratories, University of South Carolina and Ohio State University. The differences between MOCVD AlGaN layers grown on top of sapphire substrates and grown with additional AlN buffer layers are investigated. In the second section of the chapter, MBE samples grown on different substrates, namely AlN/sapphire templates and native AlN substrates are examined. WDX was employed for the determination of the AlN content in the top AlGaN layers. Optical characterization at room temperature was performed using cathodoluminescence in order to analyse near band edge emission as well as various deep impurity transition peaks. CL and WDX mapping were also utilized to correlate the compositional and optical with surface properties. The characterization of different sets of MOCVD and MBE samples showed that the type of growth method and choice of the substrate has a great influence on the surface morphology and luminescence homogeneity of the AlGaN layer.

For the MOCVD AlGaN on sapphire set, the highest intensity of the NBE emission is observed for sample with highest level of Si doping and lowest AlN content. In addition, the CL energy map revealed variations in the NBE intensity and energy due to occurrence of hexagonal 3D features. WDX and CL mapping

confirmed lower emission energy coming from the middle of the hexagon area due to the lower AlN content and thus chemical inhomogeneity of the sample. The MOCVD sample with the highest AlN at%, showed defect emission which had higher intensity than the NBE emission, although the NBE energy emission is more homogeneous due to lack of 3D features. With the increase of AlN at% in the MOCVD set the intensity of the NBE emission is lower, but chemical homogeneity improves. Addition of an AlN buffer layer for MOCVD sample results in only NBE emission but with reduced intensity which was not expected. Also the FWHM of the NBE peak was smallest within the MOCVD set due to non-optimal growing condition for the AlN buffer layer.

MBE AlGaN/AlN on sapphire sample only shows defect emission peak. NBE emission is absent due to same problem with growth of AlN buffer layer. CL mapping revealed uniform defect emission across the sample.

For the MBE samples grown on native AlN substrate, samples with middle AlN at% exhibit NBE and defect emission. Samples with highest and lowest AlN at% only exhibit defect emissions and no NBE peak. Overall, chemical homogeneity of MBE samples is improved compared to MOCVD samples. It is possible to conclude that the same type of impurity emission is present in both MOCVD and MBE samples. The different textures of the MOCVD and MBE samples are confirmed, with compositional inhomogeneity of the MBE samples on sub µm level compared to µm size inhomogeneity observed in MOCVD samples. The MBE emission intensity is also lower compared to MOCVD samples probably due to vast majority of threading dislocations occurring at the boundaries of the nano-size domains. Alloy fluctuations in MBE samples will affect the sample mobility and have negative effect on the device performance, such as transistor current density.

8.1.2 Measurement of Si at low concentration

Chapter 5 explains challenges associated with trace element measurements using WDX in EPMA. Detailed steps of the procedure to accurately quantify trace elements are presented. The whole process of measurement optimization is described and final recipe on how to measure the concentration of major (alloy) and minor Si (dopant) elements is presented. Samples employed in this

chapter consisted of different AlGaN and GaN:Si doped samples originating from multiple sources including: Tyndall Institute, Technische Universität Berlin (TUB), IQE Ltd. The previously reported limitation of over-estimated Si content was thoroughly investigated and the problem was assigned to the unavoidable contamination of the sample surfaces with Si. An analytical routine was introduced for measuring trace Si levels, consisting of separate measurement of Si with high current and long counting times followed by calibration using SIMS measurements in order to correct for the overestimation in measured Si concentration. By measuring silicon intensities and using a calibration curve method obtained from SIMS data on the same samples, along with calculated ZAF correction values it was possible to determine doping levels of order $(3–10) \times 10^{18}$ cm^{-3} in Al$_x$Ga$_{1-x}$N layers with varying AlN contents and polarity.

8.1.3 Polar and semipolar Si-doped AlGaN alloys

Chapter 6 reports on a systematic study of polar and semipolar n-type doped AlGaN/AlN layers grown on sapphire by (MOCVD) with varied Si/group-III ratios in the gas phase. The samples were provided by the group of Prof. P. J. Parbrook (Tyndall National Institute). The samples studied had Si concentrations in the range from 2×10^{18} cm^{-3} to 1×10^{19} cm^{-3}, and are grown along polar (0001) and semipolar (11-22) planes. This chapter explores how the different AlGaN crystal orientations affect group-III composition and Si incorporation. WDX microanalysis and CL spectroscopy were used to evaluate the doping characteristics and optical properties of samples. The Si-doping concentration was measured by WDX, using calibration data from SIMS (as in Chapter 5). Comparison of the measured AlN alloy fraction for samples with different crystal orientations showed that the AlN incorporation was higher in the polar samples. The highest values of Si incorporations were observed for the polar samples with the highest Si/III ratios, while saturation of Si incorporation was seen for the semipolar samples at higher Si/III ratios. CL spectroscopy allowed analysis of near band edge emission as well as various deep impurity transition peaks. CL hyperspectral imaging of the polar samples revealed significant reductions in near-band-edge luminescence intensity from the middle of surface hexagonal features where a threading dislocation is expected

to be terminated. CL point spectra showed how changes in the relative intensity of the NBE peaks and impurity transitions depend strongly on the growth conditions and surface orientations. WDX mapping confirmed higher Ga incorporation around the hexagon edges. The semipolar samples showed no such features, corresponding to a better compositional homogeneity. The analysis of CL data can help reduce point defect densities by guiding the optimisation of growth parameters. The technique is potentially also informative for other layers grown under similar conditions where point defects cannot be directly measured, such as quantum wells (QWs). The CL and WDX results presented in this chapter provide information on how point defect incorporation in the doped AlGaN contact layers is influenced by crystal orientation, alloy composition, and Si incorporation, as well as on the existence of different compensating defects. This chapter also highlights challenges associated with growth of high AlN content AlGaN layers such as the occurrence of hexagonal platelet structures in c-plane samples and compositional inhomogeneity.

8.1.4 Measurement of Mg at low concentration at low concentration

In the first section of Chapter 7 the accuracy of the WDX technique was checked for the analysis of Mg dopant concentration by comparing the data to SIMS results obtained by growers. This GaN: Mg samples were grown by Drs. Chris Deatcher and Ian Watson using MOCVD technique at Strathclyde University. It was demonstrated how to use WDX technique for the measurement of Mg dopant concentration and how to optimize analytical conditions (e.g., accelerating voltage, beam current, etc.). It was demonstrated how care must be taken to avoid interfering peaks of other elements both on the peak and the background positions and how important is to correctly set the PHA baseline and window positions.

The second part of the chapter covered AlGaN:Mg samples originating from Nanjing University. They are grown using a combination of MBE and MOCVD epitaxial techniques. This is done in order to benefit from the separate advantages of each technique: the high quality of the MBE layer and the fast growth rate offered by MOCVD. At the moment, the MBE method falls behind MOCVD in terms of growth rates or throughput in fabrication, so the

combination of methods offers a solution to overcome this problem. Samples were characterised by CL to study the impurity transitions and luminescence properties in Mg-doped AlGaN alloys structures. They consisted of non LED epilayer samples grown on MOCVD AlN/sapphire template and more complicated LED structures, these were split into three categories, according to the number of MBE layers within the structure. A hybrid 1 structure consisting of a top MBE p-AlGaN layer with the rest of the layers being MOCVD grown. In hybrid 2 structure, the EBL layer is also grown by MBE. One sample contained a special MQB (multiquantum-barrier) EBL structure developed by Prof Hirayama. The third type of the hybrid structure consisting of all MBE-grown layers on top of the template.

One of the non-LED samples had stepped Mg concentration and was grown as a test sample for the determination of Mg concentration by SIMS method. This sample showed defect peaks associated with Mg donors. On the contrary, the non-LED sample with single Mg doping (not stepped Mg concentration) was free of defect emission. Surprisingly none of the non-LED samples exhibited emission peaks from the MBE p-AlGaN layer. From the SIMS data for the non-LED sample with stepped Mg concentration it was evident that the point of the interface between MBE and MOCVD AlGaN layer will be accompanied with the increase of impurities level due to the transfer between reactors. Another conclusion drawn from the SIMS data is the impurities signal seems constant through all MBE layers and that the impurity signal from MOCVD layers is lower. From the CL hyperspectral maps of the two samples it was determined that the compositional difference is much smaller in the sample with single Mg level compared to sample with stepped Mg levels, but still small local compositional variation was present, as was also confirmed with the WDX mapping. The surface of the sample with single Mg doping was free from any hillock features unlike the sample with stepped Mg levels. In that sample step formation and step bunching are present, as well as the presence of large hexagonal shaped defects. While for the sample with single Mg level only the surface roughening is common, in terms of small islands formation (2D nucleation growth mode). For that sample higher AlN content is also measured and it was possible to conclude that with the increase in the AlN mole fraction, phase separation is also reduced.

Hybrid 2 structure resulted in higher QW intensity compared to hybrid 1 structure. Comparing two samples with hybrid 2 structures, MQB layer has improved overall emission characteristics of the sample. CL mapping of other hybrid 2 sample revealed energy shifts due to the variation in AlN content within micron size regions. From the CL maps acquired with different accelerating voltages of sample with MQB layer it was possible to conclude that the compositional difference is smaller for the MBE layers of LED structure when compared to the MOCVD layer. One of the samples from the third type of the hybrid structure has increased overall QW emission and undesirable luminescence from other layers within the structure were eliminated, but the defect peak associated with the Mg donors was still present. For other samples with hybrid 3 structure, emission properties were surprisingly different. QW emission was absent and the only emission present was from defect peak, probably because of occurrence of some problems during the growth.

Overall, it is possible to conclude that emission properties of all MBE sample are superior to other combinations of MBE and MOCVD structures. The main problem with the combination of different growth techniques is the transfer of sample from one reactor to other and introduction of impurities that will form different defects within material. The University of California Santa Barbara (UCSB) has been developing a hybrid technique to create III-nitride tunnel junctions (TJs) using a combination of MOCVD and MBE methods, the n-type side of the tunnel junction was grown by MOCVD on the MBE p-GaN . Unlike p-GaN grown by MOCVD, p-GaN grown by MBE is conductive as grown, which allows for its use in a tunnel junction. A commonly explored limitation of p-GaN is that it is a poor current spreading layer and that traditional p-contacts will increase operating voltages in III-nitride devices. The introduction of tunnel junctions solves these issues. This type of the tunnel junctions could replace indium tin oxide (ITO) current-spreading layers with n-type gallium nitride (GaN) in light-emitting diodes and lasers. In their work they have found that the hydrogen level which is responsible for the passivation of the magnesium doping, is several orders of magnitude lower in the ammonia MBE than that found in MOCVD growth processes. They have also found that the presence of oxygen at the interface will lead to formation of the donor–acceptor complex between O and Mg at the interface. This complex will effectively

prevent free surface Mg from incorporating into the n-side of the TJ during regrowth which could lead to a more abrupt drop-off in Mg concentration, improving the tunnelling through the depletion layer and ultimately enhancing performance of the device. The tunnel junction LED showed a lower forward operating voltage and a higher efficiency at a low current density than the transparent conducting oxide (TCO) layer LED.

MBE layers studied in this thesis are showing more compositional homogeneity compared to MOCVD layers. However, it is not possible to completely eliminate the inhomogeneity seen in MBE samples, due to the different surface kinetics of Al and Ga adatoms. It was concluded how it is necessary to control the surface morphology during the growth of the AlGaN alloys in order to improve the device performance.

8.2 Future work

Future research on AlGaN materials is necessary in order to optimize the material properties for which demand is rapidly increasing. Both n- and p-type AlGaN layers are needed in devices for electronic and optoelectronic applications, such as LED structures, lateral and vertical transistor devices, AlGaN PiN Diodes or for heterogeneous integration devices. AlGaN is growing in importance with its use in the next generation of RF Devices, such as HEMTs and it is targeting high-power devices. The advantageous material properties of AlGaN is the main driver for its usage in the power electronics, such as strong scaling of the critical electric field for avalanche breakdown with increasing AlN content, which results in a very favourable figure of merit for devices.

The material demands on this device are much more stringent and in order to address the limitations on p-type doping and n-type doping efficiencies, better understanding of compensation mechanisms and the deep impurity levels are necessary. The first-principles calculations of total energies within the framework of density functional theory may be further connected with the experimental results to study dopants incorporation behaviour and occurrence of different defect levels. The ultimate goal is to achieve effective doping

without compromising material quality in order to obtain high efficiency of AlGaN based devices.

It is necessary to continue studying material properties, because the experimental findings can significantly help growers in optimisation of growth parameters. At the moment literature overview regarding examination of growth parameters is scarce, that will hopefully change in the future in order to help guide growers so they can optimize the material properties.

Collaboration with multiple groups for the growth of these device, in terms of broadening the group of collaborators, so that samples from multiple sources can be compared in order to help us better understand the influence of the various growth parameters on the quality of the material in terms of composition, doping levels, cathodoluminescence and defects luminescence.

AlGaN structures are grown by either metal-organic vapor phase epitaxy or molecular beam epitaxy, some of the benefits of MBE grown layers such as better compositional uniformity of the layers was shown in this thesis. Still more work has to be done in optimizing growth methods, especially on how to avoid transfer between different growth chambers, which has shown to introduce some defects in the material and hinder near band edge emission properties.

AlGaN layers with relatively low dislocation density are required for different applications, and the problem is of course availability of the lattice matched substrates. At present, both free-standing bulk GaN and AlN can be used, but their lattice parameters are still significantly different, resulting in high threading dislocation densities. As a result, AlGaN-based UV light-emitting diodes suffer in terms of efficiency, steady operations, and lifetime. More work has to be done on finding the best substrate, such as the recent reports on free-standing wurtzite films grown by plasma assisted MBE method.

WDX method has showed extremely valuable for studying semiconductor properties, so it was necessary to find the optimum protocol for measuring of major element composition, and to use the best practise for trace element measurements. So far discrepancy was found between SIMS and WDX Si doping levels and a way forward was proposed using a new calibration method enabled calculation of Si level using EPMA instrument. Future work will consist

of collection of additional SIMS and WDX data in order to check the method. SIMS data for samples covering a wide range of Si doping levels (specially for the ranges for which data is not available at the moment) could help in refining proposed calibration method. Also, it would be interesting to compare results obtained with different SIMS techniques, such as Dynamic-SIMS and Time-of-Flight SIMS.

Further improvement in WDX technique will open new realms in trace element analysis. Certainly some aspects of WDX analysis have to be further investigated, as influence of crystallographic orientation on dopant signal, effect of the spectrometer dead time, different matrix corrections etc. Apart from quantitative abilities of the EPMA instrument, another major advantage lies in the correlation of WDX data with other microscopy techniques such as CL and ECCI as well as the high resolution mapping capabilities. Therefore, more work has to done on simultaneous collection of multiple signals because acquired multispectral data sets will provide detailed chemical and structural information of semiconductor materials at high spatial resolution.

Overall, the results presented in this thesis indicate a promising future for versatile nitride based devices.